Jordan Journal of Mechanical and Industrial Engineering (JJMIE)

JJMIE is a high-quality scientific journal devoted to fields of Mechanical and Industrial Engineering. It is published by The Hashemite University in corporation with the Jordanian Scientific Research Support Fund.

SUBMISSION ADDRESS:

Prof. **Mousa S. Mohsen**, Editor-in-Chief
Jordan Journal of Mechanical & Industrial Engineering,
Hashemite University,
PO Box 330127, Zarqa, 13133 , Jordan
E-mail: jjmie@hu.edu.jo

Hashemite Kingdom of Jordan

Hashemite University

Jordan Journal of Mechanical and Industrial Engineering

JJMIE

An International Peer-Reviewed Scientific Journal

http://jjmie.hu.edu.jo/

ISSN 1995-6665

Jordan Journal of Mechanical and Industrial Engineering (JJMIE)

JJMIE is a high-quality scientific journal devoted to fields of Mechanical and Industrial Engineering. It is published by The Jordanian Ministry of Higher Education and Scientific Research in corporation with the Hashemite University.

Introduction: The Editorial Board is very committed to build the Journal as one of the leading international journals in mechanical and industrial engineering sciences in the next few years. With the support of the Ministry of Higher Education and Scientific Research and Jordanian Universities, it is expected that a heavy resource to be channeled into the Journal to establish its international reputation. The Journal's reputation will be enhanced from arrangements with several organizers of international conferences in publishing selected best papers of the conference proceedings.

Aims and Scope: Jordan Journal of Mechanical and Industrial Engineering (JJMIE) is a refereed international journal to be of interest and use to all those concerned with research in various fields of, or closely related to, mechanical and industrial engineering disciplines. Jordan Journal of Mechanical and Industrial Engineering aims to provide a highly readable and valuable addition to the literature which will serve as an indispensable reference tool for years to come. The coverage of the journal includes all new theoretical and experimental findings in the fields of mechanical and industrial engineering or any closely related fields. The journal also encourages the submission of critical review articles covering advances in recent research of such fields as well as technical notes.

Guide for Authors

Manuscript Submission

High-quality submissions to this new journal are welcome now and manuscripts may be either submitted online or mail.

Online: For online submission upload one copy of the full paper including graphics and all figures at the online submission site, accessed via E-mail: jjmie@hu.edu.jo. The manuscript must be written in MS Word Format. All correspondence, including notification of the Editor's decision and requests for revision, takes place by e-mail and via the Author's homepage, removing the need for a hard-copy paper trail.

By Mail: Manuscripts (1 original and 3 copies) accompanied by a covering letter may be sent to the Editor-in-Chief. However, a copy of the original manuscript, including original figures, and the electronic files should be sent to the Editor-in-Chief. Authors should also submit electronic files on disk (one disk for text material and a separate disk for graphics), retaining a backup copy for reference and safety.

Note that contributions may be either submitted online or sent by mail. Please do NOT submit via both routes. This will cause confusion and may lead to delay in article publication. Online submission is preferred.

Submission address and contact:

Prof. **Mousa S. Mohsen**, Editor-in-Chief
Jordan Journal of Mechanical & Industrial Engineering,
Hashemite University,
PO Box 330127, Zarqa, 13115 , Jordan
E-mail: jjmie@hu.edu.jo

Types of contributions: Original research papers

Corresponding author: Clearly indicate who is responsible for correspondence at all stages of refereeing and publication, including post-publication. Ensure that telephone and fax numbers (with country and area code) are provided in addition to the e-mail address and the complete postal address. Full postal addresses must be given for all co-authors.

Original material: Submission of an article implies that the work described has not been published previously (except in the form of an abstract or as part of a published lecture or academic thesis), that it is not under consideration for publication elsewhere, that its publication is approved by all authors and that, if accepted, it will not be published elsewhere in the same form, in English or in any other language, without the written consent of the Publisher. Authors found to be deliberately contravening the submission guidelines on originality and exclusivity shall not be considered for future publication in this journal.

Supplying Final Accepted Text on Disk: If online submission is not possible: Once the paper has been accepted by the editor, an electronic version of the text should be submitted together with the final hardcopy of the manuscript. The electronic version must match the hardcopy exactly. We accept MS Word format only. Always keep a backup copy of the electronic file for reference and safety. Label the disk with your name. Electronic files can be stored on CD.

Notification: Authors will be notified of the acceptance of their paper by the editor. The Publisher will also send a notification of receipt of the paper in production.

Copyright: All authors must sign the Transfer of Copyright agreement before the article can be published. This transfer agreement enables Jordan Journal of Mechanical and Industrial Engineering to protect the copyrighted material for the authors, but does not relinquish the authors' proprietary rights. The copyright transfer covers the exclusive rights to reproduce and distribute the article, including reprints, photographic reproductions, microfilm or any other reproductions of similar nature and translations.

PDF Proofs: One set of page proofs in PDF format will be sent by e-mail to the corresponding author, to be checked for typesetting/editing. The corrections should be returned within 48 hours. No changes in, or additions to, the accepted (and subsequently edited) manuscript will be allowed at this stage. Proofreading is solely the author's responsibility. Any queries should be answered in full. Please correct factual errors only, or errors introduced by typesetting. Please note that once your paper has been proofed we publish the identical paper online as in print.

Author Benefits

Page charge: Publication in this journal is free of charge.
Free off-prints: Three journal issues of which the article appears in along with twenty-five off-prints will be supplied free of charge to the corresponding author. Corresponding authors will be given the choice to buy extra off-prints before printing of the article.

Manuscript Preparation:

General: Editors reserve the right to adjust style to certain standards of uniformity. Original manuscripts are discarded after publication unless the Publisher is asked to return original material after use. If online submission is not possible, an electronic copy of the manuscript on disk should accompany the final accepted hardcopy version. Please use MS Word for the text of your manuscript.

Structure: Follow this order when typing manuscripts: Title, Authors, Affiliations, Abstract, Keywords, Introduction, Main text, Conclusions, Acknowledgements, Appendix, References, Figure Captions, Figures and then Tables. For submission in hardcopy, do not import figures into the text - see Illustrations. For online submission, please supply figures imported into the text AND also separately as original graphics files. Collate acknowledgements in a separate section at the end of the article and do not include them on the title page, as a footnote to the title or otherwise.

Text Layout: Use double spacing and wide (3 cm) margins. Ensure that each new paragraph is clearly indicated. Present tables and figure legends on separate pages at the end of the manuscript. If possible, consult a recent issue of the journal to become familiar with layout and conventions. All footnotes (except for table and corresponding author footnotes) should be identified with superscript Arabic numbers. To conserve space, authors are requested to mark the less important parts of the paper (such as records of experimental results) for printing in smaller type. For long papers (more that 4000 words) sections which could be deleted without destroying either the sense or the continuity of the paper should be indicated as a guide for the editor. Nomenclature should conform to that most frequently used in the scientific field concerned. Number all pages consecutively; use 12 or 10 pt font size and standard fonts. If submitting in hardcopy, print the entire manuscript on one side of the paper only.

Corresponding author: Clearly indicate who is responsible for correspondence at all stages of refereeing and publication, including post-publication. The corresponding author should be identified with an asterisk and footnote. Ensure that telephone and fax numbers (with country and area code) are provided in addition to the e-mail address and the complete postal address. Full postal addresses must be given for all co-authors. Please consult a recent journal paper for style if possible.

Abstract: A self-contained abstract outlining in a single paragraph the aims, scope and conclusions of the paper must be supplied.

Keywords: Immediately after the abstract, provide a maximum of six keywords (avoid, for example, 'and', 'of'). Be sparing with abbreviations: only abbreviations firmly established in the field may be eligible.

Symbols: All Greek letters and unusual symbols should be identified by name in the margin, the first time they are used.

Units: Follow internationally accepted rules and conventions: use the international system of units (SI). If other quantities are mentioned, give their equivalent in SI.

Maths: Number consecutively any equations that have to be displayed separately from the text (if referred to explicitly in the text).

References: All publications cited in the text should be presented in a list of references following the text of the manuscript.

Text: Indicate references by number(s) in square brackets in line with the text. The actual authors can be referred to, but the reference number(s) must always be given.

List: Number the references (numbers in square brackets) in the list in the order in which they appear in the text.

Examples:

Reference to a journal publication:

[1] M.S. Mohsen, B.A. Akash, "Evaluation of domestic solar water heating system in Jordan using analytic hierarchy process". Energy Conversion & Management, Vol. 38, No. 9, 1997, 1815-1822.

Reference to a book:

[2] Strunk Jr W, White EB. The elements of style. 3rd ed. New York: Macmillan; 1979.

Reference to a conference proceeding:

[3] B. Akash, S. Odeh, S. Nijmeh, "Modeling of solar-assisted double-tube evaporator heat pump system under local climate conditions". 5th Jordanian International Mechanical Engineering Conference, Amman, Jordan, 2004.

Reference to a chapter in an edited book:

[4] Mettam GR, Adams LB. How to prepare an electronic version of your article. In: Jones BS, Smith RZ, editors. Introduction to the electronic age, New York: E-Publishing Inc; 1999, p. 281-304

Free Online Color: If, together with your accepted article, you submit usable color and black/white figures then the journal will ensure that these figures will appear in color on the journal website electronic version.

Tables: Tables should be numbered consecutively and given suitable captions and each table should begin on a new page. No vertical rules should be used. Tables should not unnecessarily duplicate results presented elsewhere in the manuscript (for example, in graphs). Footnotes to tables should be typed below the table and should be referred to by superscript lowercase letters.

JJMIE

Volume 5, Number 6, Dec. 2011
ISSN 1995-6665
Pages 478 - 482

Jordan Journal of Mechanical and Industrial Engineering

Finite element analysis for short term O-ring relaxation

Mohammed Diany*,[a] , Hicham Aissaoui[b]

[a]Mechanical Engineering Dept, Faculté des Sciences et Techniques de Béni Mellal, Mghila BP 523 Béni Mellal, 23000 Morocco
[b]Electrical Engineering Dept, Faculté des Sciences et Techniques de Béni Mellal, Mghila BP 523 Béni Mellal, 23000 Morocco

Abstract

O-rings are used in machine devices like the seals components. They are inexpensive, and have simple mounting requirements. In this article, an axisymmetric finite element model is proposed to study the O-ring relaxation during the first day of its installation in the unrestrained axial loading case. The results of the numerical model are compared with those of an analytical approach based on the classical Hertzian theory of the contact. The contact stress profiles and the peak contact stresses are determined versus the time relaxation in order to specify the working conditions thresholds.

Keywords: O-ring; contact pressure; analytical modelling;relaxation; FEA

Nomenclature

F	total compression load (N)
e	initial O-ring axial displacement (mm)
d	the O-ring cross-section diameter (mm)
D	the O-ring mean diameter (mm)
C	the ratio e/d
R	the axial compression ratio
b	the contact width between the gasket and plat (mm)
x	radial position compared to the vertical axis of the O-ring cross-section (mm)
p_o	maximum contact pressure value or peak contact stress (MPa)
E_{relax}	relaxation modulus (MPa)
E_i	elastic modulus for gasket (MPa)
α_i	coefficient
τ_i	relaxation time (s)

F	total compression load (N)
e	initial O-ring axial displacement (mm)
d	the O-ring cross-section diameter (mm)
D	the O-ring mean diameter (mm)
C	the ratio e/d
R	the axial compression ratio
b	the contact width between the gasket and plat (mm)
x	radial position compared to the vertical axis of the O-ring cross-section (mm)
p_o	maximum contact pressure value or peak contact stress (MPa)
E_{relax}	relaxation modulus (MPa)
E_i	elastic modulus for gasket (MPa)
α_i	coefficient
τ_i	relaxation time (s)

1. Introduction

The elastomeric O-ring gaskets are widely used in hydraulic and pneumatic equipments to ensure the sealing of shafts, pistons and lids. The correct operation is due to the good tightening of the joint that generate a contact pressures able to confine the fluids inside a rooms or to prevent their passage from one compartment to another.

Several studies are carried out to model the O-ring behaviour but without taking in account the effect of the relaxation and creep phenomena. The equations developed until today to determine analytically the distribution and the values of the contact pressure are deduced from the conventional Hertzian theory of the contact [1]. The correct operation of the O-ring is conditioned, on the one hand, by the maximum value of the contact pressure created during the O-ring compression and on the other hand by maintaining in operating stage a minimal threshold value below which the sealing of the joint is blamed. So the evaluation of the maximum value of contact pressure evolution in time has a primary importance to ensure the correct O-ring function during its nominal lifespan. In this article, it is proposed to study the O-ring relaxation during the first hours of its installation in the unrestrained axial loading case, figure 1.

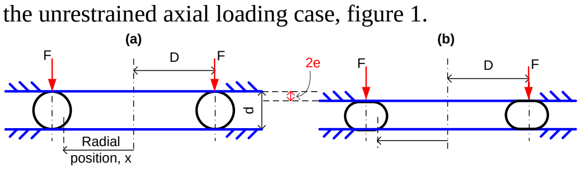

Figure 1: Unrestrained axial loading assembly.

* Corresponding author. e-mail: mdiany@yahoo.com

2. Background

Several teams were interested in O-ring assembly used in various industrial services. A temporal reading of published works on this subject can be classified on three categories. An analytical approach based in all cases on the Hertzian classical theory, an experimental part using various assemblies allowing to characterize the O-ring itself in traction and compression loads and to model its real behaviour. In the third shutter, finite elements models are developed to numerically simulate assemblies with the O-ring.

George and al. [2] used a finite elements model to study the behaviour of the O-ring compressed between two plates. The gasket characteristics were introduced into the program according to parameter defining the total deformation energy or by using the Neo-Hookean model. The results of this analysis were compared with those of several experimental studies and analytical approaches based on the Hertzian theory. Dragoni et al. [3] proposed an approximate model to study the O-ring behaviour placed in rectangular grove. The influence of the grove dimensions variation and the friction coefficient was investigated.

The work of I. Green and C. English [4] reviewed the majority of used O-rings configurations. A finite elements Models were developed considering hyperelasticity behaviour. The results of these models were confronted with those of empirical studies. New relations expressing the maximum contact pressure and the width of contact were proposed. Rapareilli et al. [5] present a validation of the experimental results by a numerical model which regarded the joint as an almost incompressible elastic material. The effects of the fluid pressure as well as the friction effect between the gasket and the shaft are studied. The two part of the study were in perfect agreement. In an experimental study [6], the authors tried to determine the influence of the fluid pressure on the contact pressure which ensures of sealing as well as the ageing deterioration of the joint. Kim et al. [7, 8] tried to find an approximate solution for the mechanical behaviour of the O-ring joints in several configurations. The influence of the friction coefficient is highlighted. An experimental study was carried out to find more realistic elastic modulus values for elastomeric O-ring. They compared their results with those obtained in experiments and by the finite element analysis. They found that the values given by the Lindley [9, 10] to calculate the compressive force are similar to those determined by the finite elements model. The O-ring relaxation was treated by K.T. Gillen et al. [11]. In this study, the O-ring degradation is caused by oxidation or nuclear irradiation. The authors describe several improvements to the methods used in there previous studies like substituting the O-ring segments for difficult-to-prepare a mini-disk samples.

In this article, a 2D axisymmetric model is developed to simulate the O-ring relaxation when it is axially compressed by initial tightening between two rigid plans. The effect of the temporal variation of the longitudinal elasticity modulus as well as the influence of the axial compression ratio will be analyzed. The model of the classical contact theory will be confronted with the results of the numerical study. The O-ring material behaviour is similar to the stuffing-box packings one used to study the creep and relaxation phenomena [12].

3. Conventional analytic Theory

Most of the work dedicated to the study of the O-ring gasket behaviour used the same analytical model based on the Hertzian theory of the pressure contact. By adopting this classical theory, Lindley [9, 10] developed a simple approximate formula, relation (1), expressing the compressive force, F, according to the ratio of initial compressed displacement by the cross-section O-ring diameter, $C = \frac{e}{d}$.

$$F = \pi DdE(1.25.C^{\frac{3}{2}} + 50.C^{6}) \tag{1}$$

The same theory allowed determining the contact width, b, and the maximum value of the contact stress po, according to the formulas (2) and (3).

$$b = d.\sqrt{\frac{6}{\pi}(1.25.C^{\frac{3}{2}} + 50.C^{6})} \tag{2}$$

$$p_o = 4.E.\sqrt{\frac{(1.25.C^{\frac{3}{2}} + 50.C^{6})}{6\pi}} \tag{3}$$

The contact pressure distribution according to the radial position on the gasket is given by the equation (4).

$$p(x) = p_0\sqrt{1-\left(\frac{2x}{b}\right)^2} \tag{4}$$

These formulas do not utilize the mechanical characteristics of the plates in contact with the joint. Only the O-ring longitudinal elasticity modulus, E, are used. By consequence, the same equations remain valid for the evolution study of the O-ring behaviour according to time but using a time varying Young modulus, called relaxation modulus E_{relax}. The viscoelastic behaviour of the gasket is given by the modified Maxwell model [13], presented in figure 2.

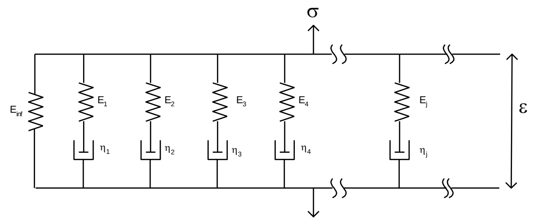

Figure 2: A generalized Maxwell model.

The relaxation modulus is defined by the following equation:

$$E_{relax}(t) = E_{\infty} + \sum_{j} E_j e^{-\frac{t}{\tau_j}} \tag{5}$$

With

$$\alpha_j = \frac{E_j}{E_\infty} \quad \text{and} \quad E_0 = E_\infty + \sum_j E_j \tag{6}$$

The relaxation modulus of the equation (5) becomes:

$$E_{relax}(t) = E_0\left[1 - \sum_j \alpha_j (1 - e^{-\frac{t}{\tau_j}})\right] \tag{7}$$

The initial elasticity modulus, E_0, and the eight coefficients α_j, called Prony series coefficients, are deduced from the experimental data of the reference [14].

The relaxation study aims to evaluate the variation of the contact stress versus time, when an initial axial displacement, e, characterized by an axial compression ratio R, given by the equation (8), is imposed to the gasket. For each axial compression ratio, R, the variation of the contact pressure distribution as well as the change of the contact surface width are recorded.

$$R = 100 \times 2.\frac{e}{D} = 200.C \tag{8}$$

4. Finite element analysis

In order to characterize the O-ring relaxation, an axisymmetric finite elements model, showed in figure 3, was developed using ANSYS software [15]. The O-ring is compressed between two rigid plates.

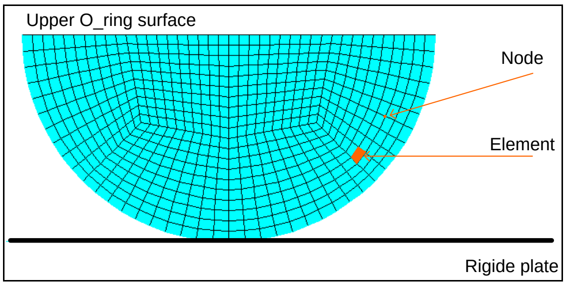

Figure 3: Finite elements model.

Since the problem is axisymmetric and the median horizontal plane cutting the O-ring in two equivalent parts is a symmetry plane, the joint is modelled by a half-disc with 2D plane elements having four nodes. The O-ring material is regarded as viscoelastic characterized by the Prony coefficients. The plates are modelled by rigid elements whose displacements are constrained in all directions. The geometric and mechanic characteristics of the O-ring joint are summarized in table I. In order to check the influence of the O-ring rigidity two initial Young modulus values are considered. The mesh refinement is optimized to have the convergence while using less memory capacity.

Table 1: O-ring characteristics

	O-ring	
Subscript	*1*	*2*
d (mm)	6.98	
D (mm)	123.19	
E (MPa)	2.82	46.20
ν	0.49967	

The value of the vertical displacement imposed on the upper surface of the joint is calculated by the axial compression ratio, R, which varied between 7.5 and 25 % compared to the O-ring cross-section diameter. Thereafter, the distribution of the contact pressure is recorded according time.

5. Results and discussions

The suggested analytical model calculates the maximum contact pressure, in the assembly sealing conditions, according to initially imposed displacement. In addition, the finite elements model in the same working conditions is used to investigate the O-ring material proprieties effect on the contact pressure values. Figure 4 presents the contact pressure distribution according to the radial position for a compression ratio of 15% with various intervals of operating time. It is noticed that the contact pressure is maximum in the average diameter position. All the curves have the same appearance and admit the middle diameter like a symmetrical position. The relaxation speed is more important at the beginning and becomes null after 18 operating hours.

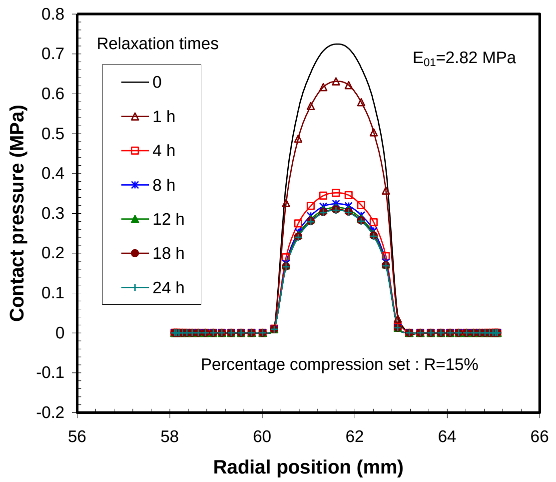

Figure 4: Contact pressure distribution for R=15%.

To inspect the effect of the rigidity of the O-ring, two values of the longitudinal modulus of elasticity were used. Figure 5 compares the contact pressure distributions for the two cases. For a given position, the contact pressure value depends on the value of the corresponding elasticity modulus. When E is larger the contact pressures are higher. When the contact pressure is divided by the initial elastic modulus, the curves depend only on the relaxation time and the compression ratio as illustrated in figure 6. Consequently, we can conclude that the effect of the gasket rigidity does not appear when the curve of the ratio p/EO is represented according to the radial position for several cases.

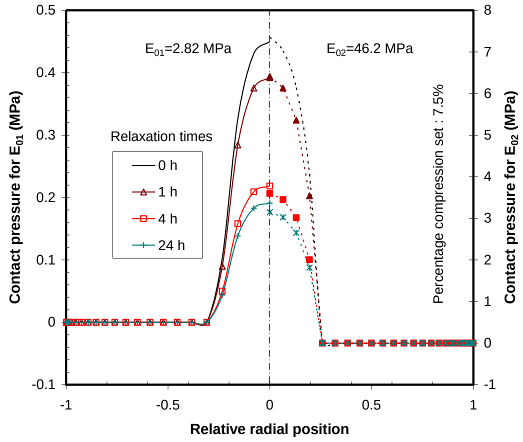

Figure 5: Contact pressure in the two elastic modulus cases.

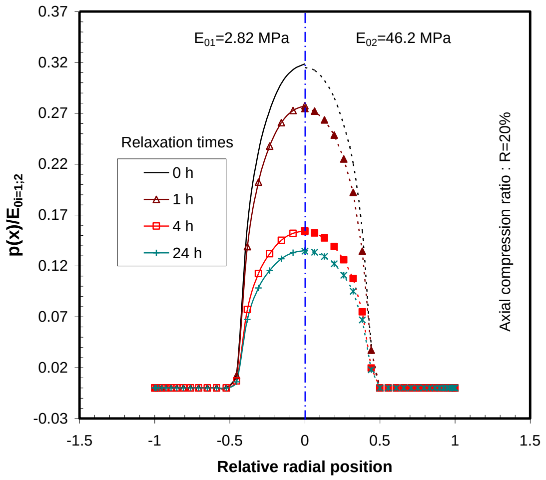

Figure 6: Initial elastic modulus effect.

During the installation of the joint, the analytical model envisages the same stresses distributions as the finite elements model for any imposed axial displacement value as shown in figure 7. The surface of contact and the maximum contact pressure are larger when the compression ratio or the relaxation time are more significant. The difference between the results of the two models is rather negligible and does not exceed 10%. It can be affirmed that the analytical model deduced from the classical theory of the contact pressure remains valid even for the study of the O-ring relaxation.

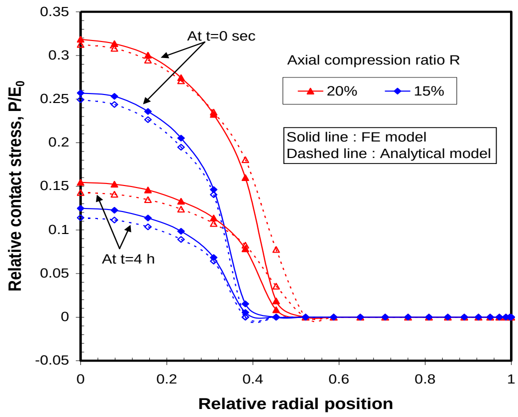

Figure 7: FE and Analytical models comparison.

Figure 8 compares the influence of the compression ratio on the speed and the values of contact pressure due to the viscoelastic relaxation. It is clear that in all the cases the maximum contact pressure loses a great percentage of its initial value with time. This loss is very fast in the first operating hours.

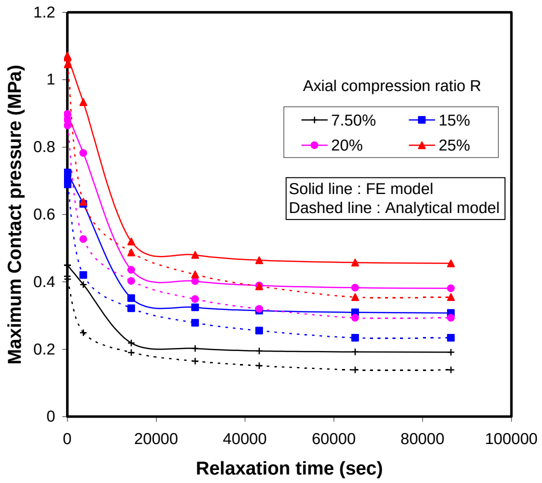

Figure 8: Relaxation of maximum contact pressure in the first material case.

6. Conclusion

This study shows that the classical theory of contact, developed initially for steady operation, remains valid for the relaxation case but with some modifications on the O-ring mechanical characteristics. In addition, the finite elements model developed produces the same results as the analytical model.

In order to generalize these remarks, other cases might be regarded as the radial loading and the grooves configuration.

References

[1] S. Timoshenko, J.N.Goodier, Theory of elasticity. 3rd ed. New York: McGraw-Hill; 1987.

[2] AF. George, A. Strozzi, J.I. Rich, "Stress Fields in a Compressed Unconstrained Elastomeric O-ring Seal and a Comparison of Computer Predictions and Experimental Results". Tribology International, Vol. 20, No. 5, 1987, 237-247.

[3] E. Dragoni, A. Strozzi, "Theoretical Analysis of an Unpressurized Elastomeric O-ring Seal Inserted into a Rectangular Groove". Wear, No.130, 1989, 41-51.

[4] I. Green, C. English, "Stresses and Deformation of Compressed Elastomeric O-ring Seals". 14th International Conference on Fluid Sealing, Firenze, Italy, 1994.

[5] T. Rapareilli, A.M. Bertetto, L. Mazza, "Experimental and Numerical Study of Friction in an Elastomeric Seal for Pneumatic Cylinders". Tribology International, Vol. 30, No 7, 1997, 547-552.

[6] K. Yokoyama, M. Okazaki, T. Komito, "Effect of Contact Pressure and Thermal Degradation on the Sealability of O-ring". JSAE, No. 19, 1998, 123-128.

[7] H.K. Kim, S.H. Park, H.G. Lee, D.R. Kim, Y.H. Lee, "Approximation of Contact Stress for a Compressed and Laterally One Side Restrained O-ring". Engineering Failure Analysis, No. 14, 2007, 1680-1692.

[8] H.K. Kim, JH. SH. Nam, J.S. Hawong, Y.H. Lee, "Evaluation of O-ring Stresses Subjected to Vertical and One Side Lateral Pressure by Theoretical Approximation Comparing with Photoelastic Experimental Results". Engineering Failure Analysis, doi:10.1016/j.engfailanal.2008.09.028.

[9] PB. Lindley, "Compression Characteristics of Laterally-Unrestrained Rubber O-ring". JIRI, No. 1, 1967, pp. 220-13.

[10] PB. Lindley, "Load-Compression Relationships of Rubber Units". J Strain Anal, Vol. 1, No. 3, 1966, pp. 190-5.

[11] K.T. Gillen, M. Celina, R. Bernstein, "Validation of Improved Methods for Predicting Long-term Elastomeric Seal Lifetimes from Compression Stress-Relaxation and Oxygen Consumption Techniques". Polymer Degradation and Stability, No. 82, 2003, pp. 25-35.

[12] M. Diany, A.H Bouzid, "Analytical Modelling of Creep Relaxation of Stuffing Box Packing". ASME-PVP Conference, Paper N° PVP2007-26094, San Antonio, Texas, 2007.

[13] N. G. McCrum, C. P. Buckley, C. B. Bucknall. Principles of Polymer Engineering. New York: Oxford University Press; 2004.

[14] R. M. Christensen. Theory of Viscoelasticity - An Introduction. 2nd ed., New York: Academic Press; 1982.

[15] ANSYS, ANSYS Standard Manual, Version 11.0, 2003.

JJMIE

Volume 5, Number 6, Dec. 2011
ISSN 1995-6665
Pages 483 - 488

Jordan Journal of Mechanical and Industrial Engineering

Exergy Analysis of Ceramic Production in Jordan

Montasir A. Hader[a], Tariq T. Darabseh*[,a], Hussam A. AlOthman[a]

[a]Department of Aeronautical Engineering, Jordan University of Science and Technology, P.O. Box 3030, Irbid 22110, Jordan.

Abstract

In this paper, the ceramic production in Jordan is investigated using the methodology of exergy analysis in order to use energy more efficiently. The major aim of the ceramic industry in Jordan is to minimize the energy cost in order to be a competent industry. The energy and exergy of inputs and outputs for different processes of ceramic production are evaluated. The exergy efficiency is found to be about 48.5% which is considered to be low. This fact in addition to the high cost of energy explains why the ceramic industry in Jordan can't be a strong competent to ceramics imported from other countries. One of the main suggestions to improve this industry is to reuse the waste energy from the kilns in the drying process. Another suggestion is to use the heavy fuel oil (HFO) instead of diesel and kerosene.

Keywords: Exergy; Exergy analysis; Ceramic production; Exergy efficiency; Exergy losses

1. Introduction

The ceramic production in Jordan is encountering many problems related to the waste energy, high energy cost and the environmental effects. The exergy analysis is considered as a powerful method in the performance evaluation of an engineering process. In this paper, the exergy analysis method will be used to investigate the ceramic production in Jordan in order to use energy more efficiently. This analysis will be conducted on the most exergy consuming units in the Jordan Ceramic Factory / Zarqa from which the data were taken. The exergy efficiency and losses will be calculated. These calculations give a clear view of the performance of this factory. The chemical exergy of the reactions involved in the various stages will also be calculated and examined. Based on these calculations, some suggestions will be given to improve this industry.

Many researchers investigated the exergy analysis in different engineering applications. Among them carried out the exergy investigations of the energy consumption in the industrial sector, such as Oladiran and Meyer [1]. They analyzed the energy consumption in the industrial sector in South Africa by considering only four principal sub-sectors. They calculated the average energy and exergy efficiencies for each sub-sector and then they obtained the overall values for the industrial sector based on the primary energy utilization data. Koroneos et al. [2] examined the cement production in Greece by using the method of exergy analysis in order to minimize the energy costs and environmental effects.

Camdali et al. [3] applied the energy and exergy analyses for a dry system rotary burner in a cement plant in Turkey. Utlu and Hepbasli [4] evaluated the energy and exergy efficiencies in the Turkish utility sector for a period from 1990 to 2004. They performed the energy and exergy analyses for eight power plants based on the actual data over the period studied.

The exergy analysis method has also been used in the areas of residential, transportation, environmental and trading sectors. Taufiq et al. [5] described the modeling and optimization analysis for HVAC in Malysia. They used the exergy analysis method in evaluating the overall and component efficiencies and to determine the losses. Talens et al. [6] suggested exergy analysis method to assess the environmental performance of a system like the process of biodiesel production.

Saidur et al. [7] applied the energy and exergy analyses for different modes of transport in Malaysia and they compared their results with other countries like Turkey. Jaber et al. [8] made historical investigation from 1985 to 2006 to determine the energy and exergy efficiencies of the Jordanian transportation sector.

Chen and B. Chen [9] investigated the resource inflow to the Chinese society between 1980 and 2002 based on the exergy analysis method. Tsatsaronis [10] presented the definitions of some terms and nomenclature that are used in exergy analysis.

The production of ceramic consumes a large amount of energy in any industrial sector. The energy cost of the ceramic industry has a great percentage of the total production cost. A large number of studies have been published in this area. A handy manual sponsored by United Nations Industrial Development Organization (UNIDO) investigated the ceramic production from different points of view [11]. Dincer and Rosen [12] illustrated in details how an exergy analysis could be done for industrial processes. They also showed the relation between exergy and energy with the sustainable development. Cengel and Boles [13] and Sonntag et al.

* Corresponding author. e-mail: darabseh@just.edu.jo

[14] introduced and explained the fundamental of thermodynamics including exergy concept in addition to a comprehensive illustration of the concept of chemical exergy.

Based on the previous studies conducted in the literature, it is clear that no one investigated the exergy analysis of the ceramic production. In this study, exergy analysis of the processes involved in the production of ceramic in a ceramic factory in Zarqa, Jordan performed for evaluating the performance of the factory using the actual factory operational data. The exergy losses will also be calculated and the chemical exergy of the reactions will be calculated and examined.

2. Manufacturing Processes of Ceramic

The main stages of ceramic production in the factory under consideration are illustrated in Figure 1. These stages are:

1. Raw materials: The raw materials are all from Jordan. They contain:

   - Kaolin (Al2O3.SiO2.2H2O): this comes from two main areas in Jordan, Batn AlGhol and Mahis.
   - Calcium Carbonate (limestone) (CaCo3): it comes from the Jordan Carbonate Company in Amman. Both Kaolin and Calcium Carbonate are used to increase the thermal expansion of the ceramic block in order to make it straight.
   - Sand: it is brought from AlDisi area. The sand is used to increase the absorption of the mixture.
   - Water (H2O): it is used as a solvent media.

2. Grinding: In this process, the raw materials are mixed with water in a proper proportion and are grinded in a ball mill to make a homogeneous mixture. Ball mills and blungers are used for grinding. This process continues until we get slurry of the required density.

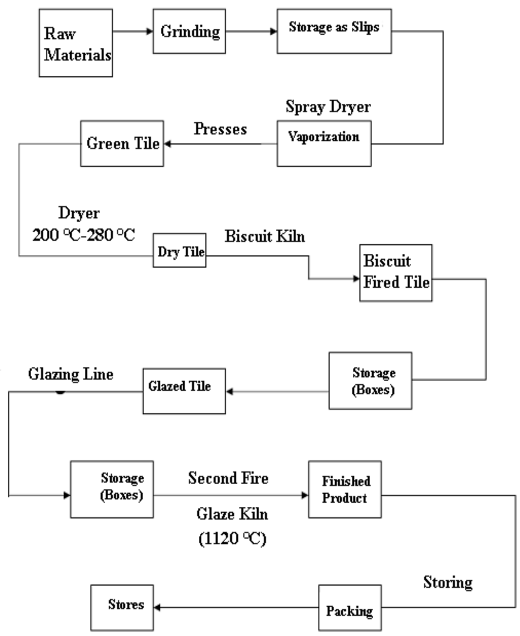

Figure 1: Ceramic production stages.

3. Storing: After preparation of the slurry of required density, it is stored in as slips. Slurry is then pumped at the ambient temperature through a hydraulic pump into the spray dryer where the slurry is sprayed through nozzles.
4. Vaporization in the spray dryer: Material is dried in spray dryer, so the moisture added during grinding process is removed in the spray dryer.The solution is vaporized in the spray dryer at a temperature range of 300°C to 550°C. The maximum temperature may reach 560°C. Hot flue gases are used as a heating source. Hot gases are generated by combustion of fuels such as diesel and kerosene. Input moisture to spray dryer is 35 to 40%, which is dried to 5 to 6 %. This process produces the powder which is then stored in silos and left to cool naturally. Storing: After preparation of the slurry of required density, it is stored in as slips. Slurry is then pumped at the ambient temperature through a hydraulic pump into the spray dryer where the slurry is sprayed through nozzles.
5. Pressing or Forming: The powder in silos is then sent to the hydraulic press where the required sizes of biscuit tiles are formed and sent to dryer through conveyer. This process occurs at a temperature range of 40°C to 50°C in order to prevent the coherence of the pressed powder with the press itself. The pressing process produces the green tile. Metal molds patterns are used for ceramics forming in the factory under consideration. The shape of these molds should consider the shrink of the ceramics when fired.
6. Drying: After press, biscuits containing about 5% to 6% moisture are sent to dryer and dried to about 2% to 3% moisture level. The green tile produced in the previous stage is dried at a temperature range of 200°C-280°C to produce the dry tile. After that, the dry tile is entered to the biscuit kiln with a maximum temperature of 1150°C. The result is a biscuit fired tile. This tile is stored in boxes and moved using kiln cars to the glaze line.
7. Glazing: The biscuit fired tile is entered to the glazing line to produce the glazed tile which is also stored in boxes. The glazed tile is entered to a second fire which is the glaze kiln where the glaze is melted on a maximum temperature of 1100°C without any reaction to produce the finished product.
8. Sorting and packing: The finished product is sorted to different classes then packed and stored.

3. Exergy Analysis

3.1. Equations of Exergy Analysis on Ceramic Production:

The exergy balance (as shown in Figure 2) for the considered process is given by the following equation [2]:

$$E_{input} = E_{product} + E_{losses} + E_{waste} \quad (1)$$

The exergy of inputs (Einput) is the sum of exergies of the raw materials and energy inputs. The exergy of products (Eproducts) is the sum of exergies of the products and by products, in other words, is the useful exergy in the exit streams. The exergy of waste (Ewaste) is the sum of exergies of waste heat, gasses vented to the environment without use, and in solid waste. The exergy losses (Elosses) are the amount of exergy consumed in a system due to internal irreversibilities in the process for raw materials and energy resources and flow conversion.

The exergy of products can be calculated from equation (1) as:

$$E_{product} = E_{input} - E_{losses} - E_{waste} \tag{2}$$

The exergy efficiency is the ratio of the exergy of the useful products to the exergy of all input streams. Exergy efficiency of the process (η) is defined as [15]:

$$\eta = \frac{E_{product}}{E_{input}} = 1 - \frac{E_{losses} + E_{waste}}{E_{input}} = 1 - \frac{\text{exergy destroyed}}{\text{exergy input}} \tag{3}$$

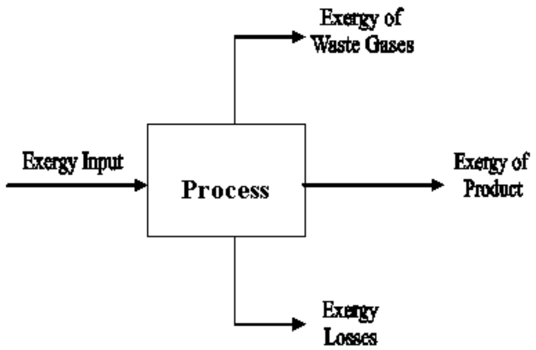

Figure 2: Exergy balance.

The exergy of a system is the sum of the physical exergy, the mixing exergy and the chemical exergy, when other forms of contributions, such as kinetic exergy or potential exergy, etc., are neglected. The total exergy of a stream is given by:

$$E = E_{ph} + E_{mix} + E^{CHEM} \tag{4}$$

where E_{ph} is the physical exergy due to temperature and pressure difference with the environment, E_{mix} is the mixing exergy due to the mixing of the different components, and E^{CHEM} is the chemical exergy due to differences in the materials composition with the environment.

The physical exergy of a given stream is given by the following equation [2]:

$$E_{ph} = H - H_0 - T_0(S - S_0) \tag{5}$$

where H is the enthalpy, H_0 is the enthalpy at atmospheric conditions, T_0 is the temperature of the surroundings, S is the entropy and S_0 is the entropy at atmospheric conditions.

The mixing energy of a gaseous stream is given by the following equation [2]:

$$E_{mix} = RT_0 \sum y_i \ln \frac{y_i}{y_{oi}} \tag{6}$$

where R is the universal gas constant, y_i is the mole fraction in the stream and y_{oi} is the mole fraction in the environment.

The chemical exergy of a substance is given by the following equation [2]:

$$E^{CHEM} = (\mu^0 - \mu_0^0) + RT_0 \ln(\frac{C}{C_0}) \tag{7}$$

where μ^0 is the chemical potential at the standard state, μ_0^0 is the chemical potential at the environmental state, C is the concentration of a substance at the present state and C_0 is the concentration of a substance at the environmental state.

The exergy of heat which represents the maximum amount of work that can be gained reversibly from an amount of thermal energy Q at temperature T is given by the following equation:

$$E_{heat} = (1 - \frac{T_o}{T})Q \tag{8}$$

3.2. Exergy Analysis of Spray Dryer:

The exergy losses as mentioned earlier come mainly from the firing and drying processes. The main exergy losses for drying processes are associated with irreversibilities. The spray dryer which the ceramic factory under consideration uses is of the type air drying. The schematic diagram of the spray dryer is shown in Figure 3. A large amount of exergy is lost with existing air from the dryer. The exergy existing with the product is quite small, since a little exergy is put in the solid products. The exergy loss due to heat rejection from the walls of the dryer is very significant. This loss should be taken into consideration. This amount may reach up to 25% of the total exergy input. This loss can be reduced by appropriately insulating the dryer. The size of the dryer is another important aspect. The jet type ring dryer has smaller dimensions than a spray dryer of an equivalent capacity. Then the jet type ring dryer has a much smaller loss from its walls than a spray dryer [12]. For our ceramic factory, one may recommend to replace the existing spray dyer with a jet type ring dryer.

The inputs and outputs in the spray dryer are shown in Figure 3.

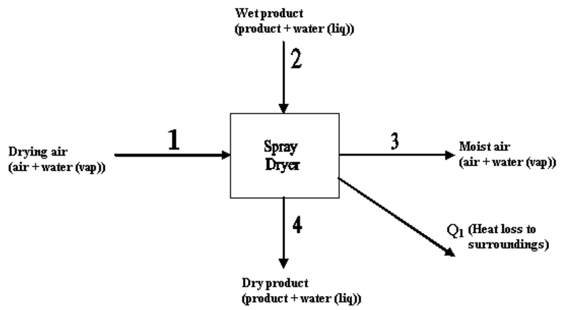

Figure 3: Schematic diagram of the inputs and outputs in the spray dryer.

In this paper, we can use the model of a drying process presented by Dincer and Sahin [16]. Here, the reference environment used in our paper is shown in Table 1.

Table 1: Reference environment model [12].

Temperature	T_0 = 298.15K	
Pressure	P_0 = 1 atm.	
Composition	Atmospheric air saturated with water at Reference conditions has the following composition:	
	Air Constituents	Mole fraction
	N_2	0.7567
	O_2	0.2035
	H_2O	0.0303
	Ar	0.0091
	CO_2	0.0003
	H_2	0.0001

Also, the raw data for the spray dryer in addition to some necessary data are shown in Tables 2 and 3, respectively. These data are used to conduct the exergy analysis to determine the exergy efficiency of the drying process.

Table 2: Raw data associated with the spray dryer.

State	*T* (K)	*P* (kPa)	*ha* or *hw* (kJ/kg)	*hv* or *hp* (kJ/kg)
1	373	150	402	2680
2	298	101.3	104.87	23.17
3	343	125	345	2630
4	363	195	380.9	57.2

Table 3: Some necessary data.

$(C_p)_a$	1.005 kJ/kg.K
$(C_p)_v$	1.8723 kJ/kg.K
R_a	0.287 kJ/kg.K
R	0.4615 kJ/kg.K
ω_o	0.0153
$(x_v)_o$	0.024

Now, the exergy efficiency for the drying process can be defined as the ratio of exergy use in the drying of the product to the exergy of the drying air supplied to the system [12]. That is:

$$\eta = \frac{\text{Exergy input for evaporation of moisture in product}}{\text{Exergy of drying air supplied}} \tag{9}$$

The analysis has been carried out based on the raw data by applying the procedure given by Dincer and Sahin [16]. The results are given in Tables 4, 5 and 6.

Table 4: Mass balance results.

Mass Balance	
$\dot{m}_p$	3000 kg/h
$\dot{m}_a$	25000 kg/h
ω_1	0.018
$(\dot{m}_w)_2$	300 kg/h
$(\dot{m}_w)_4$	130 kg/h
ω_3	0.0248

Table 5: Energy balance results.

Energy Balance	
h_1	450.24 kJ/kg
h_3	410.72 kJ/kg
$\dot{Q}_1$	867854 kJ/kg
$\dot{E}_q$	321087.63 kJ/kg

Table 6: Exergy balance results.

Exergy Balance	
$(\dot{m}_w)_{ev}$	170 kg/h
$(e_w)_3$	391.03 kJ/kg
$(e_w)_2$	52.9 kJ/kg
e_1	28.82 kJ/kg
η	51%

3.3. Exergy Analysis of the Kilns:

The biscuit and glaze kilns used in the factory considered are roller hearth kilns. This type of kilns is designed as a continuous kiln. A roller conveyer is installed from the kiln inlet to the kiln outlet. Each roller rotates to carry the product to be fired from the inlet to the outlet. This structure eliminates the use of the kiln car.

The kilns consume great amount of energy in the production processes. The kilns consume about 50% of the total energy consumption while the spray dryer consumes approximately the other 50%.

The input exergy comes mainly from the combustion of diesel and kerosene in addition to electricity in the following percentages: 9% from electricity, 50.05% from kerosene and 40.95% from diesel. The exergy coefficient of electricity is assumed to be 1. This means that electrical energy and exergy are equivalent.

The composition of diesel and kerosene is given in Table 7. The composition of both diesel and kerosene does not sum up to 100% because there is also a small percentage of water and ash in both of them.

Table 7: Composition of diesel and kerosene as percentage of mass.

Fuel	Carbon (C)	Hydrogen (H)	Oxygen (O)	Nitrogen (N)	Sulfur (S)	Heating value, DH (MJ/kg)
Diesel	87.5	11.5	0.11	0.21	0.5	42.4
Kerosene	86	12	0.09	0.26	0.44	40.2

The chemical exergy of both diesel and kerosene entering the system is calculated by using the following equation [2]:

$$E^{CHEM} = \Delta H(1.0401 + 0.1728\frac{x_H}{x_C} + 0.0432\frac{x_O}{x_C} + 0.2196\frac{x_S}{x_C}(1 - 2.0628\frac{x_H}{x_C})) \quad (10)$$

where xH, xC, xO, and xS are mass fractions of H, C, O, and S, respectively.

Applying equation (10) for diesel and kerosene we get:

$$E^{CHEM}_{Diesel} = 45.1 MJ/kg.$$
$$E^{CHEM}_{Kerosene} = 42.824 MJ/kg.$$

Exergy of the system for both Biscuit and Glaze kilns can be calculated form Equation 8. The results are summarized in Table 8 shown below.

Table 8: Heat input, exergy and energy availability.

	Biscuit kiln	Glaze kiln
Q [kJ]	26946×10^3	69992.72×10^3
E [kJ]	12425.37×10^3	30111.59×10^3
λ_Q	0.46	0.43

The exergy input to the biscuit kiln 2704.64×103 kJ/kg. While, the exergy output is 1257.66×103 kJ/kg.

Thus, the exergy efficiency for the biscuit kiln is:

$$\eta = \frac{1257.66\times10^3}{2704.64\times10^3}\times100\% = 46.5\%.$$

In a similar way, the exergy input to the glaze kiln is 7026.45×103 kJ/kg. While, the exergy output is 3471.07×103 kJ/kg
Thus, the exergy efficiency for the glaze kiln is:

$$\eta = \frac{3471.07\times10^3}{7026.45\times10^3}\times100\% = 49.4\%.$$

Now, an analysis of the exergy losses in both the biscuit and glaze kiln is done and shown in Table 9.

Table 9: Exergy losses in the biscuit and glaze kilns.

Heat Loss	Exergy loss glaze kiln [kJ/kg]	% of exergy loss	Exergy loss biscuit kiln [kJ/kg]	% of exergy loss
From the waste exhaust heat	461.12×10^3	32	888.85×10^3	25
From irreversibilities	792.71×10^3	55	2275.30×10^3	64
From radiation and conduction	158.54×10^3	11	248.86×10^3	7
From kilns cars	28.83×10^3	2	142.06×10^3	4

It should be noted that for both kilns the radiation and conduction losses are calculated from the differnces between the energy input and output [11].

As a final result, since the spray dryer, biscuit and glaze kilns are the most energy consuming units in the ceramic production; one can calculate the overall exergy efficiency for the ceramic production in the Jordan ceramic factory to be about 49.48%.

These results are shown schematically using Sankey diagrams, Figures [4] and [5], respectively.

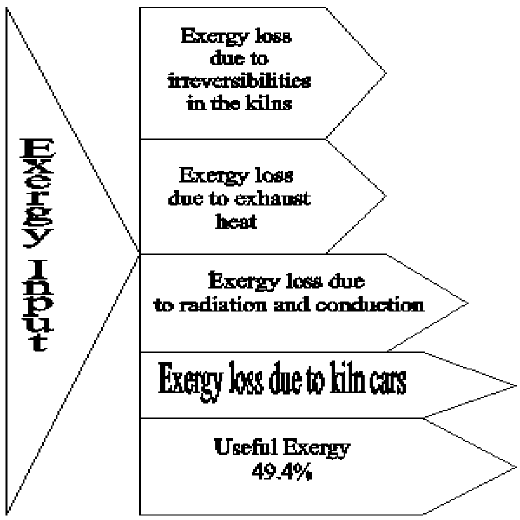

Figure 4: Sankey diagram of the exergy balance for the glaze kiln.

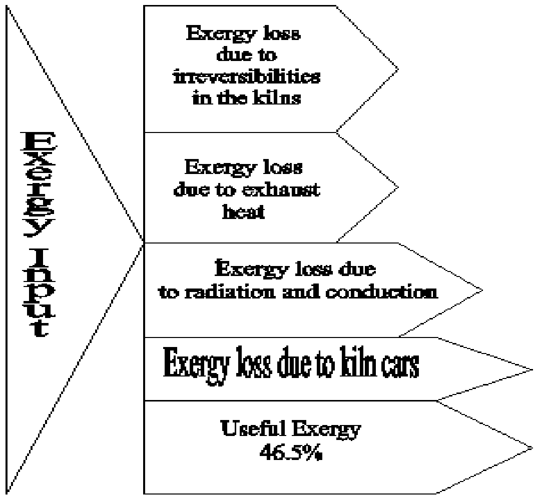

Figure 5: Sankey diagram of the exergy balance for the biscuit kiln.

4. Conclusion

The exergy analysis method is a powerful tool for measuring the efficiency of processes or systems. The results obtained with regard to the exergy efficiency and losses give a clear view of the performance of the considered factory. The exergy efficiency of the ceramic production is calculated to be 49.48. This efficiency is low and means that there is a huge amount of exergy losses.

The spray dryer is the largest energy and exergy consuming unit. Its exergy input represents about 50% of the total consumption of the Jordan ceramic factory. The exergy efficiency of the spray dryer is about 51% which shows that the exergy losses concerned with the spray dryer are 49%. This means that a loss rate is about 433927 kJ/h. The drying equipment is large and it operates at high temperatures. As a result, there is a large amount of heat loss from both convection and radiation. Insulation of the equipment is important to ensure energy efficiency. Large part of these losses is due to internal irreversibilities occurring in the spray dryer.

The second exergy consuming part of the Jordan ceramic factory is the biscuit kiln. The exergy efficiency of the biscuit kiln is about 46.5%. This means that there is an exergy loss of 53.5%. Main loss is due to the irreversibilties during the preheating and cooling processes in addition to the exergy losses of the exhaust gases and waste heat.

The glaze kiln is the third exergy consuming unit. The exergy efficiency of the glaze kiln is about 49.4% which refers to exergy loss of 50.6%. Of these losses, the irreversibilties due the preheating and cooling processes occurred in the glaze kiln represent the largest part as in the biscuit kiln. Also, the exergy losses related to the waste heat and exhaust gases.

Exergy losses by conduction and radiation from the biscuit and glaze kilns are about 7% and 11% of the total exergy losses. This ratio is low but with the time the total amount of losses is considerable. This radiation loss can be reduced by replacing the damaged insulation and improving the existing insulation of the kilns.

A very small exergy loss is due to kiln cars. Kiln cars move the tiles to and from both the glaze and biscuit kilns. These losses are 4% and 2% for the biscuit kiln and glaze kiln respectively.

References

[1] M.T. Oladiran, J.P. Meyer, “Energy and exergy analyses of energy consumptions in the industrial sector in South Africa”. Applied Energy, Vol. 84, 2007, 1056–1067.

[2] C. Koroneos, G. Roumbas, N. Moussiopoulos, “Exergy analysis of cement production”. International Journal of Exergy, Vol. 2, No. 1, 2005, 55-68.

[3] U. Camdali, A. Erisen, F. Celen, “Energy and exergy analyses in a rotary burner with pre-calcinations in cement production”. Energy Conversion and Management, Vol. 45, 2004, 3017–3031.

[4] Z. Utlu, A. Hepbasli, “Assessment of the Turkish utility sector through energy and exergy analysis”. Energy Policy, Vol. 35, 2007, 5012–5020.

[5] B.N. Taufiq, H.H. Masjuki, T.M.I. Mahlia, M.A. Amalina, M.S. Faizul, R. Saidur, “Exergy analysis of evaporative cooling for reducing energy use in Malaysian building”. Desalination, Vol. 209, 2007, 238–243.

[6] L. Talens, G. Villalba, X. Gabarrel, “Energy analysis applied to biodiesel production”. Conservation and Recycling, Vol. 51, 2007, 397–407.

[7] R. Saidur, M.A. Sattar, H.H. Masjuki, S. Ahmed, U. Hashim, “An estimation of the energy and exergy efficiencies for the energy resources consumption in the transportation sector in Malaysia”. Energy Policy, Vol. 35, 2007, 4018–4026.

[8] J.O. Jaber, A. Al-Ghandoor, S.A. Sawalha, “Energy analysis and exergy utilization in the transportation sector of Jordan”. Energy Policy, Vol. 36, 2008, 2995-3000.

[9] G.Q. Chen, B. Chen, “Resource analysis of the Chinese society 1980–2002 based on exergy part 1: fossil fuels and energy minerals”. Energy Policy, Vol. 35, 2007, 2038–2050.

[10] G. Tsatsaronis, “Definitions and nomenclature in exergy analysis and exergoeconomics”. Energy, Vol. 32, 2007, 249-253.

[11] The Energy Conservation Center. Energy conservation in ceramic industry. United Nations Industrial Development Organization and Ministry of International Trade and Industry (MITI); Japan; Handy Manual, 1994.

[12] Dincer I, Rosen MA. Exergy: energy, environment and sustainable development. Oxford, UK: Elsevier; 2007, p. 277-302.

[13] Cengel YA, Boles MA. Thermodynamics: an engineering approach. New York: McGraw Hill; 2006, p. 1-50, p. 423-487 and p. 751-793.

[14] Sonntag RE, Borgnakke C, Van Wylen GJ. Fundamentals of thermodynamics. New York: John Wiley and Sons Inc.; 1997, p. 272-330.

[15] I. Dincer, Y.A. Cengel, “Energy, entropy and exergy concepts and their roles in thermal engineering”. Entropy, Vol. 3, 2001, 116-149.

[16] I. Dincer, A.Z. Sahin, “A new model for thermodynamic analysis of a drying process”. International Journal of Heat and Mass Transfer, Vol. 47, 2004, 645-652.

JJMIE

Volume 5, Number 6, Dec. 2011
ISSN 1995-6665
Pages 489 - 494

Jordan Journal of Mechanical and Industrial Engineering

Modeling and Optimization of Wind Turbine Driving Permanent Magnet Synchronous Generator

Mayouf.Messaoud*[,a], Rachid.Abdessamed[a]

[a]Department of Electrical Engineering, Faculty of engineer's sciences, University of El Hadj Lakhdar, Batna, Algeria

Abstract

In this paper, we propose a control strategy of a variable speed wind generation system with permanent magnet synchronous generator connected to the network using two converters PWM having jointly a DC bus. The aim of this control strategy is to allow the permanent magnet generator to operate for different wind speed in order to optimize the generated power from wind turbine on the one hand, and control the forwarded flows of power, on the other hand.

Keywords: Permanent magnet; DC bus; Wind turbine; pulse width-modulated (PWM) power converters

1. Introduction

The world consumption of energy has known enormous increase these last years, because of the massive industrialization that has tendency to intensify rapidly in some geographical areas in the world, notably in countries of Asia. The risks of shortage of fossil matters and their effects on the climatic change indicate once more the importance of renewable energies. Several sources of renewable energies are under exploitation and search, in order to develop power extraction techniques aiming to improve the reliability, lower the costs (of manufacture, use, and retraining), and to increase the energizing efficiency [1]. In this general context, this work carries on the conversion of the wind energy in electric energy that became competitive thanks to three essential factors [2]:

The motivating nature of this energy, the development turbines industry, and the evolution of semiconductors technology, as well as the new methodologies of control of variable speed turbines. Nevertheless, several problems are met, bound to the complexity of wind conversion systems; as the necessity to use gear box between the turbine and the generator, and the instability of wind speed [3]. The use of other wind power structures like for example, permanent magnet synchronous generator (PMSG) with big number of poles, makes variable wind conversion systems more attractive than those with fixed speeds, because of the possibility of extraction of the optimal energy for different speeds of wind, reduction of mechanical constraints by elimination of gear box, which improves reliability of system; and reduction of maintenance expenses [3]. Permanent magnet synchronous machine (PMSG) is characterized by weak inductances, elevated torque, and very weak inertia [4]. All these features offer elevated performances for the generator, important output, and better controllability; which makes this machine real competitor of the asynchronous generator [4]. The principle of horizontal axis wind turbine with variable-speed based on permanent magnet synchronous generator is presented in a first time, following by an analytic model of different components of the conversion chain proposed. These models are associated to control strategies adopted for the generator in one hand, and the grid link in the other, while passing by the DC bus control. All developed models during this survey, are simulated in MATLAB.

2. Modeling of the permanent magnet generator conversion chain

2.1. Modeling of P.M.S.G:

In order to get a dynamical model for the electrical generator that easily allows us to define the generator control system, the equations of the generator are projected on a reference coordinate system rotating synchronously with the magnet flux (Figure. 1).

In the synchronous machines with sinusoïdale distribution of conductors, flux and are linear functions of currents id and iq situated on the rotor. And they are given by the equations:

* Corresponding author. e-mail: mayouf71@yahoo.fr

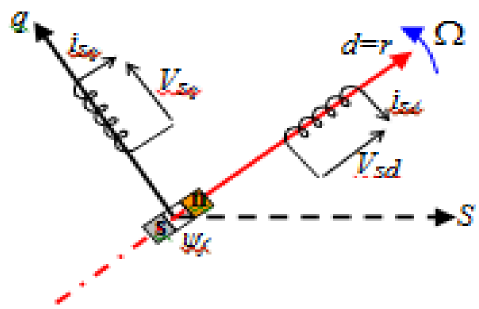

Figure 1: PARK model for PMSG.

$$\begin{cases} \psi_d = L_d i_d + \psi_f \\ \psi_q = L_q i_q \end{cases}$$

Where:

L_d : Stator inductance in d-axis**;**

L_q : Stator inductance in q-axis;

L_d and L_q are supposed independent of θ;

ψ_f : Magnets flux;

The wind turbine driven PMSG can be represented in the rotor reference frame as:

$$\begin{cases} V_d = -R_s I_d - L_d \dfrac{d}{dt} I_d + \omega L_q I_q \\ V_q = -R_s I_q - L_q \dfrac{d}{dt} I_q - \omega L_d I_d + \omega \psi_f \end{cases}$$

The electromagnetic torque is expressed by:

$$C_{em} = \frac{3}{2} P(\psi_d i_q - \psi_q i_d)$$

After affectation of the expressions of ψ_d and ψ_q,

The expression of the electromagnetic torque becomes:

$$C_{em} = \frac{3}{2} P[(L_q - L_d) i_d i_q + i_q \psi_f]$$

2.2. Modeling of the wind turbine:

The wind energy conversion system is complex because of the multiplicity of existing fields, aerodynamic, mechanical, and electric; and factors determining the mechanical power, as wind speed, dimension, and turbine shape.

Input and output variables of the wind turbine can sum up as follows:

1. Wind speed that determines the primary energy to the admission of turbine.
2. Tip-Speed ratio (T.S.R) defined by the ratio of the linear speed in tip of blades of the turbine on the instantaneous wind speed, and given by the following expression [5].

$$\lambda = \frac{\Omega_t R_t}{V}$$

Rt : Radius of the wind turbine rotor (m)
V : Velocity of the wind (m/s)
Ωt : Rotation speed of the turbine (rd/s)

3. Speed of turbine, slant of blades, and angle of wedging.
4. The power cœfficient C_p definite as the ratio of the extracted wind power and the total power theoretically available. It depends of the wind speed, rotation speed of the turbine, and blades parameters of the turbine as incidence angle and wedging angle [5]. It is often represented according to the tip-Speed ratio λ. The maximal theoretical value possible of the power coefficient, named limit of Betz, is of 0.593 [5]. The output quantities of the turbine are the power or the torque that can be controlled while varying the previous input quantities.

2.3. Gear box model:

The role of gear box is to transform the mechanical speed of the turbine to the generating speed, and the aerodynamic torque to the gear box torque according to the following mathematical formulas:

$$G = \frac{C_{aer}}{C_g}$$

$$G = \frac{\Omega_{mec}}{\Omega_{tur}}$$

The fundamental equation of dynamics permits to determine the mechanical speed evolution from the total mechanical torque applied to the rotor that is the sum of all torques applied on the rotor:

$$J.\frac{d\Omega_{mec}}{dt} = C_g - C_{em} - C_f$$

Ω_{tur} : Mechanical speed of the turbine;

Ω_{mec} : Generator speed;

C_{aer} : Torque applied on the shaft of turbine;

C_g : Torque applied on the shaft of the generator;

C_{em} : Electromagnetic torque;

C_f : Resistant torque due to frictions;

$$C_f = f.\Omega_{mec}$$

J: Total inertia brought back on the generator shaft, containing inertia of the turbine, the generator, the two shafts, and the gear box;

f: the total friction coefficient of the mechanical coupling ;

2.4. Power converter model:

Given that the two converters used in the realization of the proposed wind conversion chain have the same structure and control technique; all that is necessary is to model only one. The converter chosen in this part is the one bound to the grid.

To facilitate the modeling and reduce the time of simulation, we model the converter by a set of ideal switches: that means hopeless resistance in the state passing, infinite resistance to the blocked state, instantaneous reaction to control signals.

We define for every switch a function said of "connection" associated to every switch. It represents the ideal orders of commutation and takes the values [6]:

$S_{ic}=1$ when the switch is closed.

$S_{ic}=0$ when the switch is open.

$$S_{ic} \in \{1,2,3\}, \text{ with } \begin{cases} c \in \{1,2,3\} \\ i \in \{1,2\} \end{cases}$$

The c indication corresponds to the cell of commutation, and the index i corresponds to the location of the switch of this cell.

For the three phases of the converter, we define the following conversion functions $\underline{m}$ [6]:

$$\underline{m} = [m_1 \quad m_2] = \begin{bmatrix} 1 & 0 & -1 \\ 0 & 1 & -1 \end{bmatrix} \begin{bmatrix} S_{11} \\ S_{12} \\ S_{13} \end{bmatrix}$$

The state of conduction of the converter components can be represented by a matrix of connection composed of three cells of commutation of which the switches control of a same cell are complementary [6].

$$S_{i1} + S_{i2} = 1 \quad \forall i \in \{1,2,3\}$$

The converter's modeling consists in expressing voltages in lines, according to DC bus voltage and switches states.

The modulated voltages are gotten from DC bus voltage and conversion functions according to the expressions [6], [7]:

$$\begin{cases} u_{m13} = m_1.u \\ u_{m23} = m_2.u \end{cases}$$

The modulated simple voltages are stem from the modulated composed voltages according to the following expressions:

$$\begin{cases} v_{m-1} = \frac{2}{3}.u_{m13} - \frac{1}{3}.u_{m23} \\ v_{m-2} = -\frac{1}{3}.u_{m13} + \frac{2}{3}.u_{m23} \end{cases}$$

The modulated current is gotten from the filter currents and conversion functions:

$$i_{m-res} = m_1.i_{t1} + m_2.i_{t2}$$

2.5. DC bus Modeling:

The capacitor current is stem from a node where circulates two modulated currents by every converter:

$$i_c = i_{m-mac} - i_{m-res}$$

i_{m-mac} : Current provided by the generator

i_{m-res} : Current modulated by the converter MLI_2

DC bus is modeling by knowledge of capacitor terminals voltage gotten while integrating the following differential equation:

$$\frac{du}{dt} = \frac{1}{C}.i_c$$

Where:

$$u = \int \frac{du}{dt} + u(t_0)$$

$u(t_0)$ is the voltage value to t_0 instant.

3. Control strategies

3.1. Vector control of PMSG:

The strategy of applied vector control consists in imposing a reference of the direct current I_{sd} to zero. This choice is justified in the goal to avoid the demagnetization of the permanent magnets due to the armature reaction according to the *d* axis [2].

The electromagnetic torque is given therefore by the following expression:

$$C_{em} = \frac{3}{2} P.\psi_f i_{sq}$$

We propose to make use of PI regulators in the control structure. The mathematical model equations of the permanent magnet synchronous machine can be written as:

$$\begin{cases} V_{sd}(p) = R_s.I_{sd}(p) + P.L_s.I_{sd}(p) - \omega.\psi_{sq}(p) \\ V_{sq}(p) = R_s.I_{sq}(p) + P.L_s.I_{sq}(p) + \omega.\psi_{sd}(p) \end{cases}$$

The coupling terms $E_{dq} = \omega.\psi_{sdq}$ are considered as measurable disruptions.

The transfer function of the machine can be written in the form:

$$G_s(p) = \frac{I_{sd,q}(p)}{V_{sd,q}(p) + E_{d,q}(p)} = \frac{1}{R_s}.\frac{1}{1+T_e.p}$$

With

$$T_e = \frac{L_s}{R_s}$$

3.2. MPPT:

The characteristic of the optimal power of a wind is strongly non linear and in the shape of "bell" [5]. For every speed of wind, the system must find the maximal power what is equivalent in search of the optimal rotational speed.

Figure. 2 illustrates the characteristic curves of the wind in the plan power, rotational speed of the turbine.

Every dotted line curve corresponds to a speed of wind *Vv* data.

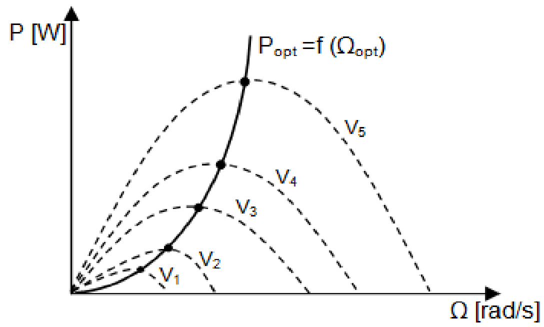

Figure 2: Feature of wind turbine in the plan power, rotational speed.

An ideal functioning of the wind system requires a perfect follow-up of this curve. To approach of this goal, a specific control known by the terminology: Maximum Power Point Tracking (MPPT) must be used. The strategy of this control consists in controlling electromagnetic torque in order to adjust the mechanical speed in order to maximize the generated electric power. So that the extracted power is maximal, we associate to the parameter λ its optimal value λ_{opt} corresponds to the maximum of power coefficient $C_{p\,max}$. The value of the reference electromagnetic torque is then adjusted to the following maximal value:

$$C_{em-ref} = \frac{1}{2}.\frac{C_{p\,max}}{\lambda_{opt}^3}.\rho.\pi.R^5.\frac{\Omega_{mec}^2}{G^3}$$

This expression can be written as:

$$C_{em-ref} = K_{opt}.\Omega_{mec}^2$$

The MPPT algorithm controlled with the help of the measured rotational speed in N stage, determine the reference torque in N+1 stage of the way shown on figure 3.

$$\Omega[N] \longrightarrow \boxed{K_{opt}.\Omega^2[N]} \longrightarrow C_{ref}[N+1]$$

Figure 3. Reference torque according to the rotational speed.

3.3. Powers regulation:

The active and reactive powers passed through the grid are given in Park model by the following relations:

$$P = v_{pd}.i_{td} + v_{pq}.i_{tq}$$
$$Q = v_{pq}.i_{td} - v_{pd}.i_{tq}$$

By inversion of these relations, it is possible to impose some references for the active power P_{ref} and reactive power Q_{ref} while imposing the following reference currents:

$$i_{td-ref} = \frac{P_{ref}.v_{pd-mes} + Q_{ref}.v_{pq-mes}}{v_{pd-mes}^2 + v_{pq-mes}^2}$$

$$i_{tq-ref} = \frac{P_{ref}.v_{pq-mes} - Q_{ref}.v_{pd-mes}}{v_{pd-mes}^2 + v_{pq-mes}^2}$$

3.4. DC bus regulation:

While neglecting losses in the capacitor, in the converter and in the filter compared with the power passed through the grid, it is sufficient to know the available power stemmed from the rectifier P_{dc} and the power to stock in the capacitor $P_{cap-ref}$ to determine the necessary reference power.

$$p_{cap-ref} = u_{cap}.i_{cap-ref}$$
$$p_{ref} = p_{dc} - u_{cap}.i_{cap-ref}$$

3.5. Functioning limits:

Given that the rectifier MLI1 has a voltage elevator nature; its DC bus must be of voltage sufficiently high to assure the piloting of the generating to maximal speed.

The association synchronous machine - MLI rectifier with six switches - battery must satisfy a DC bus voltage level sufficiently high so that the machine control can be achieved. In the case of strong values of wind speed, the boundary-marks voltage of the generator becomes high according to the rotational speed as indicates the following equation.

$$E_{ab}^{max} = \sqrt{3}p.\Omega.\psi_f$$

The control condition of the rectifier defined by this relation imposes the minimum of voltage of DC bus side according to the boundary-marks maximal composed voltage of the machine.

$$U_{cap} \geq E_{ab}^{max}$$

Then:

$$U_{cap} \geq \sqrt{3}p.\Omega.\psi_f$$

While supposing that the system works to the optimal point, the minimal DC bus voltage can, so determined according to the wind speed:

$$U_{cap} \geq \sqrt{3}p.\psi_f.\frac{\lambda_{opt}}{R}.V_v$$

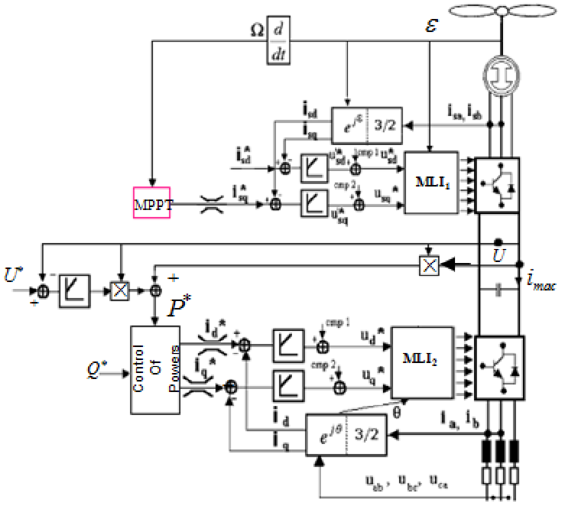

Figure 4: Global diagram of the permanent magnet synchronous generator control.

4. Results and Discussion

The power coefficient Cp of the turbine used during this simulation is represented according to λ on the figure 5. It takes its maximal value when λ=7.5. This value is superior to the limit of BETZ because of the polynomial approximation of features of the wind turbine studied.

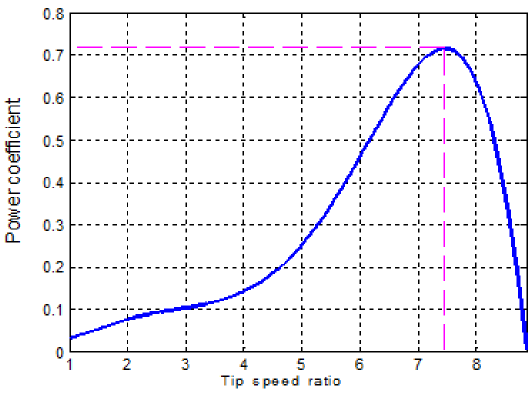

Figure 5: Characteristics.

Figure 6 illustrates the tip-speed ratio variations for a wind speed that varies from 6m/s to 8m/s at the instant t=20(s) according to an echelon. It is clear that the tip-speed ratio stabilizes at a value of 7.5 what maintains an optimal value for the coefficient of power, held account that the initial speed of the turbine is 20(rd/s).

Figures 7.a, 7.c represent respectively rectifier MLI1 and inverter MLI2 currents for a single phase, for a wind speed of 6m/s. These same currents are represented on the figures 7.b and 7.d for a wind speed of 8m/s.

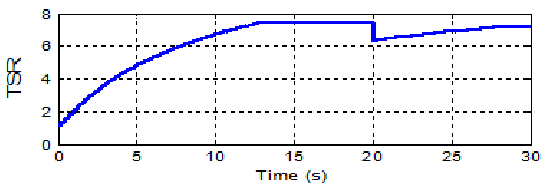

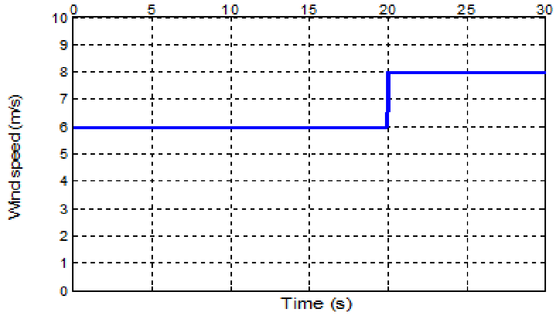

Figure 6: Variations of tip-speed ratio according to wind speed.

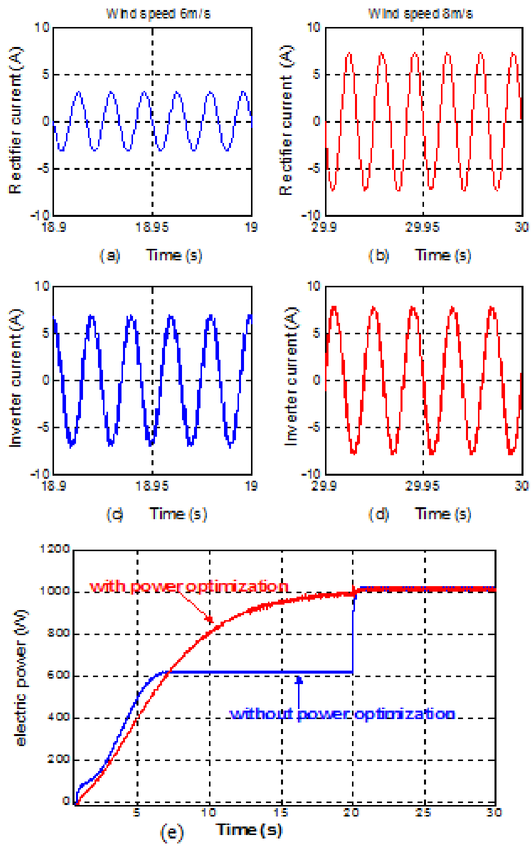

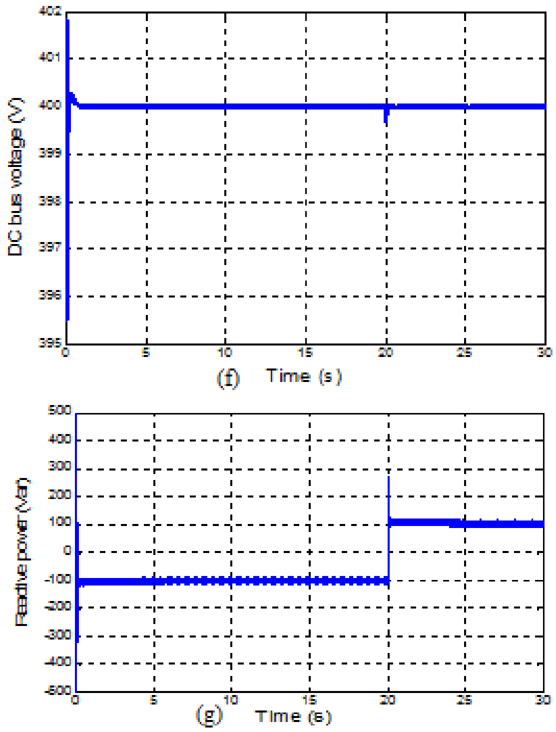

Figure 7: Simulation results.

From the previous figures, we can observe the influence of the wind speed, and therefore the kinetic energy of wind on the amplitudes of currents. With the increase of the wind speed, currents values become more important either of generating side, or grid side. The method used to optimize the power extracted of wind is validated by the illustrated results of simulation on the figure 7.e. It is clear that the power provided to the grid with optimization is more important than one provided without optimization, notably in the case where the wind speed is insufficient.

The figure 7.g represents DC bus voltage that is maintained constant to 400(V). As soon as the capacitor is putting into charge, it undergoes some variations around 400(V) caused by the load transient current, in fact that the capacitor is previously charged to 400(V). A light variation noted to the instant 20(s) caused by the abrupt variation of the generator current, and therefore, the current produced by the rectifier MLI1.

The performances of the reactive power control strategy are validated by the gotten results. While choosing a reference of -100(VAR) before the instant 20(s), and a reference of 100(VAR) after, the reactive power is gotten without meaningful fluctuations of the DC bus voltage.

5. Conclusions

Simulation results permitted to consider the objectives fixed by these control strategies. With this end in view it was possible to examine the validity of the power optimization algorithm on the active power and specific speed curves that is maintained to the optimal value in steady state, and to observe wind speed influence on current, voltage, and power that become more important with the increase of the wind speed. The performances of DC bus regulation strategies and reactive power control have been put in evidence through the results of simulation.

References

[1] Ackermann T, Söder L., «An Overview of Wind Energy-Status» 2002. Renewable and Sustainable Energy Reviews, 2002, Vol. 6, pp. 67-128.

[2] D. Schreiber, «State of art of variable speed wind turbines», 11th International symposium on power electronics - Ee 2001, Novi Sad, Oct. - Nov. 2001, CD - proceedings.

[3] M. Chinchilla, S. Arnaltes, J. Carlos Burgos, « Control of Permanent-Magnet Generators Applied to Variable-Speed Wind- Energy Systems Connected to the Grid », IEEE Transaction on energy conversion vol 21, n°, 1, Mars 2006.

[4] B. N. Mobarkah, « Commande vectorielle sans capteur mécanique des machines synchrones à aimants : Méthodes, Convergence, Robustesse, Identification ‘en ligne’ des paramètres », Thesis for the degree of doctor of the university of Tehran, Iran. December 2001.

[5] Dr. Gary L. Johnson, « Wind Energy Systems », Chapter 4- Wind Turbine Power, Nov, 2001.

[6] A. Bouscayrol, Ph. Delarue, X. Guillaud, « Power strategies for maximum control structure of a wind energy conversion system with a synchronous machine », Renewable Energy 30 (2005) 2273–2288.

[7] S. El Aimani, B. Fran¸cois, B. Robyns, « Modélisation de générateurs éoliens à vitesse variable Connectés à un bus continu commun», Forum International sur les Energies Renouvelables, FIER 2002, T´etouan, Maroc, 8-10 mai 2002.

Appendix: Simulation Parameters

Wind Turbine: Air density ρ=1.08 Radius R= 1.525 m

Initial speed=20 rps, Gear Ratio=5.0

PMSG: P=2, Rs=2.35 Ω, L_d=0.01H, L_q=0.01 H,

$\psi_f = 0.314$ Wb, J=2 Kg.m^2

Rectifier Parameters: L_{sr}=0.001 H, C=500 µf

Inverter Parameters: R_f=0.5 Ω, L_f=0.01 H

Grid Parameters: $100\sqrt{2}\ (3\sim)\ \mathrm{V},\ 50\ \mathrm{HZ}$

JJMIE

Volume 5, Number 6, Dec. 2011
ISSN 1995-6665
Pages 495 - 507

Jordan Journal of Mechanical and Industrial Engineering

Four-Port Noise Model for the Diesel Particulate Filters (DPF)

Sayel M. Fayyad[a], Mohammad N. Hamdan*[,b], Suleiman Abu-Ein[a]

[a]*Al-Balqa Applied University, Mechanical Engineering Department, Jordan*
[b]*University Cincinnati, School of Aerospace and Mechanical Engineering , USA*

Abstract

This work presents a 2-D field model for the study of sound propagation in a diesel particulate filter (DPF) unit. The 2-D model is formulated using Navier-stocks, energy, and continuity equations in which the normal as well as transverse component of gas velocity are retained. Temperature, pressure, density, and velocities variations with time are assumed to be harmonic. By substituting these quantities in the governing Navier-stock, energy, and continuity equations, a set of 2-D partial differential equations with respect to space are obtained . The obtained 2-D partial differential equations are solved using an approximate Fourier series expansions. The main outcome of this approximate analytical study is a 2-D acoustic model for the exhaust gases emission, with the existence of the diesel particulate filter. The approximate 2-D model is used in this work for calculating values of wave propagation constant which includes both attenuation and phase shift, finding the acoustics impedance of the DPF unit, comparing between different types of the DPF based on sound transmission losses, soot loading and on noise and vibration damping characteristics, in addition to calculating the noise reduction factor (NRF). The obtained results are compared with those presented by other investigators and a good agreement and improvements can be noticed for the presented study.

1. Introduction

One of the leading technologies for meeting future particulate matter (PM) emission standards is the diesel particulate filter (DPF). These devices generally consist of a wall-flow type filter positioned in the exhaust stream of a diesel vehicle. As the exhaust gases pass through the system, particulate emissions are collected and stored. Because the volume of diesel particulates collected by the system will eventually fill up and even plug the filter, a method for controlling trapped particulate matter and regenerating the filter is needed. Diesel particulate filter is a superior system in the reduction of particulate matters because it can lead to a reduction of about 70% of the PM. It contains a large numbers of thin tubes or cavities with a diameter of about (1-2 mm), and (0.15-0.5 cm) length.

There are many types of DPF's such as: electric heater type, burner type (ceramic filter), and fuel additive type; the latter type is a honey-comb ceramic. The honey-comb type constitutes an additive supply and an electronic system. In this type Fe is used as an additive whereby iron oxide is formed which reacts with carbon and then it is converted to iron. The DPF is connected on the exhaust pipe, hence noise and vibration characteristics of exhaust system are changed and consequently affect the performance of the engine by developing back pressure, change temperature and velocity of the exhaust gases...etc. Hence building an acoustic model for the DPF is necessary for the assessment of the diesel engine performance.

The performance of a DPF has been the subject of many theoretical and experimental studies over the last two decades, e.g. [1-13]. Greevesm [2] studied the origin of hydrocarbons emission from diesel engines and he found that DPF can eliminate some of PM and it is very promising as an after-treatment technique. Yu and Shahed [3] studied the effects of injection timing and exhaust gas recirculation on emissions from a diesel engine and they classified DPF as filtration and regenerative technique.

Konstandopoulous et al. [4] studied the wall-flow diesel particulate filters pressure drop and coolant efficiency and described the coupling between neighboring channels using Daracy's law to model flow through a porous medium. Peal [5] made an approximation to the effect of mean flow on sound propagation in capillary tubes. Astley and Cumings [6] presented FEM solutions, based on simplified equations for waves in a visco-thermal fluid, for the problem of sound propagation in capillary tubes. They made analysis for the laminar flow with a parabolic velocity distribution and a quadratic cross-section. The simplification of the governing equations is based on that the axial gradients are much smaller than the gradients over the cross-section.

Dokumaci [7] using the same set of simplified equations showed that for the case of a plug flow and a circular cross-section an exact solution is possible. Using this model the acoustic two-port for a catalytic converter unit was derived. Ih et al. [8] developed an analytical solutions for sound propagation in capillary cylindrical tubes with a parabolic mean flow, by neglecting the radial component of the particle velocity. Jeong and Ih [9] showed by numerical solutions of the governing equations,

* Corresponding author. e-mail: mnader@ju.edu.jo

that including the radial particle velocity has a small but noticeable effect. Dokumaci [10,11] extended his earlier work to the case of rectangular narrow tubes with a plug flow. He used a solution procedure based on a weak (Galerkin) formulation, where the fields over the channel cross-section are expanded as double Fourier sinus series. Allam and Abom [12] studied the acoustic modeling and testing of DPF and considered it as an eigenvalue 1D problem. Allam and Abom [1] modified the 1D model using the classical (exact) Kirchhoff solution for a plane wave in a narrow tube. Their model is shown to be in close agreement with the predictions of the model presented in this work. Furthermore their model, which assumes isothermal sound propagation, works satisfactorily up to 800-1000 Hz for a typical filter at operating (hot) conditions. The above studies treated the ease of tubes with rigid and non-porous walls, which are not applicable for the case of DPF. In this work the model developed by Allam and Abom [1] as well as that developed in [13]are used and modified by taking into account the effect of transverse velocity.

2. Formulation and solution of the problem

The DPF will be divided, as in [1], into five parts, see Fig. 1 below. The inlet (IN), narrow pipes with impermeable walls (1) and (3), the ceramic section (2), and the outlet section (OUT). The DPF may be manufactured from different materials (Cordierite or Silicon Carbide for example) and in its most common form consists of a substrate of narrow channels in which each channel is blocked at one end. Adjacent channels have this blockage at alternate ends with this construction exhaust gas may enter at one end, but must pass through the wall of a channel before exiting and is thus termed a wall flow device. From this it is clear that the flow in y-direction can have a significant effect i.e. the transverse velocity may play a vital role and has an affect in by making the problem a 2-D one.

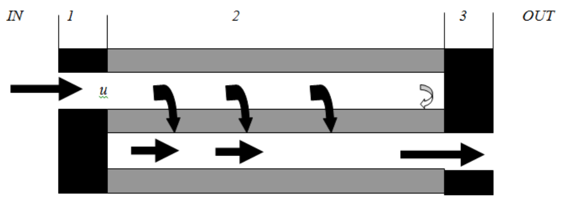

Figure (1) DPF sections and the 2D flow of gases.

2.1. Derivation of the Governing Equations:

The structure of diesel particulate filler (DPF) cells will be considered approximately square in the cross- section with a width about (1-2) mm. To develop an acoustic model for the sound propagation in the DPF unit after it is connected on the exhaust pipe, knowledge of the propagation constant for two – neighboring cells in the filter is required.

To derive the governing equations that describe the behavior of sound propagation in the filter and which may help in understanding of noise and vibration of the exhaust pipe after DPF unit is connected, the following simplifying assumptions are made :

- The DPF unit is considered completely as porous media.
- The transverse "normal" component of velocity (vyj) will not be neglected i.e. the model will be treated as a 2-D one.
- Flow in porous DPF unit is considered as viscous-thermal , incompressible, laminar, steady and Newtonian ideal gas flow.
- Chemical reactions are neglected.
- Pressure, temperature, velocities, and density are considered to vary harmonically with time.

To derive the governing equations the following basic forms of Navier – Stocks (momentum), continuity, energy and state equations are used.

Navier -Stocks equations:

$$\rho_{0j}\left[\frac{\partial u_{xj}}{\partial t}+u_{xj}\frac{\partial U_{0j}}{\partial x}+v_{yj}\frac{\partial U_{0j}}{\partial y}+w_{zj}\frac{\partial U_{0j}}{\partial z}\right]+\rho_{0j}U_{0j}\frac{\partial u_{xj}}{\partial x}= -\frac{\partial P_j}{\partial x}+\mu_j\left(\frac{\partial^2 u_{xj}}{\partial x^2}+\frac{\partial^2 u_{xj}}{\partial y^2}+\frac{\partial^2 u_{xj}}{\partial z^2}\right) \quad (1)$$

$$\rho_{0j}\left[\frac{\partial v_{yj}}{\partial t}+u_{xj}\frac{\partial V_{0j}}{\partial x}+v_{yj}\frac{\partial V_{0j}}{\partial y}+w_{zj}\frac{\partial V_{0j}}{\partial z}\right]+ \rho_{0j}V_{0j}\frac{\partial v_{yj}}{\partial y}=-\frac{\partial P_j}{\partial y}+\mu_j\left(\frac{\partial^2 v_{yj}}{\partial x^2}+\frac{\partial^2 v_{yj}}{\partial y^2}+\frac{\partial^2 v_{yj}}{\partial z^2}\right) \quad (2)$$

Continuity equation:

$$\frac{\partial \rho_j}{\partial t}+u_{xj}\frac{\partial \rho_{0j}}{\partial x}+U_{0J}\frac{\partial \rho_j}{\partial x}+\rho_j\frac{\partial U_{0j}}{\partial x}+\rho_{0j}\nabla .u_j=0 \quad (3)$$

Energy equation

$$\rho_{0j}Cp_j\left[\frac{\partial T_j}{\partial t}+U_{0j}\frac{\partial T_j}{\partial x}+u_{xj}\frac{\partial T_{0j}}{\partial x}\right]+\rho_j Cp_j U_{0j}\frac{\partial T_{0J}}{\partial x}= -\frac{\partial P_j}{\partial t}+U_{0j}\frac{\partial P_j}{\partial x}+\frac{\partial P_{0j}}{\partial x}u_{xj}+K_{thj}\nabla_s^2 T_j \quad (4)$$

State equation:

The gasses emission upon the exhaust pipe will be considered as an ideal gas so the state equation takes the form

$$\rho_j=\left(\frac{p_j}{R_j T_{0j}}\right)-\left(\frac{\rho_{0j}T_j}{T_{oj}}\right), \qquad \rho_j=\rho_j(x,y,z,t). \quad (5)$$

where

.

$$\rho_j=\rho_j(x,y,t)$$
$$T_j=T_j(x,y,z,t) \quad (6)$$
$$P_j=P_j(x,y,t)$$

x, y denotes the channel axis, u, v are the acoustic particle velocities, j = 1, 2 represent the inlet and outlet pipes, respectively, p, T and ρ are the acoustic pressure, temperature and density, respectively, μ is the shear viscosity coefficient, kth is the thermal conductivity of the fluid, R is the gas constant, Cp is the specific heat coefficient at constant pressure, P0, T0 and ρ0 denote the ambient pressure, temperature and density, respectively, U0, V0 denotes the axial mean flow velocity and transverse velocity respectively, and denotes the Laplacian over the channel cross-section.

To describe the coupling between neighboring channels (which describes the porosity of diesel particulate filter) Darey's law is applied to the fluctuating fields:

$$p_1 - p_2 = R_w u_w \tag{8}$$

Where uw is the acoustic velocity through the wall and Rw is the wall resistance, which is given by Rw = μwht/σw, μw is the dynamic viscosity, ht is the wall thickness and σw is the wall permeability.

As indicated in the previous section, the problem will be treated as a 2D one, i.e.

$$\frac{\partial U_{0j}}{\partial z} = \frac{\partial^2 U_{0j}}{\partial z^2} = \frac{\partial V_{0j}}{\partial z^2} = \frac{\partial^2 V_{0j}}{\partial z^2} = 0 \tag{9}$$

At this stage u, v, P_j, ρ_j, T_j are considered to be varying with time only i.e. (time- harmonic variation) , that is

$$u_{xj} = A_0 e^{iwt}$$
$$v_i = B_0 e^{iwt} \tag{10}$$

$$\rho_j = \rho_0 e^{iwt},\ P_j = P_0 e^{-iwt},\ T_j = T_0 e^{iwt} \tag{11}$$

where $A_0, B_0, \rho_0, P_0, T_0$ are constant amplitudes. Substituting equation (9)-(11) into equations (1) to (4) one obtains:

$$\begin{aligned}&\rho_{0j}\left[iw + U_{0j}\frac{\partial}{\partial x}\right]u_{xj} + \rho_{0j}\frac{\partial U_{0j}}{\partial x}u_{xj} + \rho_{0j}\frac{\partial U_{0j}}{\partial y}v_{yj} = \\ &-\frac{\partial P_j}{\partial x} + \mu_j\left(\frac{\partial^2 u_{xj}}{\partial x^2} + \frac{\partial^2 u_{xj}}{\partial y^2} + \frac{\partial^2 u_{xj}}{\partial z^2}\right)\end{aligned} \tag{12}$$

$$\begin{aligned}&\rho_{0j}\left[iw + V_{0j}\frac{\partial}{\partial y}\right]v_{yj} + \rho_{0j}\frac{\partial V_{0j}}{\partial y}v_{yj} + \rho_{0j}\frac{\partial V_{0j}}{\partial x}u_{xj} = \\ &-\frac{\partial P_j}{\partial y} + \mu_j\left(\frac{\partial^2 v_{yj}}{\partial x^2} + \frac{\partial^2 v_{yj}}{\partial y^2} + \frac{\partial^2 v_{yj}}{\partial z^2}\right)\end{aligned} \tag{13}$$

$$\begin{aligned}&\rho_{0j}Cp_j\left[iw + U_{0j}\frac{\partial}{\partial x}\right]T_j + \rho_j Cp_j\frac{\partial T_{0J}}{\partial x}u_{xj} \\ &+U_{0J}Cp_j\frac{\partial T_{0j}}{\partial x}\rho_j = (U_{0j}\frac{\partial}{\partial x} + iw)P_j + \frac{\partial P_{0j}}{\partial x}u_{xj} + K_{thj}\nabla_s^2 T_j\end{aligned} \tag{14}$$

For verification if the problem is back treated as a 1D linear problem equations (12) -(14) will be shown later on to reduce to those given by Allam and Abom [1].

To get a full description to the acoustic model of the DPF unit, and then to find impedance, transmission losses, and other parameters used to assess the DPF unit performance, equations ((12) -(14) are solved analytically using the following approximations for the system variables:

$$\begin{aligned}&P_j = A_J\exp(-i\Gamma k_1 x),\\ &u_{xj} = H_j(x,y,z)P_j,\\ &T_j = F_j(x,y,z)P_j,\\ &v_{yj} = B_j\exp(-i\Gamma k_1 y)\end{aligned} \tag{15}$$

where Γ is a wave propagation constant.

Differentiating all terms in equation (15) and substituting them in equations (12) and (13) leads to

$$\begin{aligned}&\rho_{0j}iwH_jP_j + \rho_{0j}iU_{0j}H_j\Gamma k_1 P_j \\ &+\rho_{0j}\frac{\partial U_{0j}}{\partial x}H_jP_j + \rho_{0j}\frac{\partial U_{0j}}{\partial y}H_jP_j \\ &= i\Gamma k_1 P_j + \mu_j\left(\frac{\partial^2 H_j}{\partial x^2} + \frac{\partial^2 H_j}{\partial y^2} + \frac{\partial^2 H_j}{\partial z^2}\right)\end{aligned} \tag{16}$$

Then dropping P_j and introducing the parameters

$$S_j^2 = \frac{\rho_{0j}w}{\mu_j} \quad , \quad M_j = \frac{U_{0j}}{C} \tag{17}$$

where S_j is the shear wave number, and M_j is Mach number, equation(16) becomes

$$\begin{aligned}&\frac{\partial^2 H_j}{\partial x^2} + \frac{\partial^2 H_j}{\partial y^2} + \frac{\partial^2 H_j}{\partial z^2} - i\left(1 - \Gamma M_j + \frac{1}{iw}\frac{\partial U_{0j}}{\partial x} + \frac{\partial U_{0j}}{\partial y}\right)S_j^2 H_j \\ &= \frac{-i\Gamma k_1}{\mu_j}\end{aligned} \tag{18}$$

Next using the commonly employed definitions[1]

$$\beta_{xj}^2 = \left(1 - \Gamma M_{jx} + \frac{1}{iw}\frac{\partial U_{0j}}{\partial x} + \frac{\partial U_{0j}}{\partial y}\right)S_j^2 \tag{19}$$

$$\beta_{yj}^2 = \left(1 - \Gamma M_{jy} + \frac{1}{iw}\frac{\partial V_{0j}}{\partial y} + \frac{\partial V_{0j}}{\partial x}\right)S_j^2 \tag{20}$$

into equation (18), leads to

$$\frac{\partial^2 H_j}{\partial x^2} + \frac{\partial^2 H_j}{\partial y^2} + \frac{\partial^2 H_j}{\partial z^2} - i\beta_{xj}^2 H_j = \frac{-i\Gamma k_1}{\mu_j} \tag{21}$$

$$\frac{\partial^2 H_j}{\partial x^2} + \frac{\partial^2 H_j}{\partial y^2} + \frac{\partial^2 H_j}{\partial z^2} - i\beta_{yj}^2 H_j = \frac{-i\Gamma k_1}{\mu_j} \tag{22}$$

where $M_{jy} = \frac{V_0}{C}$ is the Mach number, and $k_1 = \frac{w}{C}$ is the wave number. Also substituting equation (15) in equation (14) one obtains

$$\rho_{0j}Cp_j iwF_J P_j - \rho_{0j}Cp_j iU_{0j}F_j\Gamma k_1 P_j + \rho_{0j}Cp_j\frac{\partial T_{0j}}{\partial x}H_jP_j + \rho_j Cp_j\frac{\partial T_{0j}}{\partial x}P_j = iw_1P_j - iU_{0j}\Gamma kP_j\frac{\partial \rho_{0j}}{\partial x}H_jP_j + K_{thj}\left(\frac{\partial^2 F_j}{\partial x^2}+\frac{\partial^2 F_j}{\partial y^2}+\frac{\partial^2 F_j}{\partial z^2}\right)P_j \tag{23}$$

Next using state equation (5), rearranging and divided by P_j, and K_{thj} equation (23) yields

$$\frac{\partial^2 F_j}{\partial x^2}+\frac{\partial^2 F_j}{\partial y^2}+\frac{\partial^2 F_j}{\partial z^2}-\sigma_{jx}^2F_j=\sigma_{0j}^2+\sigma_{1j}^2H_j \tag{24}$$

Where

$$\sigma_{jx}^2 = iS_j^2\Pr\left(1-\Gamma M_{jx}-\frac{U_{0j}}{iwT_{0j}}\frac{\partial T_{0j}}{\partial x}\right),$$
$$\sigma_{0jx}^2=\frac{-iw}{K_{thj}}\left(1+\frac{Cp_jU_{0j}}{iwR_jT_{0j}}\frac{\partial T_{0j}}{\partial x}-\Gamma M_{jx}\right),$$
$$\sigma_{1jx}^2=\frac{1}{K_{thj}}\left(\rho_{0j}Cp_j\frac{\partial T_{0j}}{\partial x}-\frac{\partial P_{0j}}{\partial x}\right), \tag{25}$$
$$\Pr=\sqrt{\frac{\mu_J Cp_J}{K_{thj}}}$$

where Pr is the Prandtle number. In order to find a solution to equations (21) , (22) and (24) in a weak (Galerkian) sense, the fields *H*, and *F* are expanded in double Fourier Sine series [1] such that $H_{jx}(x, y, z)$ and *F* are assumed to be just varying in y and z directions only which implies that

$$\frac{\partial H_j}{\partial x}=0,\quad \frac{\partial^2 H_j}{\partial x^2}=0,\quad \frac{\partial F_j}{\partial x}=0,\quad \frac{\partial^2 F_j}{\partial x^2}=0 \tag{26}$$

And

$$H(0,y,z)=\sum_{m,n}a_{mn}\sin\frac{m\Pi y}{2a_j}\sin\frac{n\Pi z}{2a_j} \tag{27}$$

$$H(x,0,z)=\sum_{\ln}a_{\ln}\sin\frac{l\Pi x}{2a_j}\sin\frac{n\Pi z}{2a_j} \tag{28}$$

where m, l, n=1, 3, 5, 7,…, and the expansion for *F* will be, for convenience, presented in a later part of this section. The above series includes only symmetric terms since the assumed pressure distribution is symmetric over the cross- section and the no slip wall boundary condition is assumed.

To calculate (a_{mn} *and* $a_{\ln}$)the above series are substituted into equation (21) the result is integrated over the cross-section and using the orthogonality property of the terms in these series one obtains ,

$$\sum_{m,n}a_{mn}\beta_j^2\alpha_{mn}(\beta_ja_j)I_1=\frac{-ik\Gamma_1}{\mu_j}I_2 \tag{29}$$

where

$$\alpha_{mn}(\beta_ja_j)=1+\frac{-\Pi^2}{4(\beta_ja_j)^2(m^2+n^2)} \tag{30}$$

$$I_1=\iint_{a_j*a_j}\sin\frac{m\Pi y}{2a_j}\sin\frac{n\Pi z}{2a_j}\sin\frac{m'\Pi y}{2a_j}\sin\frac{n'\Pi z}{2a_j}dydz \tag{31}$$

$$I_2=\iint_{a_j*a_j}\sin\frac{m'\Pi y}{2a_j}\sin\frac{n'\Pi z}{2a_j}dydz \tag{32}$$

Next carrying out the above integrations for m=m', n=n' and m ≠ m', n≠n', leads to

$$I_1=\begin{cases}a_j^2, & m=m', n=n'\\ 0 & m\neq m'\\ 0 & n\neq n'\end{cases} \tag{33}$$

$$I_2=\frac{16a_j^2}{m'n'\Pi^2} \tag{34}$$

where m, n and m', n' are odd integers= (1,3,5…..) . Substituting equations (33) and (34) into equation (29) gives

$$a_{mn}\beta_j^2\alpha_{mn}(\beta_ja_j)a_j^2=\frac{i\Gamma k_1}{\mu_j}\frac{16a_j^2}{mn\Pi^2} \tag{35}$$

Then solving the above equation for a_{mn} , one obtains

$$a_{mn}=\frac{16i\Gamma k_1}{mn\Pi^2\beta_j^2\alpha_{mn}(\beta_ja_j)\mu_j} \tag{36}$$

Also following the same procedure as above, using equation (22) instead of equation (21), leads to

$$a_{\ln}=\frac{16i\Gamma k_1}{mn\Pi^2\beta_{jy}^2\alpha_{mn}(\beta_{jy}a_j)\mu_j} \tag{37}$$

Similarly, an approximate solution to equation (24), and as indicated above, is obtained by using the approximations

$$F(x,y,z)=\sum_{mn}b_{mn}\sin\frac{m\Pi y}{2a_j}\sin\frac{n\Pi z}{2a_j} \tag{38}$$

$$F(x,y,z)=\sum_{\ln}b_{\ln}\sin\frac{l\Pi x}{2a_j}\sin\frac{n\Pi z}{2a_j} \tag{39}$$

Then following the same procedure used in calculating a_{mn}, a_{ln}, yields

$$b_{mn} = \frac{-1}{\sigma_j^2 \alpha_{mn}(\sigma_j a_j)\mu_j}\left(\frac{16\sigma_{0j}^2}{\Pi^2 mn} + \sigma_{1j}^2 a_{mn}\right) \quad (40)$$

where b_{ln} are undefined and thus will be neglected, e.g, so the problem will be treated only in x- direction and the y- direction variations are ignored.

In order to get a complete solution for the acoustic problem, continuity equation (3) is solved as follows. First averaging equation (3) and sate equation (5) ,one has.

$$(iw + U_{0j}\frac{\partial}{\partial x}) < \rho_j > + < u_{xj} > \frac{\partial \rho_{0j}}{\partial x} + U_{0J}\frac{\partial \rho_j}{\partial x} + < \rho_j > \frac{\partial U_{0j}}{\partial x} + < \rho_{0j}\nabla .u_j >= 0 \quad (41)$$

$$< \rho_j >= \frac{P_j}{R_j T_j}(1 - \rho_{0j} R_j < F_j >) \quad (42)$$

where

$$< f >= \frac{1}{4a_j^2}\iint_{2a_j * 2a_j} f dydz \quad (43)$$

$$< F_j >= \sum_{m,n}\frac{4b_{mn}}{mn\Pi^2} \quad (44)$$

$$< u_{xj} >= P_j < H_j >, \ and \quad < H_j >= \sum_{m,n}\frac{4a_{mn}}{mn\Pi^2}, \quad (45)$$

To find $< \nabla .u_j >$, one writes

$$< \nabla .u_j >= \frac{1}{4a_j^2}\iint_{2a_j * 2a_j}\left(\frac{\partial u_{xj}}{\partial x} + \frac{\partial v_{yj}}{\partial y} + \nabla_s .u_j\right)dydz = \frac{\partial < u_{xj} >}{\partial x} + \frac{\partial < v_{yj} >}{\partial y} + \frac{1}{4a_j^2}\oint_{c_j} u_j .n_j ds \quad (46)$$

but

$$\oint_{c_j} u_j .n_j ds = (-1)^{j-1}\oint_{c_j}\bar{u}_w ds \quad (47)$$

and

$$\frac{\partial < u_{xj} >}{\partial x} = -ik_1\Gamma P_j < H_j >, and \quad \frac{\partial < v_{xj} >}{\partial y} = -ik_1\Gamma P_j < H_j >, \quad (48)$$

where c_j is the curve around the channel perimeter and u_w is the acoustic wall velocity.
Then using Darcy's law (equation (7)).

$$\bar{u}_w = \frac{P - P_{21}}{R_w} \quad (49)$$

and substituting equations (48) and (49) into equation (47)gives:

$$\oint_{c_j} u_j .n_j ds = (-1)^{j-1}\frac{8a_j(P_1 - P_2)}{R_w} \quad (50)$$

Then substituting equations (48) and (50) into equation (41) yields

$$(iw + U_{0j}\frac{\partial}{\partial x})\left(\frac{P_j}{R_j T_{0j}}(1 - \rho_{0j} R_J < F_J >)\right) + \frac{\partial \rho_{0j}}{\partial x} P_j < H_j > + \rho_{0j}(-2i\Gamma k_1 < H_J > P_j) + \frac{\partial U_{0j}}{\partial x}\left(\frac{P_j}{R_j T_{0j}}(1 - \rho_{0j} R_J < F_J >)\right) + < \rho_{0j}\nabla .u_j > + (-1)^{j-1}\frac{\rho_{0j} * 8a_j(P_1 - P_2)}{4a_j^2 R_w} = 0 \quad (51)$$

Rearrange equation (51) and substituting the value of P_j (given in equation (15)) one obtains

$$\begin{bmatrix} \frac{1}{R_j T_{0j}}(iw - \Gamma k_1 U_{0J} + \frac{\partial U_{0j}}{\partial x})(1 - \rho_{0j} R_j < F_j >) \\ + (\frac{\partial \rho_{0j}}{\partial x} - 2ik_1\Gamma\rho_{0j}) < H_j > \end{bmatrix} A_j + (-1)^{j-1} * \frac{2\rho_{0j}(A_1 - A_2)}{a_j R_w} = 0 \quad (52)$$

Then multiplying the above equation by ($\frac{R_W a_j}{2\rho_{0j}}$), leads to

$$\begin{bmatrix} \frac{R_w a_j}{2\rho_{0j} R_j T_{0j}}(iw - \Gamma k_1 U_{0J} + \frac{\partial U_{0j}}{\partial x})(1 - \rho_{0j} R_j < F_j >) \\ + \frac{R_w a_j}{2\rho_{0j}}(\frac{\partial \rho_{0j}}{\partial x} - 2ik_1\Gamma\rho_{0j}) < H_j > \end{bmatrix} A_j + (-1)^{j-1}(A_1 - A_2) = 0 \quad (53)$$

The above equation represents a set of two linear homogeneous equations for the amplitudes of pressure waves A_1, A_2 in neighboring channels 1 and2 which can be written as [1]

$$\begin{bmatrix} K11 + K21 & -K12 \\ K21 & K12 - K22 \end{bmatrix}\begin{bmatrix} A_1 \\ A_2 \end{bmatrix} = \begin{bmatrix} 0 \\ 0 \end{bmatrix} \quad (54)$$

where

$$K_{1j} = \begin{bmatrix} \frac{R_w a_j}{2\rho_{0j} R_j T_{0j}}(iw - \Gamma k_1 U_{0J} + \frac{\partial U_{0j}}{\partial x})(1 - \rho_{0j} R_j < F_j >) + \\ \frac{R_w a_j}{2\rho_{0j}}(\frac{\partial \rho_{0j}}{\partial x} - 2ik_1\Gamma\rho_{0j}) < H_j > \end{bmatrix} \quad (55)$$

and

$$K_{2j} = (-1)^{j-1} \quad (56)$$

For a non trivial solution the determinant

$$\begin{vmatrix} K11+K21 & -K12 \\ K21 & K12-K22 \end{vmatrix} \tag{57}$$

is set equal to zero which leads to a transcendental equation for the propagation constant "Γ". By substituting numerical values of different constants and physical quantities, and by using "Matlab" for the case of no-mean flow i.e. (U_{0j}, V_{0j}=0) the obtained results for the values of the propagation constant are as follows.

For the case of cold conditions (T=293˚K,w=200-300 Hz):

Γ1=0.0005+0.0027i, Γ2=-0.0005-0.0023i,
Γ3= 0.0014+0.0008i, and Γ4=0.0014-0.0008i.

While for the specified hot conditions, (e.g, T=773˚K, w=400-1000 Hz), the obtained results are:

Γ1= (0.2451+0.9873i)10^{-3}, Γ2= (-0.2451-0.9873i)10^{-3}, Γ3= (-0.7032+0.3440i)10^{-3}, and Γ4= (0.7032-0.3440i)10^{-3}.

Plots and discussion of wave propagation constant variations with shear wave number are presented and discussed later on. Note that for each root of eigenvalues of Γ there is a corresponding 2-D mode (eigenvector) e_n. Using these eigenvectors and modes the general expression of these eigenvectors can be written as follows for the time harmonic variation.

$$\begin{pmatrix} \hat{p}_1(x) \\ \hat{p}_2(x) \end{pmatrix} = \sum_{n=1}^{4} \hat{a}_n e^{-ik_1\Gamma_n x} e_{,jn} \tag{58}$$

where $\hat{a}_n$ is the modal amplitude and $\hat{p}\,(x)$ is the acoustics pressure. For each acoustics pressure there is an acoustics volume velocity $\hat{q}_j(x)$ given by

$$\begin{pmatrix} \hat{q}_1(x) \\ \hat{q}_2(x) \end{pmatrix} = \sum_{n=1}^{4} \hat{a}_n e^{-ik_1\Gamma_n x} e'_{,jn} \tag{59}$$

Where

$$e'_{j,n} = 4a_j^2 < H_{j,n} > e_{j,n}$$

Then using equations (58) and (59) the total four port matrix can be written as:

$$\begin{pmatrix} \hat{p}_1(x) \\ \hat{p}_2(x) \\ \hat{q}_1(x) \\ \hat{q}_2(x) \end{pmatrix} = \begin{pmatrix} e^{-ik_1\Gamma_1 x} e_1 & e^{-ik_1\Gamma_2 x} e_2 & e^{-ik_1\Gamma_3 x} e_3 & e^{-ik_1\Gamma_4 x} e_4 \\ e^{ik_1\Gamma_1 x} e_1 & e^{ik_1\Gamma_2 x} e_2 & e^{ik_1\Gamma_3 x} e_3 & e^{ik_1\Gamma_4 x} e_4 \\ e^{-ik2\Gamma_1 x} e_1 & e^{-ik2\Gamma_2 x} e_2 & e^{-ik_2\Gamma_3 x} e_3 & e^{-ik_2\Gamma_4 x} e_4 \\ e^{ik_2\Gamma_1 x} e_1 & e^{ik_2\Gamma_2 x} e_2 & e^{ik_2\Gamma_3 x} e_3 & e^{ik_2\Gamma_4 x} e_4 \end{pmatrix} \begin{pmatrix} \hat{a}_1 \\ \hat{a}_2 \\ \hat{a}_3 \\ \hat{a}_4 \end{pmatrix} \tag{60}$$

where [1]

$$k_2 = k_1\sqrt{1-8i\beta/k_1} \quad \beta = C_j\rho_w / dh_j R_w \quad <Hj>=4a_{11}/\Pi^2 \tag{61}$$

Next applying boundary conditions at x=0, x=L, one has

$$\begin{pmatrix} \hat{p}_1(0) \\ \hat{p}_2(0) \\ \hat{q}_1(0) \\ \hat{q}_2(0) \end{pmatrix} = H(0) \begin{pmatrix} \hat{a}_1 \\ \hat{a}_2 \\ \hat{a}_3 \\ \hat{a}_4 \end{pmatrix} \tag{62}$$

and

$$\begin{pmatrix} \hat{p}_1(L) \\ \hat{p}_2(L) \\ \hat{q}_1(L) \\ \hat{q}_2(L) \end{pmatrix} = H(L) \begin{pmatrix} \hat{a}_1 \\ \hat{a}_2 \\ \hat{a}_3 \\ \hat{a}_4 \end{pmatrix} \tag{63}$$

From equation (64) it can be shown that

$$\begin{pmatrix} \hat{a}_1 \\ \hat{a}_2 \\ \hat{a}_3 \\ \hat{a}_4 \end{pmatrix} = H^{-1}(L) \begin{pmatrix} \hat{p}_1(L) \\ \hat{p}_2(L) \\ \hat{q}_1(L) \\ \hat{q}_2(L) \end{pmatrix} \tag{64}$$

$$\begin{pmatrix} \hat{p}_1(0) \\ \hat{p}_2(0) \\ \hat{q}_1(0) \\ \hat{q}_2(0) \end{pmatrix} = H(0)\, H^{-1}(L) * \begin{pmatrix} \hat{p}(L)_1 \\ \hat{p}_2(L) \\ \hat{q}_3(L) \\ \hat{q}_4(L) \end{pmatrix} \tag{65}$$

Introducing the notation $H(0)\, H^{-1}(L)$ =S, the four-port matrix S can be used to find the two-port matrix T_2 by using rigid wall boundary conditions in channel 1 and 2 i.e.

$$\hat{q}_2(0) = 0, \ \hat{q}_1(L) = 0,$$

and

$$\begin{pmatrix} \hat{p}_1(0) \\ \hat{p}_2(0) \\ \hat{q}_1(0) \\ \hat{q}_2(0) \end{pmatrix} = \begin{pmatrix} S11 & S12 & S13 & S14 \\ S21 & S22 & S23 & S24 \\ S31 & S32 & S33 & S34_4 \\ S41 & S42 & S43 & S44 \end{pmatrix} \begin{pmatrix} \hat{p}(L)_1 \\ \hat{p}_2(L) \\ \hat{q}_3(L) \\ \hat{q}_4(L) \end{pmatrix} \tag{66}$$

which yields

$$\begin{aligned} \hat{p}_1(0) &= S11\left(\frac{-S44\hat{q}_2(L) - S42\,\hat{p}_2(L)}{S41}\right) + S12\,\hat{p}_2(L) + S14\hat{q}_2(L) \\ &= (S12 - S11S42/S41)\,\hat{p}_2(L) + (S14 - S11S44/S41)\hat{q}_2(L) \end{aligned} \tag{67}$$

and

$$\begin{aligned} \hat{q}_1(0) &= S31\left(\frac{-S44\hat{q}_2(L) - S42\,\hat{p}_2(L)}{S41}\right) + S32\,\hat{p}_2(L) \\ &= (S32 - S31S42/S41)\,\hat{p}_2(L) + (S34 - S31S44/S41)\hat{q}_2(L) \end{aligned} \tag{68}$$

Thus the two-port matrix can be written as

$$\begin{pmatrix} \hat{p}_1(x) \\ \hat{q}_2(x) \end{pmatrix} = T_2 \begin{pmatrix} \hat{p}_2(L) \\ \hat{q}_2(L) \end{pmatrix} \tag{69}$$

Where

$$T_2 = \begin{pmatrix} T11 & T12 \\ T21 & T22 \end{pmatrix}$$

If the number of channels at inlet (x=0) and outlet (x=L) is N then the total volume flow in all the open channels should be added, such that

$$T_2 = \begin{pmatrix} T11 & T12/N \\ NT21 & T22 \end{pmatrix} \tag{70}$$

where

$$\begin{aligned} T11 &= S12 - S42S11/S41 \\ T12 &= S14 - S44S11/S41 \\ T21 &= S32 - S42S31/S41 \\ T22 &= S34 - S44S31/S41 \end{aligned} \tag{71}$$

Substituting values of from above obtained results leads to the following expressions for the S matrix:

$S_{COLD} = 1*e^3$

$$\begin{pmatrix} 2.2079+0.3830i & -1.4236-0.1530i & -3.6978-0.9379i & -2.3229-0.7576i \\ 2.2079+0.3830i & -1.4236-0.1530i & -3.6978-0.9379i & -2.3229-0.7576i \\ (0.0009-0.0000i & -0.0005+0.0008i & 0.0003+0.0001i & 0.0002+0.0001i)*10\text{^}{-2} \\ (-0.0009+0.0000i & 0.0005-0.0008i & -0.0003-0.0001i & -0.0002-0.0001i)*10\text{^}{-2} \end{pmatrix} \tag{72}$$

$S_{HOT} = 1*e^2$

$$\begin{pmatrix} 9.4804+6.0904i & -5.9253-3.8065i & 3.4061-7.1114i & -2.6799-9.8755i \\ 9.4804+6.0904i & -5.9253-3.8065i & 3.4061-7.1114i & -2.6799-9.8755i \\ (-0.0012+0.0045i & 0.0011+0.0033i & 0.0064+.0002i & 0.0039-0.0001i)*10\text{^}{-2} \\ (0.0012-0.0045i & -0.0011-0.0033i & -0.0064-.0002i & -0.0039+0.0001i)*10\text{^}{-2} \end{pmatrix} \tag{73}$$

To obtain the acoustic resistance of the DPF, it is assumed that the acoustic field acts as a quasi-stationary disturbance of the steady state pressure drop (ΔP) over the filter unit. This pressure drop is modeled using Darcy's law with a quadratic Forcheimer extension - equation

$$\Delta p = R_1\, U + R_2\, U^2 \tag{74}$$

By differentiating this equation with respect to U one obtains

$$\begin{aligned} \frac{d(\Delta P)}{dU} &= \left(\frac{R_1 + 2R_2U}{A_f}\right) * A_f \\ d(\Delta P) &= \left(\frac{R_1 + 2R_2U}{A_f}\right) * A_f\, dU \end{aligned} \tag{75}$$

But since $dQ = A_f * dU$, one has

$$d(\Delta P) = R_{ac}\, dQ \tag{76}$$

Where

$$R_{ac} = \frac{R_1 + 2R_2U}{A_f} \tag{77}$$

R_{ac} is the acoustics resistance, and A_f is the filter cross-sectional area.

The above lumped impedance model can be used for the inlet and outlet sections including the adjacent short pipes. This implies that (for a two-port model)

$$T_x = \begin{pmatrix} 1 & Z_x \\ 0 & 1 \end{pmatrix} \tag{78}$$

Where

x=IN+1, or 3+OUT sections of the DPF.

$$Z_x = r_x + \frac{i\rho_x w l_x}{d_{hj}^2} \tag{79}$$

(79)
r is the acoustic resistance of the filter section , *L* is the end correction length and
d_{hj} is the hydraulic radius [1].
Note that, as indicated in [1],

$$r_{1+IN} = r_{3+OUT} = \frac{R_2U_0}{A} \tag{80}$$

where R_2 can be given as

$$R_2 = \begin{cases} \rho_{IN}(1 - 1/m_{IN})^2/4 \\ \rho_{OUT}(1 - 1/m_{OUT})^2/2 \end{cases} \tag{81}$$

and m $_{IN}$, m $_{OUT}$ are the open area ratios at inlet and outlet respectively. So by multiplying equation (81) by (C_j/C_j) and substitute equations (81) into equation (80) one obtains

$$Z_x = \begin{cases} Z_{IN}M_{IN}(1/m_{IN}^2 - 1) + \dfrac{i\rho w l_1}{d_{hj}^2 N} \\ 2Z_{OUT}M_{IOUT}(1 - 1/m_{OUT}) + \dfrac{i\rho w l_3}{d_{hj}^2 N} \end{cases} \tag{82}$$

Using equation (82) the full transforming matrices for different sections of the DPF can be written as follows

$$T_{IN} = \begin{pmatrix} 1/2 & Z_{IN}M_{IN}(1/m_{IN}^2 - 1) \\ 0 & 1/2 \end{pmatrix} \tag{83}$$

$$T_1 = \begin{pmatrix} 1/2 & \dfrac{i\rho w l_1}{d_{hj}^2 N} \\ 0 & 1/2 \end{pmatrix} \tag{84}$$

$$T_{OUT} = \begin{pmatrix} 1/2 & 2Z_{OUT}M_{OUT}(1 - 1/m_{OUT} \\ 0 & 1/2 \end{pmatrix} \tag{85}$$

$$T_3 = \begin{pmatrix} 1/2 & \dfrac{i\rho w l_3}{d_{hj}^2 N} \\ 0 & 1/2 \end{pmatrix} \tag{86}$$

Where

$$Z_{IN} = \frac{\rho_{IN} C_{IN}}{A_{IN}}, Z_{out} = \frac{\rho_{out} C_{outt}}{A_{out}} \tag{87}$$

Finally using the relations

$$T_{DPF} = T_{IN}\, T_1\, T_2\, T_3\, T_{out}, \tag{88}$$

$$TL = 20 \log |T_{DPF}/2| \tag{89}$$

Taking all terms of the matrix T_{DPF} in series and then applying equation (89) one obtains the transmission losses, which take the form

$$
\begin{aligned}
TL_{DPF} &= 10\log_{10}(|\ (1/16)T_{11} + (1/8)iY_1NT_{21} + \\
&(1/8)NT_{21}Z_{IN}M_{IN}(1/m_{IN}^2 - 1) + (1/4)T_{11}Z_{OUT}M_{OUT}(1 - 1/m_{OUT}) \\
&+ (1/2)iY_1NT21 + 0.5NT_{21}Z_{IN}M_{IN}(1/m_{IN}^2 - 1) + \\
&Z_{OUT}M_{OUT}(1 - 1/m_{OUT}) + (1/8)iY_3T_{11} - 0.25Y_3Y_1NT_{21} \\
&+ 0.25iY_3NT_{21}Z_{IN}M_{IN}(1/m_{IN}^2 - 1) + (1/16)T_{12}NiY_3 - (1/8)Y_1Y_3T_{22} \\
&+ (1/8)iY_3T_{22}Z_{IN}M_{IN}(1/m_{IN}^2 - 1) + (1/16)NT_{21} + \\
&0.25NT_{21}Z_{OUT}M_{OUT}(1 - 1/m_{OUT}) + (1/8)NT_{21}iY_3 + (1/16)T_{22}\ |)
\end{aligned} \tag{90}
$$

where *Y1* is the plug mass impedance of section 1 ($Y_1 = \frac{i\rho wl_1}{d_{hj}^2 N}$) and *Y3* is the plug mass impedance of section3 ($Y_3 = \frac{i\rho wl_3}{d_{hj}^2 N}$).

Note that the noise reduction factor can be calculated by using the following equation

$$NRF = LP_2 - LP_1 = 20\log\frac{P_2}{P_1} \tag{91}$$

Equation (90) will be used to find the values of transmission losses for different system parameters and for different types of DPF shown in Table (1).. The obtained results will be discussed in the next section .

3. Results and Discussion

3.1. Results:

For the case of time harmonic variation the attenuation are represented by the real parts of the propagation constant, as indicated in the previous section. Figure (2) represents the attenuation of the four real parts of the wave propagation constants for the cold conditions (293˚K. w=200-300Hz).

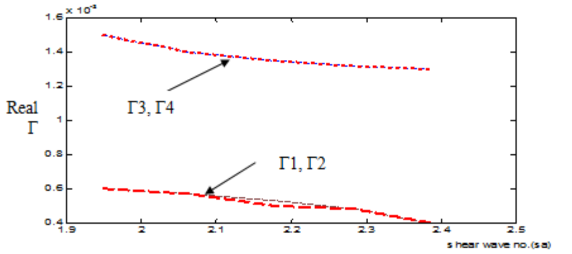

Figure 2: Real part of Γ vs. shear wave number (attenuation), ------ Γ1, ----- Γ2 propagation constants for uncoupled waves, …… Γ3,…… Γ4 propagation constants for coupled waves. (at cold conditions).

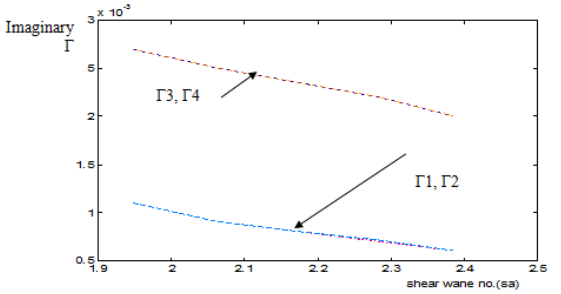

Figure 3: imaginary part of Γ vs. shear wave number (phase shift), ------ Γ1, ----- Γ2 propagation constants for uncoupled waves, …… Γ3,…… Γ4 propagation constants for coupled waves. (At cold conditions).

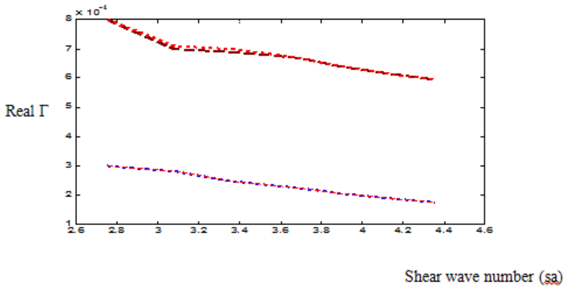

Figure 4: Real part of Γ vs. shear wave number (attenuation), ------ Γ1, ----- Γ2 propagation constants for uncoupled waves, ------- Γ3, ----- Γ4 propagation constants for coupled waves. (At hot conditions, T=773C, w=400-1000 Hz.).

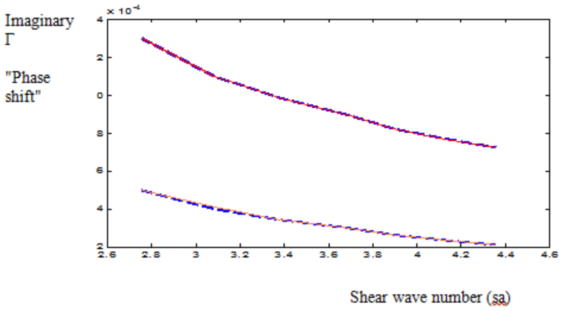

Figure 5: imaginary part of Γ vs. shear wave number (phase shift), ------ Γ1, ----- Γ2 propagation constants for uncoupled waves, …… Γ3,…… Γ4 propagation constants for coupled waves. (At hot conditions).

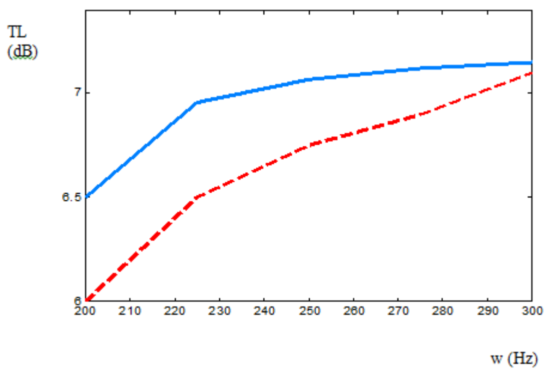

Figure 6: transmission losses vs. frequency in the case of cold conditions compared with last recent study [Allam], ----- red for Allam, while ____ blue is the proposed study, (With no soot layer) and Mach=0.02.

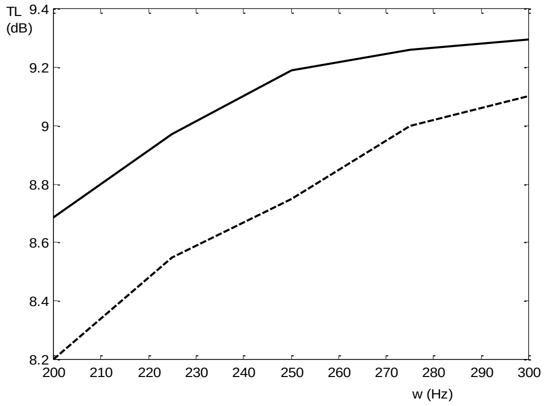

Figure 7: transmission losses vs. frequency in the case of cold conditions compared with last recent study [Allam], ----- for Allam, while _____ is for the proposed study, (With soot layer) and Mach=0.02.

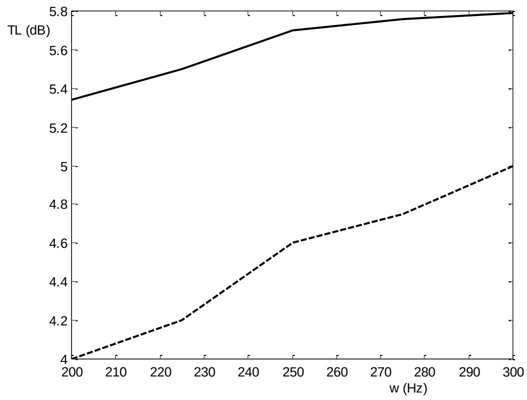

Figure 8: transmission losses vs. frequency for RC:200/12 DPF unit type in the case of cold conditions compared with last recent study [Allam], --- for Allam, while ___ is for the proposed study. (With no soot layer). Mach=0.02.

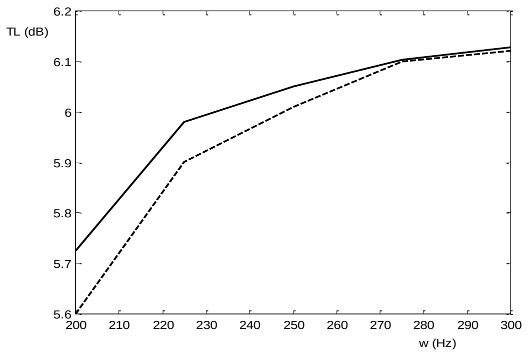

Figure 9: transmission losses vs. frequency for RC:200/20 DPF unit type in the case of cold conditions compared with last recent study [Allam], --- for Allam, while ____ is for the proposed study. (With no soot layer). Mach=0.02.

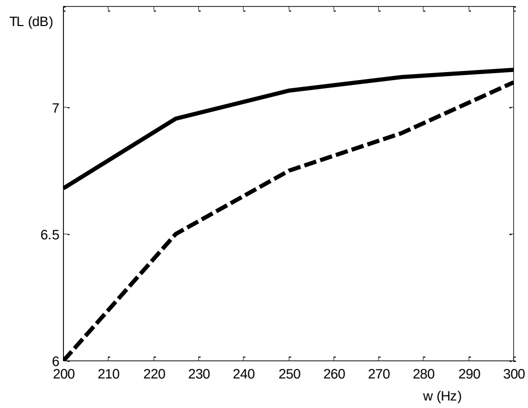

Figure 10: transmission losses vs. frequency for EX 80:200/14 DPF unit type in the case of cold conditions compared with last recent study [Allam], --- for Allam, while ____ for the proposed study. (With no soot layer). Mach=0.02.

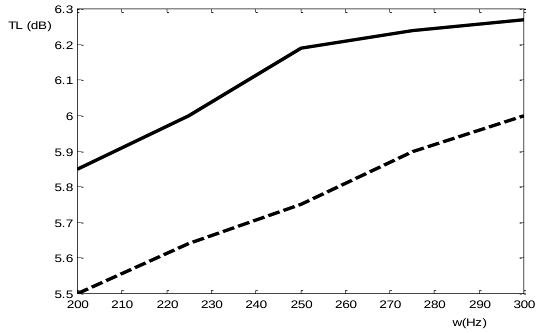

Figure 11: transmission losses vs. frequency for EX 80:100/17 DPF unit type in the case of cold conditions compared with last recent study [Allam], --- for Allam ____ is for the proposed study. (With no soot layer). Mach=0.02.

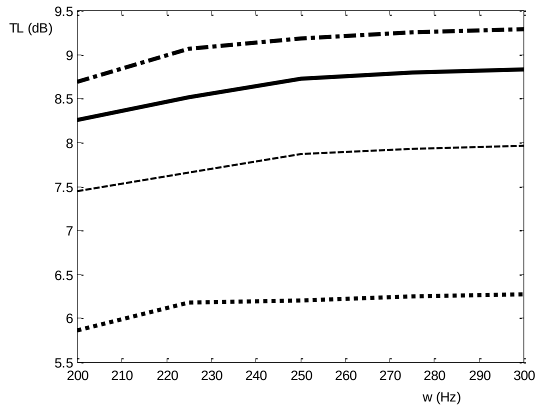

Figure 12: transmission losses vs. frequency, ___ for RC:200/12, -.-.-.for EX80:200/14, ……..for EX80:100/17, and----- for RC:200/20 DPF unit type in the case of cold conditions, (With soot layer). Mach=0.02.

 © 2011 Jordan Journal of Mechanical and Industrial Engineering. All rights reserved - Volume 5, Number 6 (ISSN 1995-6665)

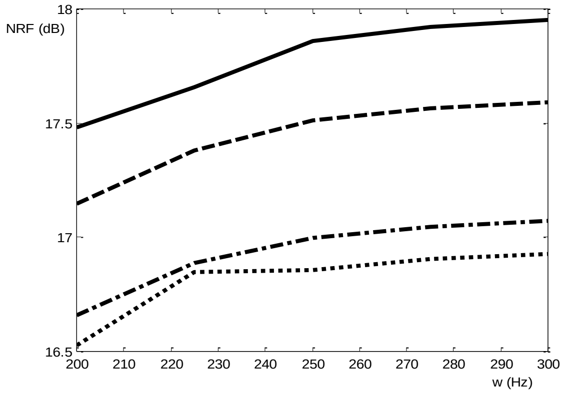

Figure 13: NRF vs. frequency, ------for RC: 200/12, ____ for EX80:200/14, -.-.-.-. for EX80:100/17, and……..for RC: 200/20 DPF unit type in the case of cold conditions, (With no soot layer). Mach=0.02.

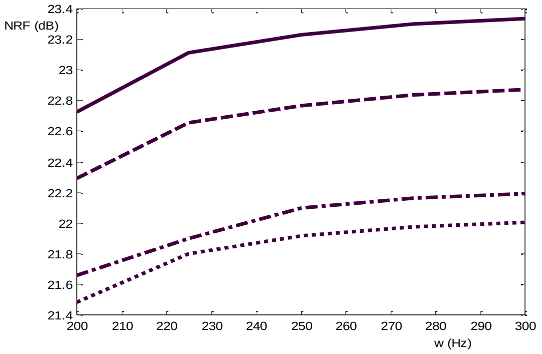

Figure 14: NRF vs. frequency, ------for RC: 200/12, ___ for EX80:200/14, -.-.-.-. for EX80:100/17, and……..for RC: 200/20 DPF unit type in the case of cold conditions, (With soot layer). Mach=0.02, cold conditions.

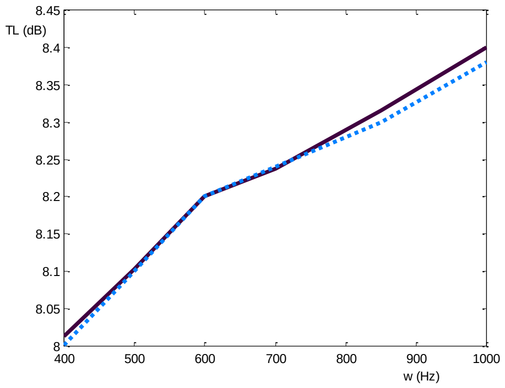

Figure 15: transmission losses vs. frequency in the case of hot conditions compared with last recent study [Allam], ----- for Allam, while ____ for the proposed study, (With no soot layer) and Mach=0.02.

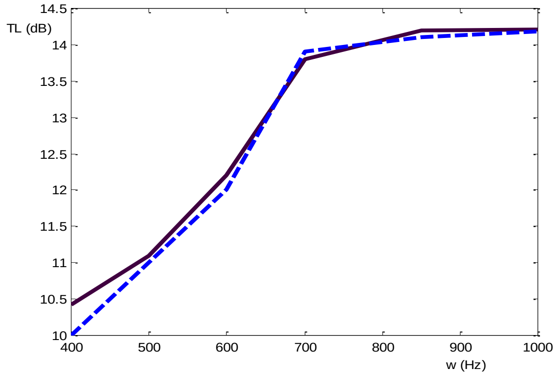

Figure 16: transmission losses vs. frequency in the case of hot conditions compared with last recent study [Allam], ----- for Allam, while ____ for the proposed study, (With soot layer) and Mach=0.02.

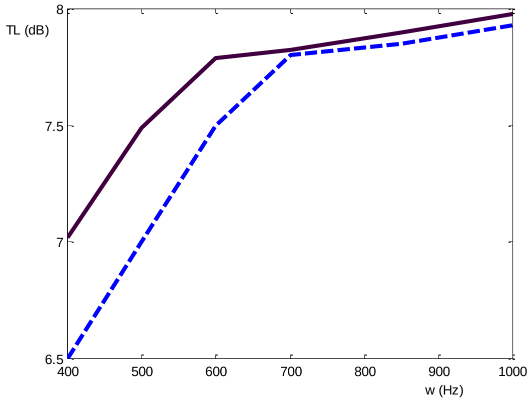

Figure 17: transmission losses vs. frequency for RC:200/12 DPF unit type in the case of hot conditions compared with last recent study [Allam], --- for Allam, while ____ is for the proposed study. (With no soot layer). Mach=0.02.

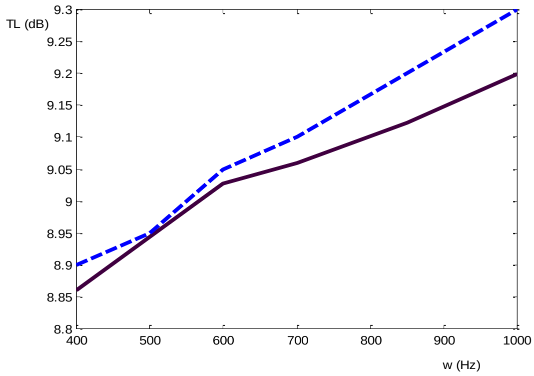

Figure 18: transmission losses vs. frequency for RC:200/20 DPF unit type in the case of hot conditions compared with last recent study [Allam], --- for Allam, while ___ is for the proposed study. (With no soot layer). Mach=0.02.

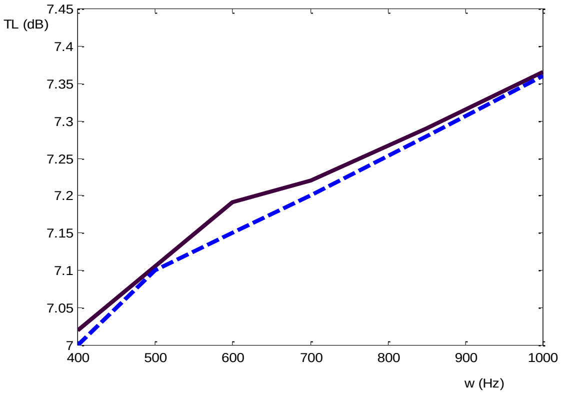

Figure 19: transmission losses vs. frequency for EX80:100/17 DPF unit type in the case of hot conditions compared with last recent study [Allam], ---for Allam ____ for the proposed study. (With no soot layer). Mach=0.02.

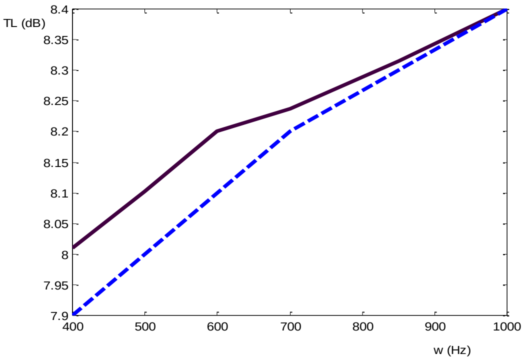

Figure 20: transmission losses vs. frequency for EX80:200/14 DPF unit type in the case of hot conditions compared with last recent study [Allam], ----for Allam, ____ is for the proposed study. (With no soot layer). Mach=0.02.

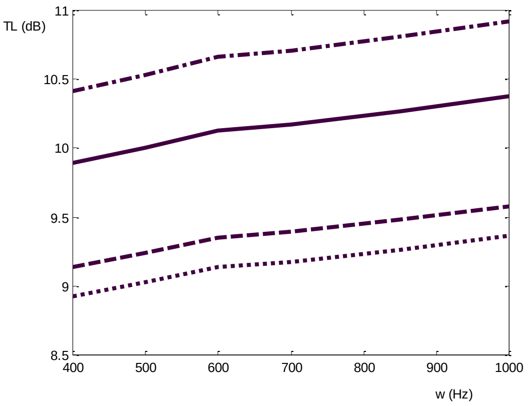

Figure 21: transmission losses vs. frequency, ___ for RC:200/12, -.-.-.for EX80:200/14, -----for EX80:100/17, and…..for RC:200/20 DPF unit type in the case of hot conditions, (With soot layer). Mach=0.02.

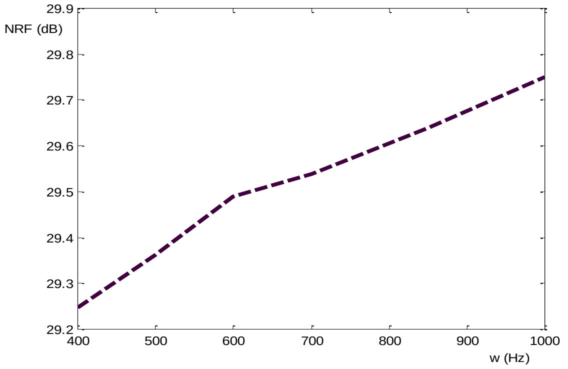

Figure 22: NRF vs. frequency for typical DPF in the case of hot conditions, (With soot layer). Mach=0.02.

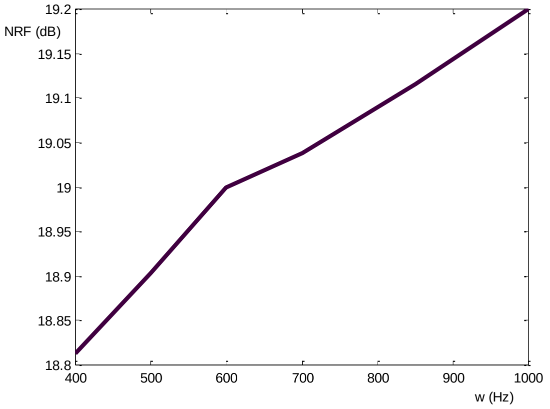

Figure 23: NRF vs. frequency for typical DPF in the case of hot conditions, (With no soot layer). Mach=0.02.

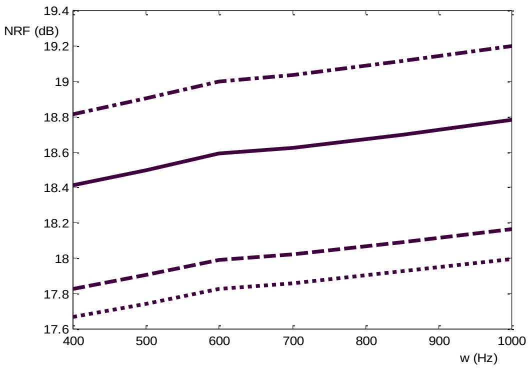

Figure 24: NRF vs. frequency, ___ for RC: 200/12, -.-.-. for EX80:200/14, -------for EX80:100/17, and……..for RC: 200/20 DPF unit type in the case of cold conditions, (With no soot layer). Mach=0.02.

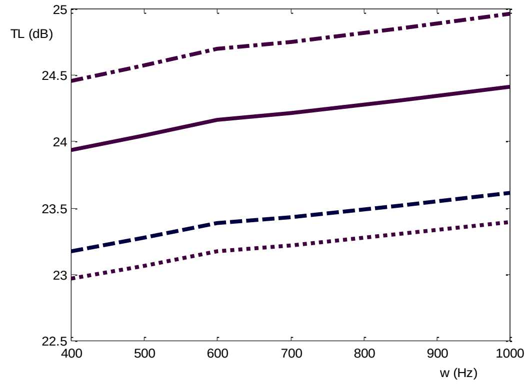

Figure 25: NRF vs. frequency, ____ for RC: 200/12, -.-.-. for EX80:200/14, -------for EX80:100/17, and……..for RC: 200/20 DPF unit type in the case of cold conditions, (With soot layer). Mach=0.02.

3.2. Discussion:

The propagation constants for a typical the diesel particulate filter (with specifications shown in table (1)), are shown in figures (2) to (5) for both cold and hot conditions for time harmonic variation. These roots can be divided into two parts: real and imaginary parts. The real parts , shown in figures (2), (4), represent the attenuation and correspond to uncoupled waves. While the imaginary parts of these roots represent the phase shift, figure (3), and (5). These parts correspond to coupled waves that are significantly more damped than the uncoupled waves. To investigate the predictions resulting from the proposed models and comparing them with the previous 1-D model by Allam [1] a typical DPF unit is analyzed. The results are plotted in two cases time harmonics variation (cold and hot). Figure (6) describes the transmission losses (TL) against the frequency in the case of time harmonic variation for the typical filter with no soot layer and for cold conditions. It can be noticed from figure (6) that the transmission losses are increased with frequency, by comparing TL of the proposed study with that of Allam [1] it can be noticed that there is an improvement in the proposed study, the more TL the more noise reduction. The reason that TL values for the proposed study are higher than that given by Allam [1] is that the proposed study deals with the flow of gases emission as a 2-D flow and so the flow in y-direction is not negligible as in last studies, hence TL can be of a noticeable value in y-direction. At w=300 Hz it can be noticed that there is a good agreement between two studies. Figure (7) describes TL for the typical filter with soot layer compared with Allam [1] at Mach =0.02. It can be noticed from the figure that there is a good agreement in the behavior but the TL for the proposed study is higher than that of Allam [1] (the dashed line), but a more agreement at higher frequency is achieved. Figures from (8) to (11) represent TL of different types of DPF unit with no soot layer, compared with results given by Allam [1], and it can be noticed from these figures that there is a good agreement in the behavior of TL against the frequency between the two studies, but there is an improvement for the proposed study. Figure (12) represents the TL of different types of DPF against frequency with soot layer, it can be noticed that EX80:200/14DPF type has the best capability of transmission losses, but EX80:100/17 DPF type has the lowest capability to do this. Figure (13) shows noise reduction factor (NRF) against frequency for different types of DPF unit, with no soot layer, it can be noticed that EX80:200/14 filter type has the best capability in noise reduction comparing with other types. In the same way figure (14) proves this but with soot layer. Figure (15) shows the TL versus frequency for the typical DPF unit in hot condition, time harmonic variation case compared with results given by Allam [10], with no soot layer, and M=0.02. From the figure a full agreement can be noticed between the proposed study and that given by Allam [1]. Also figure (16) shows TL versus frequency for the typical filter at hot conditions, time harmonic variation, M=0.02, and with soot layer. From last figure a good agreement between results given by last pervious study for Allam [1], and the proposed study. Figure (17) represents the relation between TL and frequency for RC: 200/12 DPF unit type at hot conditions, with no soot layer, M=0.02, and time harmonic variation. From last figure a good agreement between results given by last pervious study for Allam [1], and the proposed study. It can be noticed from last figure that the agreement between the proposed study and results of Allam is more at high frequencies. Figure (18) represents the relation between TL and frequency for RC: 200/20 DPF unit type at hot conditions, with no soot layer, M=0.02, and time harmonic variation. This figure shows a good agreement between results given by last pervious study for Allam [1], and the proposed study, but it can be noticed that TL values given by Allam for this type of DPF is higher than the proposed study. A full agreement between values of TL for EX80: 11/17 DPF unit type at the same previous conditions for the proposed study and values given by Allam [10] for the case of no soot layer can be seen in figure (19). Figure (20) represents the relation between TL and frequency for EX80: 200/14 DPF unit type at hot conditions, with no soot layer, M=0.02, and time harmonic variation. These figures show a good agreement between results given by Allam [1], and the present study specially at higher frequencies. Figure (21) represents transmission losses for different types of DPF unit, at hot conditions, time harmonic variation, M=0.02, and with soot layer. From lthe results in this figure it can be noticed that the EX80: 200/14 DPF unit type is the best one while RC: 200/20 DPF unit type is the worst. The variation of NRF with frequency for a typical filter at the same conditions is represented in figure (22) with soot layer and in figure (23) for no soot layer. The results in these two figures indicate that NRF with the existence of soot layer is more than that with no soot layer. An explanation for this behavior is that the soot layer forms a new absorber for noise but this is bad for gas emission reduction because the channels of the DPF unit becomes dirty and has less capability to make a reduction for gases emission. Figure (24) and figure (25) represent the relation between NRF and frequency (w), with no soot layer and with soot layer, respectively. From these two figures it can be noticed that EX80: 200/14 DPF unit type is the best type in noise reduction, while RC: 200/20 DPF unit type is the less efficient type in noise reduction operations.

3.3. Conclusion:

The main conclusions drawn from the results of this investigation can be summarized as follows:

- Wave propagation through the DPF unit leads to both attenuation and phase shift, and both attenuation and phase shift are damped as shear wave number increase.
- Both transmission loses and noise reduction factor for the typical filter and other types of DPFs tend to increase as frequency increases.
- Transmission losses for the case of existing soot layer are higher than those with no soot layer.
- EX80:200/14 DPF type has the best capability of transmission losses, but EX80:100/17 DPF type has the lowest capability to do this, and this appears in all cases and conditions.
- Transmission losses and NRF have a positive relationship with frequency.

Table 1: Filter Specifications.

1- Typical filter.

Diameter/length mm	channels/m² $n \times 10^{-5}$	channels width mm $d_h \times 10^3$m	wall thickness mm $ht \times 10^4$m	wall permeability $\sigma_w \times 10^{13}$ m²
150/250	3.10	1.44	3.55	2.5

2- Different types of filters.

Filter name	channels/m² $n \times 10^{-5}$	channels width $d_h \times 10^3$m	wall thickness $ht \times 10^4$m	wall permeability $\sigma_w \times 10^{13}$ m²	R1	R2
RC: 200/12	3.87	1.5	3.04	25	87.1	29.2
RC: 200/20	2.48	1.3	5.04	25	233.3	41.56
EX80: 100/17	1.55	2.11	4.3	2.5	199.8	30.92
EX80: 200/14	3.10	1.44	3.55	2.5	184.1	39.2

References

[1] S. Allam, S. M. Abom, “Sound propagation in an array of narrow porous channels with application to diesel particulate filters”. Journal of Sound and Vibration, Vol. 291, 882-901, 2006.

[2] G. Greevesm, I. M. Khan, C. H. T. Wang, I. Fenne, “Origins of hydrocarbon emission from diesel engines”. Society of Automotive Engineering, SAE Paper No. 770259, 1977, 02-01.

[3] R. Yu, Yu, S. M. Shahed, “Effects of injection timing and exhaust gas recirculation on emissions from a DI diesel engine”. Society of Automotive Engineering, SAE Paper No. 811234, 1981.

[4] G. Konstandopoulos, J. H. Johnson, “Wall-flow diesel particulate filters - their pressure drop and collection efficiency”, Society of Automotive Engineering, SAE Paper No. 890405, 1989.

[5] K. S. Peat, “A first approximation to the effects of mean flow on sound propagation in capillary tubes”, Journal of Sound and Vibration Vol. 175, 1994, 475–489.

[6] R. J. Astley, A. Cummings, A., “Wave propagation in catalytic converter formulation of the problem and finite element scheme”. Journal of Sound and vibration, Vol.188 , No. 5, 1995, 635–657.

[7] E. Dokumaci, “Sound transmission in narrow pipes with superimposed uniform mean flow and acoustic modeling of automobile catalytic converters”, Journal of Sound and Vibration, Vol. 182 , 799–808, 1995.

[8] J.-G Ih, C. M. Park, H-J. Kim , ” A model for sound propagation in capillary ducts with mean flow”. Journal of Sound and Vibration Vol. 190, No.2, 163–175, 1996.

[9] K.-W. Joeng, J.-G. Ih, (1996). “A numerical study on the propagation of sound through capillary tubes with mean flow”, Journal of Sound and Vibration, Vol. 198, No. 1, 67–79, 1996.

[10] E. Dokumaci, “On transmission of sound in circular and rectangular narrow pipes with superimposed mean flow”. Journal of sound and vibration, Vol. 210, No. 3, 1998, 375–389,1998.

[11] E. Dokumaci, “An approximate dispersion equation for sound waves in a narrow pipe with ambient gradients”. Journal of Sound and Vibration, Vol. 240, No. 4, 2001, 637–646.

[12] S. Allam, S. M. Abom, “Acoustic modeling and testing of diesel particulate filters .”Journal of Sound and Vibration, Vol. 288 (1/2) , 255–273, 2005.

[13] S. Fayyad, “Sound propagation in porous media with application to diesel” particulate filters.” PhD Thesis, University of Jordan, 2006.

JJMIE

Volume 5, Number 6, Dec. 2011
ISSN 1995-6665
Pages 509 - 519

Jordan Journal of Mechanical and Industrial Engineering

Analysis of Face Milling Operation Using Acousto Optic Emission and 3D Surface Topography of Machined Surfaces for In-Process Tool Condition Monitoring

B. Srinivasa Prasad*,[a], M.M. Sarcar[a]

Department of Mechanical Engineering, Gitam University, Visakhapatnam-530045,India

Abstract

In machining as a result of the cutting motion, the surface of workpiece will be influenced by cutting parameters, cutting force and vibrations etc. But the effects of vibrations have been paid less attention. Thus, by monitoring the machined surface topography of the workpiece and extracting the relevant information the cutting process and tool wear state should be able to be monitored and quantified. In a automated manufacturing systems, an accurate detection of the tool conditions under given cutting conditions so that worn tools can be identified and replaced in time. This work is aimed at to predict the effects of displacements due to vibration during face milling and to examine the surface topography of different workpiece materials so as to develop a base for on-line tool condition monitoring system. First part consists of a data acquisition and signal processing using acousto optic emission sensor (i.e., laser doppler vibrometer) for on line tool condition monitoring and the second part of the work presents the vision based surface topography analysis of machined surfaces during the progression of the tool wear. The encouraging results of the work paves the way for the development of a real-time, low-cost, and reliable tool-condition-monitoring system.

Keywords: Tool condition monitoring, acousto optic emission, surface textural analysis, laser doppler vibrometer and CCD camera.

1. Introduction

In manufacturing environments, it is often a challenge to find an effective means of reducing costs and improving product quality. The continuous demand for higher productivity and product quality asks for better understanding and control of the machining process. A better understanding can be achieved through experimental measurement and theoretical simulations and modeling of the process and its resulting product. On line tool wear identification is finding an important role in modern engineering. Many approaches have been proposed to accomplish tool condition monitoring, and some have been successfully employed in industry. Several conventional tool condition monitoring methods are compared on the basis of their strengths and weaknesses for on line monitoring. Most methods essentially involve processing information such as acoustic emission (AE), tool tip temperature, vibration signatures (acceleration signals), cutting force, etc. However acousto optic emission methods have recently introduced as a reliable way detect the vibration amplitudes with non contact mode to identify the corresponding tool wear. When employed efficiently, tool condition monitoring aids in attaining the above objectives in machining applications.

The wear and breakage of cutting tools will affect the accuracy of dimension and the surface quality of machined workpieces, even breakdown the machine. Tool wear dramatically affects the texture of the machined surface. Analyzing the texture of machined surfaces has been shown to be promising for tool wear monitoring [1]. Tool wear monitoring is a critical operation in automatic manufacturing. The recent development of highly automated machine tools and increase of competitiveness makes on-line tool condition monitoring (TCM) as an alternative to statistical tool life prediction more and more interesting for the reduction of manufacturing costs [2]. Although several models [3-6] have been developed to predict cutting tool life, none of these are universally successful due to the complex nature of the machining process. All these studies have pointed out the importance of sensing technology in the development of flexible manufacturing systems. Research has proved that the vibration produced by a machine tool gives useful information for the maintenance of its structural parts [7]. This is very important when the goal is to monitor the cutting process in real time and to establish automatically the end of tool life. If the vibration signal can indirectly monitor the tool wear growth, it is also able to monitor surface roughness growth and, consequently, to establish the end of tool life in this kind of operation.

One of the main difficulties of monitoring the tool life through vibration signal is to identify the frequency range

* Corresponding author.e-mail: bsp.prasad@gmail.com

that is actually influenced by the tool wear, since the machining process has a lot of factors that produces vibration, many of them not correlated with the wear and breakage processes. Frequency ranges sensitive to tool wear are discussed elaborately in and values are tabulated [8]. A.E.Diniz et al [9] have conducted experiments in an attempt to monitor the changing of workpiece surface roughness caused by the increase of tool wear, through the variation of acoustic emission in finish turning. G.H.Lim [10] performed vibration signature analysis during in-process turning. This work affirms that vibration acceleration feed direction consistently produces two peak amplitudes just prior to rapid tool degradation. This information can be can be used to assess the tool wear state. Martin et al. [11], after choosing the frequency range sensitive to tool wear, concluded that, when the ratio between the vibration signal generated by the worn tool and the signal generated by the fresh tool exceeded 10, it is time to change the tool. Measurement of vibration is a vital factor that limits the precision and accuracy of machining.

B.K.A.Ngoi et al [12]., proposed a novel method for measurement of vibration using an acousto-optic modulator which highlights an improved approach in measuring vibration. One of the main difficulties in on line monitoring the tool life through vibration signal is to identify the frequency range that is actually influenced by the tool wear being non - contact, to solve the problem S.J.Rothenberg et al [13] gave a comprehensive theory and practical application for rotational vibration measurement using laser Doppler Vibrometry. Peter Norman et al[14] demonstrated the use of non – contact Laser Doppler Vibrometer in the investigation for the behaviour of a high-speed rotating system, such as a machine tool spindle. Yuji Sugiyama et al [15] developed a method for on-line monitoring of chatter vibration in end milling process using laser Doppler Vibrometer. There are numerous machining factors that affect surface quality in machining using cutting tools, but those effects have not been adequately quantified. Feng and Wang [16]., demonstrated the procedure for calculating the experimental exponents for the regression models for surface roughness and flank wear by applying a logarithmic transformation. W. H. Cubberly et al [17],. developed a rough general rule, forces and power consumption increase with increasing workpiece hardness. As a result of the cutting motion, the surface of workpiece will be influenced by cutting conditions (cutting parameters, cutting force, and cutting tool state), and the surface topography of the workpiece will include much information pertaining to the cutting process [19] . Thus, by monitoring the machined surface topography of the workpiece and extracting the relevant information the cutting process and tool wear state should be able to be monitored and quantified.

L.Blunt et al [20], outlined the procedure based on surface texture parameters to characterise the machined surfaces of workpieces in order to evaluate the tool wear is outlined. A set of areal surface roughness parameters have been listed in [21] are used to differentiate anisotropic and isotropic machined surface textures. Evaluation of the surface topography on component functionality, a set of 3D surface parameters have studied and developed relation with functional aspects in J. Kundrak et al [22,23]. Roughness of the hard turned surfaces are analysed with and are the amplitude parameters of the so-called "Birmingham 14" parameters. A comprehensive characterization of 3D surface topography for isotropic and anisotropic surfaces is outlined in [24].

The present paper presents the application of acousto optic emission (AOE) techniques for tool condition monitoring (TCM) in face turning operation. An optic signal from laser doppler vibrometer (LDV) is focused on rotating workpiece and the way of mode conversion and reflection from the surfaces workpiece can lead to interference pattern during the machining. In the analysis of acousto optic signature in experimental data, a time domain is converted into frequency domain to obtain output in the specified range of frequency. In the present work the problem of overlapping of the modes is made for force calculation there by determination surface roughness (Ra) and flank wear(VB). An experimental setup is developed for acousto optic pulse generation and different cutting tool materials with different conditions (sharp, semi sharp & dull) of tool state introduced are tested in their stable, chatter and severe chatter vibratory conditions on the test setup.

In the present study multi point cutting operation face milling is identified to examine the effectiveness of proposed methodology for TCM. Forces and vibration are always a matter of concern in metal cutting. Forces relevant to size control and power requirements. Vibrations can be beneficial if they lead to lower friction and forces. On the other hand they can aggravate the problems associated with surface finish, tool life, energy requirements and temperature. Therefore a series of studies devoted to these problems. Vibration monitoring studies are made with workpiece stationary in the present case of face milling. Establishment of correlation between vibration analysis and workpiece surfaces texture is made with experimental data.

2. Mechanism in face milling

A milling operation is an 'intermittent cutting action' , where each individual cutting insert continuously enters and exit's the cut, unlike turning, which is basically a continuous machining operation, once the cut has been engaged. It follows that with each cutting tooth impacting onto the work's surface ('intermittent cutting'), its operation will be affected by: the cutter's inherent robustness, the machine tool's condition and the spindle power availability. These factors will have a great influence on the cutter's ability to efficiently machine the desired component features. The cutting operation is done by a rotating tool that moves along various axes while the workpiece is fixed. More complex parts can be produced by milling operation. Figure.1 presents the cutter path and this is the trajectory followed by the centre of the cutter. The cutting speed is the rate at which the cutter edge moves relative to part surface. The feed rate is the rate at which the uncut part moves towards the cutter. Schematic diagram for face milling operation shown in figure 2 is selected for experimental investigation where D is the diameter of the face mill, V is the cutting speed, fz is the feed per tooth, aa is the axial depth of cut, ar is the radial depth of cut and z is the number of teeth. Different kinds of damages can develop on the tool during the cutting process and some of these damages are called as tool wear. The amount of total tool wear and time horizon to reach the maximum limit of wear determine the tool life.

Milling forces can be modeled for given cutter geometry, cutting conditions, and work material. In face milling, cutter is perpendicular to the machined surface. The cutter axis is vertical. In face milling, machining is performed by teeth on both the end and periphery of the face-milling cutter. In face milling, the cutter rotates at 90° to that of the direction of radial feed against the workpiece. In conventional face milling operation the face-milling cutter machines the entire surface. The cutter diameter is greater than the workpart width.

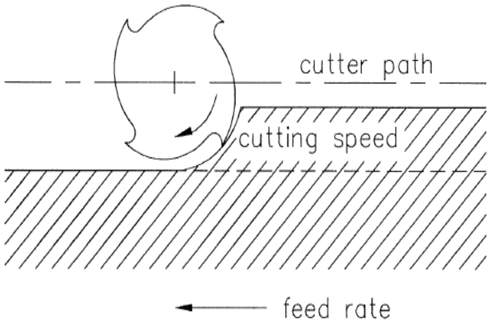

Figure 1: Cutter path motion.

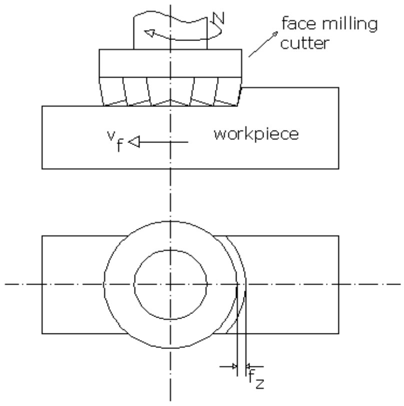

Figure 2: Schematic view of face mill.

The cutting forces exerted by the cutting tool on the work piece during a machining action to be identified in order to control the tool wear and occurrence of vibration, thus to improve tool-life. Modeling of cutting force in milling is often needed in machining automation to predict the effects of cutting parameters on the variations of cutting forces during face milling operation. Displacements in cutter due to cutting forces are measured for various feed rates using Laser Doppler Vibrometer. Free body diagram for Self excited vibration system for face milling operation is presented in figure .4 and actual machining zone is shown in figure 3.

Static deflection of workpiece in face milling may cause tolerance violation on machined parts. These deflection need to be modeled in order to check the tolerance integrity for potential compensation of the errors. Workpiece having rectangular cross-section is considered for static analysis. A cantilever beam model is used to perform the static analysis of the workpieces under load. Therefore, the primary objective of the static analysis is to determine the maximum deflection on the workpiece at the end.

The work piece deflection is important to evaluate surface error. In order to perform static analysis, a model of the workpiece is needed to determine the necessary geometric and loading parameters, moment of inertia and bending moments. A model has been developed to determine the maximum deflection using cantilever method. The cutting force is represented by a point force, which is an approximation. However, it should be noted that this model is used for both stiffness calculation and for final tool deflection also. Accurate surface generation models can be used for form errors, once the stiffness is determined. The cutting force in the feed direction is determined using the feed back signal from LDV.

Modeling and FEA can be impractical and time consuming for each tool configuration in a virtual machining environment. Therefore, simplified equations are created to predict deflections of workpiece for given geometric parameters and material properties (elastic modulus and density). The static characteristics of cutting workpiece can be easily determined by analytical expressions. Analytical model for workpiece deflection is developed and later compared with experimental results. In the analytical deformation equations, the evaluation of the integral formulas is very complex. In an attempt to further simplify the deflection calculation, the following analysis is performed. The maximum deflection could be determined using laser Doppler Vibrometer (LDV).

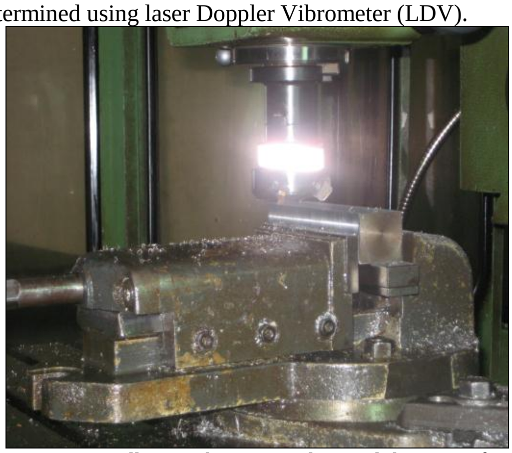

Figure 3: Face milling teeth are spaced around the circumference of the cutter body.

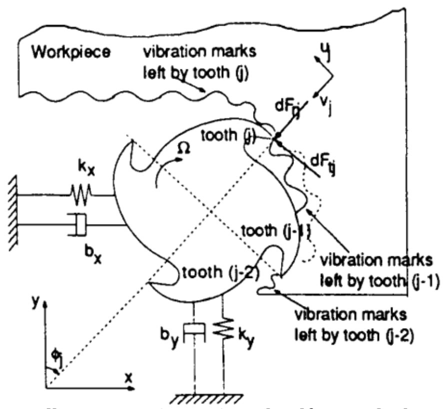

Figure 4: Milling system (2 DOF), with self-excited vibrations.

The boundary and loading condition shown in figure .5 in which the applied force (F) can be calculated by using the following equation:

$$F = k.q \tag{1}$$

where k- is the stiffness(N/mm) and q- is displacement (mm).

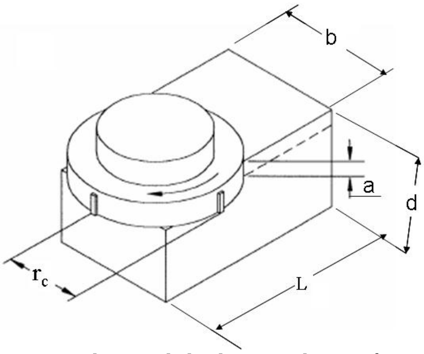

Figure 5: Boundary and loading conditions for rectangular specimen.

If the shape of the workpiece is assumed to be a rectangular the stiffness can be obtained from simplified equation.

$$k = \frac{3EI}{L^3} \tag{2}$$

$$I = \frac{b.d^3}{12} \tag{3}$$

where I-moment of inertia , diameter (D) and length (L) of the rectangle, width (b) and thickness(d) are in mm. E is elastic modulus in Gpa and q is the displacement (mm) measured with LDV.

2.1. Modeling of surface roughness and tool wear:

The mathematical model adopted for estimating the surface roughness and tool wear in this is similar to previous case except the change in values of stiffness of the workpiece after every pass of the cut. This change is due to cross section of the specimen used in the experimental investigation. In the case of steel, empirical relationships between hardness and specific power consumption (E_{sp}) or cutting force can be stated in terms of the E_{sp} value. Kronenberg has found the following approximate relationships:

For steel:

$$H = \frac{F^2}{A^2.(4.26)^2(85-\gamma_n)} \tag{4}$$

where cutting force (F), metal removal factor K_n (or specific power consumption, E_{sp}), depth of cut (d) , feed per revolution (f), A= (depth of cut).(feed per revolution) = $d.f$, γ_n – rake angle, and C_F is a constant whose value depends on the material being cut and the true rake angle of the tool, x and y are exponents. In machining of parts, surface quality is one of the most specified customer requirements. Major indication of surface quality on machined parts is surface roughness. Because of the elevated temperature in the cutting zone, the tool tip temperature increases, this softens the tool material and which in turn causes increased tool wear (VB). In addition, surface roughness also increases. The variation in the hardness of material and case depth are the other parameters affecting surface finish and tool wear. Machined surfaces with surface roughness(R_a) values above 6.3 μm are treated as highly rough surfaces and the surface roughness parameters (Ra) and corresponding flank wear(VB) can be derived from experimental data by using the following relations.

$$Ra = C_{Ra}.H^a.f^y.\gamma_n{}^n.d^p.v^x.t^z \ \mu m \tag{5}$$

$$R_q = (1.25)R_a \ \ \mu m \tag{6}$$

$$VB = C.H^a.\gamma_n{}^n.v^x.f^y.L^b \text{ in mm} \tag{7}$$

The face milling tests are continued till tool wear reaches the limiting criterion of flank wear of 0.3mm. where v is cutting speed (m/min), t machining time (min), L is the length of the cut (mm) and n, x, y, a, b, p, z are exponents.

3. Experimental Design and Methodology

The present work is planned to develop a base for on-line tool condition monitoring strategies and experimental plan is presented in figure 6. The block diagram for vision and acousto optic based tool condition monitoring in the present work is shown in figure 6. The objective of the present work is also to analyse the proposed methodology in face milling for tool condition monitoring. In the present work, data acquisition has been done in two ways, one of them is on-line continues data in the form of acousto optic emission signal and the other one is off line discrete mode of data acquisition through measurements and capturing of surface textures using machine vision systems. To achieve the objectives of the present work, a methodology has been developed and it is presented in the figure 7. An experimental setup is designed for face milling to validate this methodology.

Table .1 gives the various machining combinations and test conditions used in the work. The cutting parameters are selected according to the tool supplier's recommendation for tool and work piece combinations. Cutting tests are conducted at dry machining conditions. This condition decreases tool life and also experimental time. Cutting velocity and feed rates are selected based on the tool manufacturer's (Sandvik) recommendations for work-piece material and tool combination. During experimentation for every test condition cutting speed (V) and feed rate (h) are kept constant. The depth of cut value (b) varies in every chatter condition the same logic is applied in the face milling for validation of results. For evaluating the experimental results, AISI 1040 and AISI 4140 steels are used as workpiece materials. The vibration measuring equipment shown in figure .8 is kept at two meters away from the machine and an optic signal from laser doppler vibrometer is focused on to a rotating object (rotating milling cutter) and the way of mode conversion and reflection from the surfaces workpiece can lead to interference pattern during the machining. In case of face milling this is generally cutting direction and regarded as the direction in which most significant increase in vibration amplitude is observed. This signal is amplified and fed to the FFT analyser which is connected to computer for analysis.

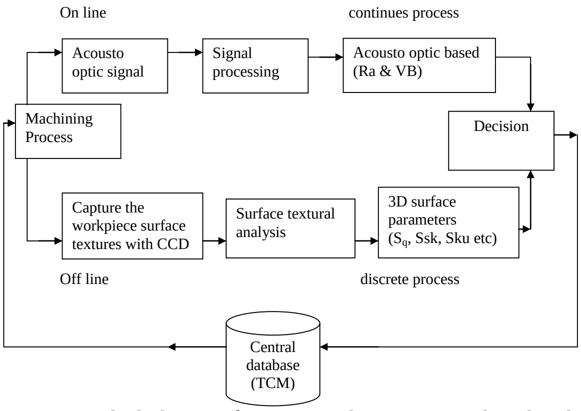

Figure 6: Block diagram for vision and acousto optic based tool condition monitoring.

When all instruments are ready, a CNC program is executed to perform face milling operation. With this designed experimental setup the following procedural steps have been implemented to carry out experimental investigation in face milling. In the analysis of acousto optic signature in experimental data, a time domain is converted into frequency domain to obtain output in the specified range of frequency. In the present work the problem of overlapping of the modes is made for force calculation there by determination surface roughness (R_a) and flank wear (VB). Experimental setup developed in the work is used for acousto optic pulse generation with different workpiece materials at different conditions (sharp, semi sharp & dull) of tool state are tested in their stable, chatter and severe chatter vibratory conditions on the test setup. When all instruments are ready, a CNC program is executed to perform facing operation, with this designed experimental setup the following procedural steps have been implemented to carry out experimental investigation.

Step 1. Each test started with a fresh insert tip , experiment has been started with test conditions 1 and machining is stopped at the end of every 4^{th} pass of cut. The workpiece has been machined four times (with depth of cut) and this process continued up to 40 passes of cut.

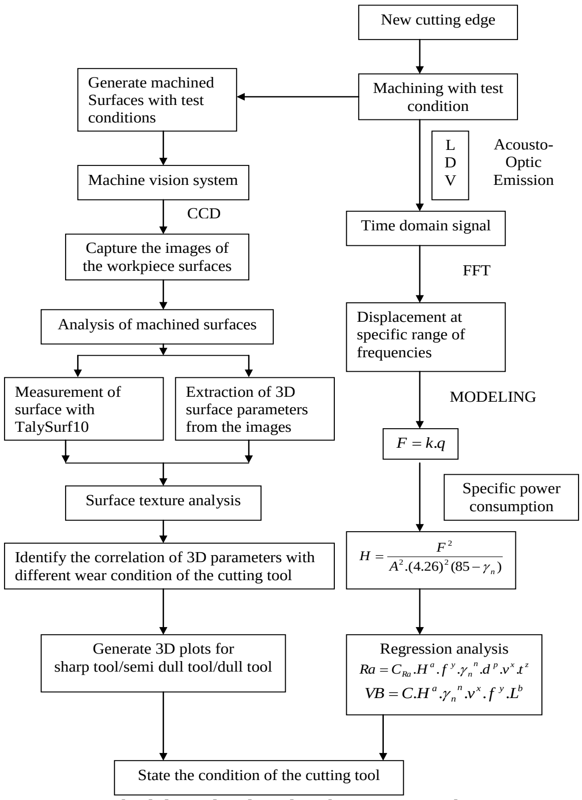

Figure 7: Methodology developed in the present work.

Step 2. Vibration signals are measured just before the machining is stopped.

Step 3. Surface textures are captured under CCD using rapid vision inspection system.

Step 4. A new workpiece is loaded on to the machine and machining is initiated with next test condition and step 3 and step 4 are repeated for this test condition.

Step 5. For remaining test condition also the same procedure has been implemented.

Step 6. In the experiment, besides measuring the surface roughness and vibration, the tool was removed from the machine after a given cutting time to have its flank wear measured and to be photographed under rapid vision inspection system.

4. Experimental setup and procedure for face milling

Schematic diagram for face milling is shown in figure .9. In a milling process, the cutting parameters are the cutting speed, feed rate, axial and radial depth of cut. Table .1 gives the details of test conditions. The axial depth of cut depends on the vibration displacement.


(a) Laser doppler vibrometer


(b) Workpieces used in experiment

(c) Tool maker's microscope for flank wear.

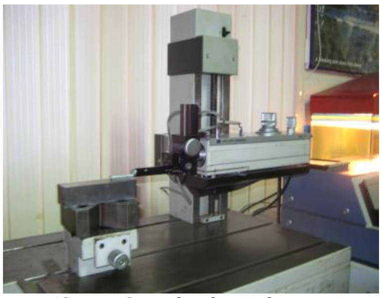
(d) TalySurf10 for surface roughness.

Figure 8: Data acquisition systems used in the experiment.

Tables 1: Test conditions selected for face milling.

Face milling	Carbide insert tip
Cutting speed(m/min)	92,115, 138
Feed rate(mm/tooth)	0.254, 0.381, 0.508
Depth of cut(mm)	0.5, 0.8,1.5

The cutting is a dry cutting process with no coolant. This condition decreases tool life and also experimental time. The metallurgical properties and cutting parameters of AISI 1040 and AISI 4140 presented in table 1. The workpieces used in the experiment are shown in figure 8(b). The feed rate was kept constant during machining and depth of cut values 0.5, 0.8 and 1.2 mm are varied for stable to severe vibratory conditions respectively. The cutting tool has four teeth in order to distribute the wear among four different teeth.

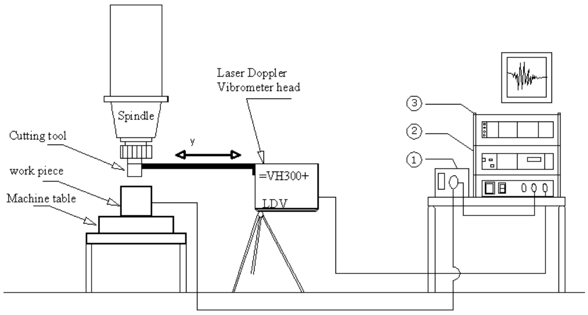

1. Piezoelectric accelelrometer (Bruel & Kjaer)
2. Pre-amplifier (Bruel & Kjaer)
3. FFT analyser (Bruel & Kjaer)

Figure 9: Schematic diagram for experimental setup in face milling.

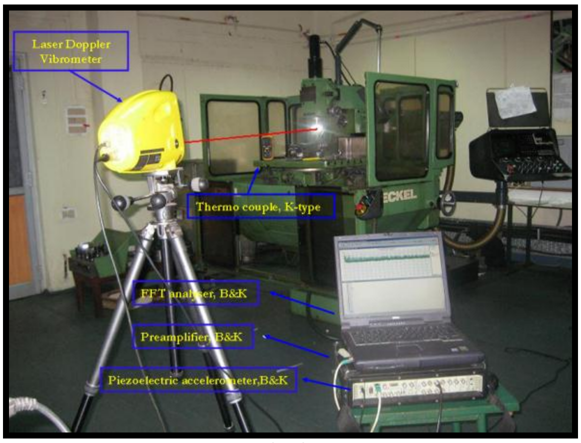

Figure 10: Experimental setup for face milling.

The cutting tool is clamped to the holder with a torque about 35 Nm for both tool lengths. With this designed setup, ISO recommended machining conditions are tested on AISI 1040 and AISI 4140 steels with common face milling cutter with four carbide tip flutes has been used. Based on the ISO standards, three conditions of the tool are considered; sharp tool (0 m of the flank wear), semi dull tool (0.3mm of tool flank wear), dull tool (0.6mm of tool flank wear) in face milling. Tool maker's microscope is used for flank wear is measurement and it is shown in figure 8(c).

5. Surface textural analysis for tool condition monitoring using machine vision system

In recent years surface texture has been recognized as being significant in many fields. In particular the surface roughness is an important factor in determining the satisfactory performance of the workpiece and cutting tool combination. Second part of the proposed methodology is that analyzes images of workpiece surfaces that have been subjected to machining operations and investigates the correlation between tool wear and quantities characterizing machined surfaces.

The machine vision system consists of CCD camera and frame grabber it is shown in figure.11 is used to process the image data. The CCD camera operates at 768 x 574 pixels. The images were analysed in the surface metrology software TRUEMAP and the values of different surface amplitude parameters were obtained. A sub image of the original image, of size 100 × 100, used for further processing with image metrology software. Then the comparison is made between Ra and 3D parameter values extracted from images of the machined surfaces. This system provides sufficient information about a machined surface and is much faster than a stylus based system. The following 3D parameters used in the analysis. Figure 8(d) shows the conventional measurement of surface roughness with TalySurf10.

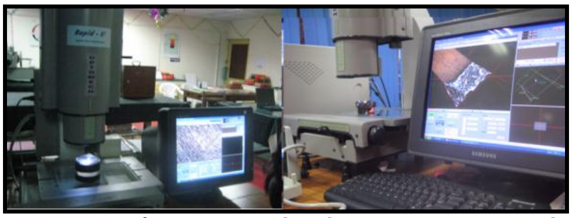

Figure 11: Surface texture and tool wear measurement under machine vision system.

5.1. Surface texture parameters used for cutting tool condition monitoring:

The following 3D parameters are used for surface textural analysis of workpiece surface. Root mean square roughness (S_q) parameter is assumed to provide an estimate of the average asperity height measured from datum, Skewness of surface height distribution(S_{sk}) to measure the asymmetry of surface deviations about the mean plane, Kurtosis of surface height distribution, (S_{ku}) to measure peakedness or sharpness of the surface height distribution, Texture aspect ratio (S_{tr}) is used to identify texture pattern, i.e., isotropy or anisotropy.

6. Results and Discussion

In the present work, identification of changes in displacement characteristics due to tool wear condition for worn tool with respect to its fresh tool state is used for on line tool condition monitoring. All the time domain signals in these experiments were filtered using a 100-1000 kHz band-pass filter. The sampling frequency was 4MHz and signal processing using blocks of 8000 data points collected over a period of sampling interval 1ms. Time and frequency domain spectrographs for face tuning and face milling are presented in figure 7. Flank wear value of 0.3mm is considered as tool life rejection criterion as per ISO 3685 throughout the present study.

6.1. Correlation between tool wear and displacement:

When a tool is new there is relatively little friction between the tool and the workpiece, therefore the amplitude of vibration will naturally be lower.

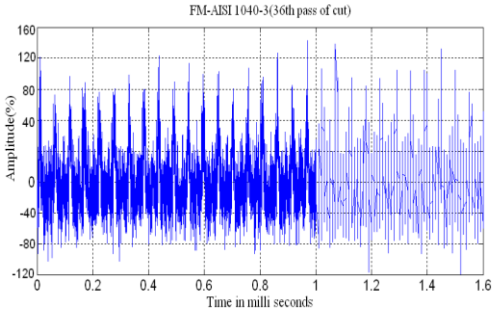

(a) FM-AISI 1040-3-Time.

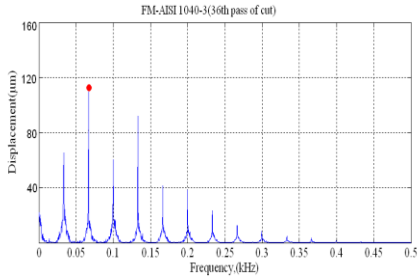

(b) FM-AISI 1040-3-FFT.

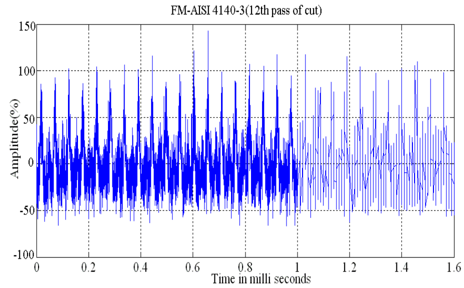

(c) FM-AISI 4140-3-Time.

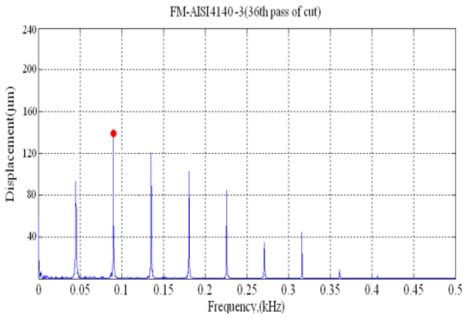

(d) FM-AISI 4140-3-FFT.

Figure 12: Time and frequency domain spectrograph in face milling.

Further, as the workpiece has a heavier mass during the early cutting stage, there will be an increase in vibration spectra can be considered to represent the system characteristics. As the increase in stiffness of the workpiece increases, a corresponding increase in vibration amplitude is recorded. Further increase in vibration spectra is due to the increasing friction between the workpiece and cutting tool as the tool wear increases. Therefore, second peak is taken as the indicator for tool state and its wear limits.

The vibration is measured in the feed direction since this direction has more dominant signals than other two directions. In this work, vibration parameter considered for the experimental analysis is displacement. The peak amplitude varies from $5\mu m$ to 150 μm depending on the severity of the chatter and cutting speed as shown in figure 12. As per ISO 2372(10816) for vibration severity standards, displacements in rotating cutter up to 20 μm do not have any effect on tool flank wear. Tool flank wear is found to be effected by the measured displacements in the range between 20 μm to 60 μm. A displacement value beyond 60 μm is not a acceptable as per ISO 10816. The results plotted in figure 13(a) justify this standard. All the test condition in each curve indicates the same. Any displacement beyond this value is showing excessive vibration which deteriorating the work piece surface and reducing the tool life. In figure.12 the correlation between tool wear and vibration amplitude is presented for test condition FM AISI 4140-3 and FM AISI 1040-3.

6.2. Surface roughness and tool flank wear:

The graphs in figure.13 (b) exhibits a correlation between surface roughness and flank wear in all test conditions with different workpiece materials. The rate of the tool wear increases as the number of passes increases. The effect of cutting speed on tool life is pronounced but it becomes less descent for higher speeds. Surface roughness is almost remains constant when tool is sharp irrespective of workpiece material. It can be seen that the growth in surface roughness is similar to the increase with flank wear in figure 13(b). From results table .2, it is clear that the severe chatter (dull tool) results in surface quality nearly two times worse than the stable cutting(sharp tool). Surface roughness values remained almost constant although flank wear increases with feed rate, depth of cut and cutting speed. However the magnitude of surface roughness (Ra) is higher for higher feed rates and depths o cuts.

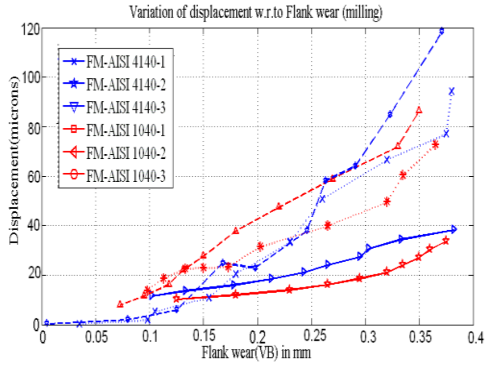

(a)

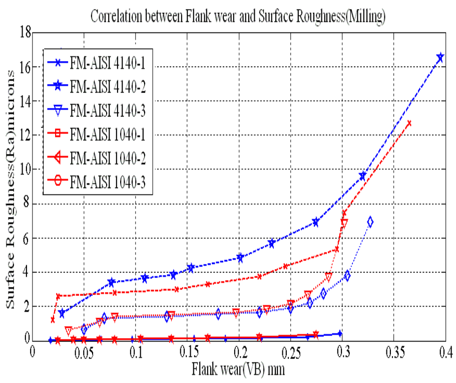

(b)

Figure 13: Variations of displacement and surface roughness with respect to wear.

The test results for face milling are summarized in table 2. If red and blue colored curves are compared, it can be seen that the variation in tool life at stable condition for two different workpiece materials is more regular and the slopes are very similar to each other. The same result is not valid for test conditions with excessive displacements due to vibration because the variation between tool life and vibratory conditions for different stiffnesses in workpiece is much higher and irregular. That difference of displacement is more obvious at higher cutting speeds.

From results tables 2 it is found that hardness of the specimen and its stiffness at different test conditions is influencing the displacement in cutter during the machining. Because of this variations tool life at vibratory conditions is much higher and irregular. The effects of displacement variation on tool life in milling are shown in figure 13(a).

Figure 14 is the carbide insert tip after 38 minutes. The flank wear under vibration is obviously greater than the results of stable cutting condition. The cutting forces in feed direction only derived from displacements measured with LDV this can be done many times throughout the total experimentation i.e,. up to 40 pass of cuts with a test condition. The time interval between two displacement measurements varies 16 sec to 19 minutes.

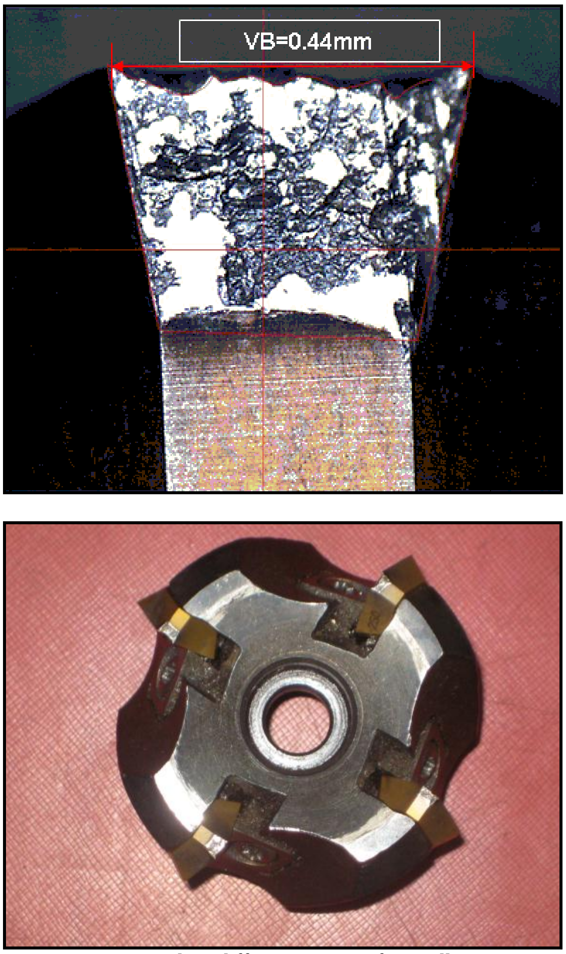

Figure 14: Worn tools at different stages in face milling.

6.3. Analysis of machined surfaces:

When the tool is worn, the texture distribution strength in feed direction is weakened. With the increasing tool wear the effect of randomly occurring deeper furrows along the feed direction on the machined surface is more apparent. This is indicated in the figures in table .3 shows the 3D plot of machined surface when tool is in semi dull condition. Table 2 also compares the traces of the work piece surfaces. It is observed that the surface topography has good texture in the feed direction, the surface is very flat, and it has low levels of waviness when tool is new; with increasing tool wear the regular texture loses “strength” with scuffs and furrows appearing, with further tool wear, the surface appears very irregular having alternate rough and smooth zones.

6.3.1. 3D RMS roughness (Sq) and flank wear:

S_q , the 3D root mean square roughness, increases with tool wear increase, with the amplitude of the roughness rising with the increasing tool wear i.e., between test condition1 and test condition 2 for two machined surfaces with two cutting tool. A good understanding is found between 3D rms roughness with flank wear in the results table 3.

Table 2: Images of the machined surfaces in face milling.

Traces of workpiece surfaces in face milling		
Sharp condition	Semi sharp condition	Dull condition
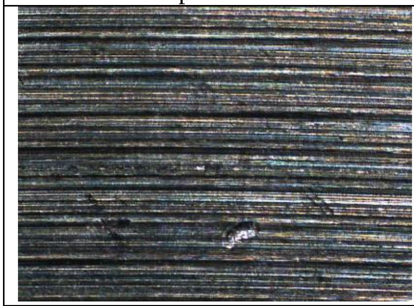	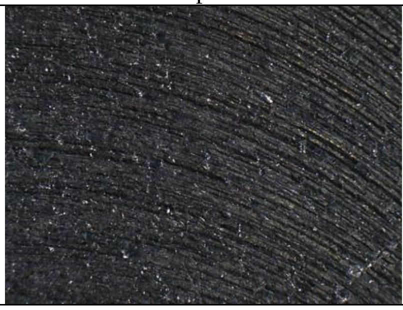	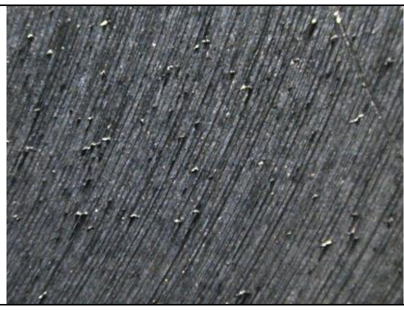
3D plots for anisotropic surfaces in face milling		
0 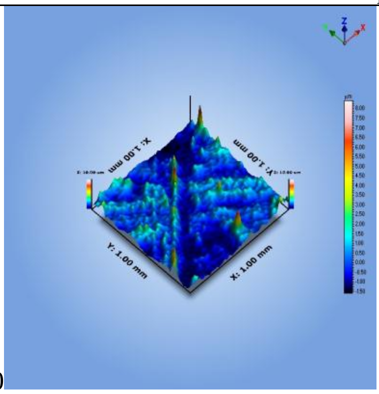	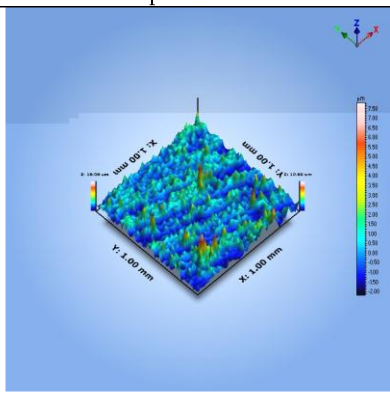	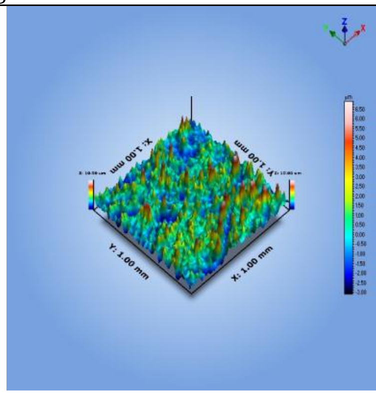

6.3.2. Skewness and tool wear:

Skewness (S_{sk})is the measurement of asymmetry of surface deviations about the mean/reference plane. From the figure 10(a), S_{sk} is near zero when the cutting tool is in good condition, which means that the surface height distribution curve is very like a standard normal distribution and a symmetrical distribution. When the tool is worn, Ssk becomes increasingly negative, due to the fact that the height distribution curve is changed to an asymmetrical distribution with a negative skew, which shows that the height of the surface is mainly above the mean plane with the surface tending towards having a “flatter top” with some deep valleys below the mean surface plane.

6.3.3. Kurtosis and tool condition:

Graphs developed for kurtosis parameters are presented in figure 10(b). Kurtosis ( ) characterises the spread of the height distribution. These curves indicate that the Sku is near 3 when cutter in good conditions, which shows that the surface surface height distribution is very close to a Gaussian distribution. When tool is worn, the machined surface has greater “peakedness”, with the Sku will lee than 3.

Variation in hardness of the samples with progress in machining time is more in case of AISI 4140 steels compared to AISI 1040 steel, the reason being higher tool tip temperatures generated in carbide tool. However in both cases, samples machined using different test conditions vary significantly in terms of hardness. The observations of milling tests bring some conclusions. Chatter results significant reduction on tool life about 30% when the tool in semi dull state and more than 50 % in when tool reaches to dull state are presented in results table 3. Displacement has direct influence on tool life. Higher vibration amplitude means lower the tool life and all the results indicate the same.

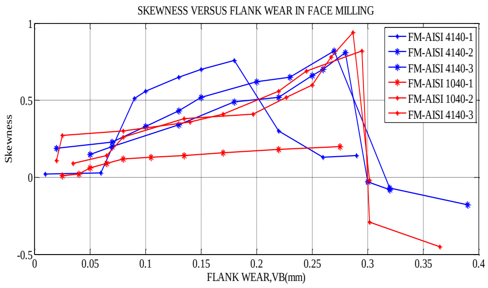

(a)

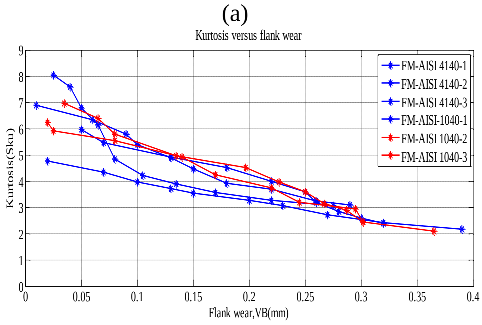

(b)

Figure 15:Variation skewness and kurtosis with tool flank wear.

Cutting time, derived cutting force, displacements and hardness are given. The cutting force data also presented in tables for all tests. It is easily seen that the displacement due to vibrations generally increase cutting forces. The increase of cutting forces is directly proportional with the severity of vibration. It is clearly seen in the milling tests with carbide tipped cutter that chatter vibration increases tool wear.

A logarithmic transformation is applied to convert the non linear form equations 4.15 and 4.17 into the following linear from:

$$\ln R_a = \ln C_{Ra} + a\ln H + y\ln f + n\ln\gamma_n + p\ln d + x\ln v + z\ln t \quad (9)$$

$$\ln VB = \ln C + a\ln H + n\ln\gamma_n + x\ln v + y\ln f + b\ln L \quad (10)$$

This most popularly used data transformation method as per literature review [16]. Table 4 gives the new functions for flank wear and surface roughness after processing extensive experimental data of the present work. From the results table 3, texture aspect ratio parameter, Str is found to be greater than 0.5 it indicates the texture strength of isotropic face milled surface this trend confirms ISO 25178 standards .

Table 3. Experimental results for test condition FM AISI-4140-3.

No.of passes	Cutting force (N)	Displacement (μm)	Time (min)	Hardness	Sq (µm)	Ssk	Sku	Sds	Str	VB (mm)	Ra (μm)	Rq (μm)
4	281.36	3	0.67	197	1.60	0.19	4.77	1235	0.63	0.02	1.54	1.92
8	282.29	6	1.21	198.7	3.94	0.23	4.33	1249	0.62	0.07	3.25	4.06
12	283.69	8	2.10	199	4.23	0.33	3.97	1256	0.61	0.10	3.49	4.36
16	286.09	24	2.42	201	4.65	0.43	3.72	1269	0.59	0.13	3.79	4.73
20	287.37	30	3.22	203	5.04	0.52	3.54	1277	0.57	0.15	4.15	5.18
24	288.95	38	4.31	205	5.67	0.62	3.27	1285	0.55	0.20	4.67	5.83
28	290.70	58	4.53	209	6.6	0.70	3.07	1309	0.52	0.23	5.44	6.8
32	292.36	65	5.32	210	8.16	0.82	2.71	1325	0.50	0.27	6.72	8.4
36	293.71	85	6.43	213	13.27	- 0.07	2.42	1339	0.47	0.32	9.35	11.6
40	295.49	117	6.59	215	22.65	- 0.18	2.17	1350	0.41	0.39	15.95	19.9

Table 4. Experimentally derived function for surface roughness and tool wear.

Test condition	New developed functions for surface roughness(R_a) and flank wear(VB) based experimental data
FM-AISI 4140 -1	$Ra = 0.7571.H^{0.393}.f^{0.733}.\gamma^{0.0988}.d^{0.507}.v^{-0.063}.t^{0.245}$ $VB = 2.433.x10^{-8}.H^{2.8173}.\gamma^{0.1020}.v^{-0.0533}.f^{-0.2487}.L^{0.514}$
FM-AISI 4140 -2	$Ra = 0.946.H^{0.4972}.f^{0.9162}.\gamma^{0.1235}.d^{0.633}.v^{-0.078}.t^{0.3062}$ $VB = 3.406.x10^{-8}.H^{3.944}.\gamma^{0.1428}.v^{-0.0742}.f^{-0.3481}.L^{0.7196}$
FM-AISI 4140 -3	$Ra = 1.3244.H^{0.6960}.f^{1.282}.\gamma^{0.1729}.d^{0.886}.v^{-0.1092}.t^{0.4286}$ $VB = 4.768.x10^{-8}.H^{4.5216}.\gamma^{0.1999}.v^{-0.1038}.f^{-0.4873}.L^{0.986}$
FM-AISI 1040 -1	$Ra = 0.605.H^{0.314}.f^{0.586}.\gamma^{0.079}.d^{0.4058}.v^{-0.0509}.t^{0.195}$ $VB = 1.946.x10^{-8}.H^{2.2534}.\gamma^{0.0807}.v^{-0.042}.f^{-0.1989}.L^{0.4113}$
FM-AISI 1040 -2	$Ra = 0.726.H^{0.3977}.f^{0.7032}.\gamma^{0.0948}.d^{0.4869}.v^{-0.0610}.t^{0.234}$ $VB = 2.432.x10^{-8}.H^{2.8167}.\gamma^{0.1008}.v^{-0.0525}.f^{-0.2486}.L^{0.5141}$
FM-AISI 1040 -3	$Ra = 0.980.H^{0.596}.f^{0.9493}.\gamma^{0.1279}.d^{0.6573}.v^{-0.0823}.t^{0.3159}$ $VB = 3.404.x10^{-8}.H^{3.9433}.\gamma^{0.14112}.v^{-0.0735}.f^{-0.3480}.L^{0.7197}$

7. Conclusion

In this study, relationship between the surface textural analysis, vibration and tool wear is investigated during face milling. Vibration signature analysis during face milling appears to be a promising method for tool flank wear detection. Measurements have shown that the analysis of vibration displacement amplitudes are used to assess tool wear in face milling. Vibration displacement in the feed direction consistently produces two peak amplitudes just prior to rapid tool degradation. Throughout the experimentation the vibration amplitudes are found to be increases as the progression of tool wear. As expected, with increase of speed, feed rate, depth of cut tool life became shorter. It is demonstrated that the AOE signal can be used successfully to distinguish between new and worn tools. The non contact monitoring capability of laser doppler vibrometer allows automatic tool wear classification with minimum human interaction.

Face milled surfaces with isotropy are extensively analysed in the present work. The level of isotropy in face milled surfaces is clearly revealed by texture aspect ratio parameter Str. Tool wear influences almost all the 3D surface parameters. The surface textural analysis of machined surfaces is very effective in tool condition monitoring. Thus, combined analysis of 3D surface topography of workpiece surface textures and acousto optic emission method for vibration displacement during the machining can be a choice for on line monitoring the tool wear state and can be used to monitor the machine states; therefore, it could provide a means to optimise the machining process. The encouraging results of the work paves the way for the development of a real-time, low-cost, and reliable tool-condition-monitoring system. A high degree of correlation is established between the results of the AOE signal and vision based surface textural analysis in identification of tool wear state.

Reference

[1] A.A. Kassim, M.A. Mannan and Zhu Mian "Texture analysis methods for tool condition monitoring" Image and Vision Computing, 25, 1080–1090, 2007.

[2] C. Bradley and S. Kurada" A review of machine vision sensors for tool condition monitoring", Computers in Industry 34 ,55-72, 1997.

[3] V. Solaja and E. Kulanic, Effect of tool life data analysis on tool life equation, Annals of CIRP 25 ,105-l 10, 1976.

[4] Yorem Koren, Flank wear model of cutting tools using control theory, Journal of Engineering for Industry 100, 103-109, 1978.

[5] E. Usui, T. Shirakashi and T. Kitigawa, Analytical prediction of cutting tool wear, Wear 100 ,129-151, 1984.

[6] E. Kannatey-Asibu, A transport diffusion equation in metal cutting and its application to analysis of the rate of flank wear, Journal of Engineering for Industry 107, 81-89, 1985.

[7] M.E.R. BonifGo and A.E. Diniz "Correlating tool wear, tool life, surface roughness and tool vibration in finish turning with coated carbide tools" Wear,173, 137-144, 1994.

[8] Y.C. Jiang and J.H. Xu, "In-process monitoring of tool wear stage by the frequency band energy method", Ann. CIRP, 36,45-48,1987.

[9] E. Diniz "Correlating tool life, tool wear and surface roughness by monitoring acoustic emission in finish turning" Wear, 152, 395-407, 1992.

[10] G.H.Lim "Tool wear monitoring in machine turning" Journal of materials processing technology 51, 25-36, 1995.

[11] P. Martin, B. Mute1 and J.D. Drapier, Influence of lathe tool wear on the vibration sustained in cutting, Proc. 15th int. Machine Tool Design and Research Conf , pp. 251-274,1974.

[12] B.K.A.Ngoi and K.Venkatakrishan "An acousto-optic vibrometer for measurement of vibration in ultra-precision machine tool" Int.J. Adv.Manuf.Technology, 16:830-834, 2000.

[13] S.J.Rothenberg and J. R. Bell "Rotational vibration measurements using Laser doppler vibrometry: comprehensive Theory and practical application journal of sound and vibration 238(4), 673}690, 2000.

[14] M. Rantatalo, K. Tatar and P. Norman "Laser Doppler Vibrometry measurement of a rotating milling machine spindle" International Conference on Vibrations in Rotating Machinery – ImechE Conference Transactions, 7th to 9th September , Swansea, UK, Event Publications, p 231-240, 2004.

[15] Heisaburo Nakagawa, Yutaka Kurita, Keiji Ogawa, Yuji Sugiyama, and Hideyasu Hasegawa "Experimental Analysis of Chatter Vibration in End-Milling Using Laser Doppler Vibrometers" Int. J. of Automation TechnologyVol.2No.6, 2008.

[16] C.X Feng and X.Wang "Development of empirical models for surface roughness prediction in finish turning" International journal of advanced manufacturing technology, 20: 348-356, 2002.

[17] Tool and manufacturing engineer's handbook -W. H. Cubberly, Ramon Bakerjian, Society of Manufacturing Engineers pp: 19.11,2002.

[18] R.M.Sundaram and B.K.Lambert."Mathematical models to predict surface finish in fine turning of steels, Parts I and II" International journal of production research, 19, pp547-564, 1981.

[19] Stout KJ, Sullivan PJ and Dong WP The development of methods for the characterisation of roughness in three dimensions. Commission of the European Communities, Brussels, ISBN 07044131327, 1993.

[20] Blunt L, Jiang X Advanced techniques for assessment surface topography, 1st edn. London Penton, London, 2003.

[21] F. Hashimoto,S.N. Melkote, R. Singh and R. Kalil "Effect of finishing methods on surface characteristics and performance of precision components in rolling/sliding contact "Int. J. Machining and Machinability of Materials, Vol. 6, Nos. 1/2, 2009.

[22] J. Kundrak & K. Gyani & V. Bana "Roughness of ground and hard-turned surfaces on the basis of 3D parameters" Int J Adv Manuf Technol 1086-90,2007.

[23] B.S.Prasad and M.M.M.Sarcar "Experimental investigation to predict the condition of cutting tool by surface texture analysis of images of machined surfaces based on amplitude parameters" Int. J. Machining and Machinability of Materials, Vol. 4, Nos. 2/3, 217-236, 2008

[24] R.A.Waikar and Y.B. Guo "A comprehensive characterization of 3D surface topography induced by hard turning versus grinding" journal of materials processing technology 197 ,189–199,2008.

JJMIE

Volume 5, Number 6, Dec. 2011
ISSN 1995-6665
Pages 521 - 526

Jordan Journal of Mechanical and Industrial Engineering

Studying the Effects of Varying the Pouring Rate on the Casting Defects Using Nondestructive Testing Techniques

Wisam M. Abu Jadayil*,[a]

[a]Department of Industrial Engineering, The Hashemite University, Zarqa 13135, Jordan

Abstract

In this paper Aluminum casting defects when the pouring rate is varying are investigated using green sand casting process by the aid of two nondestructive testing techniques. Ten Al casting samples have been prepared with different pouring rate for each. Then they have been tested using the Penetrant Test (PT) and the Ultrasonic Test (UT) to describe the surface and subsurface defects respectively. It was found that when the pouring rate is increases surface defects are significantly increases as the penetrant testing results showed. On the other hand when the pouring rate is increases, there are much less defects appeared internally as the ultrasonic testing showed.

Keywords: Pouring rate; Penetrant testing; Ultrasonic testing; Casting defects

1. Introduction

Cast aluminum alloys are widely used in the automotive industry due to their excellent cast ability, corrosion resistance, and especially their high strength to weight ratio.

There are many surface and subsurface casting defects occur during casting process. Some of these defects which are related to the molten material pouring rate are mention in this paper. Short Casting (the mold didn't fill all the way. This is usually caused by the metal solidifying before it fills the cavity. It could also be a restriction: too small a sprue, gate, not enough venting keeping the metal from going in or pouring rate is varying small). Gas defects which resulted from Gas pockets come from gas dissolving in the melt then coming out when it solidifies. This usually manifests itself as a rough surface on areas exposed to air (such as the top of the sprue, riser or ingots) or pockets of varying size in the cross-section of the metal. Gas comes from melting too long or heating too hot, 'stewing' the metal (keeping it molten longer than needed), using an unusually oxidizing or reducing flame in the furnace, getting water (or pretty much anything else that has hydrogen in it, or will burn; painted scrap for instance) in the melt, and the alignment of the Moon with the Earth and Sun. A good idea is to recycle scrap into ingots as a first step since the scrap might be wet, oily or painted and will add gas to the melt. The gas comes out in the ingots, not your casting).

2. Literature Review

A method for detecting the surface defects of cast metals was proposed by Okawa [1]. The proposed automatic inspection system consists of an industrial television camera (ITVC) and a microcomputer. A picture is taken from the ITVC in I-bit digital form and stored in the memory of the microcomputer. The computer calculates features from the picture and decides if there is any defect on the surface of the cast metal. On the other hand, Wang et. al. [2] studied the influence of casting defects on the room temperature fatigue performance of a Sr-modified A356-T6 casting alloy has been studied using un-notched polished cylindrical specimens. The numbers of cycles to failure of materials with various secondary arm spacings (SDAS) were investigated as a function of stress amplitude, stress ratio, and casting defect size. Atzori et. al. [3] studied fatigue behavior too to verify the applicability of the Atzori–Lazzarin diagram to the AA356-T6 cast Aluminum alloy. They found that the mechanical properties of AA356-T6 are strongly influenced by the metallurgical and microstructural features, and the accurate study of these parameters is the main way to improve the fatigue performance of a material. Mayer et. al. [4] worked influence of porosity on the fatigue limit of die cast magnesium and aluminum alloys. They used ultrasonic fatigue tests to show mean fatigue limits of approx. 38–50 MPa (magnesium alloys) and 75 MPa (AlSi9Cu3) in the tested casting condition. Similar results were found for low and high frequency ultrasonic tests in detecting porosity of castings. Linder et. al. [5] worked too on the influence of porosity on the fatigue life for sand and permanent mould cast aluminum.

* Corresponding author. e-mail: wisam@hu.edu.jo

Fatigue testing of sand cast and permanent mould cast specimens has been performed. They concluded that for smooth specimens an increased porosity level has been found to decrease the fatigue strength compared to notched specimen geometry where almost no influence of the pore fraction on the fatigue strength could be found. Avalle et. al. [6] produced a comparison between standard specimens and production components by casting defects and fatigue strength of a die cast aluminum alloy. Their experimental and numerical results showed that static characteristics, like tensile strength, are sensitive to defects. Nadot et. al. [7] worked on Influence of casting defects on the fatigue limit of nodular cast iron. They showed in their study that the near surface defects are much more dangerous with regard to the fatigue limit than internal defects. Webster [8] used images in a language and culture-independent expert system for diagnosing pressure die-casting defects. Experiments were conducted using the JPEG compression method. The compression and re-expansion times are very short, adding only a few seconds to the normal images disk access. The conclusion drawn was that defect catalogue and its interface to the expert systems are now essentially complete and satisfying the original purpose of providing a language and a culturally- independent interface. A study was carried out by Dharmar et. al. [9] to determine the defects in the internal microstructure of clasps of cast chromium cobalt removable partial denture frameworks. Dharmar et. al. used radiographic and metallographic evaluation of porosity defects and grain structure of cast chromium cobalt removable partial dentures. The aim of this study was to determine the defects in the internal microstructure of the clasp assemblies. The radiographic study revealed a large number of internal defects in various parts of the removable partial denture frameworks. Balaskloa et. al. [10] continued the work started by Dharmar et. al [9] and added neutron radiography in revealing the defects in an Al casting. The joint application of NR and XR revealed hidden defects located in the Al casting. Image analysis of the NR and XR images unveiled a cone-like dimensionality of the defects. The spectral density analysis of the images showed a distinctly different character for the hidden defect region of Al casting in comparison with that of the defect-free one. Ahameda et. al. [11] detected the casting defects by using UT. They worked on detecting defects in cold flakes and crack propagation in aluminum alloy die-cast plate. Their results show the ability of nondestructive detection of cold flakes by the ultrasonic microscopy. Cendrea et. al. [12] established X-ray methods for inspection of cast aluminum components by combining two approaches, a radioscopic inspection, and a photon-counting system. Cendrea et. al. [12] concluded that the radioscopic system is not well adapted to high thicknesses; defects are detected in thin parts of the cast component. Verran et. al. [13] studied the influence of the speed injection parameters in the first and second phases and of the upset pressure over the die casting parts quality, in 305 aluminum alloys is investigated. Initially, an experiment planning was performed, where several combinations of the three injection parameters were used, in order to enable the evaluation of their influence on the occurrence of foundry defects, such as porosities and cold shuts. The obtained castings sanity evaluation was performed by visual inspections and quantitative metal graph analyses, as well as by density measurements in a significant casting region, in which great quantities of porosities appear after surface machining.

Based on the previously discussed literature review, it can be clearly seen that many researchers tried to detect the casting defects using fatigue performance. The main disadvantage of this method is that it will damage the sample and it's not as accurate as needed to describe the surface and subsurface defects, because crack initiation occurs depending on shape of void or porosity. Other researchers tried to use other methods to detect the defects such as UT and RT. So, no researches studied have been in the literatures which discuss the effect of pouring rate on the formation of surface and subsurface defects.

3. Experimental Procedure

In this paper we will use ten samples of casted aluminum pieces to study the effect of pouring rate on the surface and subsurface defects. The samples should be tested without destroy them by using UT and PT.

The first step was to choose the casting piece. The key shown in Figure 1 was chosen. It has flat surface besides curved surfaces. That makes testing surface defects using PT easy. The thickness of the piece was around 2 cm. That makes using the UT possible, especially it needs the surfaces to be grinded first. The molten material was aluminum without any additives. The green sand casting process was used by making the mold and pattern. The pattern was made from wood. For each sample of the 10, a sand mold was made to exclude the effect of the mold surfaces in creating surface defects on the sample. The total volume of the mold cavity and the gates and risers was almost 46 cm3. So each time a volume of 46 cm3 of molten Al was added and the required time to finish pouring was recorded. Since the pouring speed was changed each time, the pouring rate was estimated and recorded as shown in Table 1.

After collecting the samples from the casting molds and the risers were cut, the 10 samples were tested, first using the PT and pictures describing the surface defects were takes (Figures 1-10), and then the upper surfaces of the samples were polished and tested using the UT. The results of the UT are shown in Figures 11-20.

Penetrant Testing (PT) is a method that is used to reveal surface breaking flaws by bleed out of a colored or fluorescent dye from the flaw. The technique is based on the ability of a liquid to be drawn into a "clean" surface breaking flaw by capillary action. After a period of time called the "dwell," excess surface penetrant is removed and a developer applied. Colored (contrast) penetrants require good white light while fluorescent penetrants need to be used in darkened conditions with an ultraviolet "black light". Fluorescent dyes were added to the liquid penetrant. These dyes would then fluoresce when exposed to ultraviolet light. Using this nondestructive technique, the surface defects of the casted sample can be detected.

Ultrasonic Testing (UT) is a technique for detecting internal defects through introducing high frequency sound waves into a material which are reflected back from surfaces or flaws. Reflected sound energy is displayed versus time, and inspector can visualize a cross section of the specimen showing the depth of features that reflect sound.

Table 1: Pouring rate of samples 1-10.

SAMPLE NO.	POURING TIME (S)	VOLUME (CM^3)	POURING RATE (CM^3/S)
1	13.5	46	3.4
2	7.3	46	6.3
3	5.3	46	8.7
4	4.9	46	9.4
5	3.7	46	12.6
6	3.6	46	12.7
7	3.1	46	14.9
8	2.5	46	18.6
9	2.4	46	19.2
10	1.9	46	24

Using data provided in Table 1, and using the following equation, the pouring rate could be calculated:

$$PR = V/t \tag{1}$$

Where

PR : Pouring rate (cm3/s)
V : Volume (cm3)
t : Time

4. Discussion of the Results

Figures 1-10 show the ten samples when tested using the PT. The red color indicates the surface roughness and surface defects. So, as you proceed from the first sample to the tenth sample the defects are getting more on the surface, as a result of increasing the pouring rate. Increasing the pouring rate entrapped more gases and inclusions melted in the molten material. Those inclusions and gases appear on the sample surface as the high pouring rate pressurizes them outside the material body, so they appear on the surface. Moreover, high pouring rate may mean turbulent flow which hits the mold cavity harder and results in rough surfaces.

Figure 1: Sample 1 surface defects using PT at PR = 3.4 (cm^3/s).

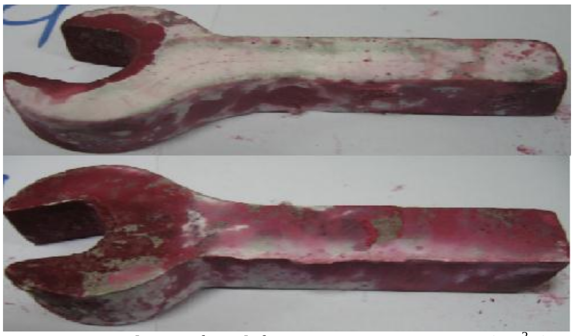

Figure 2: Sample 2 surface defects using PT at PR = 6.3 (cm^3/s).

Figure 3: Sample 3 surface defects using PT at PR = 8.7 (cm^3/s).

Figure 4: Sample 4 surface defects using PT at PR = 9.4 (cm^3/s).

Figure 5: Sample 5 surface defects using PT at PR = 12.6 (cm^3/s).

Figure 6: Sample 6 surface defects using PT at PR = 12.7 (cm^3/s).

  - Volume 5, Number 6 (ISSN 1995-6665)

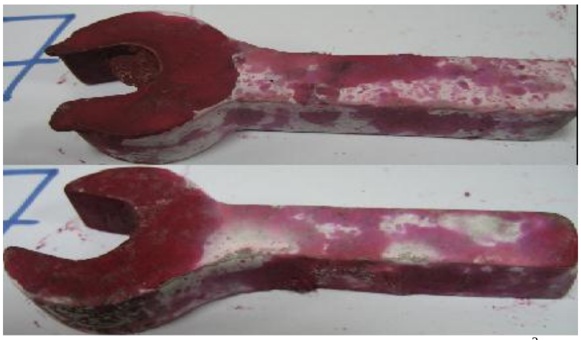

Figure 7: Sample 7 surface defects using PT at PR = 14.9 (cm^3/s).

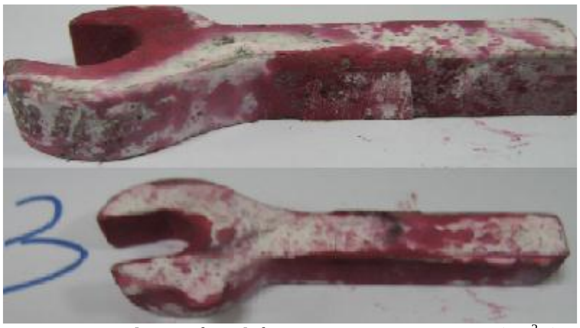

Figure 8: Sample 8 surface defects using PT at PR = 18.6 (cm^3/s).

Figure 9: Sample 9 surface defects using PT at PR = 19.2 (cm^3/s).

Figure 10: Sample 10 surface defects using PT at PR = 24 (cm^3/s).

To perform UT to investigate subsurface defects in the ten samples, they were grinded to make their surfaces smooth so that the probe moves easily on the surface to detect internal defects. The results of the UT are shown in the Figures 11-20 for the ten samples. The first highest peak and the last large peak are the boundary surfaces of the sample, while the intermediate peaks represents the defects inside the sample. As the number and the amplitude of these peaks are increasing, the internal defects are getting more. It can be easily found that as the pouring rate is getting higher, as the internal (subsurface) defects are getting less for the same reason mentioned above. High pouring rate means more pressurized molten material, that pushes the inclusions and gases outside the molten material and so they stay on the sample surface.

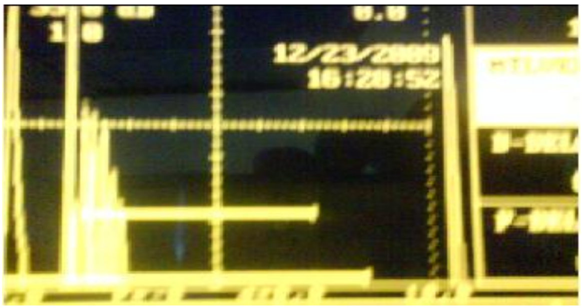

Figure 11: Sample 1 subsurface defects using UT at PR = 3.4 (cm^3/s).

Figure 12: Sample 2 subsurface defects using UT at PR = 6.3 (cm^3/s).

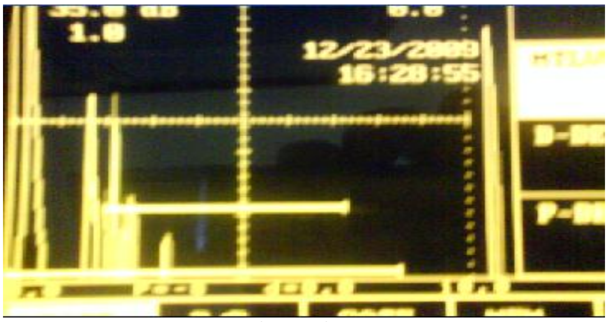

Figure 13: Sample 3 subsurface defects using UT at PR = 8.7 (cm^3/s).

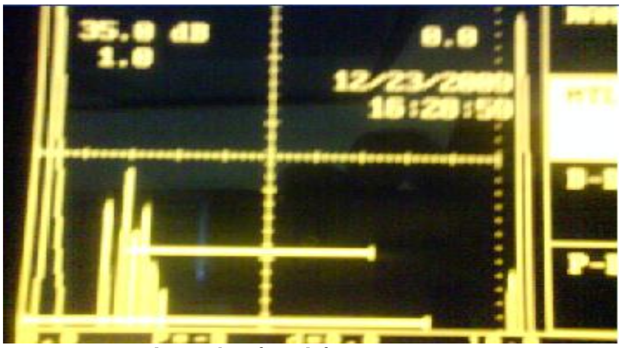

Figure 14: Sample 4 subsurface defects using UT at PR = 9.4 (cm^3/s).

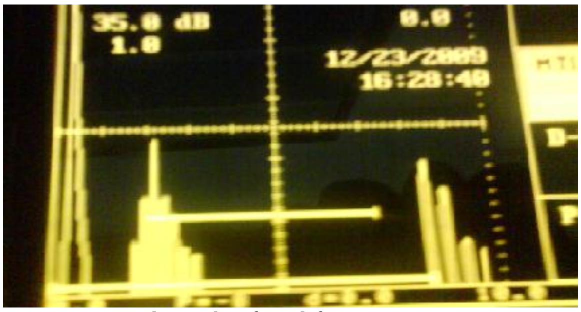

Figure 15: Sample 5 subsurface defects using UT at PR = 12.6 (cm^3/s).

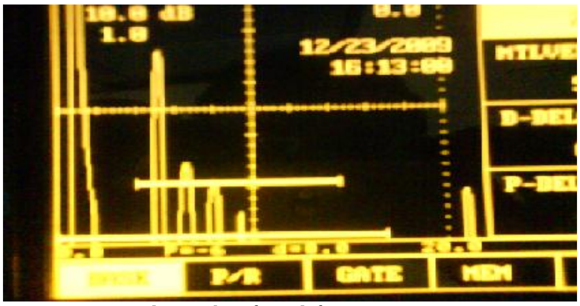

Figure 16: Sample 6 subsurface defects using UT at PR = 12.7 (cm^3/s).

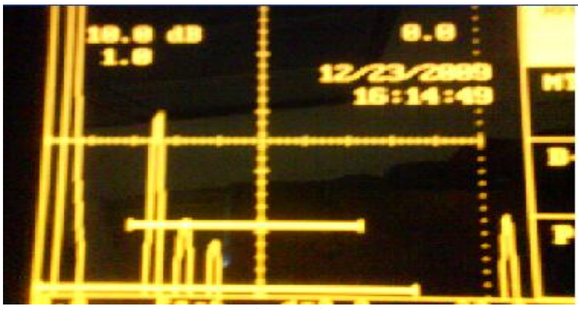

Figure 17: Sample 7 subsurface defects using UT at PR = 14.9 (cm^3/s)

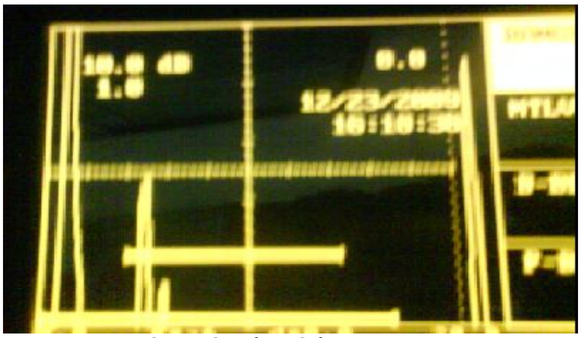

Figure 18: Sample 8 subsurface defects using UT at PR = 18.6 (cm^3/s).

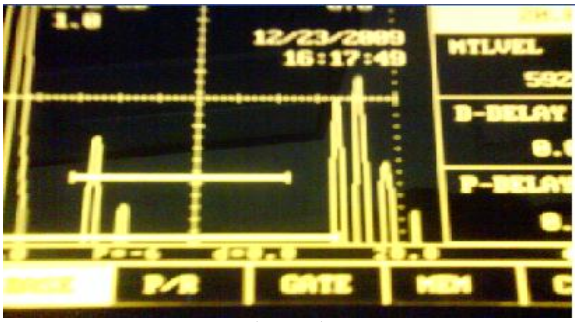

Figure 19: Sample 9 subsurface defects using UT at PR = 19.2 (cm^3/s).

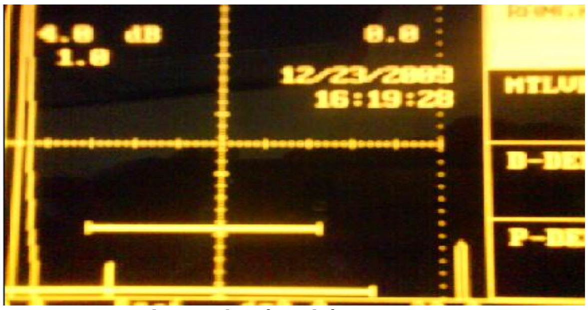

Figure 20: Sample 10 subsurface defects using UT at PR = 24 (cm^3/s).

5. Conclusions

Based on the two nondestructive testing used, the PT and the UT for the ten Al sand casted samples, the following conclusions might be drawn:

- The PT is very good tool for investigating the surface defects of casted samples with no need to damage the sample structure. Also the UT is very good tool for investigating the internal defects with no need to damage or destroy the structure of the sample.
- Both PT and UT are easy to perform and give reasonable results in case of inspecting casting samples.
- As the pouring rate of the molten material is increasing, as the surface defects of the casted sample are getting more, and the internal (subsurface) defects are getting less.
- Since the pouring rate has an opposite effect on surface and subsurface defects a compromise must be made to obtain the optimum pouring rate, and depending on the application where the surface or the internal structure is more important.

References

[1] Y. Okawa, "Automatic Inspection of the Surface Defects of Cast Metals". Computer Vision, Graphics and Image Processing, Vol. 25, 1984, 89-112.

[2] Q. Wang, D. Apelian, D. Lados, "Fatigue behavior of A356-T6 aluminum cast alloys. Part I. Effect of casting defects". Journal of Light Metals, Vol. 1, 2001, 73-84.

[3] B. Atzori, G. Meneghetti, L. Susmel, "Fatigue behaviour of AA356-T6 cast aluminium alloy weakened by cracks and notches". Engineering Fracture Mechanics, Vol. 71, 2004, 759-768.

[4] H. Mayer, M. Papakyriacou, B. Zettl, S. Stanzl-Tschegg, "Influence of porosity on the fatigue limit of die cast magnesium and aluminium alloys". International Journal of Fatigue, Vol. 25, 2003, 245–256.

[5] J. Linder, M. Axelsson, H. Nilsson, "The influence of porosity on the fatigue life for sand and permanent mould cast aluminium". International Journal of Fatigue, Vol. 28, 2006, 1752–1758.

[6] M. Avalle, G. Belingardi, M. Cavatorta, R. Doglione, "Casting defects and fatigue strength of a die cast aluminium alloy: a comparison between standard specimens and production Components". International Journal of Fatigue Vol. 24, 2002, 1-9.

[7] Y. Nadot, J. Mendez, N. Ranganathan, "Influence of casting defects on the fatigue limit of nodular cast iron". International Journal of Fatigue Vol. 26, 2004, 311–319.

[8] C. Webster, "The use of images in a language- and culture-independent expert system for diagnosing pressure die-casting defects". Journal of Materials Processing Technology, Vol. 55, 1995, 296-302.

[9] S. Dharmar, R. Rathnasamy, T. Swaminathan, "Radiographic and metallographic evaluation of porosity defects and grain structure of cast chromium cobalt removable partial dentures". The Journal of Prosthetic dentistry, Vol. 10, 1993, 369-373.

[10] M. Balaskloa, F. Korosi, Zs. Szalay, "Semi-simultaneous application of neutron and X-ray radiography in revealing the defects in an Al casting". Applied Radiation and Isotopes, Vol. 61, 2004, 511-515.

[11] Aziz Ahameda, H. Kato, K. Kageyamab, T. Komazaki, "Acoustic visualization of cold flakes and crack propagation in aluminum alloy die-cast plate". Materials Science and Engineering, Vol. 423, 2006, 313-323.

[12] E. Cendrea, V. Kaftandjianb, G. Lecomteb, K. Kjaer, "Complementarity of a photon-counting system and radioscopy for inspection of cast aluminium components". NDT&E International, Vol. 38, 2005, 239-250.

[13] G. Verran, R. Mendes, M. Rossi, "Influence of injection parameters on defects formation in die casting Al12Si1, 3Cu alloy: Experimental results and numeric simulation". Journal of Materials Processing Technology, Vol. 179, 2006, 190-195.

JJMIE

Volume 5, Number 6, Dec. 2011
ISSN 1995-6665
Pages 527 - 532

Jordan Journal of Mechanical and Industrial Engineering

The Development and Implementation of Lean Manufacturing Techniques in Indian garment Industry

Ravikumar Marudhamuthu*[a], Marimuthu krishnaswamy[b], Damodaran Moorthy Pillai[c]

[a]*Department of Mechanical Engineering, Faculty of Automation and Robotics, Pallavan College of Engineering, Anna University, Thimasamudram, Kanchipuram-631502, India.*
[b]*Coimbatore Institute of Technology, Coimbatore, India.*
[c]*Principal, Pallavan College of Engineering, Kanchipuram, India.*

Abstract

This research addresses the implementation of lean principles in an Indian garment export industry. The objective is to evolve and test various strategies to eliminate waste and to improve the productivity. This paper briefly describes the application of Value Stream Mapping (VSM) and Single Minute Exchange of Die (SMED). Existing state production floor was modified by using VSM efficiently to improve the production process by identifying waste and its causes. At the same time, set up time is also reduced considerably. We conclude with evidence of the early results of the programmes as well as a number of key learning points for other organizations wishing to follow similar path.

Keywords: Lean Manufacturing; Garment industries; Value Stream Mapping (VSM); Single Minute Exchange of Die (SMED)

1. Introduction

In the 1980's the garment industry was led by fashion and retailing and the emphasis was on technologies in the demand-related parts of the supply chain. India ranks among the top target countries for any company sourcing textiles and apparel. Indeed, apart from China, no other country can match the size, spread, depth, and competitiveness of the Indian textile and apparel industry.

Moreover, the global elimination of quotas at the end of 2004 has greatly enhanced the opportunities for sourcing from India. India supplies over US$13 billion worth of textiles and apparel to the world markets. And exports are growing rapidly as more and more buyers around the world turn to India as an alternative to China. In 2005 – spurred by the global elimination of quotas – shipments to the EU soared by 30% and those to the USA shot up by 34%. These increases are remarkable, given that EU imports from all sources rose by only 8% while US import growth was just 6%.

Consumer spending is slowing down all over the world. Retailers are looking for real innovation from their suppliers. They want really new garments made from new fabrics and yarns. They want new services to offer their customers. Competition in the late 1990s will be based on the capabilities and core competences of textile and clothing companies and on the building of long-term supply relationships. There are many opportunities to be addressed. Textile and clothing machinery will continue to be improved but the most interesting technologies for the 2000s are in the areas of fibres, fabrics, measurement, control and multimedia. We can say a garment industry is an independent industry from the basic requirement of raw material to final products, with huge value addition at every stage of processing, Apparel industry is largest foreign exchange earning sector contributing 15% of the total country export.

In this scenario, the Indian garment industries have witnessed substantial improvements in recent years. But the unnecessary capital investment is not going to solve the problem entirely; moderately this will turn out the waste in long run. The implementation of lean manufacturing is greatly recommended, in order to identify the waste and to eliminate them. This research addresses the implementation of lean tool in the shop floor. We reveal that how Value Stream Mapping can be integrated to show a best picture of non value added activities present in the system and, hereby eliminating the problem that causes wastes.

2. Literature Review

In recent years, many literatures have extensively documented the implementation of lean manufacturing, in various manufacturing sectors. Lean production is a conceptual frame work popularized in many western industrial companies since the early 1990's. Initially, the publication of the book "The Machine that Changed the World" [1] started diffusion of some lean manufacturing practices developed by the most competitive auto manufactures in the world.

The interest on lean production is mostly based on empirical evidence that it improves the company's

* Corresponding author. e-mail: mmr.head@gmail.com

competitiveness [2-3]. Lean manufacturing is most frequently associated with elimination of seven wastes [4]. The purpose of implementing it is to increase productivity, reduce lead time and cost, and improve quality [5]. Quality is a major focus in lean manufacturing, because poor quality management should result in huge waste and scraps. Right quality management at right time will help to control the manufacturing process [6]. Companies such as Toyota, Pratt and Whitney, Sikorsky, Delphi, Ford and many other companies have achieved large savings by implementation of lean principles in their manufacturing activities [7]. Lean manufacturing is an integrative concept which can be adopted by selective set of keys or factors. Those key areas are believed to be very critical for its implementation.

Though many literatures on lean implementation are comprehensively available, very few have addressed the garment industry. [8]The pressure placed on firms in the garment industry from international competition has been enormous. The increase in competition has led to an increased focus on customer satisfaction as a survival of the company in the long run".

The garment industry has opportunities to improve, but requires some changes. Under the highly competitive environment, the garment industry has numerous opportunities for improvement using lean principles [9]. Lean practices can fulfil the customer demands with high quality and services at right time. Now, many countries have started to practice lean tools in the garment industry and observed tremendous improvement [10]. In addition to this lean production involves, motivates and develops employee skills through education and multi-skilling program.

The companies that adopt lean manufacturing as a working philosophy within their organizations can make significant improvement in terms of their operational performance even if it is in a modified format that best suits their particular business culture [11]. The organisations intending to go for any Japanese manufacturing technology and practices should first understand the need to use that tools and its application, prepare for its adaption and then identify the ways and measures required for its successful implementation[12].To implement lean thinking in any organization the first step is to identify the value stream map[13,14] .Value Stream Mapping is a functional method aimed at recognizing production systems with lean vision.VSM has been applied in variety of manufacturing industries[15]. In this paper we also describe an application of VSM in order to identify the various forms of waste in garment shop floor. Work process across the value stream should be performed with a minimum of Non Value Added Activities(NVAA) in order to reduce waiting time, quieng time, moving time, setup time and other delays [16].. In this research the authors have successfully applied VSM and SMED. In the previous years there were many illustrations on application of VSM and SMED tools in various manufacturing industries, but rarely addressed the application of lean manufacturing in garment industry.

3. Problem Statement: Transportation & Machine Assembly

In general, the key activities usually practiced in every garment industry shop floor include: After receiving an order from the customer, the design is made and it is marked in the marker sheet.

- The proper size of the material is calculated, taking in to account the various allowances from the available empirical relationships, the existing database, and prior experiences.
- After procuring the raw material of the desired quality, the pieces were cut in to required size.
- Thereafter, the various processes were carried out.
- In addition inspection is carried out to ascertain the desired quality.
- Finally, finishing and cleaning operations are performed to complete the process. The finished component is then sent to the customer.

Basically the transportation section has various problems such as

- Weight carried by a worker was too heavy
- Distance between each floor was more
- Time taken for transportation was high
- Increased delay time.

In order to avoid all these NVAA the company decided to implement Lean concepts, so that overall performance will be increased.

4. Case Study

The case study considered in this research is one of the leading garment industries in India. The face of the industry was not publicized; but, we shall after refer to the industry as G.L. fashions. The organization has 14 branches. This industry produces various types of inner garments to European and American continents. The annual turnover of this industry was US $ 18 million. In most of the branches, the company was facing severe pressures, both externally and internally, to improve the performance of production flow line. The industry has made huge capital investments to take initiatives in expansions, modernizations etc. The company management has endeavoured to implement 5S+safety and total productive maintenance; but the results achieved were not significant compared to the investments made.

The activities performed in a company can be simply categorized as Value Added Activities (VAA), Non Value Added Activities (NVAA), necessary but Non Value Added Activities (NNVAA). After extreme brain storming and a thorough study of the shop floor, it was found that the material flow line contains various forms of Non Value Added Activities as follows:

- Distance between the material floor and shop floor was high.
- Floors needed to be converted as sections.
- Change of machine setup time between styles needs to be reduced.

Certainly, all of these above factors lead to low production rate and high setup time. In the existing state the average production rate was 70 products per hour and setup time was 28 minutes. In the coming section, the lean principles are implemented on the garment shop floor.

5. Implementation and Results

5.1. Select the process to be mapped:

The process that we had selected for mapping was manufacturing. In this sector we focused to improve the production rate of the production line and to reduce the fatigue of the worker. We mapped the processes from releasing of raw material to finished goods. We studied about the flow of materials between various floors.

5.2. Collection of data and mapping of existing state:

The second step was collecting all the data from various floors and to draw the existing state map. We collected the time taken for transfer of raw materials from cutting floor to production floor and for doing operations.

5.2.1. Existing state map:

In existing state map, the design of the product was issued by the design engineer to the cutting floor. In cutting floor the designs were given to the operators to cut the raw material. After finishing the cutting process the material release order was issued by the production manager. Then the material is transferred to the production floor.

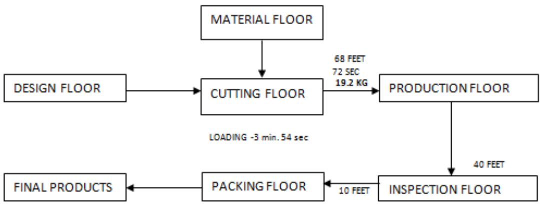

Figure 1: Existing State Map.

5.2.2. Flow of material from cutting floor to production floor:

Materials were transferred from cutting floor to production floor using trolley. For a single shift of trolley 6 boxes of materials were transferred. Every box contains 100 pieces, in total 600 pieces were transferred per shift. The weight of material that was packed per box was 3.2 kg. The total weight of load in trolley was 19.2 kg (for 6 boxes). The time taken for loading materials per box was 36 seconds. Time taken for exchange of box was 3 seconds. For loading of materials in trolley the total time taken was 3minutes and 54 seconds. The distance from cutting floor to production floor was measured as 68 feet.

The time taken for travelling 68 feet with load by the trolley was 72 seconds and for unloading of materials from the box is 36 seconds per box. Time for exchange of box was 3 seconds. The return time from production floor to cutting floor was 58 seconds without load. Total time taken for transfer of materials per shift of trolley was 9 minutes and 58 seconds. Production rate of the company was 70 products per hour. Total number of products produced per shift was 19600. Two shifts running per day. Total number of products produced per day were 39200. Totally 5 workers required per shift for transfer of materials from cutting floor to production floor.

Total number of pieces transferred by one employee was 3920 per shift. Number of boxes transferred by one employee was 39.2 say 40 boxes. Load carried by the worker per shift was 40*3.2=128 kg. Total load carried by worker was 128*2=256 kg. (Both loading and unloading). 80 times back bone of the worker was strained. This leads to severe back pain of the worker within 10 years if he does the work continuously.

5.2.3. Production floor:

In production floor same type were arranged as groups. Ten types of operations were done in the production floor, so, ten groups of were formed. There were nine junctions between ten groups. Total time required for transfer of materials between sections was 25*9 = 225 seconds. Weight of material transferred by worker per single time was 3.4 kg/100 pieces. For 19600 pieces weight transferred was 3.4*196 = 666.4 kg. Worker travels about 600 feet/shift with load. Delay time occurs whenever machine breaks down. Then completed products were transferred to packing floor. The distance between production floor and packing floor was 40 feet. Time taken to transfer of products was 35 seconds.

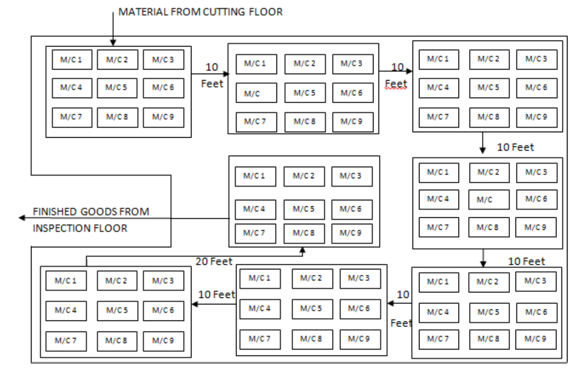

Figure 2: Existing State Production Floor.

5.3. Analyze the Existing State:

The third step for implementation of Value Stream Mapping was analyzing the existing state map. We analyzed thoroughly to find out the various Non Value Added Activities of the existing state map. The time taken for transfer of materials from cutting floor to production floor and from production floor to packing floor was high. The workers were stressed heavily by transferring more loads. The production rate was very low. More machines were set to idle due to the unavailability of the raw material. This is due to the distance from cutting floor to production floor. Rework of the product was difficult, because after inspection the product which has defect was returned to the production floor. This will take more time. If a problem occurred in a single machine the production time was affected.

5.4. Mapping and Implementation of Future State:

We mapped the future state in order to avoid the Non Value Added Activities of the existing state map that we had analyzed in the third step. We hardly concentrate to reduce the time taken to transfer of materials from cutting floor to the production floor. Avoid the fatigue of the workers. Improve the production rate. Reduce machine break downs. Improve the rework process and to reduce the time taken for rework. Avoid the machine idleness. We constructed the future state map by integrating all the floors as a single floor. This single floor contains various sections. Those section were,

- Cutting section.
- Production section.
- Inspection section.
- Packing section.

In the future state map, the input was raw material and the output was the finished product (packed one).

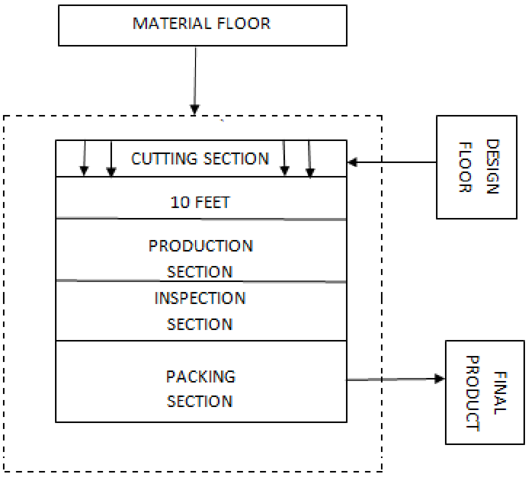

Figure 3: Single Shop Floor Layout.

5.4.1. Transfer of Materials in Future State Map:

Since the floors were integrated, the distance between the cutting section and production section was reduced to 10 feet. The team leader himself transfer the material from cutting section to production section, so separate worker was not required. The material was transferred by box only not by the trolley so human fatigue was reduced. Time taken for loading and unloading of products was calculated as 36*2=72 seconds. Travelling time for 10 feet with load was 10 seconds. Total time taken=36*2+10=82 seconds. Time taken for transfer of 100 pieces of material was 82 seconds.

5.4.2. Production Section in Future State Map:

Arrangement of machines in groups was eliminated and separate teams were formed. Every team was organized by a team leader and the team had 12 workers. Since the machines were arranged as per sequence of operation, the transfer of materials was made easy and time required for transfer of materials in the production section was reduced.

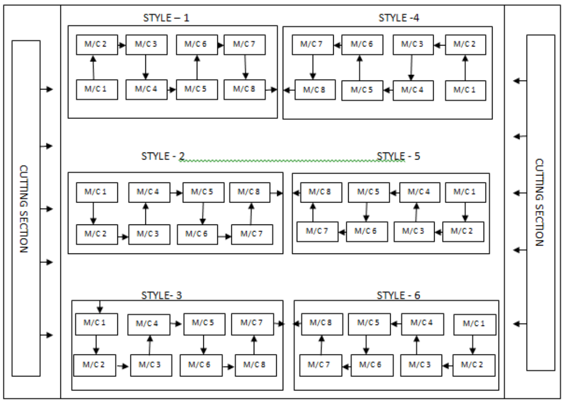

Figure 4: Production Section in Future State Map.

As the material was transferred between the machines in the production section, the weight carried by a worker between the groups was avoided, which reduces human fatigue. The inspection and packing section were integrated within the module, so the time taken for transfer of material to the packing floor was avoided.

5.5. Non Value Added Activities:

In the existing state map the time taken to transfer of 100 pieces = 598 / 6= 99.7 seconds say 100 seconds. In future state map the time taken to transfer of 100 pieces was 82 seconds. Time saved after implementation of future state map was 100-82=18 seconds per 100 pieces. Time saved per shift= 18*196=3528 seconds = 58 minutes and 48 seconds. Since load carrying capacity and distance were reduced which leads to reduction of human fatigue.

5.6. SMED:

After implementing VSM, the machines were arranged as per the sequence of operations. In the existing state the time required for change of setup from one style to another was 28 minutes. SMED was implemented by the following steps; the sequence of operations performed on the future style was derived. After completion of first operation in the existing style, the first machine of the existing style was replaced by the first machine of the future style. The time required for this process was 49 seconds. The same procedure was followed for the next 9 operations. So the total time required for change of setup from existing style to future style was 8 minutes and 10 seconds.

5.7. Graphical Representation for Clear Understanding:

5.7.1. Material Transfer:

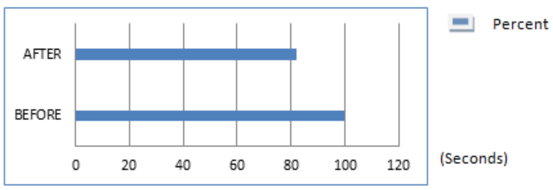

- Time taken to transfer 100 pieces was 100 seconds. After Implementation it took only 82 seconds for 100 pieces.
- 100-82=18 seconds. Therefore Percentage reduction of material transfer is 18.

5.7.2. Travelling Distance:

5.7.2.1. Distance from Cutting floor to production floor:

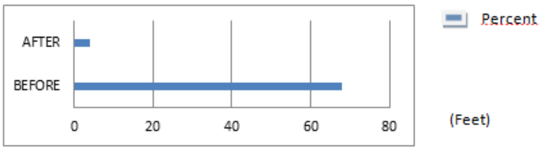

- The Travelling distance from cutting floor to production floor was 68 feet. After implementation the distance was reduced to 10 feet. Therefore reduction of distance from cutting floor to production floor is 85.3%.

5.7.2.2. Distance from Cutting floor to production floor:

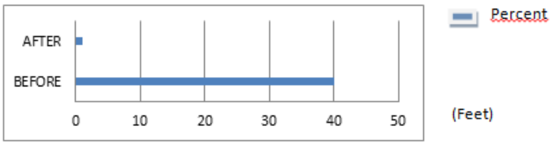

- The Travelling distance from production floor to inspection floor was 40 feet. After implementation the distance was reduced to 1 foot. Therefore reduction of distance from production floor to inspection floor is 97.5%.

5.7.2.3. Distance from Cutting floor to production floor:

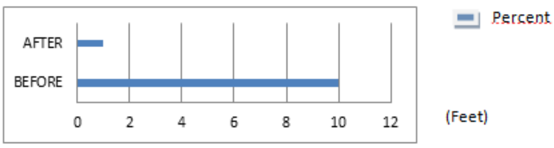

- The Travelling distance from inspection floor to packing floor was 10 feet. After implementation the distance was reduced to 1 foot. Therefore reduction of distance from inspection floor to packing floor is 90%.

5.7.3. Distance from Cutting floor to production floor:

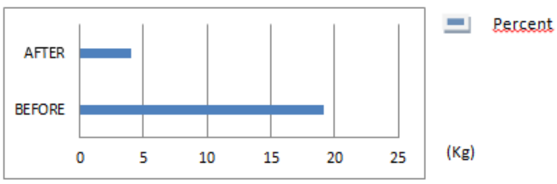

The load carrying capacity was 19.2 Kg. After implementation the capacity was reduced to 4 kg. Therefore the load carrying capacity is reduced to79.17%.

5.7.4. Production Rate

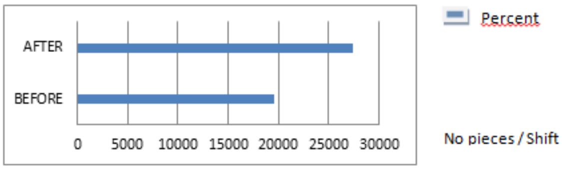

- At the earlier stage the production rate was19600 pieces/shift. After implementation the production rate was increased to 27440 pieces/shift. Therefore 40.0 % of production rate is increased.

5.7.5. Production Rate:

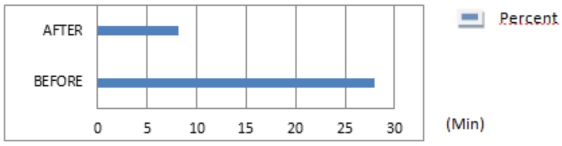

- In the existing state the time required for change of setup from one style to another was 28 minutes. Later it was reduced to 8 min 10 sec. Therefore the setup time percentage is reduced to 70.84.

6. Conclusion

Finally, this research has the proof of advantages when applying lean principles to the garment shop floor. According to our familiarity, it is the prime time that lean thinking has successfully implemented in the garment shop floor. We hope that this paper contains its worth for practitioners in the garment industries.

Due to increased customer expectations and severe global competition, the Indian garment industries try to increase productivity at lower cost and to produce with best product and service quality. Under these considerations, the authors have implemented lean manufacturing techniques to improve the process environment with reasonable investment. In this paper, the effectiveness of lean principles is substantiated in systematic manner with the help of various tools, such as Value Stream Maps and SMED.

Even though, the complete success of the application of lean thinking in the extensive run depends on close understanding between the management and shop floor personnel. Effective management information systems are required for instilling proper organizational values and continuous improvement programs. If these management principles are fully integrated with shop floor principles, then lean systems can be applied efficiently to attain the maximum output. The uneven supply base creates barriers in attaining integration between the links in supply chain. Therefore future studies can be made on supply chain management, to achieve good control, reliability and consistent performance.

References

[1] Womack.J. et al (1990), “The machine that changed the World” Rawson associates, newyork, NY.

[2] Lowe .J. et al (1997) “High- performance manufacturing evidence from the automotive components industry” Organization Studies, Vol. 18 No. 5, pp. 783-98.

[3] Oliver.N. et al (1996), :lean production practices international comparisons in the auto component industry” british journal of management, vol.7 special issue, pp. 529-44

[4] Shah,R and Ward, P.T., 2007 “defining of developing measure of lean production” Journal of operation management25, pp 785-805.

[5] Karlsson, C. and Ahlstrom, p., 1996. “Assessing changes towards lean production”, International Journal of Operation & Production management 16, pp. 24-41

[6] Nakamura, M., Sakakibara, S. and Schroeder, R., 1998. “Adoption of Just-In-Time manufacturing methods at US. – and Japanese Owned Plants: some empirical evidence”, IEEE transactions on engineering management 45, pp. 230-240.

[7] Schmidt.M. (2000), “Application of lean principles to an enterprise value stream; a lean analysis of an automotive fuel system development process” International Journal of Production Research, Vol. 15 No. 6, pp. 553-64.

[8] Kapuge, A.M. & Smith, M. (2007). Management Practices and Performance Reporting in the Sri Lankan Apparel Sector. *Managerial Auditing Journal*, 22 (3), 303-318.

[9] Mercado, G. (2007). *Question Garments- Ask the Lean Manufacturing Experts Applying Lean in the Garment Industry* Retrieved January 12, 2008, Thomas Publishing Company.

[10] Mazany, P. (1995). A Case Study- Lessons from the Progressive Implementation of Just-in-Time in a Small Knitwear. Manufacturer. *International Journal of Operations and Production Management,* 15, (5), 271-228.

[11] Farhana Ferdousi &Amir Ahmed(2009) An Investigation of Manufacturing Performance Improvement through Lean Production: A Study on Bangladeshi Garment Firms, international journal of business management, vol 4(9),106-116

[12] Jamal A.Farooquie, and Asit B. Mohapatra., 2009. “ Japanese Manufacturing Techniques and Practices : An Indian Perspective”. Jordan Journal of Mechanical and Industrial Engineering, pp. 174-181.

[13] Pavanskar .S.J., (2003) “Classification scheme for lean manufacturing tools” production and inventory management journal vol. 32 NO.3, pp. 5-11.

[14] Rother.M. and Shook.J (1999), “Learning to see value Stream Mapping to added value and eliminate muda” International Journal of Physical Distribution & Logistics Management, Vol. 30 No. 9, pp. 731-49.

[15] Mc Donald. J, Van Aken EM, Rentes. AF (2002)”utilizing simulation to enhance VSM: a manufacturing case application” Int I logist: Res Appl 5(2): 2(3-232).

[16] Pattanaik, L.N. and Sharma, B.P., 2009. “Implementation of Lean Manufacturing with Cellular Layout: a case study”. The International Journal of Advanced manufacturing Technology 42, pp. 772-779.

JJMIE

Volume 5, Number 6, Dec. 2011
ISSN 1995-6665
Pages 533 - 541

Jordan Journal of Mechanical and Industrial Engineering

Strengthening of Aluminum by SiC, Al2O3 and MgO

A.R.I. Kheder[a],G.S. Marahleh*[,a], D.M.K. Al-Jamea[a]

[a]Department of Mechanical Engineering, Faculty of Engineering Technology, Al-Balqa' Applied University, Jordan

Abstract

The objective of this experimental investigation is to produce a metal matrix composite (MMC) using pure aluminum as a base material reinforced with one of the following ceramic additives each time (alumina Al2O3, silicon carbide SiC, and magnesium oxide MgO) with different volume fractions. Liquid state mixing technique was employed for the different constituent. Temperature was checked frequently while mixing using a thermocouple. Degasser was added to the content of the composite while mixing to minimize gas bubbles at the final cast.After melting and mixing, melts were poured in metallic mould then we got a cast from which specimens for various tests were prepared. Complete mixing between the Al matrix and the additives was checked by taking specimens from different parts from the cast (from the upper middle and the upper edge, and from the middle, then from the lower middle and lower edge then subjected to microscopic observation. Microstructure examination and microanalysis were carried out using optical microscope and scanning electron microscope equipped with energy dispersive x-ray analysis, moreover tensile mechanical properties were determined in each case.The addition of SiC, MgO & Al2O3 particulates into the matrix alloy increased the yield strength, the ultimate tensile strength & the hardness, & decreased elongation (ductility) of the composites in comparison with those of the matrix. Increasing wt% of SiC, MgO & Al2O3 increased their strengthening effect but SiC is the most effective strengthening particulates, for higher strength, hardness, & grain size reduction. On the other hand, it decreases ductility & toughness.

Key words: Composite materials; Liquid state mixing; Mechanical properties; Microstructural examinations

1. Introduction

It is very important to study the composite materials because it is the material for advanced technology, high temperature application where high strength / stiffness to-weight ratio is required. Composite Technology combines the most important properties of the components together in order to obtain a material with overall properties suitable for the design of the engineering part required. So it is a technology where you can tailor the material for the purpose set up. Composite materials consist of two or more physically and / or chemically distinct phases, suitably arranged or distributed. It has the characteristics that are not depicted by any of its components in isolation. Generally the continuous phase is referred to as the matrix, while the distributed phase is called the reinforcement.

A lot of work was done in this subject for the last decades since the production advances was highly affected by composites where you can tailor material properties as you need by mixing two different materials without chemical reaction. Some of composites are of metallic matrices with ceramics additives to have what we call metal matrix composite (MMC), and some polymeric matrices (PMC) and others are of ceramic matrices (CMC).

Most of the studies on metal matrix composites (MMC) has focused on aluminum (Al) as the matrix metal. The combination of lightweight, environmental resistance and adequate mechanical properties has made Al and its alloys composites very popular. The melting point of aluminum is high enough to satisfy many application requirements, yet low enough to render composite processing reasonably convenient. It can accommodate a variety of reinforcing agents [1].

Particulate Al-MMCs are reinforced usually with SiC and Al2O3. Conventional processing methods include powder metallurgy and molten metal methods [1]. Discontinuous Al/SiC-MMC and Al/Al2O3-MMC have found widespread applications in aerospace, transport, military energy and electric industries, for example, they have been used in electronic packaging aerospace structures, aircraft and internal combustion engine components and a variety of recreational products [2-5].

A number of other reinforcing materials such as graphite, illite clay, Zirconia etc have been incorporated in Al using molten metal method. The basic limitation of this method is the poor wettability of ceramic particles with liquid Al alloys,[6-8]. Wettability can be defined as the ability of a liquid to spread on a solid surface, and it represents the extent of intimate contact between a liquid and a solid [24], and this enhances the tendency of reinforcement agglomeration. This represents a great challenge of producing cast metal matrix composites. This would normally result in poor distribution of the particles, high porosity content, and low mechanical properties. For that we need improve the wettability of matrix with additives. For improving wettability of SiC and Al2O3

* Corresponding author. e-mail: g_marahle@yahoo.com

studies proved a high efficiency of wettability improvement by addition of silicon or magnesium.

The retention & distribution of the particulates are very important in production of composites materials. MgO addition improves the retention and distribution of Al2O3 within the matrix [8],[9]. Stirring was useful to obtain a range of particulate percentages [10].

J. Hashim et al. studied the improvement of wettability by using clean SiC particles and magnesium as a wetting agent, and stirring continuously while the MMC slurry is solidifying were found to promote wettability of SiC with A359 matrix alloy. Decreasing this solidification time was also found to improve the wettability whereas increasing the volume fraction of SiC particles present will give the opposite effect [23].

Sajjad et al. employed a new method for uniform distribution of very fine SiC particles with average size of less than 3 μm was employed. The key idea was to allow for gradual in situ release of properly wetted SiC particles in the liquid metal. For this purpose, SiC particles were injected into the melt in three different forms, i.e., untreated SiCp, milled particulate Al–SiCp composite powder, and milled particulate Al–SiCp–Mg composite powder. The resultant composite slurries were then cast from either fully liquid (stir casting) or semisolid (compocasting) state. Consequently, the effects of the casting method and the type of the injected powder on the microstructural characteristics as well as the mechanical properties of the cast composites were investigated. The results showed that the distribution of SiC particles in the matrix and the porosity content of the composites were greatly improved by injecting milled composite powders instead of untreated-SiC particles into the melt. Casting from semisolid state instead of fully liquid state had similar effects. The average size of SiC particles incorporated into the matrix was also significantly reduced from about 8 to 3 μm by injecting milled composite powders. The ultimate tensile strength, yield strength and elongation of Al356/5 vol.%SiCp composite manufactured by compocasting of the (Al–SiCp–Mg)cp injected melt were increased by 90%, 103% and 135%, respectively, compared to those of the composite manufactured by stir casting of the untreated-SiCp injected melt [25].

W. Zhou et al. studied a composites based on two aluminum alloys (A536 and 6061) reinforced with 10% or 20% volume fraction of SiC particles were produced by gravity casting and a novel two-step mixing method was applied successfully to improve the wettability and distribution of the particles. The SiC particles were observed to be located predominantly in the inter-dendrite regions, and a thermal lag model is proposed to explain the concentration of particles [21].

K. R. Suresh et al. studied tensile and wear properties of aluminum composites fabricated by squeeze casting method and checked uniform particulate distribution. The squeeze cast composites show peak strength of 216 MPa showing an increase of 11.6% in tensile strength. The new composites also have improved wear resistance when compared to gravity cast composites. [22]

Elimination of casting defects such as pores and non-uniform distribution of the particulates is essential in improving the properties of the composite materials [10], [11].

The matrix should bond strongly with the reinforcement but should not be chemically affected by adverse reactions. Proper matrix and reinforcement selection will promote part formability by various processes [13].

Reinforcement, as either continuous or discontinuous may constitute 10 to 60 vol % of the composite [14].

The aim of this study was to investigate the production of Al-MMC using a modified liquid state mixing called stir casting method. The technique was examined by employing the ceramic particulates of SiC, Al2O3 and MgO to aluminum in the liquid state where heating temperature and casting temperature was determined after some trials to achieve two targets:

- High enough to add the additives and mix it properly and then cast before the aluminum starts to solidify.
- Not too high so that it may burn the most of the additives before mixing them with the matrix and not to take a lot of time to solidify after casting so that the particulates may settle in the bottom of the mould due to gravity.

After mixing properly and casting, specimens subjected to various mechanical tests and micro-structural observation.

2. Experimental Procedure

Melting was carried out in an electric resistance furnace and heated to the temperature of 900ºC (220°C higher than melting point of Al). This temperature was found convenient to compensate for the temperature drop during transferring the crucible and mixing the particulates. It was determined after making many trails at various temperatures. The ceramic particles were heated to 300˚C before addition into the molten Al to avoid high drop of temperature just after addition of particulates in case of adding them in the cold state. It found that it gives time for impeller to stir the mixture & cast the aluminum before solidifying.

As reinforcement particulates, the following ceramic powders were added into the molten Al after separating a particle size using cylinder mill grinding and sieving:

- SiC powder of 50 μm particle size.
- Al2O3 powder of 60 μm particle size.
- MgO powder of 50 μm particle size.

Before addition of Al2O3 or SiC, the furnace was opened & 10 wt %Si was added to the melt & stirred then furnace was closed & reheated to 900°C, where Si addition was not needed for MgO addition due to its high wettability with aluminum. After addition of particulates with different constituents for each cast stirring process was employed to make the ceramic powders uniformly dispersed through the matrix (the liquid Al) before casting into the metallic mould. The apparatus used during the composite mixing are shown in schematic figure 1 which consists of: a drilling machine, a steel rod fixed to the drill grip welded from the other side to a steel impeller to be inserted in the graphite crucible containing the liquid aluminum through a hole in the center of the steel cover that was added to avoid splashing of the liquid metal during the impeller rotation while mixing. Also, we needed a stand of a steel plate to hold the graphite crucible firmly on the table of the drilling machine during mixing. Operating the drill at 450 RPM for mixing, where the temperature of the melt during mixing was monitored by a thermocouple every minute until temperature becomes 700°C, then the degassing powder was added to remove gasses from the melt & stirred for seconds then cast carefully in a metallic mould of dimensions (15x8x1cm) ensuring that it is completely full. After 10 min cooling the mould was opened. Details of the melts are shown in table 1.

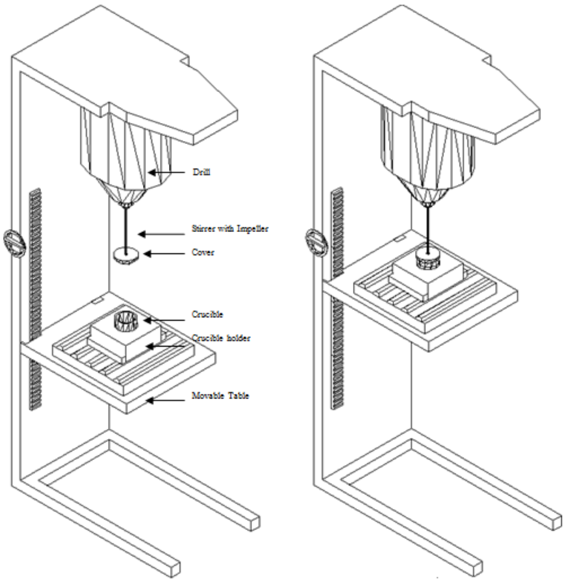

Figure 1: Schematic presentation of mixing process.

Table 1: Specimens groups & their constituents.

Melt number	Alloy
1	Al Pure
2	Al- 10 wt% Si, 5.0 wt %SiC
3	Al- 10 wt% Si, 7.5 wt %SiC
4	Al- 10 wt% Si, 10.0 wt %SiC
5	Al- 10 wt% Si, 15 wt %SiC
6	Al- 10 wt% Si, 20 wt %SiC
7	Al- 5 wt %MgO
8	Al- 10 wt %MgO
9	Al- 15 wt %MgO
10	Al- 20 wt %MgO
11	Al- 10 wt% Si, 5.0 wt %Al_2O_3
12	Al- 10 wt% Si, 10.0 wt %Al_2O_3
13	Al- 10 wt% Si, 15.0 wt %Al_2O_3
14	Al- 10 wt% Si, 20 wt %Al_2O_3

Specimens for various tests were prepared from each melt. For microstructure observations, the constitutional metallographic technique was utilized. The volume fractions of the particulates and their distribution, and the grain size of the Al matrix were determined.

For tensile test samples was prepared according to ASTM-E8-95a and impact test samples were prepared according to the ASTM E23.

Chemical analysis of the samples was done using EDX system attached to SEM, Model XL-30W/TMP Philips.

3. Results and Discussion

3.1. Mechanical properties:

3.1.1. Tensile test:

All tensile tests were carried out on Universal Tensile Testing Machine (Dartic). Figures 2, 3, and 4 show the stress-strain curves for various composites studied in this work. These curves are shown from load-elongation curves obtained from the tensile testing machine.

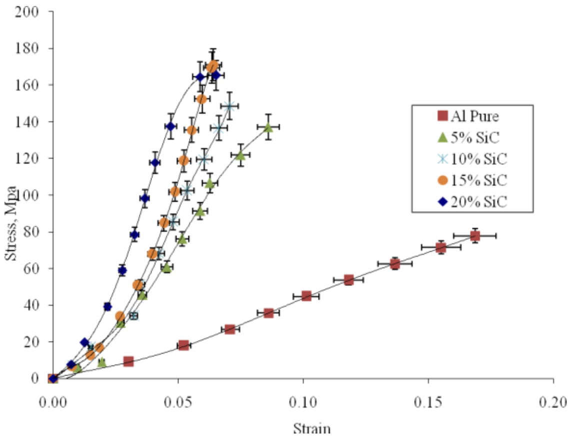

Figure 2: Stress strain diagrams for Al-SiC MMC.

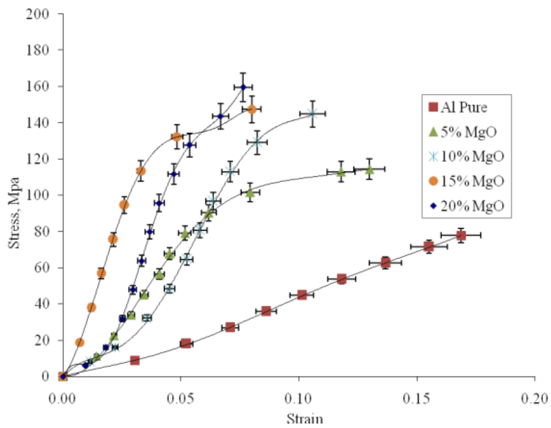

Figure 3: Stress strain diagrams for Al-MgO MMC.

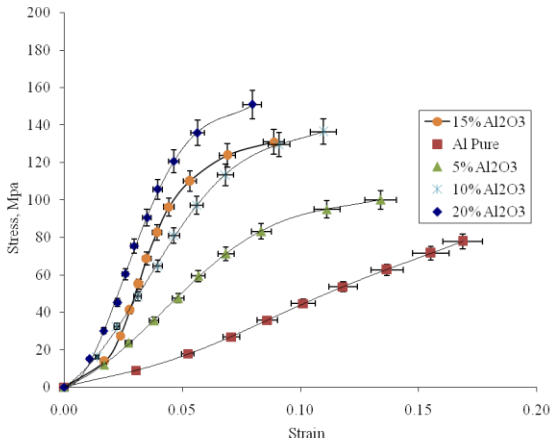

Figure 4: Stress strain diagrams for Al-Al2O3 MMC.

To show the effect of various ceramic particulates at different percentages on the ultimate tensile strengths (UTS), figure 5 was drawn for comparison. The results show that the UTS increase in all cases with increasing wt% of the ceramic particulates, the largest increase being in Al-SiC MMC, and the least being in Al-Al2O3 MMC. These results indicate the effectiveness of the particulates in strengthening of the Al.

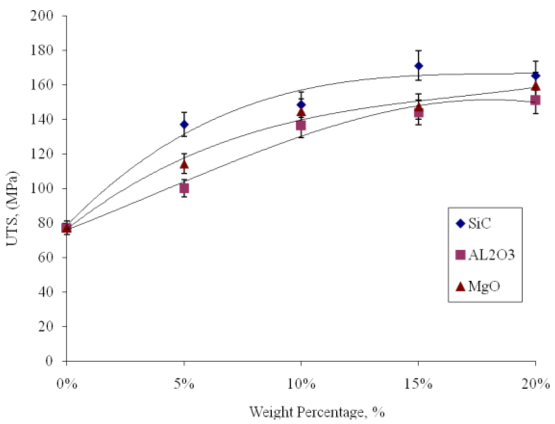

Figure 5: Ultimate tensile strength vs. particulate weight percentage.

The UTS of the composites represent an increase of 121%, 108% and 92% over the corresponding values of the as cast pure Al at ambient temperature for Al-SiC, Al-Al2O3 and Al-MgO respectively.

The increase in UTS of the composites is accompanied by a decrease in strains (ductility) with increasing wt% of the ceramic particulates. The lowest strain was observed in case of Al-SiC MMC, as shown in figure 6. So the retention of the particulates confers an overall embrittling effect on the composites. The increase of UTS of the composites over the pure Al matrix can be related to the interaction between the particulates and dislocations within the matrix, and to the grain refinement of Al with increasing addition of the particulates.

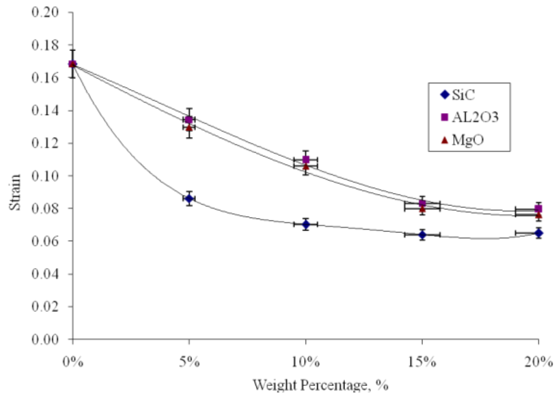

Figure 6: Strain vs. particulate weight percentage.

3.1.2. Impact test:

Figure 7 shows the variation of the impact strengths (ak) in Joules (J) for various Al-MMCs with different wt% of the particulates. The results show that the ak value for Al-Al2O3 and Al-MgO MMCs increase slightly in general by increasing wt% of the particulates while in case of Al-SiC MMC the ak decreased slightly by increasing wt% of SiC particulates.

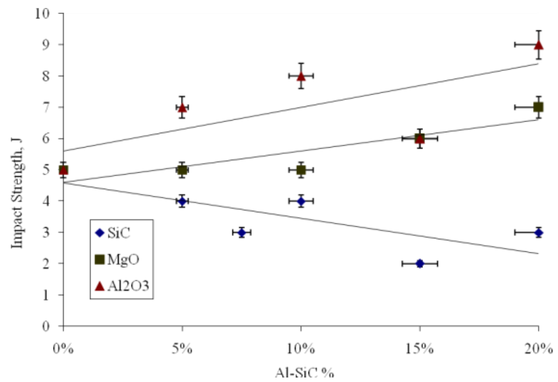

Figure 7: Impact strength vs. particulate weight percentage.

3.1.3. Hardness test:

The results of the Brinell hardness measurements are shown in figure 8. It increases with increasing wt% of the particulates used in this work. These increases can be related -as mentioned before- to the interaction of the dislocations with the particulates and grain refinement with increasing wt% of the particulates.

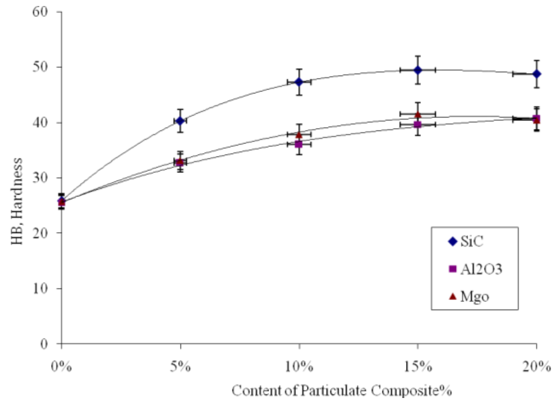

Figure 8: Brinell hardness vs. particulate weight percentage.

3.2. Microstructure:

Optical microscope was utilized to determine the particulate volume fractions (Vf), their distribution in the casting and the grain size of the Al matrix. 1 mm square grid attached to the eye piece of the microscope at a magnification of x50 was used for Vf determination [16]. Vf was calculated from various parts of the cast and the results are shown in table 2. The results indicate that the Vf across the casting, horizontally and vertically are quite uniform at various parts of the cast, and the variation of Vf in horizontal direction is less than that in vertical direction as shown in figures 9 and 10. These results indicate that the method used in the composite preparation was successful and this was reflected in the morphology and relatively uniform distribution of the particulates within the matrix as shown in figures.

Table 2: The volume fraction of different constituents through the specimen horizontally & longitudinally.

	Optimal	Up Edge	Up Center	Mid Edge	Mid Center	Low Edge	Low Center
Al Pure	5.00%	4.41%	4.28%	4.17%	4.20%	3.68%	3.64%
Al-10 wt% Si, 5.0 wt %SiC	7.50%	6.60%	6.47%	6.29%	6.32%	5.81%	5.88%
Al-10 wt% Si, 7.5 wt %SiC	10.00%	8.77%	8.66%	8.29%	8.32%	7.53%	7.35%
Al-10 wt% Si, 10.0 wt %SiC	15.00%	13.35%	13.08%	12.55%	12.59%	11.17%	11.50%
Al-10 wt% Si, 15 wt %SiC	20.00%	17.53%	17.09%	16.81%	16.84%	15.77%	15.14%
Al-10 wt% Si, 20 wt %SiC	5.00%	4.47%	4.34%	4.13%	4.16%	3.88%	4.04%
Al-5 wt %MgO	10.00%	8.87%	8.57%	8.41%	8.45%	7.98%	7.65%
Al-10 wt %MgO	15.00%	13.15%	12.97%	12.47%	12.51%	11.70%	11.80%
Al-15 wt %MgO	20.00%	17.67%	17.47%	16.66%	16.71%	15.37%	15.89%
Al-20wt %MgO	5.00%	4.45%	4.35%	4.17%	4.17%	3.64%	3.77%
Al-10wt% Si, 5.0wt%Al_2O_3	10.00%	8.95%	8.67%	8.47%	8.47%	7.35%	7.45%
Al-10wt% Si, 10.0wt%Al_2O_3	15.00%	13.13%	12.77%	12.43%	12.43%	11.34%	11.66%
Al-10wt% Si, 15.0wt %Al_2O_3	20.00%	17.51%	17.44%	16.66%	16.66%	14.92%	15.74%
Al-10wt% Si 20.0wt %Al_2O_3	20.00%	17.67%	17.47%	16.66%	16.71%	15.37%	15.89%

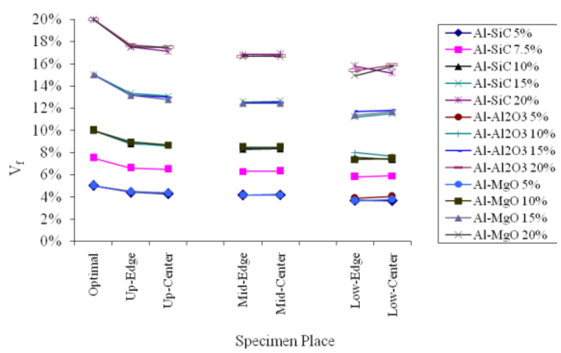

Figure 9: Longitudinal variation of V_f.

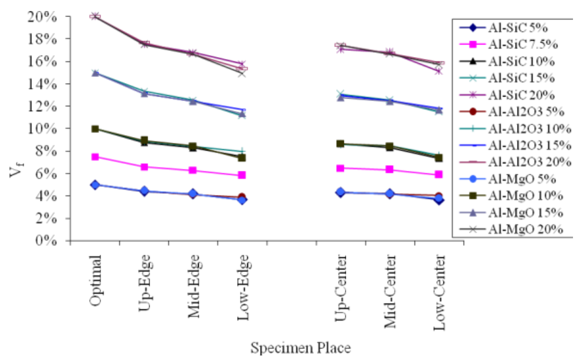

Figure 10: Horizontal variation of V_f.

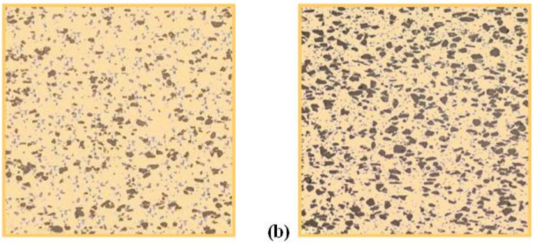
(a) (b)

Figure 11: Photographs of MMCs microstructure at X50; (a) Al-10%SiC, (b) Al -20% SiC.

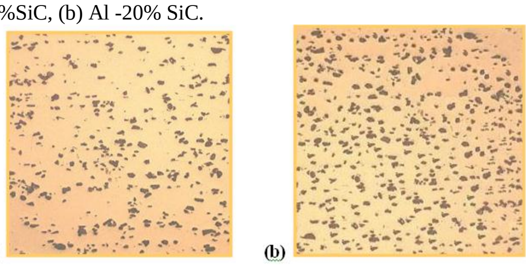
(a) (b)

Figure 12: Photographs of MMCs microstructure at X50; (a) Al-10% Al2O3, (b) Al-20% Al2O3.

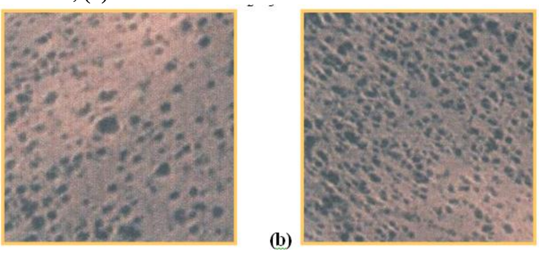
(a) (b)

Figure 13: Photographs of MMCs microstructure at X50; (a) Al-10%MgO, (b) Al-20%MgO.

The grain size of the Al matrix was measured by mean lineal intercept method from the same specimens used for V_f determination. The average grain sizes are given in table 3.

Table 3: The average grain size measured for MMCs.

Alloy	Average Grain Size (μm)
Al_{Pure}	897
Al- 10 wt% Si, 5.0 wt %SiC	107
Al- 10 wt% Si, 7.5 wt %SiC	108
Al- 10 wt% Si, 10.0 wt %SiC	74
Al- 10 wt% Si, 15 wt %SiC	59
Al- 10 wt% Si, 20 wt %SiC	57
Al- 5 wt %MgO	158
Al- 10 wt %MgO	116
Al- 15 wt %MgO	91
Al- 20 wt %MgO	77
Al- 10 wt% Si, 5.0 wt %Al_2O_3	179
Al- 10 wt% Si, 10.0 wt % Al_2O_3	124
Al- 10 wt% Si, 15.0 wt % Al_2O_3	91
Al- 10 wt% Si, 20.0 wt % Al_2O_3	86

The average grain size for pure Al in as-cast condition was 897 μm. Addition of the particulates decreased the grain size at rates shown in table 4. the largest decrease was noticed at initial additions of the particulates, namely at 5 wt% in all cases, then the decrease was tapered and at 20 wt% particulate additions the grain sizes were almost constant. The composite grain sizes are finer than that of the monolithic matrix. This refinement is caused by the ceramic particulates acting as nuclei for the grain formation during solidification and at the same time these particulates would inhibit the processes of the grain growth [17]. The greatest effect in refining the grain size was in case of the SiC MMC. Similar observation was seen by [18] where 20% Al_2O_3 addition produced 90% reduction in the grain size of the composite.

Table 4: Average grain size reduction with increasing different particulate percentages.

Particles / %	SiC	Al_2O_3	MgO
5%	88%	82%	86%
10%	31%	27%	33%
15%	20%	22%	27%
20%	3%	15%	5%

3.3. Effect of Si:

During the fabrication of Al-SiC composite the major problem is the formation of the Al_4C_3 phase at the SiC/Al interface, because the SiC is thermodynamically unstable in the Al melt. This brittle reactant Al_4C_3 forms agglomerates at the interface leading to degradation of the composite strength, modulus and corrosion [19],[20]. In this research work, Si was added to the composite to prevent the formation of Al_4C_3 reactant. The results of the tensile test confirm this statement, although the strains and impact values for Al/SiC are lower than those for Al/Al_2O_3 and Al/MgO by a small amount as shown in figures 14 and 15 respectively. In general, Si addition reduces the melting point of the alloy, until the eutectic composition of 12.3%Si is reached. This Si addition will increase the fluidity and decrease the viscosity thus enhancing the wettability of the particles which will have positive affect on the particulate distribution and hence on the mechanical properties.

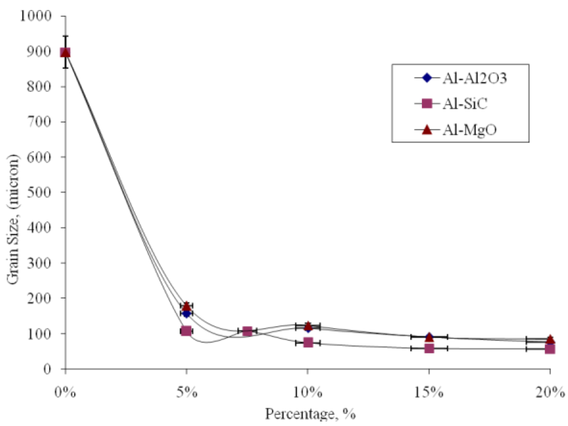

Figure 14: Average grain size of Al-MMCs Al-Si-SiC, Al-Si-Al2O3, & Al-MgO.

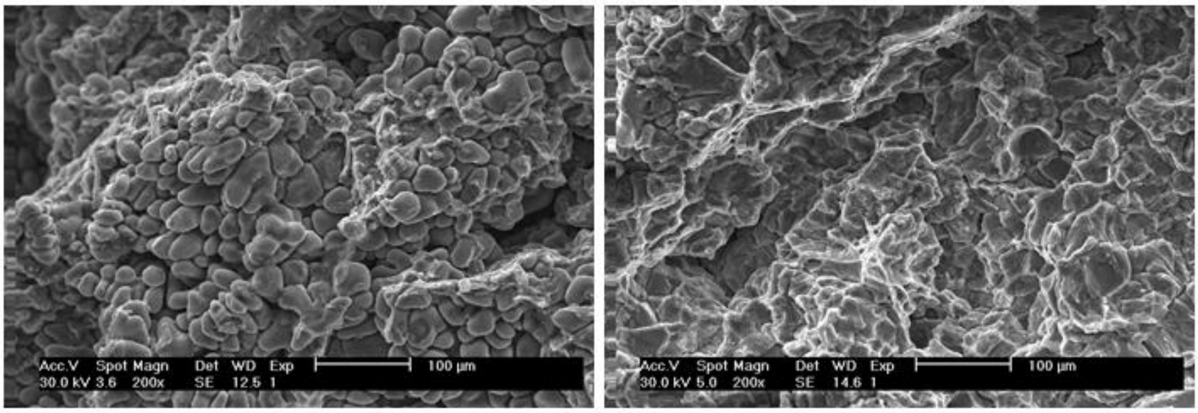

(a) (b)

Figure 15: SEM fracture surfaces of pure Al at X200. (a) Tensile. (b) Impact.

3.4. Fractography:

SEM observations of fractured matrix of pure aluminum is shown in figure 15. The fractured surface consists of dimpled morphology, revealing ductile fracture of the matrix. However, the fracture surface of the composites reinforced with SiC, Al2O3, and MgO particulates essentially consist of a bimodal distribution of dimples, as shown in figure 16, 17, and 18. The micrographs are for 20 wt% of each particulate. The dimples of large sizes are associated with the particulates and the smaller ones are associated with ductile fracture of the matrix.

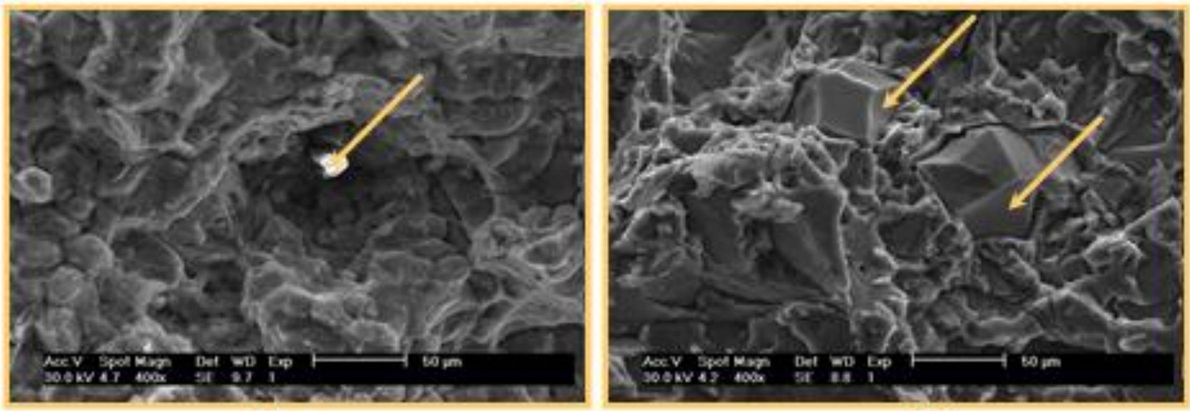

(a) (b)

Figure 16: SEM fracture surfaces of Al-20%SiC MMCs at X400. (a) Tensile. (b) Impact.

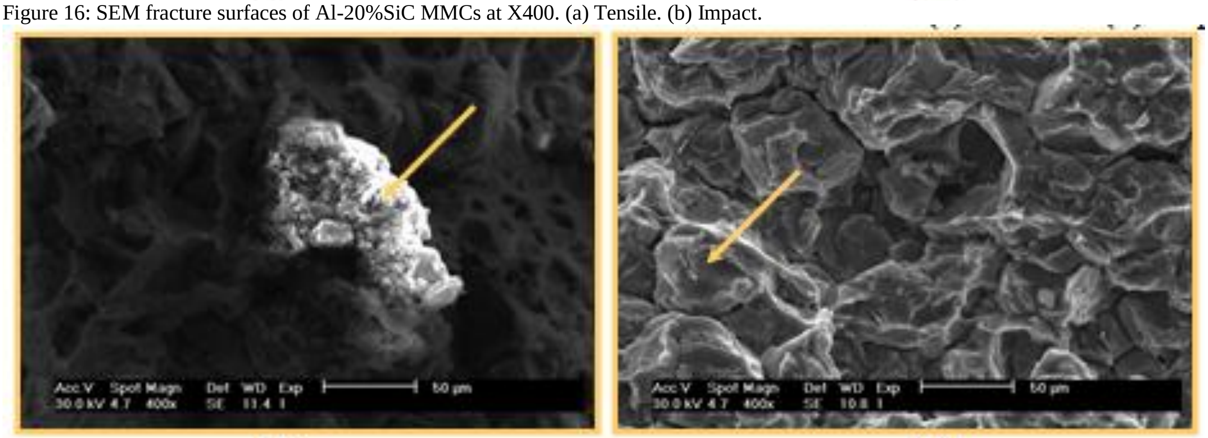

(a) (b)

Figure 17: SEM fracture surfaces of Al-20%Al2O3 MMCs at X400. (a) Tensile. (b) Impact.

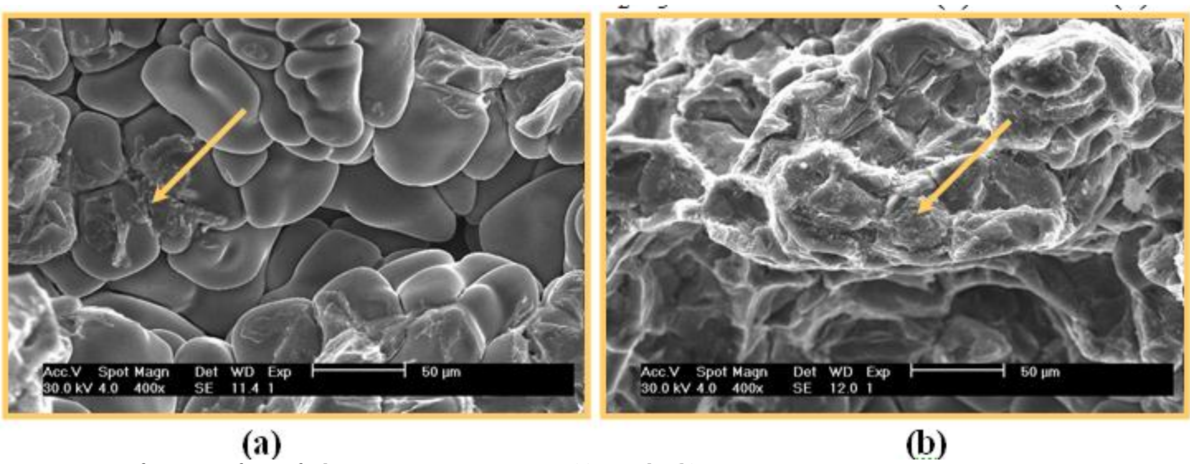

Figure 18: SEM fracture surfaces of Al-20%MgO MMCs at X400. (a) Tensile. (b) Impact.

In most cases the fracture surfaces of the particulates show smooth surfaces indicating that the particulate has fractured rather than decohered, which means that high interfacial strengths dominate in these composites and the composites failed through particulate fracture and matrix ligament rupture, similar observations were reported in the work [17].

4. Conclusion

Addition of SiC, MgO & Al2O3 individually at different percentages to aluminum matrix composite resulted in the following:

- High reduction in grain size of MMCs compared with grain size of the matrix before particulate addition. It is affected by the presence of the particulates in the matrix alloy where they act as grain nucleation cites.
- The addition of SiC, MgO & Al2O3 particulates into the matrix alloy significantly increases the yield strength, the ultimate tensile strength & the hardness, & decreases elongation (ductility) of the composites in comparison with those of the matrix alloy.
- The improvement of mechanical properties by particulate addition & homogeneous distribution depends on wettability of particles with matrix & homogeneous distribution.
- Si addition to matrix before SiC & Al2O3 addition improved wettability & facilitated homogeneous distribution.
- Increasing wt% of SiC, MgO & Al2O3 increases their strengthening effect but SiC is the most effective strengthening particulates, for higher strength, hardness, & grain size reduction. On the other hand, it decreases ductility & toughness.
- The composite reinforced with SiC, Al2O3 & MgO particulates failed mainly through particulate decohesion followed by ductile failure of the matrix, although in some cases particulate fracture was observed.
- One of the important application for Al-SiC and Al-Al2O3 MMC in internal combustion engine, like piston crown, cylinder liners where alumina & carbon fiber reinforced aluminum have proved a good substitute for cast iron.
- Al-MgO MMC have many applications in structural and industrial purposes, where light weight and high strength-to-weight is needed.

5. Recommendations

Some of the worthwhile investigating parameters:

- Study the effect of stirring speed, stirring time & mixing impeller angle on MMC's homogeneity & mechanical properties. Stirring speed allows vortex formation, & hence penetration of air to the melt increasing oxidation, where low speed decreases stirring efficiency in mixing.
- Study the effect of degasser amount addition on MMC's mechanical properties may be studied.
- The effect of addition of more than one additive on MMC's mechanical properties.
- Study the effect of application of secondary plastic deformation process on the mechanical properties.

References

[1] Davis, J.R., "Aluminum Matrix Composites, ASM specialty hand book: Aluminum & Aluminum Alloy", ASM International, P. 160-179, (1993).

[2] Smale, M.D., "The Mechanical Properties of Squeeze Cast Diesel Pistons", P. 29, (1985).

[3] Folgar, F., "Fiber FP / Metal Matrix Composite Connecting Rods", Volume 9, (Number 7-8), P. 561, (1988).

[4] Dinwoodie, J., "Automotive Applications for MMCs based on Shot Stample Aluminum Fibers", (1987).

[5] Pandey, Awadh B., "Metallic Matrices. ASM Handbook: Composites", 1(21), 150-160. (2001).

[6] Kaye, S., J. Vac. Sci. Technol. 11, 1114 (1974).

[7] Biswas, S., Srinivasa, U., Seshan, S. & Rohatgi, P.K., Trans. Amer. Foundrymen Soc. (1980), P. 159.

[8] Abdul-Lattif, N.I., Kheder, A.R.I. & Goel, S.K., J. Materials Science, 22 (1985), P. 466-472.

[9] Mcevoy, A.J., Williams, R.H. & Higginbotham, L.G., J. Materials Science, 11 (1976), P. 297.

[10] Lioyd, D.J., Composite Science Technology, vol. 35 (1989) pp. 159-179.

[11] Zhu, Z., “Cast Reinforced Metal Composites”, ASM Intl. Metal Park, OH, USA, 1988, PP. 93-100.

[12] K. R. Suresh, H. B. Niranjan, P.Martin Jebaraj and M. P. Chowdiah, "Tensile and wear properties of aluminum composites", 14th International Conference on Wear of Materials, Volume 255, 2003, Pages 638-642.

[13] Zaid, A.I.O., "Role of Manufacturing Process Parameters on the Characteristics of Aluminum Metal Matrix Composites AL-MCC". Proc. 8th International Symposium on Advanced Materials. ISAM-2003, Islamabad, Pakistan, (2003).

[14] Foltz, J.V. & Blackmon, C.M., Metal-Matrix Composites. ASM Handbook: Composites, 1(21), 903-912. (2001)

[15] The Principles of Materials Selection for Engineering Design, Pat l. Mangonon, prentice hall, 1999.

[16] Huang, Y.D., Froyen, L., Wevers, M., "Quality Control & Nondestructive Tests in Metal Matrix Composites, MMC-Assess Consortium", Thematic Network, Institute of Materials Science & Testing-Vienna Uni. of Technology MMC-Assess, 2000, vol. 5.

[17] Daoud, A., El-Bitar, T. and Abd El-Azim, A.N., "Tensile properties & fracture behavior of rolled Al5Mg-Al2O3 or Graphite Particulate Composites", International Conference on Production Engineering, Design & Control, P. 1405 (1999).

[18] Momani, L.M., Z.Kilani, A, "Effect of Grain Refiner Addition on the Mechanical Behavior and Wear Resistance of Al-Al oxide MMC", Jordan University, 2004.

[19] Luo, Z.P., "Crystallography of SiC/MgAl4C3/Al Interfaces in Pre-oxidized SiC Reinforced Al/SiC Composite", Acta Materialia, vol. 54, Issue I, 2006.

[20] Bowen Xiong, Qingsong Yan, Baiping Lu, Changchun Cai, "Effects of SiC Volume Fraction and Aluminum Particulate Size on Interfacial Reactions in SiC Nano-Particulate Reinforced Aluminum Matrix Composites", Journal of Alloys and Compounds, Volume 509, 2011, Pages 1187-1191

[21] W. Zhou and Z.M. Xu. , "Survey on wetting of SiC by molten metals", Ceramics International, volume 36, (2010) 1177–1188.

[22] S. Naher, D. Brabazon, and L. Looney, "Computational and experimental analysis of particulate distribution during Al–SiC MMC fabrication", Composites: Part A 38 , (2007), Pages 719–729.

[23] J. Hashim, L. Looney and M. S. J. Hashmi, "The enhancement of wettability of SiC particles in cast aluminum matrix composites", Journal of Materials Processing, Volume 119, (2001), Pages 329-335.

[24] K. Nogi, "The role of wettability in metal–ceramic joining", Scripta Materialia, Volume 62, (2010), Pages 945-948.

[25] Sajjad Amirkhanlou and Behzad Niroumand, "Development of Al356/SiCp cast composites by injection of SiCp containing composite powders", Materials & Design, Volume 32, 2011, Pages 1895-1902, Iran.

[26] Yoshihiro Hirata, Naoto Suzue, Naoki Matsunaga and Soichiro Sameshima, "Particle size effect of starting SiC on processing, microstructures and mechanical properties of liquid phase-sintered SiC", Journal of the European Ceramic Society, Volume 30, (2010), Pages 1945-1954.

JJMIE

Volume 5 , Number 6, Dec. 2011
ISSN 1995-6665
Pages 543 - 551

Jordan Journal of Mechanical and Industrial Engineering

Supplier Evaluation Using Fuzzy Analytical Network Process and Fussy TOPSIS

Sarojini Jajimoggala*[,a], V.V.S.Kesava Rao[b], Satyanaraya Beela[b]

[a] Department of Mechanical Engineering, GITAM Institute of Technology,GITAM University,Visakhapatnam-530 045, India.
[b] Department of Mechanical Engineering, College of Engineering, Andhra University, Visakhapatnam 530 002, India

Abstract

Supplier selection, which is the first step of the activities in the product realization process starting from the purchasing of material till to the end of delivering the products, is evaluated as a critical factor for the companies desiring to be successful in nowadays competition conditions. With the scope of this paper, supplier selection was considered as a multi criteria decision problem and its complexity is further aggravated if the highly important interdependence among the selection criteria is taken into consideration. The objective of this paper is to suggest a comprehensive decision method for identifying top suppliers by considering the effects of interdependence among the selection criteria. Proposed in this study is a hybrid model, which incorporates the technique of Analytic Network Process (ANP) in which fuzzy triangular priority weights using logarithmic least square method, Technique for Order Performance by Similarity to Ideal Solution (TOPSIS) is adopted to rank competing suppliers in terms of their overall performances. An example is solved to illustrate the effectiveness and feasibility of the suggested model also identified the most potential supplier.

Keywords: Supplier selection; Multiple criteria decision-making (MCDM); Fuzzy Analytic Network Process (FANP); Fuzzy Technique for Order Performance by Similarity to Ideal Solution (FTOPSIS); Logarithmic Least Square Method (LLSM)

1. Introduction

Due to the ever-mounting global competition, supplier management has come to play an increasingly crucial role as a key to business success. To secure competitive advantages, organizations have to integrate their internal core competencies and capabilities with those of their suppliers. How to choose capable suppliers is thus an imperative issue in the management of modern business organizations. Existing researches in the field of supplier selection can be divided into two major categories: those focusing on isolating different supply source selection criteria and assessing the degree of their importance from the purchasing firm's point of view [1]; and those aiming to identify different alternative suppliers by developing and applying specific methods, such as cluster analysis [2], case based reasoning systems [3], statistical models [1], decision support systems [1, 3], data envelopment analysis [2, 4, 5], analytic hierarchy process [2, 6], total cost of ownership models [2, 7], activity based costing [8], artificial intelligence [2, 3], and mathematical programming [9, 5, 10].

Some of the above methods tend to treat each of the selection criteria and alternative suppliers as an independent entity. Price and quality, for example, are treated as two separate criteria without affecting each other. This is, however, seldom the case in the real world business context in which selection criteria and alternative suppliers are in fact characterized by interdependence. Analytic network process (ANP) can therefore be adopted to accommodate the concern of interdependence among selection criteria or alternatives.

The traditional ANP requires crisp judgments. However due to the complexity and uncertainty involved in real world decision problems, a decision maker(DM) may sometimes feel more confident to provide fuzzy judgments than crisp comparisons. This makes fuzzy logic a more natural approach to this kind of problems.

A number of methods have been developed to handle fuzzy comparison matrices. Van Laarhoven and Pedrycz [11] suggested a fuzzy logarithmic least squares method (LLSM) to obtain triangular fuzzy weights from a triangular fuzzy comparison matrix. Wang et al. [12] presented a modified fuzzy LLSM. Buckley [13] utilized the geometric mean method to calculate fuzzy weights. Chang [14] proposed an extent analysis method, which derives crisp weights for fuzzy comparison matrices. Xu[15] brought forward a fuzzy least squares priority method(LSM). Mikhailov[16] developed a fuzzy preference programming method (PPM), which also derives crisp weights from fuzzy comparison matrices. Csutora and Buckley [17] came up with a Lambda-Max method, which is the direct fuzzification of the well-known kmax method.

Among the above approaches, the extent analysis method has been employed in quite a number of applications [18-35] due to its computational simplicity. Shin-ichi Ohnishi [36] proposed fuzzy representation of

Corresponding Author email: sarojini.jaji@gmail.com

criteria weights in order to reduce inconsistency in pairwise comparison matrix. Y-M. Wang [37] showed by examples that the priority vectors determined by the extent analysis method do not represent the relative importance of decision criteria or alternatives and that the misapplication of the extent analysis method to fuzzy AHP problems may lead to a wrong decision to be made and some useful decision information such as decision criteria and fuzzy comparison matrices not to be considered. In this work, modified fuzzy LLSM [12] is used to estimate the fuzzy priority weights in ANP.

The technique for order performance by similarity to ideal solution (TOPSIS) [38] is a widely accepted multi attribute decision-making technique due to its sound logic, simultaneous consideration of the ideal and the anti-ideal solutions, and easily programmable computation procedure [39]. This technique is based on the concept that the ideal alternative has the best level for all attributes, whereas the negative ideal is the one with all the worst attribute values. In fuzzy TOPSIS, attribute values are represented by fuzzy numbers. Using this method, the DM's fuzzy assignments with different rating viewpoints and the trade-offs among different criteria are considered in the aggregation procedure to ensure more accurate decision-making.

The objective of this paper is to suggest a comprehensive decision method for identifying top suppliers by considering the effects of interdependence among the selection criteria. The proposed method accordingly incorporates two stages: (i) Prioritizing criteria using FANP, where fuzzy triangular priority weights are obtained using modified logarithmic least square method (ii) Applying FTOPSIS for ranking of suppliers based on priority weights derived and to find the best supplier.

2. The ANP

The ANP is the most comprehensive framework for the analysis of corporate decisions. It allows both interaction and feedback within clusters of elements (inner dependence) and between clusters (outer dependence). Such feedback best captures the complex effects of interplay in human society, especially when risk and uncertainty are involved. The elements in a cluster may influence other elements in the same cluster and those in other clusters with respect to each of several properties. The main object is to determine the overall influence of all the elements. In that case, first of all properties or criteria must be organized and they must be prioritized in the framework of a control hierarchy. Then the comparisons must be performed and synthesized to obtain the priorities of these properties. Additionally, the influence of elements in the feedback system with respect to each of these properties must be derived. Finally, the resulting influences must be weighted by the importance of the properties and added to obtain the overall influence of each element [40, 41].

The modeling process can be divided into three steps for the ease of understanding which are described as follows:

2.1. Step I: the pairwise comparisons and relative weight estimation:

The pairwise comparisons and relative weight estimation before performing the pairwise comparisons, all criteria and clusters compared are linked to each other. There are three types of connections, namely one-way, two-way and loop. If there is only one-way connection between two clusters, only one-way dependencies exist and such a situation is represented with directed rows. If there is a two-way dependence between two clusters, bidirected arrows are used. Loop connections indicate the comparisons in a cluster and inner dependence. The pairwise comparisons are made depending on the 1–9 scale recommended by Thomas L. Saaty, where 1, 3, 5, 7 and 9 indicate equal importance, moderate importance, strong importance, very strong importance and extreme importance, respectively, and 2, 4, 6 and 8 are used for compromise between the above values. The score of a_{ij} in the pairwise comparison matrix represents the relative importance of the component on row (i) over the component on column (j), i.e., $a_{ij} = w_i/w_j$. The reciprocal value of the expression ($1/a_{ij}$) is used when the component j is more important than the component i. If there are n components to be compared, the matrix A is defined as

$$A = \begin{bmatrix} w_1/w_1 & w_1/w_2 \dots\dots & w_1/w_n \\ w_2/w_1 & w_2/w_2 \dots\dots & w_2/w_n \\ \vdots & \vdots \cdots \dots\dots & \vdots \\ w_n/w_1 & w_n/w_2 \dots\dots & w_n/w_n \end{bmatrix} = \begin{bmatrix} 1 & a_{12} & \cdots & a_{1n} \\ 1/a_{12} & 1 & \cdots & a_{2n} \\ \vdots & \vdots & \vdots & \vdots \\ 1/a_{1n} & 1/a_{2n} & \dots & 1 \end{bmatrix} \quad (1)$$

Once the pairwise comparisons are completed, like the AHP, a local priority vector (eigenvector) w is computed as an estimate of the relative importance accompanied by the elements being compared by solving the following equation:

$$Aw = \lambda_{max} w \quad (2)$$

where λ_{max} is the largest eigenvalue of matrix A.

Table 1: Linguistic variables describing weights of the criteria and values of ratings.

Linguistic scale	Triangular fuzzy scale	Triangular fuzzy reciprocal scale
Just equal	(1, 1, 1)	(1, 1, 1)
Equally important	(1/2, 1, 3/2)	(2/3, 1, 2)
Weakly important	(1, 3/2, 2)	(1/2, 2/3, 1)
Strongly more important	(3/2, 2, 5/2)	(2/5, 1/2, 2/3)
Very strong more important	(2, 5/2, 3)	(1/3, 2/5, 1/2)
Absolutely more important	(5/2, 3, 7/2)	(2/7, 1/3, 2/5)

2.2. Step II: formation of the initial supermatrix:

All obtained priority vectors are then normalized to represent the local priority vector. To obtain global priorities, the local priority vectors are entered in the appropriate columns of a matrix of influence among the elements, known as a supermatrix [41]. The supermatrix representation of a hierarchy with three levels is given as follows (Fig. 1a):

$$w = \begin{array}{r} Goal(G) \\ Criteria(C) \\ Alternatives(A) \end{array} \begin{pmatrix} 0 & 0 & 0 \\ w_{21} & 0 & 0 \\ 0 & w_{32} & I \end{pmatrix} \quad (3)$$

where w_21 is a vector that represents the impact of the goal on the criteria, w_32 is a vector that represents the impact of the criteria on each of the alternatives, and I is the identity matrix. W is referred to as a supermatrix because its entries are matrices. For example, if the criteria are dependent among themselves, then the (2, 2) entry of W given by w_22 would be nonzero.

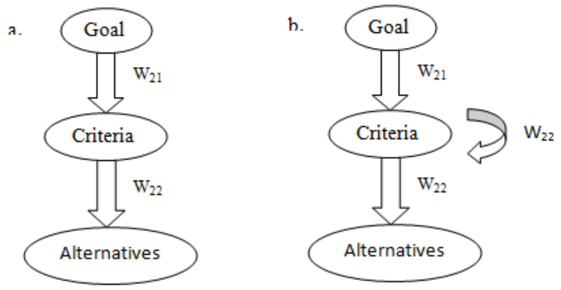

Figure 1: Hierarchy and Network (a). Hierarchy (b). Network [42].

The interdependence is exhibited by the presence of the matrix element w_{22} of the supermatrix W (Fig. 1b).

$$w = \begin{pmatrix} 0 & 0 & 0 \\ w_{21} & w_{22} & 0 \\ 0 & w_{32} & I \end{pmatrix} \quad (4)$$

The influence of a set of elements belonging to a cluster, on any element from another component, can be represented as a priority vector by applying pairwise comparisons [43]. Note that any zero value in the supermatrix can be replaced by a matrix if there is an interrelationship of the elements within a cluster or between two clusters. Fig. 1a and b shows hierarchy and network.

2.3. Step III: formation of the weighted supermatrix:

An eigenvector is obtained from the pairwise comparison matrix of the row clusters with respect to the column cluster, which in turn yields an eigenvector for each column cluster. The first entry of the respective eigenvector for each column cluster, is multiplied by all the elements in the first cluster of that column, the second by all the elements in the second cluster of that column and so on. In this way, the cluster in each column of the supermatrix is weighted, and the result, known as the weighted supermatrix, is stochastic. Raising a matrix to exponential powers gives the long term relative influences of the elements on each other [41].

3. Fuzzy Control

The fuzzy set theory introduced by Zadeh [44] and Zadeh [45] is suitable for dealing with the uncertainty and imprecision associated with information concerning various parameters. Human judgment is generally characterized by vague language, like ‘equally’, ‘moderately’, ‘strongly’, ‘very strongly’, and ‘extremely’. Using such language, DMs quantify uncertain events and objects. Fuzzy theory enables DMs to tackle the ambiguities involved in the process of the linguistic assessment of the data. The theory also allows mathematical operators and programming to apply to the fuzzy domain. It provides numerous methods to represent the qualitative judgment of the DM as quantitative data. Triangular fuzzy numbers are used in this paper to assess the preferences of DMs. Subsequently, a multi-criteria decision method can be applied to linguistic assessments to determine the best alternative [48].

Generally, the fuzzy sets are defined by the membership functions. The fuzzy sets represent the grade of any element x of X that have the partial membership to A. The degree to which an element belongs to a set is defined by the value between 0 and 1. If an element x really belongs to A, $\mu_A(x) = 1$ and clearly not, $\mu_A(x) = 0$ Higher is the membership value, $\mu_A(x)$ greater is the belongingness of an element x to a set A.

A triangular fuzzy number is defined as(l, m, u), where$l \le m \le u$. The parameters l, m and u respectively, denote the smallest possible value, the most promising value, and the largest possible value that describe a fuzzy event, (l, m, u) has the following triangular type membership function.

$$\mu_A(x) = \begin{cases} (x-l)/(m-l) & l \le x \le m \\ (u-x)/(u-m) & m \le x \le u \\ 0\ , & \text{otherwise} \end{cases} \quad (5)$$

By the extension principle [45], the fuzzy addition, the fuzzy multiplication, fuzzy division and the fuzzy subtraction of triangular fuzzy numbers are also triangular fuzzy numbers.

4. Fuzzy ANP

In the proposed methodology, the fuzzy Analytical Network Process has been used to solve the problem of supplier evaluation. It is very useful in situations where there is a high degree of interdependence between various attributes of the alternatives. In this approach, pair-wise comparison matrices are formed between various attributes of each level with the help of triangular fuzzy numbers. The FANP can easily accommodate the interrelationships existing among the functional activities [46]. The concept of supermatrices is employed to obtain the composite weights that overcome the existing interrelationships. The values of parameters such are transformed into triangular fuzzy numbers and are used to calculate fuzzy values.

In the pairwise comparison of attributes, DM can use triangular fuzzy numbers to state their preferences. Kahraman’s scale mentioned in Section 2 is precise and explicit.

To evaluate the DM preferences, pairwise comparison matrices are structured by using triangular fuzzy numbers(l,m,u)in fig2. The mxn triangular fuzzy matrix can be given as follows (Ramik, 2006).

$$\tilde{A} = \begin{pmatrix} (a_{11}^l, a_{11}^m, a_{11}^u) & (a_{12}^l, a_{12}^m, a_{12}^u) & \cdots & (a_{1n}^l, a_{1n}^m, a_{1n}^u) \\ (a_{21}^l, a_{21}^m, a_{21}^u) & (a_{22}^l, a_{22}^m, a_{22}^u) & \cdots & (a_{2n}^l, a_{2n}^m, a_{2n}^u) \\ \vdots & \vdots & \vdots & \vdots \\ (a_{m1}^l, a_{m1}^m, a_{m1}^u) & (a_{m2}^l, a_{m2}^m, a_{m2}^u) & \cdots & (a_{mn}^l, a_{mn}^m, a_{mn}^u) \end{pmatrix} \quad (6)$$

The element a_{mn} represents the comparison of component m (row element) with component n (column element). If $\tilde{A}$ is a pairwise comparison matrix, it is assumed that it is reciprocal, and the reciprocal value, i.e.,$1/a_{mn}$, is assigned to the element$\tilde{a}_{mn}$.

$$\tilde{A} = \begin{pmatrix} (1,1,1) & (a_{11}^l, a_{11}^m, a_{11}^u) & \cdots & (a_{1n}^l, a_{1n}^m, a_{1n}^u) \\ (1/a_{11}^u, 1/a_{11}^m, 1/a_{11}^l) & (1,1,1) & \cdots & (a_{2n}^l, a_{2n}^m, a_{2n}^u) \\ \vdots & \vdots & \vdots & \vdots \\ (1/a_{1n}^u, 1/a_{1n}^m, 1/a_{1n}^l) & (1/a_{2n}^u, 1/a_{2n}^m, 1/a_{2n}^l) & \cdots & (1,1,1) \end{pmatrix} \quad (7)$$

$\tilde{A}$ is also a triangular fuzzy pairwise comparison matrix. There are several methods for getting estimates for fuzzy priorities, $\tilde{w}_i$where $\tilde{w}_i = (w_i^l, w_i^m, w_i^u)$, i = 1, 2, . . ., n, from the judgment matrix $\tilde{A}$ which approximate the fuzzy ratios $\tilde{a}_{ij}$ so that $\tilde{a}_{ij} \approx \tilde{w}_i/\tilde{w}_j$One of these methods, logarithmic least squares method [12], is reasonable and effective, and it is used in this study. Hence the triangular fuzzy weights for the relative importance of the criteria, the feedback of the criteria and the alternatives according to the individual criteria can be calculated [47]. In our proposed model, only the triangular fuzzy weights for the relative importance of the criteria and the interdependence priorities of the criteria (Eq. (8)) will be used to support the fuzzy TOPSIS for selecting the best alternative.

$$w = \begin{pmatrix} 0 & 0 \\ w_{21} & w_{22} \end{pmatrix} \quad (8)$$

5. The Logarithmic Least Squares Method

Y.M. Wang et al. [12] presented a modified fuzzy LLSM for calculating triangular fuzzy weights as follows:

$$\text{Min } J = \sum_{i=1}^{n}\sum_{j=1, j\neq i}^{n} \begin{pmatrix} \left(\ln w_i^L - \ln w_j^U - \ln a_{ij}^l\right)^2 + \\ \left(\ln w_i^M - \ln w_j^M - \ln a_{ij}^m\right)^2 + \left(\ln w_i^U - \ln w_j^L - \ln a_{ij}^u\right)^2 \end{pmatrix} \quad (9)$$

Subject to

$$\begin{cases} w_i^L + \sum_{j=1, j\neq i}^{n} w_j^U \geq 1, \\ W_i^U + \sum_{j=1, j\neq i}^{n} w_j^L \leq 1 \\ \sum_{i=1}^{n} w_i^M = 1, \qquad for\ i = 1,2,3,\ldots,n \\ \sum_{i=1}^{7}\left(w_i^L + w_i^U\right) = 2, \\ w_i^U \geq w_i^M \geq w_i^L > 1 \end{cases}$$

6. Evaluation of closeness coefficient for each alternative using Fuzzy TOPSIS

In the following subsection, some basic important definitions of fuzzy sets from Zimmermann [48], Buckley [13], Zadeh [45], Kaufmann and Gupta [49], Yang and Hung [50] and Chen et al. [51] are reviewed and summarized. It is often difficult for a DM to assign a precise performance rating to an alternative for the criteria under consideration. The merit of using a fuzzy approach is to assign the relative importance of criteria using fuzzy numbers instead of precise numbers. This subsection extends TOPSIS to the fuzzy environment.

Definition 1: Let $\tilde{a} = (l_1, m_1, u_1)$ and $\tilde{b} = (l_2, m_2, u_2)$ be two triangular fuzzy numbers, then the vertex method is defined to calculate the distance between them, as:

$$d(\tilde{a}, \tilde{b}) = \sqrt{\tfrac{1}{3}\left[(l_1 - l_2)^2 + (m_1 - m_2)^2 + (u_1 - u_2)^2\right]} \quad (10)$$

The problem can be described by following sets:

- A set of m possible candidates called K = $\{K_1, K_2, \ldots K_m\}$
- A set of n criteria, C = $\{C_1, C_2, \ldots C_i\}$.
- A set of performance ratings of K_k(k=1, 2, 3. . . m) with respect to criteria C_i(i =1, 2, 3 ..., n) called $\tilde{X}$= { $\tilde{x}_{ik}$ i = 1, 2, 3. . . n, k = 1, 2, 3, . . . m }.
- A set of importance weights of each criterion w_i(i = 1, 2, 3. . . n)

As stated above, decision matrix format can be expressed as follows:

$$\tilde{X} = \begin{bmatrix} \tilde{x}_{11} & \tilde{x}_{12} & \cdots & \tilde{x}_{1n} \\ \tilde{x}_{21} & \tilde{x}_{22} & \cdots & \tilde{x}_{2n} \\ \vdots & \vdots & \vdots & \vdots \\ \tilde{x}_{m1} & \tilde{x}_{m2} & \cdots & \tilde{x}_{mn} \end{bmatrix}$$

Definition 2: Considering the different importance values of each criterion, the weighted normalized fuzzy-decision matrix is constructed as:

$\tilde{V} = [\tilde{v}_{ik}]_{n\times k}$ for i=1, 2...n, k=1, 2… m, where $\tilde{v}_{ik} = \tilde{x}_{ik}$ (.) w_i (11)

According to the briefly summarized fuzzy theory above, fuzzy TOPSIS steps can be out lined as follows:

Step 1: Choose the linguistic ratings ($\tilde{x}_{ik}$ i = 1, 2, 3 . . . , n, k = 1, 2, 3 . . . , m) for alternatives with respect to criteria. The fuzzy linguistic rating ($\tilde{x}_{ik}$) preserves the property that the ranges of normalized triangular fuzzy numbers belong to [0, 1]; thus, there is no need for normalization.

Let $\tilde{x}_{ik} = (a_{ik}, b_{ik}, c_{ik})$, $\tilde{x}_k^- = (a_k^-, b_k^-, c_k^-)$ and $\tilde{x}_j^* = (a_k^*, b_k^*, c_k^*)$.

We have

$$\tilde{r}_{ik} = \begin{cases} \tilde{x}_{ik}(\div)\tilde{x}_k^* = \left(\frac{a_{ik}}{a_k^*}, \frac{b_{ik}}{b_k^*}, \frac{c_{ik}}{c_k^*}\right) \\ \tilde{x}_j^-(\div)\tilde{x}_{ij} = \left(\frac{a_k^-}{a_{ik}}, \frac{b_k^-}{b_{ik}}, \frac{c_k^-}{c_{ik}}\right) \end{cases} \quad (12)$$

Step 2: Calculate the weighted normalized fuzzy decision matrix. The weighted normalized value $\tilde{v}_{ij}$ calculated by Eq. (11)

Step 3: Identify positive ideal (K^*) and negative ideal (K^-) solutions. The fuzzy positive ideal solution (FPIS, K^*) and the fuzzy negative ideal solution (FNIS, K^-) are shown in Eqs. 13 and 14.

$K^{*} = \{\tilde{v}_1^{*}........,\tilde{v}_i^{*}\} = \{(\max_k v_{ik}|\ i \in I')\ (\min_k v_{ik}|i \in I'')\}$
$i = 1, 2 \ldots n,\ k = 1, 2 \ldots m$ (13)

$K^{-} = \{\tilde{v}_1^{-}........,\tilde{v}_i^{-}\} = \{(\min_k v_{ik}|i \in I')(\max_k v_{ik}|i \in I'')\}$
$i = 1, 2 \ldots n,\ k = 1, 2 \ldots m$ (14)

Where I' is associated with benefit criteria and I'' is associated with cost criteria.

Step 4: Calculate the distance of each alternative from K^{*} and K^{-} using Eqs. 15 and 16.

$$D_k^{*} = \sum_{i=1}^{n} d(\tilde{v}_{ik}, \tilde{v}_i^{*})\ k = 1, 2 \ldots m \quad (15)$$

$$D_j^{-} = \sum_{i=1}^{n} d(\tilde{v}_{ik}, \tilde{v}_i^{-})\ , k = 1, 2 \ldots m \quad (16)$$

Step 5: Calculate similarities to ideal solution.

$$CC_k^{\ *} = \frac{D_k^{-}}{D_k^{*} + D_k^{-}}\ , kj = 1, 2 \ldots m \quad (17)$$

Step 6: Rank the alternatives based on closeness coefficient. Rank alternatives according to CC_k^{*} in descending order.

7. Application of Proposed Methodology for Supplier Evaluation

7.1. Step 1: Identifying criteria for supplier evaluation:

In the supplier evaluation process, an objective, unbiased decision is very hard to reach given the numerous criteria that need to be carefully considered and examined. One formal group management technique for determining a set of evaluation criteria is Nominal group technique (NGT) [52]. This well-known process forces everyone to participate and no dominant person is allowed to come out and control the proceedings. In NGT, all ideas have equal stature and will be judged impartially by the group. In this work, four potential evaluation criteria are determined as follows:

- Cost (C1): The total money, time and resources associated with a purchase or activity.
- Quality (C2): Quality is meeting the customer's needs in a way that exceeds the customer's expectations.
- Supply (C3): It is the ability to supply a good or service.
- Time to delivery (C4): It refers to the time required to a deliver a good or service according to the product specifications.

7.2. Step2: Structuring the ANP model hierarchically (goal, factors and alternatives):

The ANP model formed by the factors determined in the first step is shown in Fig. 2. ANP model is composed of three stages. In the first stage, there is the goal of determining factor weights. There are factors related to them in second. The factors of second stage are connected to the goal with a single directional arrow. The arrows in the second stage represent the inner-dependence among the factors. The third stage represents various alternate suppliers which are to be ranked.

Figure 2: ANP model for supplier evaluation.

7.3. Step3: Recognition of the interdependence between criteria:

To simplify the process and avoid any misunderstandings, the interaction between any two of these criteria is not considered in the first instance. Next, in order to reflect the interdependence property between the criteria, we need to identify the exact relationship in a network structure of ANP. Another NGT process is taken to construct the relationship of interdependency.

7.4. Step4: Determination of local weights of the criteria:

In this step, local weights of the factors which take part in the second level of ANP model are calculated. Pairwise comparison matrices are formed by the decision committee by using the scale given in Table 1. For example the question ‘‘How important is Quality when it is compared with Cost?” and the answer ‘‘strongly more important”, to this linguistic scale is placed in the relevant cell against the triangular fuzzy numbers (2/5, 1/2, 2/3). All the fuzzy evaluation matrices are produced in the same manner. Pairwise comparison matrices are analyzed by Y.M. Wang et al. [12] modified logarithmic least square method to obtain the fuzzy priority weights. The local weights for the factors are calculated in a similar fashion to the fuzzy evaluation matrices, as shown under Table 2. Pair wise comparison matrices are given in Tables 3–6 together with the priority weights.

Table 2: Pairwise comparison matrix.

CRITERIA	Cost	Quality	Supply	Time to deliver	Local Priority weights
Cost	(1, 1, 1)	(3/2, 2, 5/2)	(2/7, 1/3, 2/5)	(5/2, 3, 7/2)	(0.0012, .0016,0.0064)
Quality	(2/5, 1/2, 2/3)	(1, 1, 1)	(2/7, 1/3, 2/5)	(7/2, 4, 9/2)	(0.0013,0.0016,0.0063)
Supply	(5/2, 3, 7/2)	(5/2, 3, 7/2)	(1, 1, 1)	(5/2, 3, 7/2)	(0.7087,0.7476,0.7721)
Time to deliver	(2/7, 1/3, 2/5)	(2/9, 1/4, 2/7)	(2/7, 1/3, 2/5)	(1, 1, 1)	(0.2206,0.2492,0.2835)

Table 3: Interdependency matrix for "Cost".

CRITERIA	Quality	Time to deliver	Supply	Priority weights
Quality	(1, 1, 1)	(3/2, 2, 5/2)	(3/2, 2, 5/2)	(0.2987, 0.3238, 0.4359)
Time to deliver	(2/5, 1/2, 2/3)	(1, 1, 1)	(2/3, 1, 3/2)	(0.1846, 0.2253, 0.2478)
Supply	(2/5, 1/2, 2/3)	(2/3, 1, 3/2)	(1, 1, 1)	(0.3717, 0.4508, 0.4613)

Table 4: Interdependency matrix for "Quality".

CRITERIA	Cost	Time to deliver	Supply	Priority weights
Cost	(1, 1, 1)	(3/2, 2, 5/2)	(3/2, 2, 5/2)	(0.0010, 0.0511, 0.2003)
Time to deliver	(2/5, 1/2, 2/3)	(1, 1, 1)	(2/3, 1, 3/2)	(0.3996, 0.4745, 0.4798)
Supply	(2/5, 1/2, 2/3)	(2/3, 1, 3/2)	(1, 1, 1)	(0.3199, 0.4745, 0.5994)

Table 5: Interdependency matrix for "Supply".

CRITERIA	Cost	Quality	Time to deliver	Priority weights
Cost	(1, 1, 1)	(5/2, 3, 7/2)	(3/2, 2, 5/2)	(0.0144, 0.0287,0.0376)
Quality	(2/7, 1/3, 2/5)	(1, 1, 1)	(2/7, 1/3, 2/5)	(0.2185, 0.2428,0.2757)
Time to deliver	(2/5, 1/2, 2/3)	(5/2, 3, 7/2)	(1, 1, 1)	(0.6892, 0.7285,0.7647)

Table 6 Interdependency matrix for "Time to Deliver".

CRITERIA	Cost	Quality	Supply	Priority weights
Cost	(1, 1, 1)	(2/9, 1/4 2/7)	(2/7, 1/3, 2/5)	(0.0144, 0.0287, 0.0376)
Quality	(7/2, 4, 9/2)	(1, 1, 1)	(2/7, 1/3, 2/5)	(0.2185, 0.2428, 0.2757)
Supply	(5/2, 3, 7/2)	(5/2, 3, 7/2)	(1, 1, 1)	(0.6892, 0.7285,0.7647)

7.5. Step 5: Determination of overall weights of the criteria:

In this step, interdependent weights of the factors are calculated and the dependencies among the factors are considered. Dependence among the factors is determined by analyzing the impact of each factor on every other factor using pair wise comparisons. Based on the dependencies, pair wise comparison matrices are formed for the factors (Tables 3–6). The following question, 'What is the relative importance of 'Quality' when compared with 'Time to deliver' on controlling 'Cost'?" may arise in pair wise comparisons and lead to a value of (3/2, 2, 5/2) as denoted in Table 3. The resulting relative importance weights are presented in the last column of Tables 3–6. Using the computed relative importance weights, the dependence matrix of the factors is formed. Interdependent weights of the factors are computed by multiplying the dependence matrix of the factors we obtained with the local weights of factors provided in Table 2. The interdependent weights of the factors are in last column of the Table 7.

Table 7: overall weights of factors.

CRITERIA	Local weights	Overall weights
Cost	(0.0012, .0016,0.0064)	(0.0012,0.0016,0.0064)
Quality	(0.0013,0.0016,0.0063)	(0.0013,0.0016,0.0063)
Supply	(0.7087,0.7476,0.7721)	(0.7087,0.7476,0.7721)
Time to deliver	(0.2206,0.2492,0.2835)	(0.2206,0.2492,0.2835)

7.6. Step6: Preparation of Decision matrix:

In this step, the decision makers are asked to establish the decision matrix by comparing candidates under each criterion separately. Table8 represents the decision matrix, in this some criteria Quality and Supply are assumed to be benefit criteria and Cost and Time to deliver are cost criteria. After the decision matrices are determined, we normalize these matrices via Eq. (12). Results are shown in Table 9. Then weighted normalized decision matrix is determined using Eq. (11). The results are shown in Table 10.

Table 8: Decision matrix.

SUPPLIER	Cost	Quality	Supply	Time to deliver
Supplier1	(3/2,2,5/2)	(1/2,1,3/2)	(3/2,2,5/2)	(2,5/2,3)
Supplier2	(1/2,1,3/2)	(1,3/2,2)	(5/2,3,7/2)	(2,5/2,3)
Supplier3	(1,3/2,2)	(3/2,2,5/2)	(1,3/2,2)	(1/2,1,3/2)
Supplier4	(1/2,1,3/2)	(1,3/2,2)	(1/2,1,3/2)	(1,3/2,2)
Supplier5	(5/2,3,7/2)	(1/2,1,3/2)	(1,3/2,2)	(3/2,2,5/2)

Table 9: Normalized decision matrix.

SUPPLIER	Cost	Quality	Supply	Time to deliver
Supplier1	(1/3,1/2,3/5)	(1/3,1/2,3/5)	(3/5,2/3,5/7)	(1/4,2/5,1/2)
Supplier2	(1,1,1)	(2/3,3/4,4/5)	(1,1,1)	(1/4,2/5,1/2)
Supplier3	(1/2,2/3,3/4	(1,1,1)	(2/5,1/2,4/7)	(1,1,1)
Supplier4	(1,1,1)	(2/3,3/4,4/5)	(1/5,1/3,3/7)	(1/2,2/3,3/4)
Supplier5	(1/5,1/3,3/7)	(1/3,1/2,3/5)	(2/5,1/2,4/7)	(1/3,1/2,3/5)

Table 10: Weighted Normalized Decision matrix.

SUPPLIER	Cost	Quality	Supply	Time to deliver
Supplier1	(0.0045,0.0143,0.0246)	(0.0678,0.1213,0.1763)	(0.0916,0.1218,0.1587)	(0.0205,0.0449,0.0654)
Supplier2	(0.0134,0.0287,0.041)	(0.1356,0.1819,0.2351)	(0.1527,0.1827,0.2222)	(0.0205,0.0449,0.0654)
Supplier3	(0.0067,0.0191,0.0307)	(0.2034,0.2425,0.2938)	(0.0611,0.0913,0.1269)	(0.082,0.1123,0.1308)
Supplier4	(0.0134,0.0287,0.041)	(0.1356,0.1819,0.2351)	(0.0305,0.0609,0.0952)	(0.041,0.0749,0.0981)
Supplier5	(0.0027,0.0096,0.0176)	(0.0678,0.1213,0.1763)	(0.0611,0.0913.0.1269)	(0.0273,0.0562,0.0785)

7.7. Step 7: Ranking of supplier based on closeness coefficient:

The positive ideal solution (K^*) and negative ideal solution (K^-) are determined by using the weighted normalized values. Equations 13–14 are used to determine the positive ideal solution and negative ideal solution. The positive triangular fuzzy numbers are in the range [0, 1]. Hence the fuzzy positive ideal reference point (FPIS, K^*) is (1, 1, 1) and fuzzy negative ideal reference point (FNIS, K^-) is (0, 0, 0). In the last step, the relative closeness to he ideal solution D_k^* and D_k^- are calculated. The relative closeness to the ideal solution is defined on Eqs. 15-16. Equation 10 is used to calculate distances to ideal solutions. Table 11 summarizes the results. The higher the closeness means the better the rank, so the relative closeness to the ideal solution of the alternatives can be substituted as follows:

Supplier3>Supplier2>Supplier4>Supplier1>Supplier5. Supplier2 is defined as the most potential supplier.

Table 11: The Results.

SUPPLIER	D_k^*	D_k^-	CC^*	Rank
Supplier1	3.6979	0.1063	0.0279	4
Supplier2	3.5604	0.2222	0.0587	2
Supplier3	3.5347	0.2525	0.0667	1
Supplier4	3.6563	0.14	0.0369	3
Supplier5	3.7229	0.089	0.0233	5

8. Conclusion

Supplier selection is a complex multi-criteria decision-making problem, and its complexity is further aggravated if the highly important interdependence among the selection criteria is taken into consideration. ANP, providing a systematic approach to set priorities among alternative suppliers, can effectively capture the interdependencies among various criteria. However, ANP handles only crisp comparison ratios. To tackle uncertain decision making judgments and to accommodate the criteria with interdependence Fuzzy Analytical Network Process is used to find the priority weights. To overcome the problem of inconsistency of pairwise comparison matrix fuzzy priority weights are derived using logarithmic least square method. FTOPSIS is used for supplier ranking based on criteria weights and supplier selection. As a result of the empirical study, we find that the proposed method is practical for ranking competing suppliers in terms of their overall performance with respect to multiple interdependence criteria.

Acknowledgment

The authors express their appreciation to Prof. Mousa S. Mohsen, the Editor-in-Chief, Jordan Journal of Mechanical and Industrial Engineering (JJMIE) and two anonymous reviewers for their insightful and constructive comments on an earlier version of this manuscript.

References

[1] R. Dulmin, V. Mininno, “Supplier selection using a multi-criteria decision aid method”. J. Purchasing Supply Manage, Vol. 9, No.4, 2003, 177–187.

[2] L. Boer, E. Labro, P. Morlacchi, “A review of methods supporting supplier selection”. Eur. J. Purchasing Supply Manage, Vol. 7, 2001, 175–89.

[3] K.L. Choy, W.B. Lee, V. Lo, “Design of a case based intelligent supplier relationship management system – the integration of supplier rating system and product coding system”. Expert Syst. Appl, Vol. 25, No.1, 2003, 87–100.

[4] C.H. Weber, J.R. Current, A. Desai, “Non-cooperative negotiation strategies for vendor selection”. European Journal of Operational Research, Vol. 108, No.1, 1998, 208–223.

[5] S. Talluri, “A buyer–seller game model for selection and negotiation of purchasing bids”. European Journal of Operational Research, Vol. 143, No.1, 2002, 171–180.

[6] M.C.Y. Tam, V.M.R. Tummala, “An application of the AHP in vendor selection of a telecommunications system”. Omega, Vol. 29, No. 2, 2001, 171–182.

[7] Z. Degraeve, E. Labro, F. Roodhooft, “An evaluation of vendor selection models from a total cost of ownership perspective”. European Journal of Operational Research, Vol. 125, No. 1, 2000, 34–58.

[8] F. Roodhooft, J. Konings, “Vendor selection and evaluation an activity based costing approach”. European Journal of Operational Research, Vol. 96, No. 1, 1997, 97–102.

[9] S. Talluri, R. Narasimhan, “Vendor evaluation with performance variability: a max–min approach”. European Journal of Operational Research, Vol. 146, No. 3, 2003, 543–552.

[10] J. Zhu, “A buyer–seller game model for selection and negotiation of purchasing bids: extensions and new models”. European Journal of Operational Research., Vol. 154, No. 1, 2004, 150–156.

[11] P.J.M. Van Laarhoven, W. Pedrycz, “A fuzzy extension of Saaty’s priority theory”. Fuzzy Sets and Systems, Vol. 11, 1983, 229–241.

[12] Y.M. Wang, T.M.S. Elhag, Z.S. Hua, “A modified fuzzy logarithmic least squares method for fuzzy analytic hierarchy process”. Fuzzy Sets and Systems, Vol. 157, 2006, 3055–3071.

[13] J.J. Buckley, “Fuzzy hierarchical analysis”. Fuzzy Sets and Systems, Vol. 17, 1985, 233–247.

[14] D.Y. Chang, “Applications of the extent analysis method on fuzzy AHP”, European Journal of operational Research, Vol. 95, 1996, 649–655.

[15] R. Xu, “Fuzzy least-squares priority method in the analytic hierarchy process”. Fuzzy Sets and Systems, Vol. 112, 2000, 359–404.

[16] L. Mikhailov, “Deriving priorities from fuzzy pairwise comparison judgments”. Fuzzy Sets and Systems, Vol. 134, 2003, 365–385.

[17] R. Csutora, J.J. Buckley, “Fuzzy hierarchical analysis: The Lamda-Max method”. Fuzzy Sets and Systems, Vol. 120, 2001, 181–195.

[18] F.T. Bozbura, A. Beskese, “Prioritization of organizational capital measurement indicators using fuzzy AHP”. International Journal of Approximate Reasoning, Vol. 44, 2007, 124–147.

[19] F.T. Bozbura, A. Beskese, C. Kahraman, “Prioritization of human capital measurement indicators using fuzzy AHP”. Expert Systems with Applications, Vol. 32, 2007, 1100–1112.

[20] C.E. Bozdagˇ, C. Kahraman, D. Ruan, “Fuzzy group decision making for selection among computer integrated manufacturing systems”. Computers in Industry, Vol. 51, 2003, 13–29.

[21] G. Bu¨yu¨ko¨zkan, “Multi-criteria decision making for e-marketplace selection”. Internet Research, Vol. 14, No. 2, 2004, 139–154.

[22] G. Bu¨yu¨ko¨zkan, T. Ertay, C. Kahraman, D. Ruan, “Determining the importance weights for the design requirements in the house of quality using the fuzzy analytic network approach”. International Journal of Intelligent Systems, Vol. 19, 2004, 443–461.

[23] G. Bu¨yu¨ko¨zkan, C. Kahraman, D. Ruan, “A fuzzy multi-criteria decision approach for software development strategy selection”. International Journal of General Systems, Vol. 33, 2004, 259–280.

[24] F.T.S. Chan, N. Kumar, Global supplier development considering risk factors using fuzzy extended AHP-based approach, Omega, Vol. 35, 2007, 417–431.

[25] T. Ertay, G. Bu¨yu¨ko¨zkan, C. Kahraman, D. Ruan, Quality function deployment implementation based on analytic network process with linguistic data: An application in automotive industry, Journal of Intelligent and Fuzzy Systems, Vol. 16, 2005, 221–232.

[26] Y.C. Erensal, T. O¨ ncan, M.L. Demircan, Determining key capabilities in technology management using fuzzy analytic hierarchy process: A case study of Turkey”. Information Sciences, Vol. 176, 2006, 2755–2770.

[27] C. Kahraman, U. Cebeci, & D. Ruan, “Multi-attribute comparison of catering service companies using fuzzy AHP: The case of Turkey”. International Journal of Production Economics, Vol. 87, 2004, 171–184.

[28] C. Kahraman, U. Cebeci, Z. Ulukan, “Multi-criteria supplier selection using fuzzy AHP”. Logistics Information Management, Vol. 16, No. 6, 2003, 382–394.

[29] C. Kahraman, T. Ertay, G. Bu¨yu¨ko¨zkan, “A fuzzy optimization model for QFD planning process using analytic network approach”. European Journal of Operational Research, Vol. 171, 2006, 390–411.

[30] C. Kahraman, D. Ruan, I. Dogˇan, “Fuzzy group decision-making for facility location selection”. Information Sciences, Vol. 157, 2003 135–153.

[31] O. Kulak, & C. Kahraman, “Fuzzy multi-attribute selection among transportation companies using axiomatic design and analytic hierarchy process”, Information Sciences, Vol. 170, 2005, 191–210.

[32] C.K. Kwong, H. Bai, “Determining the importance weights for the customer requirements in QFD using a fuzzy AHP with an extent analysis approach”. IIE Transactions, Vol. 35, 2003, 619–626.

[33] Y.C. Tang, M. Beynon, “Application and development of a fuzzy analytic hierarchy process within a capital investment study”. Journal of Economics and Management, Vol. 1, 2005, 207–230.

[34] E. Tolga, M.L. Demircan, C. Kahraman, “Operating system selection using fuzzy replacement analysis and analytic hierarchy process”. International Journal of Production Economics, Vol. 97, 2005, 89–117.

[35] F. Tu¨ysu¨ z, C. Kahraman, “Project risk evaluation using a fuzzy analytic hierarchy process: An application to information technology projects”. International Journal of Intelligent Systems, Vol. 21, No. 6, 2006, 559–584.

[36] S. Ohnishi, H. Imai, and M. Kawaguchi, “Evaluation of Stability on Weights of Fuzzy Analytic Hierarchy Process using a sensitivity analysis”. J. Japan Soc. for Fuzzy Theory and Sys., Vol. 9, No. 1, 1997, 140--147,

[37] Y.M. Wang et al., “Decision support on the extent analysis method for fuzzy AHP and its applications”, European Journal of Operational Research, Vol. 186, 2008, 735–747.

[38] Hwang, C. L., & Yoon, K, “Multiple attribute decision making-methods and applications: A state of the art survey”. Springer-Verlag, 1981.

[39] Karsak, E. E, “Distance-based fuzzy MCDM approach for evaluating flexible manufacturing system alternatives”. International Journal of Production Research, Vol. 40, No. 13, 2002, 3167–3181.

[40] Saaty, R. W, “Decision making in complex environment: The analytic hierarchy process (AHP) for decision making and the analytic network process (ANP) for decision making with dependence and feedback. www.Superdecisions.com/”. 2003.

[41] Saaty, T. L, “Fundamentals of the analytic network process”. ISAHP, Kobe, Japan, 1999.

[42] Yüksel, I., & Dagdeviren, M, "Using the analytic network process (ANP) in a SWOT analysis – A case study for a textile firm". Information Sciences, Vol. 177, No. 16, 2007, 3364–3382.

[43] Saaty, T. L., & Vargas, L. G, "Diagnosis with dependent symptoms: Bayes Theorem and the analytic network process". Operations Research, Vol. 46, No. 4, 1998, 491–502.

[44] Zadeh, L, "A fuzzy-algorithmic approach to the definition of complex or imprecise concepts". International Journal of Man–Machine Studies, Vol. 8, 1976, 249–291.

[45] Zadeh, L. A, "Fuzzy sets. Information and Control", Vol. 8, 1965, 338–353.

[46] Mohanty, R. P., Agarwal, R., Choudhury, A. K., & Tiwari, M. K, "A fuzzy ANP based approach to R&D project selection: A case study". International Journal of Production Research, Vol. 43, No. 24, 2005, 5199–5216.

[47] Ramik, J, "A decision system using ANP and fuzzy inputs". In 12th international conference on the foundations and applications of utility, risk and decision theory, Roma, 2005.

[48] Zimmermann, H. J, "Fuzzy set theory and its applications (2nd ed.)". London: Kluwer Academic Publishers, 1991.

[49] Kaufmann, A., & Gupta, M. M, "Introduction to fuzzy arithmetic: Theory and applications". New York: Von Nostrand Reinhold, 1985.

[50] Yang, T., & Hung, C.-C, "Multiple-attribute decision making methods for plant layout design problem", Robotics and Computer-Integrated Manufacturing, Vol. 23, No. 1, 2007, 126–137.

[51] Chen, C. T., Lin, C. T., & Huang, S. F, "A fuzzy approach for supplier evaluation and selection in supply chain management". International Journal of Production Economics, Vol. 102, 2006, 289–301.

[52] A.L. Delbecq, A.H. Van de Ven, D.H. Gustafson, "Group Techniques for Program Planning". Scott, Foresman and Company, IL, 1975.

JJMIE

Volume 5, Number 6, Dec. 2011
ISSN 1995-6665
Pages 553 - 557

Jordan Journal of Mechanical and Industrial Engineering

On the Deformation Modes of Continuous Bending under Tension Test

A. Hadoush*[,a]

[a]Mechanical Engnieering Department, Faculty of Engineering, The Hashemite University, P.O. Box 330127, Zarqa 13115, Jordan.

Abstract

In this paper the continuous bending under tension (CBT) test is analyzed by numerical simulation. In CBT test, the material is deformed to high level of strain that is beyond the achieved strain by the standard tensile test. The main stability criterion describes the importance of compressive stress produced by bending in stabilizing the deformation. At the symmetry line of the strip, the material can be assumed simply to deform by bending and stretching in plane strain condition. The focus of this paper is to study the deformation modes through thickness at the symmetry line. It is found that the material experiences three deformations modes. The cyclic parts through thickness experiences two deformation modes: the first is limited between uniaxial tension and plane strain and the second deformation mode is limited between pure shear and uniaxial compression. The third deformation mode is observed at the middle part through thickness and it is based on tension and the contribution of through thickness stress.

Keywords: bending under tension; deformation mode

1. Introduction

The continuous bending under tension (CBT) test can be seen as a tensile test on strip material with additional bending by a set of rolls that is traveling over the length of the strip. The main effect of additional bending is that the required tensile force for the same elongation is reduced [1]. The CBT test was proposed as a method for increasing elongation to investigate material properties at high levels of straining [2]. The deformation around rolls in the CBT test bears resemblance with the deformation around the spherical tool in incremental sheet forming (ISF). This resemblance motivated Hadoush et al to present a 2-dimensional finite element model for the CBT test as a simplified test of ISF process [3]. The main focus was to study the contribution of bending in stabilizing the deformation of a strip to high strain. Experimentally, Emmens and Boogaard showed that high levels of strain are obtained for various materials using CBT test [4]. Also, the CBT test is identified as incremental forming process because the strip, that is used in CBT test, is deformed incrementally rather than continuously as in a standard tensile test, the proposed CBT setup by Emmens and Boogaard is shown in figure 1.

Figure 1: CBT setup [4].

CBT test is a simple test to perform but many aspects of the test have not been investigated yet e.g. deformation modes during the test. Hadoush et al. present a numerical investigation, focusing on the process description, to analyze the obtained cyclic force-displacement curve of CBT test [5]. It is concluded that the cyclic force-displacement curve consists of two parts: a steady part and a transient part (peak). A simple mechanical model incorporating non-constant bending radius and cyclic material behaviour is presented in [6] in addition to an extensive overview on stability and formability of CBT test.

The focus of this work is to study the deformation modes during continuous bending under tension. Numerically, part of the CBT test is simulated which mimics qualitatively half cycle of the process. The stress

* Corresponding author. e-mail: hadoush@hu.edu.jo

  - Volume 5, Number 6 (ISSN 1995-6665)

evolution near the symmetry line of the strip, in longitudinal direction, is recorded and analyzed to investigate the variation of the deformation modes through the thickness of the strip.

2. CBT Test

The experimental description of the CBT test has been explained in detail in [4]. Within this section, some of the experimental descriptions will be mentioned for their relations to the numerical model. The CBT setup is shown in figure 1. The roll set consists of 3 frictionless cylinders of 15 mm diameter. In longitudinal direction, the rolls are separated from each other by 17.5 mm. The roll set can travel in the longitudinal direction only. First, the central roll is placed such as to fit the specimen in between the rolls without deforming it. Then the central roll can move in thickness direction to introduce bending. A two dimensional schematic of the FE model is shown in figure 2.

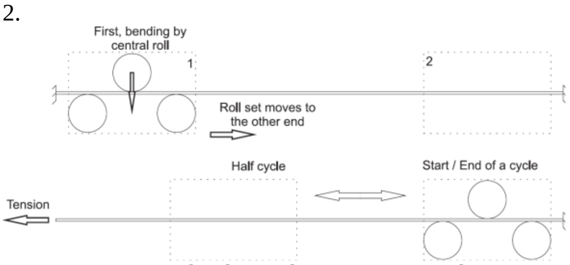

Figure 2: Continuous bending under tension process description.

The bending in the specimen is introduced by the movement of the central roll downwards. The movement of the roll set in longitudinal direction introduces the bending in a cyclic manner.

The left edge of strip, as shown in figure 2, is fixed to the cross bar of the tensile machine while the right edge of the strip is fixed to stationary part of machine. At the beginning of CBT test, the bending is introduced then the roll set is moved from left to right with zero displacement of the cross bar. After this initial part, the current position of the roll set defines the starting point of the cycle, the roll set starts traveling forward 'left' and backward 'right' performing one cycle and so on. In this work, the initial stage of the CBT test is considered only because it mimics qualitatively half cycle of the process. The clamped longitudinal force for both the initial stage and for one cycle is shown in figure 3. During the cycle, the cross bar movement introduces tension. In the initial stage, the strip has to stretch to follow the curved geometry of the roll set and this introduces the tension. The movement of the roll set introduces the bending in cyclic manner in both cases.

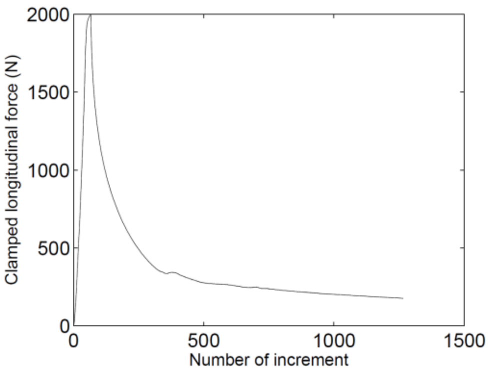

(a) Initial stage.

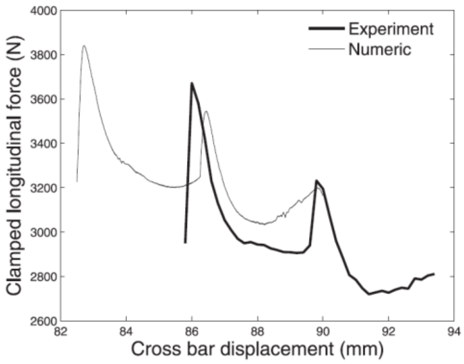

(b) One cycle.

Figure 3: The clamped longitudinal force a) The initial stage as predicted in this work b) One cycle with experimental verification [5].

3. Numerical model

The used specimen in CBT test is shown in figure 4a. Through the length of the specimen, the specimen has uniform thickness and piecewise uniform width. The cyclic bending is performed only in the middle part of the specimen. Experimentally, it is observed that the part that experiences the combined tension and bending deforms as shown in figure 4b. The plastic deformation of the wider parts is neglected and a rigid body motion of these parts can be assumed for mild steel. Only the middle part of the specimen is considered in the simulation. Because of symmetry along the longitudinal axis, half of the middle part of the specimen is modeled. The modeled part of the specimen is 200 mm in length and 10 mm in width. The thickness of the modeled part of the sheet is 1 mm. A regular mesh made of solid-shell element is used to discretize the geometry of the strip, the 200 mm length is discretized by 2000 element, the 10 mm width is discretized by 10 element and one element through thickness. The solid shell element is based on enhanced assumed strain and modified assumed natural strain methods for one-point quadrature solid-shell, the element is called MRESS [7]. MRESS element has an eight-node brick topology, three displacement degrees of freedom per node. MRESS has one integration point in-plane and a flexible number of integration points can be used through thickness, here, seven integration points are used.

The material model is kept as simple as possible. The isotropic yield behavior of the material is modeled with the von Mises criterion. The work hardening is governed by linear relation:

$$\sigma = 200 + 500\varepsilon$$

Where σ and ε are the flow stress and equivalent plastic strain, respectively. The material has a Young's modulus of 200 GPa and Poisson's ratio of 0.3. For experimental verification, it is acknowledge that a better material model is required that includes e.g. the anisotropic behavior of the sheet and a nonlinear work hardening model.

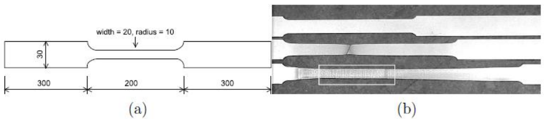

Figure 4: Specimen of CBT test a) Schematic of the specimen, dimension is in mm and the drawing is not to scale b) Unused and used specimens: untested (top), tensile tested (middle) and CBT tested (bottom). A uniform deformation is observed in the white rectangle [4].

4. Results and Discussion

In CBT test, a material portion has to be deformed by two sets of bend-unbend-bend in order to experience one complete cycle. Here, bending term is used to refer to bending by lower rolls while unbending is used to refer to bending by central roll. The material portion has to be straightened each time the strip changes its curvature direction from bending-unbending and from unbending-bending. In this demonstration, the roll set will moves 60 mm from its initial position to the right and this will mimic half cycle of CBT test. A finite element simulation is performed. The stresses are recorded for a particular location that is originally 5 mm to the right of the roll set at its initial location and it will be 5 mm to the left of the roll set at the end of its movement. This location is as close to symmetry section in longitudinal direction of the strip.

The predicted stress components are plotted in figure 5, these stresses are global stresses. The first observation to mention is that the achieved values of the shear stresses are almost negligible compared to the achieved values of the normal stresses. Focusing on the order of the normal stresses, the longitudinal stress σ_{xx} is the major stress component then σ_{yy} through width. The normal stress through thickness σ_{zz} ratio to σ_{xx} has an order of one to four. Based on this observation, It can be assumed that the normal stresses coincide with the principal stresses with acceptable margin of error. Actually, σ_{xx} and σ_{zz} can be rotated around y-axis, transformed, so that it results in reducing through thickness stress to zero except when the surface has contact with the rolls.

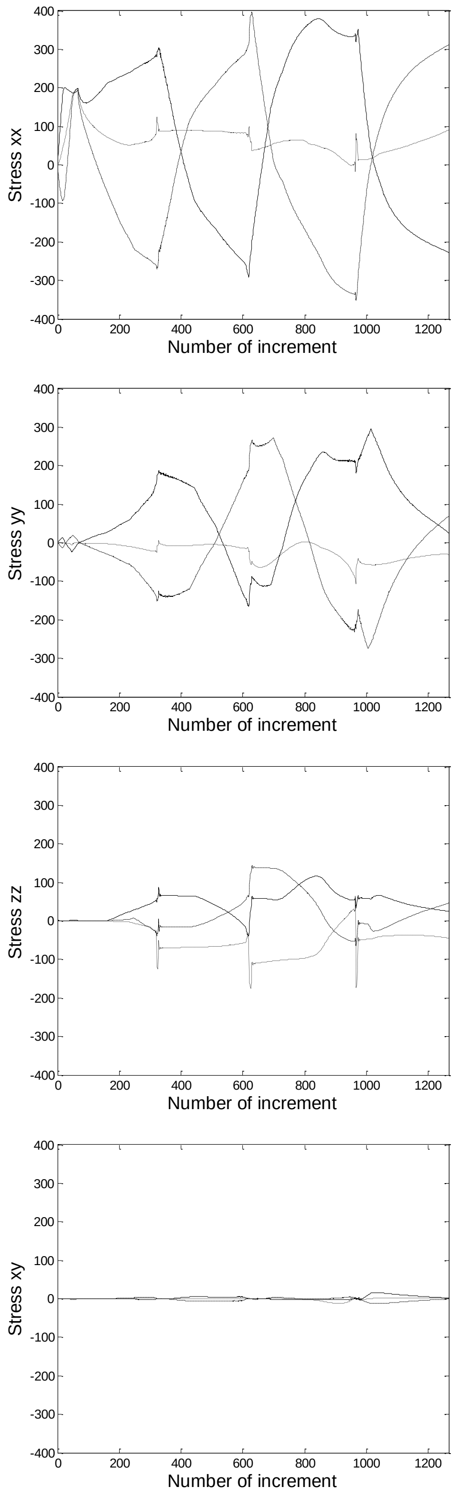

  - Volume 5, Number 6 (ISSN 1995-6665)

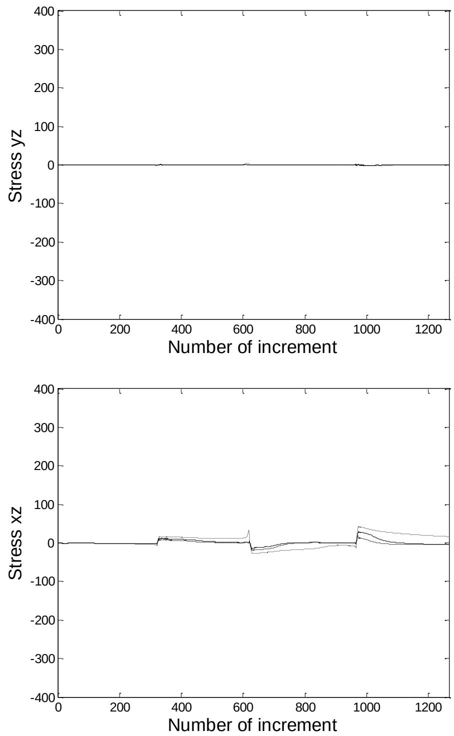

Figure 5: Stress state evolution through thickness: upper (solid line), mid (dotted line) and lower integration point (dashed line).

Prior to increment 166, the studied material portion is in tension and it is outside the roll set zone. It is bent by the right lower roll Between increment 167-466, the top surface is in tension while the bottom surface is in compression because of bending. In addition, the entire strip is under tension, therefore, the top surface has a higher stress value compared to the value of the stress at the bottom surface. This situation is flipped when the material portion experiences the central roll, it is unbent. At this stage, the material experiences the smallest radius of curvature that is larger than the radius of the roll, therefore, the bottom surface reaches a higher level of stress than the achieved level at the top surface. The longitudinal stress σ_{xx} at mid-plane is always in tension for the entire history of the process. The introduced plastic deformation will reduce the tension in the strip, this results in reducing the achieved value of the longitudinal stress when the strip is bent by the lower roll. The stress state that results in producing the plastic deformation will be the topic of the following discussion.

The material portion experiences different deformation modes when it passes the roll set. Mainly, three deformation modes are identified, two of these deformation modes (I and II) are observed in the material layers, through thickness, that are deformed by cyclic loading. The third deformation mode III is observed in mid-plane that is monotonically loaded in tension. The material portion is deformed by deformation mode I when it is bent or unbent by the rolls, a sample of the normal stresses evolution during this mode is plotted in figure 6. This deformation mode is characterized by: the normal stresses have the same sign, σ_{xx} has the largest achieved value followed by σ_{yy} then σ_{zz}, the magnitude of $\sigma_{xx} - \sigma_{yy}$ decreases, $\sigma_{yy} - \sigma_{zz}$ increases and $\sigma_{zz} - \sigma_{xx}$ increases. In case of ignoring σ_{zz}, or assuming plane stress condition, and defining α as the ratio of σ_{yy} to σ_{xx}, it is observed that the material is deformed plastically starting from a deformation mode close to uniaxial deformation in tension α = 0.128 and shifts continuously toward a deformation mode close to plane strain α = 0.54 as plotted in figure 6b. Keep in mind that in plane stress condition α = 0 indicates uniaxial deformation, α = 0.5 indicates plane strain, α = 1 indicates biaxial stretching and α = -1 indicates pure shear.

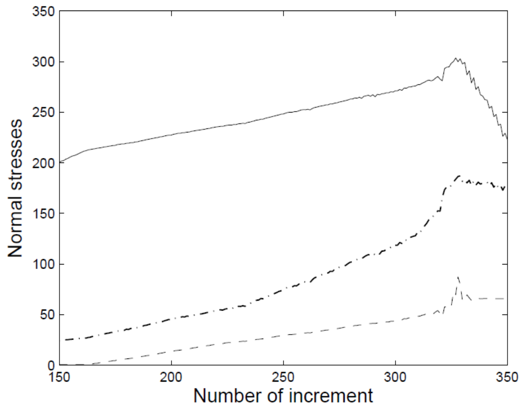

(a)

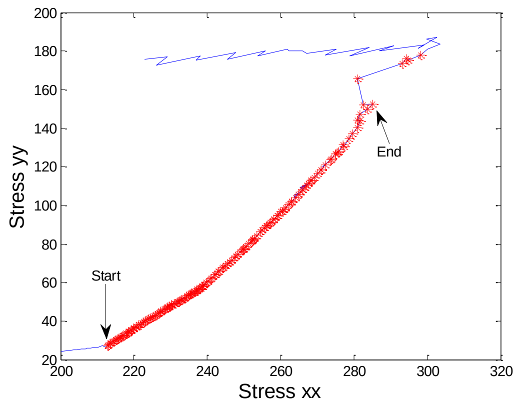

(b)

Figure 6: Deformation mode I a) Normal stresses: σxx (solid line), σyy (dashed line) and σzz (dashed-dotted line). b) Yield surface, marker indicates plastic deformation.

The material portion experiences deformation mode II when it is straightened, a sample of the normal stresses evolution during this mode is plotted in figure 7. The main characteristics of this deformation mode are: the normal stress σ_{xx} is negative while σ_{yy} and σ_{zz} are positive, the magnitude of $\sigma_{xx} - \sigma_{yy}$ decreases, $\sigma_{yy} - \sigma_{zz}$ decreases, $\sigma_{zz} - \sigma_{xx}$ increases. With similar simplification as made in deformation mode I, it can be considered that the material starts deforming plastically from a deformation mode near pure shear with α=-1.45 passing the point of pure shear to uniaxial deformation in compression at α =-0.215 as shown in figure 7b.

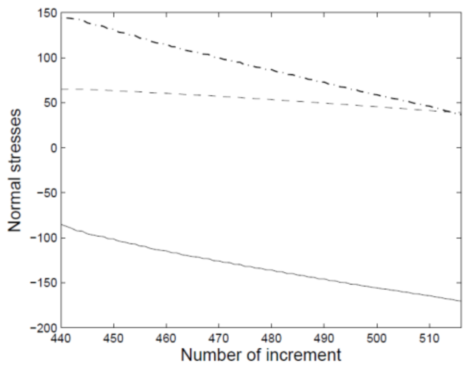

(a)

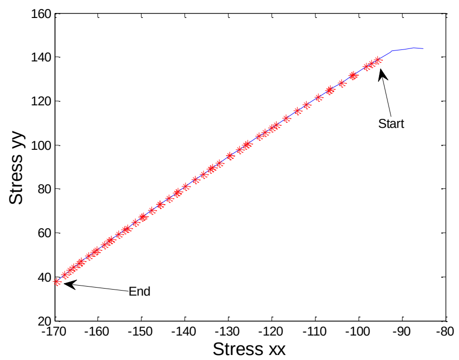

(b)

Figure 7: Deformation mode II a) Normal stresses: σxx (solid line), σyy (dashed line) and σzz (dashed-dotted line). b) Yield surface, marker indicates plastic deformation.

Deformation mode III is observed only in the mid-plane when the material is bent or unbent, it is loaded in tension. Prior to the plastic deformation, a sudden increase of σ_{xx} and a sudden decrease of σ_{zz} are observed, a sample of the normal stresses evolution during this mode is plotted in figure 8. The deformation mode is characterized by: the normal stress σ_{xx} is positive while σ_{yy} and σ_{zz} are negative, the magnitude of $\sigma_{xx} - \sigma_{yy}$ decreases, $\sigma_{yy} - \sigma_{zz}$ increases, $\sigma_{zz} - \sigma_{xx}$ increases. It is observed that the material deforms plastically in tension at a low value of σ_{xx} because of the contribution of σ_{zz}. Keep in mind that Boogaard et al. concluded that through thickness stress, contact stress, reduces the yield stress in tension if it bends over some radius [8].

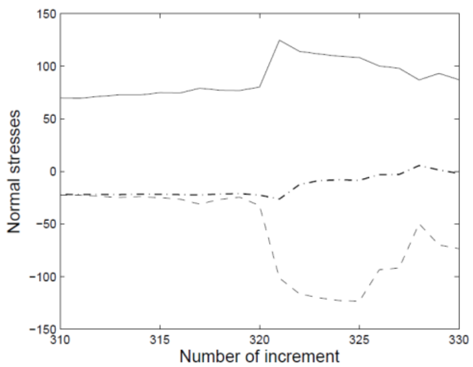

Figure 8: Normal stresses of deformation mode III: σxx (solid line), σyy (dashed line) and σzz (dashed-dotted line).

5. Conclusions

In this work, the continuous bending under tension is studied focusing on the stress state at the symmetry line along the longitudinal direction of the strip. It is observed numerically that the value of shear stresses are almost negligible compared to the value of the normal stresses. Three deformation modes are identified, two of these deformation modes (I and II) are observed in the material layers that are deformed by cyclic loading. The third deformation mode III is observed in mid-plane that is monotonically loaded in tension. Deformation mode I is active when the material is bent or unbent and it varies from uniaxial deformation in tension to plane strain. Deformation mode II deforms the material starting from pure shear mode to uniaxial deformation in compression and it is active when the material is straightened between the rolls. The third deformation mode is observed in the mid-plane through thickness and it is based on the contribution of thickness stress in reducing the required tension to plastically deform the material when it is bent. The focus of future work is to study the variation of the deformation modes through the width of the strip in CBT test incorporating anisotropic material model. The variation of deformation modes for the entire cross section, that is perpendicular to longitudinal direction, may provide a better understanding of how the deformation of material is stabilized to achieve high strain.

References

[1] Marciniak Z, Duncan JL, Hu SJ, Mechanics of Sheet Metal Forming, 2nd edition, Elsevier, 2002.

[2] J.C. Benedyk, D. Stawarz, N.M. Parikh, "A method for increasing elongation values for Ferrous and NonFerrous sheet metals", J. of Materials, Vol. 6, No. 1, 1971, 16-29.

[3] Hadoush, A. H. Van den Boogaard, J. Huetink. "Stable incremental deformation of a strip to high strain." Key Engingeering Materials, Vol. 344, 2007, 615-620.

[4] W. C. Emmens, A. H. van den Boogaard, "Incremental forming by continuious bending under tension - an experimental investigation", J. of Materials Processing Technology, Vol. 209, No. 14, 2009, 5456-5463.

[5] A.Hadoush, A.H. van den Boogaard, W.C. Emmens, "A numerical investigation of the continuous bending under tension test", J. of Materials Processing Technology, Vol. 211, No. 12, 2011, 1948-1956

[6] W.C. Emmens, A.H. van den Boogaard, "Cyclic stretch-bending: mechanics, stability and formability", J. of Materials Processing Technology, Vol. 211, 2011, 1965-1981

[7] R. P. R. Cardoso, J. W. Yoon, M. Mahardika, S. Choudhry, R. J. Alves de Sousa, R. A. Fontes Valente, "Enhanced assumed strain (EAS) and assumed natural strain (ANS) methods for one-point quadrature solid-shell elements", International Journal for Numerical Methods in Engineering, Vol. 75, 2008, 156-187.

[8] A.H. van den Boogaard, W. C. Emmens, J. Huetink, "Effect of Thickness Stress in Stretch-Bending", 10th Numiform Conference, Pohang, Korea, 2010.

JJMIE

Volume 5, Number 6, Dec. 2011
ISSN 1995-6665
Pages 559 - 565

Jordan Journal of Mechanical and Industrial Engineering

Heat Transfer and Friction Factor in a Tube Equipped with U-cut Twisted Tape Insert

P. Murugesan*,a , K. Mayilsamy[b], S. Suresh[c],

[a]Department of Mechanical Engineering, K.S. Rangasamy College of Technology, Tiruchengode-637215, India.
[b]Department of Mechanical Engineering, Institute of Road and Transport Technology, Erode- 638316, India.
[c]Department of Mechanical Engineering, National Institute of Technology, Tiruchirappalli-620015, India.

Abstract

Experimental investigation of heat transfer and friction factor characteristics of circular tube fitted with plain twisted tapes (PTT) and U–cut twisted tapes (UTT) with twist ratios y = 2.0, 4. 4 and 6.0 were studied. The experimental data obtained from plain tube and PTT were verified with the standard correlation to ensure the validation of experimental results. The experimental results reveal that heat transfer rate, friction factor and thermal enhancement factor in the tube equipped with UTT significantly higher than those in the tube fitted with PTT and plain tube. The additional disturbance and secondary flow in the vicinity of the tube wall generated by the UTT compared to that induced by the PTT is referred as the reason for the enhancement. Subsequently an empirical correlation is also formulated to match with experimental results with ± 6% and ± 5%, variation respectively for Nusselt number and friction factor.

Keywords: heat transfer enhancement; friction factor; plain twisted tape; U –cut twisted tape; secondary flo

Nomenclature

A	Area	: [m^2]
C_p	Specific heat	: [J/kg K]
d	Tube diameter,	: [m]
d_e	U-cut depth	: mm
D_h	Hydraulic diameter	: [m]
f	Friction factor	
h	Heat transfer coefficient	: [W/m^2 K]
H	Pitch length based on 180°	: [m]
k	Thermal conductivity	: [W/m K]
L	Tube length	: [m]
m	Mass flow rate	: [kg/s]
Nu	Nusselt number	
ΔP	Pressure drop	
Pr	Prandtl number	
Q	Heat transfer rate	: [W]
Re	Reynolds number	
T_h	Hot water temperature	: °C
T_c	Cold water temperature	: °C
ΔT_{lm}	Logarithmic mean temperature difference	
U	Overall heat transfer coefficient	: [W/m^2 K]
u	Velocity	: [m/s]
W	Twisted tape width	: mm
w	U- cut width	: mm
y	Twist ratio	
ρ	Density	: [kg/m^3]
μ	Dynamic viscosity	: [kg/m-s]
η	Thermal enhancement factor	

Subscripts

avg	: Average
a	: Annulus
c	: Cold water
h	: Hot water
i	: Inner
lm	: Logarithmic mean temperature
o	: Outer
p	: Plain tube
t	: Turbulator
1	: Inlet
2	: Outlet

Abbreviations

PTT	: Plain twisted tape
UTT	: U –cut twisted tape

1. Introduction

Heat transfer augmentation techniques are widely used in areas such as heat recovery process, air conditioning and refrigeration systems, and chemical reactors. Passive and active methods of heat transfer augmentation techniques have been discussed [1]. The passive techniques particularly twisted tape and wire coil insert are economical heat transfer augmentation tools [2]. The heat transfer and friction factor characteristics in a circular tube fitted with different tube inserts were experimentally investigated and correlations for Nusselt number and

* Corresponding author. e-mail: pmksrct@gmail.com

friction factor were proposed [3-7]. The heat transfer and friction factor characteristics were experimentally compared between smooth twisted tape with broken and serrated twisted tape inserts [8 & 9]. More information about heat transfer by means of twisted tapes fitted in a circular tube can be viewed in other reports [10-14].

Based on the available literature, it was pointed out that the modification on PTT i.e. small cuts on the tape [6-9], for example delta –winglet tape (DWT), peripherally –cut tape (PT), broken tape and serrated tape gave assurance for enhancement of both heat transfer rate and thermal enhancement factor. The reason behind the high thermal enhancement factor is that those small gaps bring pressure drop in the system to the reasonable level.

The present work reports the experimental work on heat transfer rate and friction factor characteristics of tube in tube heat exchanger fitted with PTT and UTT for twist ratios 2.0, 4.4 and 6.0 with Reynolds number between 2000 and 12000. The modified twisted tapes comprise U –cut alternately in the peripheral region of the tape. This type of tape is believed to perform in same manner as mentioned in the literature for the case of broken or spiky tape, delta –winglet tape and peripherally –cut tapes. The experimental results obtained for the tube fitted with UTT were also compared with those for the tube fitted with PTT and the plain tube.

2. Experimental details

Schematic diagram of the experimental set-up is shown in figure 1. It consists of two concentric tubes in which hot water flows through the inner tube (Copper tube, d_i = 25 mm, L = 2000 mm) and cold water flows in counter flow through annulus (GI pipe, d_i = 54.5 mm). The outer tube is insulated with asbestos rope and glass wool to minimize the heat loss with the surroundings (Insulation thickness = 10 mm). Two calibrated crystal rotameters having flow ranges of 0-20 l min-1 with ±0.1 l min-1 accuracy are used to measure the cold and hot water flow rates. Seven RTD Pt 100 type temperature sensors with ±0.1ºC accuracy are used to measure the inlet and outlet temperature of the hot and cold water.

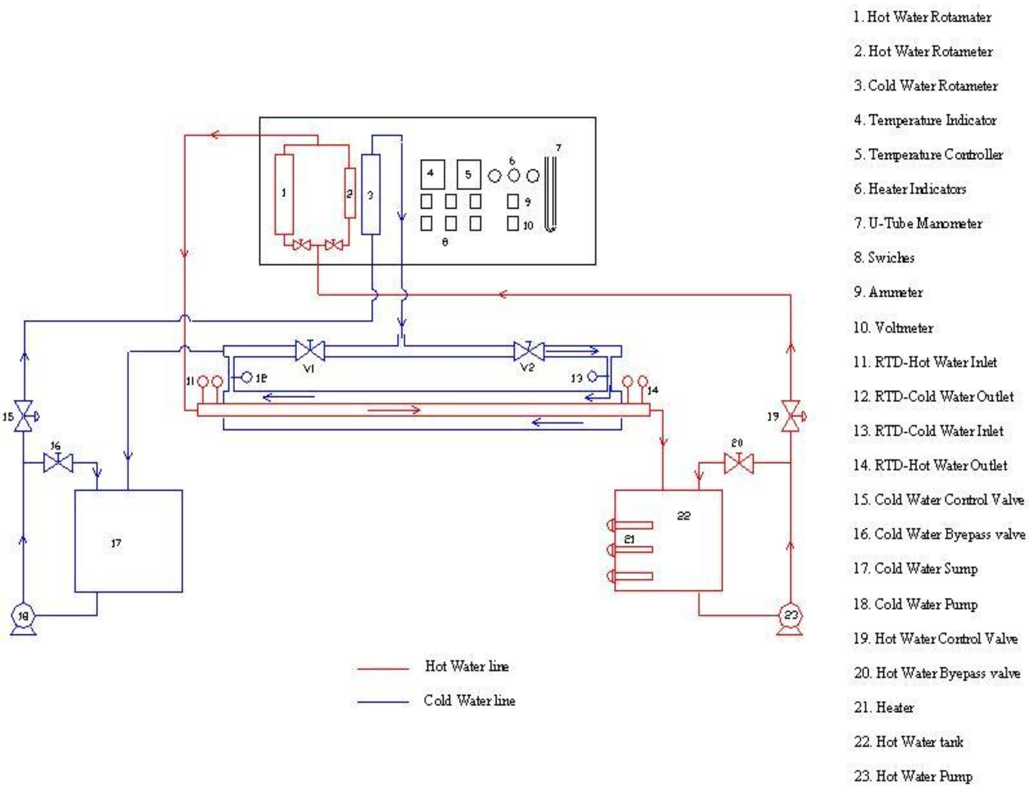

Figure 1: Schematic diagram of the experimental set-up.

Twisted tapes are made up of aluminum strips [11] of thickness 1.5 mm and width 23.5 mm. The twist ratio (y) is defined [2, 3 & 11] by ratio between one length of twist (or) pitch length (H = 50, 110, and 150 mm) to diameter. In the experimentation PTT and UTT with twist ratios 2.0, 4.4 and 6.0 are used. Geometries of the PTT and UTT are shown in figure 2(a-b). U -cut twisted tapes (figure 2b) with U –cut (8 mm depth and 8mm width) alternately in the peripheral region of the tape to increase the disturbance near the walls of the test section. The water is heated using 3 kW water heaters and the desired temperature is controlled by temperature controller. The inlet temperatures at the hot and cold water sides were kept constant at 54ºC and 30ºC, respectively. The cold water was constantly flowed at 0.166 kg s-1 whereas the hot water flow rate was adjusted from 0.033 kg s-1 to 0.12 kg s-1.

© 2011 Jordan Journal of Mechanical and Industrial Engineering. All rights reserved - Volume 5, Number 6 (ISSN 1995-6665)

As steady state conditions were reached, the inlet and outlet temperatures of hot and cold water were recorded and pressure drop was measured using U tube manometer (manometric fluid –Carbon tetra chloride) for the case of plain tube. Thereafter, the experiment was repeated for PTT and UTT.

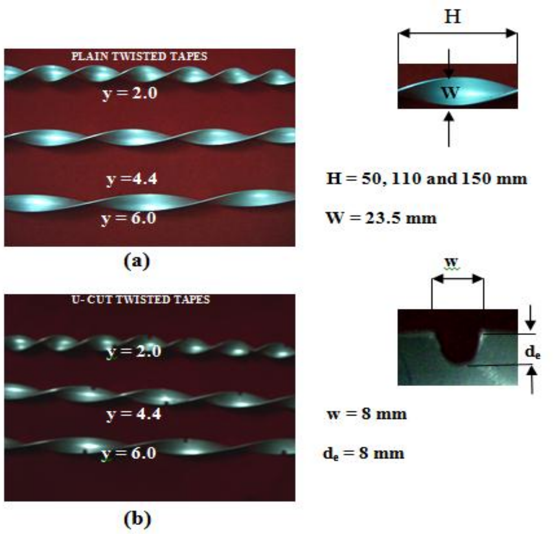

Figure 2: Geometries of twisted tapes with twist ratios y= 2.0, 4.4 and 6.0 (a) PTT (b) UTT.

3. Data reduction

The data reduction [3,10] of the measured results is summarized as follows:

Heat transferred to the cold water in the test section:

$$Q_c = m_c C_p (T_{c2} - T_{c1}) \tag{1}$$

Heat transferred from the hot water in the test section

$$Q_h = m_h C_p (T_{h1} - T_{h2}) \tag{2}$$

The error [14] in the present heat exchanger can be given as:

$$\%\text{error} = \left(\frac{Q_h - Q_c}{Q_c}\right) \times 100\% \tag{3}$$

The percentage of error was found out to be 2% to 8%. Thus it was concluded that the heat loss to the surroundings was reasonably small.

The average heat transfer rate for hot and cold water side

$$Q_{avg} = \frac{Q_c + Q_h}{2} \tag{4}$$

The over all heat transfer coefficient

$$U = \frac{Q_{avg}}{A_i \Delta T_{lm}} \tag{5}$$

Where,

$$A_i = \pi d_i L$$

The tube side heat transfer coefficient (h_i)

$$\frac{1}{U} = \frac{1}{h_i} + \frac{1}{h_a} \tag{6}$$

Where the annulus side heat transfer coefficient (h_a) is estimated using the correlation of Dittus -Boelter equation:

$$Nu_a = \frac{h_a D_h}{k} = 0.023\, Re^{0.8}\, Pr^{0.4} \tag{7}$$

Where, D_h = Hydraulic diameter = $d_i - d_o$

Thus,

$$Nu_i = \frac{h_i d_i}{k} \tag{8}$$

Friction factor

$$f = \frac{\Delta p}{\left[\frac{L}{d_i}\right]\left[\frac{\rho u^2}{2}\right]} \tag{9}$$

4. Results and Discussion

4.1. Plain tube data:

The variation of Nusselt number with Reynolds number for plain tube is shown figure 3a.

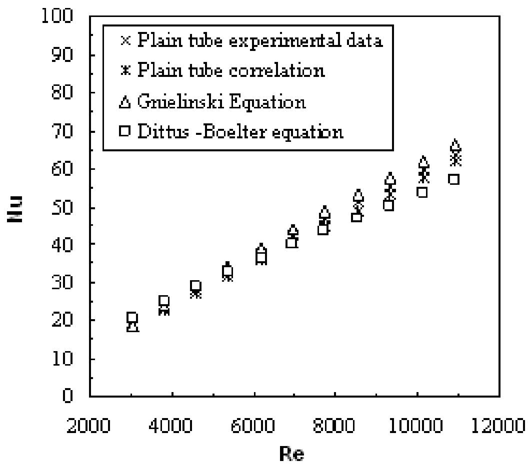

(a)

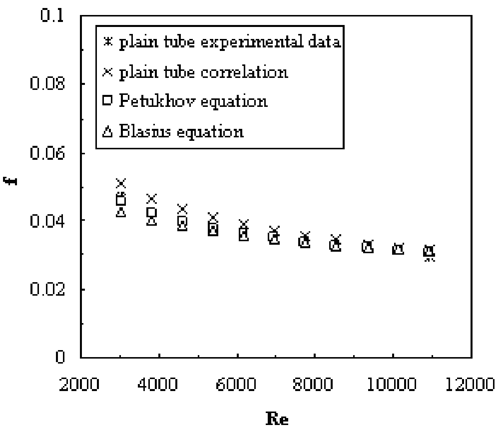

(b)

Figure 3: Validation of Plain tube: (a) Nusselt number and (b) friction factor.

The experimental data are matching with the plain tube forced convection correlations [15] of Dittus–Boelter (1930) (10) and Gnielinski (1976) equation (11) with the discrepancy of ± 8% and ± 5.0% respectively for the Nusselt number.

$$Nu = 0.023\,Re^{0.8}\,Pr^{0.3} \qquad (10)$$

$$Nu = \frac{\left(\frac{f}{8}\right)\left(Re - 1000\right)\,Pr}{1 + 12.7\left(\frac{f}{8}\right)^{0.5}\left(Pr^{\frac{2}{3}} - 1\right)} \qquad (11)$$

The variation of friction factor with Reynolds number for plain tube is shown in figure 3b. The data obtained by the experiment is compared with Blasius (12) and Petukhov (1970) equation (13) with the deviation of ± 10% and ± 8% respectively for the friction factor.

$$f = 0.0791\,Re^{-0.25} \qquad (12)$$

$$f = \left(0.790 \ln Re - 1.64\right)^{-2} \qquad (13)$$

In addition, the experimental results of the plain tube are correlated and the equation for Nusselt number (14) and friction factor (15) as follows:

$$Nu = 0.00595\,Re^{0.95}\,Pr^{0.33} \qquad (14)$$

$$f = 0.255\,Re^{-0.374} \qquad (15)$$

The equations (14) and (15) are found to represent the experimental data within ±4% for Nusselt number and ±6% for friction factor deviation is shown in figure. 3(a-b). These correlations (14) & (15) are useful to evaluate the thermal enhancement factor associated by PTT and UTT.

4.2. Plain twisted tape (PTT) data:

The tube fitted with PTT experimental results are validated using the correlations developed by Manglik and Bergles [12] which yields maximum deviation of ± 20 % [6, 7, 11 & 13] for both Nusselt number and friction factor respectively. Nusselt number and friction factor of a tube fitted with PTT are compared with the results obtained from the correlations by Manglik and Bergles [12] for the twist ratios of y = 2.0, 4.4 and 6.0 as demonstrated in figure 4(a-b). Apparently, present results reasonably agree well with the available correlations with in ± 10% for Nusselt number and ± 20% friction factor respectively.

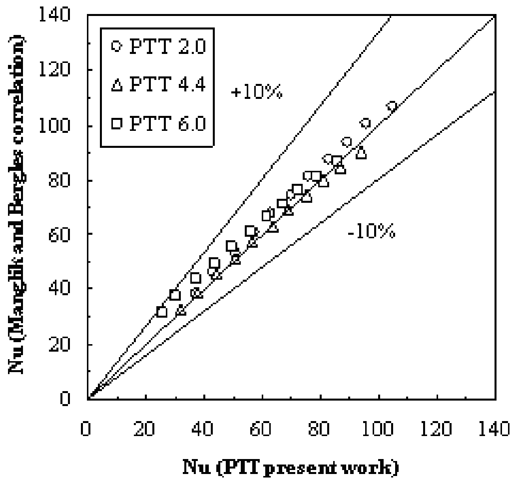

(a)

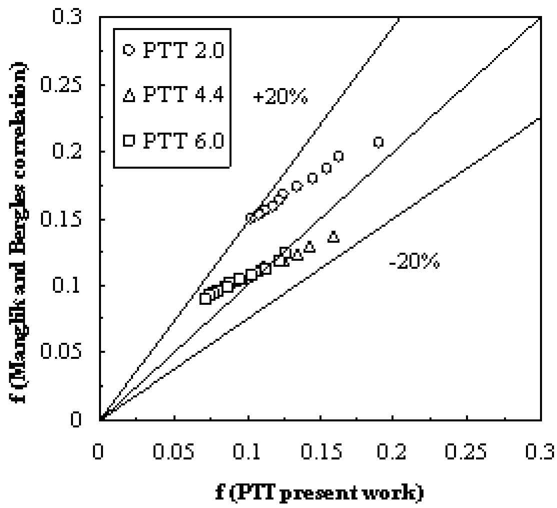

(b)

Figure 4: Validation of Plain twisted tapes (a) Nusselt number and (b) friction factor.

4.3. Effect of U –cut twisted tape (UTT) on heat transfer:

Variation of Nusselt number with Reynolds number in the tube fitted with UTT, PTT and also the plain tube are presented in figure 5. It is observed that for all cases, Nusselt number increases with increasing Reynolds number. As expected, PTT heat transfer rates are higher than those from the plain tube fitted without twisted tape and also lower twist ratio (y =2.0) heat transfer rate is higher than those from higher ones (y = 4.4 and 6.0) due to increase in turbulent intensity and flow length across the range of Reynolds number. Mean Nusselt numbers for PTT with twist ratios, y =2.0, 4.4 & 6.0 are respectively, 1.67, 1.50 and 1.32 times better than that for the plain tube.

Nusselt number (figure 5) in the tube with UTT is higher than those in the plain tube and tube with PTT insert over the range of Reynolds number 2000-12000. UTT provides an additional disturbance to the fluid in the vicinity of the tube wall and vorticity behind the cuts and thus leads to a higher heat transfer enhancement in comparison with plain tube and PTT. In the range of the present experiments considered, mean Nusselt numbers for tube equipped with UTT of twist ratios of 2.0, 4.4 and 6.0, are respectively 1.81, 1.61 and 1.40 times of that plain tube and 1.08, 1.07 and 1.06 times of that for the tube equipped with PTT.

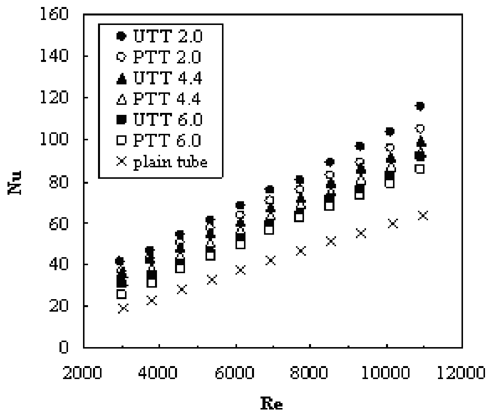

Figure 5: U–Cut (UTT) and Plain twisted tapes (PTT): Nusselt number Vs Reynolds number.

4.4. Effect of U–cut twisted tape (UTT) on friction factor:

Variation of friction factor with Reynolds number in the tube fitted with UTT, the tube fitted with PTT and also the plain tube are depicted in figure 6. It shows that friction factor continues to decrease with Reynolds number and friction factor for lower twist ratio (y = 2.0) is significantly more than that of higher twist ratios (y = 4.4 & 6.0) due to stronger swirl flow in the tube. Over range studied, the mean friction factor for the PTT with twist ratios, y =2.0, 4.4 and 6.0 are respectively, 3.48, 2.92 and 2.45 times higher than that for the plain tube.

It shows (figure 6) that UTT yields higher pressure drop those in the plain tube as well as the tube fitted with PTT. This is because of additional disturbance increases the tangential contact between secondary flow and the wall surface of the tube. Mean friction factor for the UTT with twist ratios of 2.0, 4.4 and 6.0 are respectively, 3.82, 3.28 and 2.8 times of that for the plain tube and 1.09, 1.12 and 1.16 times of that for the tube with PTT insert.

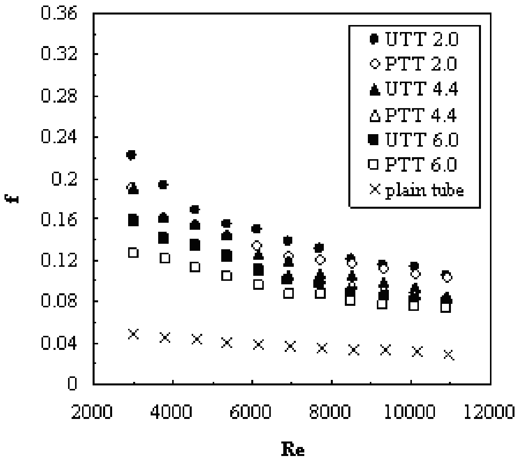

Figure 6: U–Cut (UTT) and Plain twisted tapes (PTT): Nusselt number Vs friction factor.

The following correlations for Nusselt number and friction factor developed for the present experimental results respectively for a plain tube fitted with PTT equation (16, 17) and UTT equation (18, 19) .

$$Nu = 0.027\,Re^{0.862}\,Pr^{0.33}\,y^{-0.215} \tag{16}$$

$$f = 2.642\,Re^{-0.474}\,y^{-0.302} \tag{17}$$

$$Nu = 0.044\,Re^{0.817}\,Pr^{0.33}\,y^{-0.224} \tag{18}$$

$$f = 6.705\,Re^{-0.575}\,y^{-0.257} \tag{19}$$

The fitted values are agreeing with experimental data within ± 6%, ± 5% respectively, for both Nusselt number and friction factor shown in figure 7 (a-b).

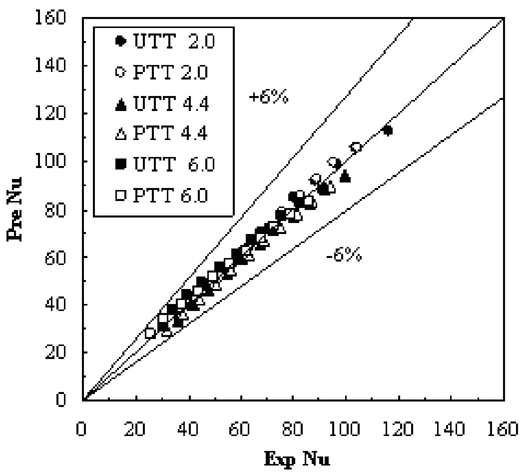

(a)

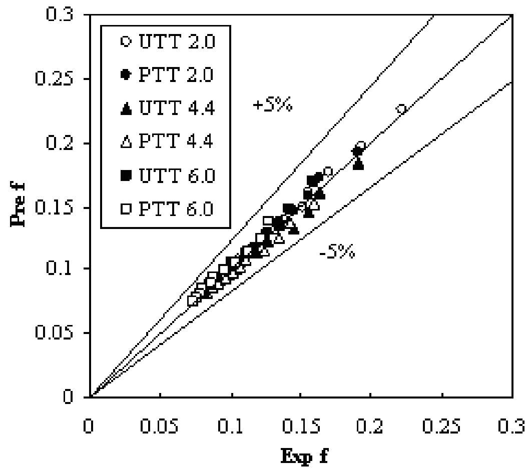

(b)

Figure 7: Comparison between predicted and experimental results (a) Nusselt number and (b) friction factor.

4.5. Thermal enhancement factor for PTT and UTT:

According to the literature studies [6-7] a comparison of heat transfer coefficients in a plain tube (p) and the tube fitted with turbulator (t) was made at the same pumping power since it is relevant to operation cost.

For constant pumping power

$$(\dot{V}\,\Delta P)_p = (\dot{V}\,\Delta P)_t \tag{20}$$

Where the relationship between friction factor and Reynolds number can drawn as below

$$(f\,Re^3)_p = (f\,Re^3)_t \tag{21}$$

Thermal enhancement factor (η) at equal pumping power is defined as ratio of the convective heat transfer coefficient of the tube with turbulator to that of the plain tube which can be expressed as

$$\eta = \left|\frac{h_t}{h_p}\right|_{pp} \tag{22}$$

Using equations (15), (17), (19) and (21), the Reynolds number for the plain tube $(Re)_p$ is written as the function of Reynolds number $(Re)_t$ for the tube with turbulator for PTT equation (23), UTT equation (24)

$$Re_p = 2.436\,Re_t^{0.962}\,y^{-0.115} \tag{23}$$

$$Re_p = 3.473\,Re_t^{0.924}\,y^{-0.098} \tag{24}$$

Employing equations (14), (16), (18) and (22), the enhancement efficiency for the plain twisted tape and U-cut twisted tape can be written as

$$\eta_{(PTT)} = \left|\frac{h_t}{h_p}\right|_{pp} = 1.95\,Re_t^{-0.052}\,y^{-0.106} \tag{25}$$

$$\eta_{(UTT)} = \left|\frac{h_t}{h_P}\right|_{PP} = 2.27\,Re_t^{-0.060}\,y^{-0.131} \tag{26}$$

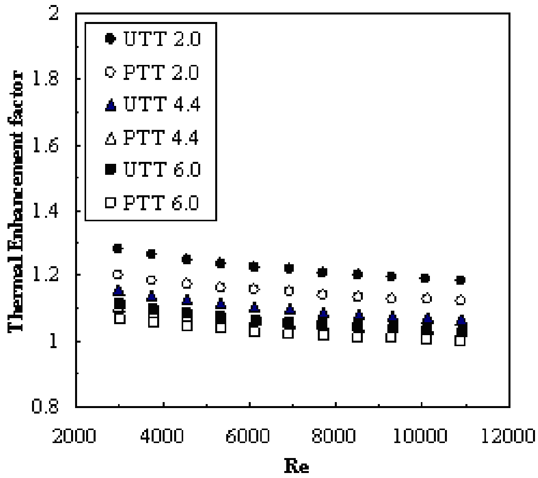

Figure 8: Thermal enhancement factor Vs Reynolds number for tube with PTT and UTT.

Thermal enhancement factor for PTT and UTT at different twist ratios y = 2.0, 4.4 and 6.0 calculated from equations (25) and (26) respectively for PTT and UTT are presented in figure 8.

At the same Reynolds number, the thermal enhancement factors for UTT are found to be greater than those for the PTT. The thermal enhancement factor for all twisted tapes tends to decrease with increasing Reynolds number. With the use of PTTs, thermal enhancement factors were in a range between, 1.12 - 1.2, 1.03 -1.10 and 1.0 - 1.06 respectively for the twist ratios y = 2.0, 4.4 and 6.0. On the other hand the use of UTTs offered thermal enhancement factors in a range between 1.19 - 1.28, 1.07 - 1.16 and 1.03 - 1.11 respectively for the twist ratios y = 2.0, 4.4 and 6.0. The above data indicates that the use of UTTs gave more efficient heat transfer enhancement than the application of PTT.

5. Conclusion

Experimental investigations of heat transfer, friction factor and thermal enhancement factor of circular tube fitted with PTT and UTT in turbulent regimes (2000<Re<12000) for twist ratios 2.0, 4.4 and 6.0 are described in the present report. The conclusions can be drawn as follows:

- The Nusselt number and friction factor values for the tube with UTT are noticeably higher than that of plain tube and also tube equipped with PTT.
- Over the range of Reynolds number considered average thermal enhancement factors in the tube equipped with PTT are found 1.15, 1.06, and 1.02 and tube equipped with UTT are 1.22, 1.10 and 1.06 respectively for twist ratios y =2.0, 4.4 and 6.0. The thermal enhancement factors for all the cases are more than unity indicates that the effect of heat transfer enhancement due to the enhancing tool is

more dominant than the effect of rising friction factor and vice versa

- The empirical correlations for the Nusselt number, friction factor and the thermal enhancement factor for PTT and UTT are developed and it was reasonably fitted with the experimental data.
- The UTT offered better heat transfer enhancement than that PTT therefore UTT can be used in place of PTT to reduce the size of heat exchanger.

References

[1] R. L. Webb, N. Hyun Kim, "Principles of Enhanced Heat transfer", Second edition, Taylor Francis Group; 2005.

[2] Dewan, P. Mahanda, K. Sumithra Raju and P. Suresh Kumar, "Review of passive heat transfer augmentation techniques", J. Power and Energy, Vol. 218, Part A, 2004, 509-527.

[3] S. Eiamsa-ard, C. Thianpong and P. Promvonge, "Experimental investigation of heat transfer and flow friction in a circular tube fitted with regularly spaced twisted tape elements", Int. Communications in Heat and Mass Transfer, Vol. 33, No. 10, 2006, 1225-1233.

[4] S. Eiamsa-ard, and P. Promvonge, "Heat transfer characteristics in a tube fitted with helical screw -tape with /with out core-rod inserts", Int. Communications in Heat and Mass Transfer, Vol. 34, No. 2, 2007, 176 -185.

[5] S. Eiamsa-ard, S. Pethkool, C.T. Pong and P. Promvonge, "Turbulent flow heat transfer and pressure loss in a double pipe heat exchanger with louvered strip inserts", Int. Communications in Heat and Mass Transfer, Vol. 35, No. 2, 2008, 120-129.

[6] S. Eiamsa-ard, K. Wongcharee, P. Eiamsa-ard and C.Thianpong, "Heat transfer enhancement in a tube using delta-winglet twisted tape inserts", Applied Thermal Engineering, Vol. 30, No. 4, 2010, 310-318 .

[7] S. Eiamsa-ard, P. Seemawute and K. Wongcharee, "Influences of peripherally –cut twisted tape insert on heat transfer and thermal performance characteristics in a laminar and turbulent tube flows", Exp. Thermal and Fluid Science, Vol. 34, No. 6, 2010, 711-719.

[8] S. W. Chang, T. L. Yang and J. S. Liou, "Heat transfer and pressure drop in a tube with broken twisted tape insert", Exp. Thermal and Fluid Science, Vol. 32, No. 2, 2007, 489-501.

[9] S. W. Chang, Y. J. Jan and J. S. Liou, "Turbulent heat transfer and pressure drop in tube fitted with serrated twisted tape", Int. Journal of Thermal Sciences, Vol. 46, No. 5, 2007, 506-518.

[10] C. Thianpong, P. Eiamsa-ard, K. Wongcharee and S. Eiamsa-ard, "Compound heat transfer enhancement of a dimpled tube with a twisted tape swirl generator" Int. Communications in Heat and Mass Transfer, Vol. 36, No. 7, 2009, 698 -704.

[11] S. K. Agarwal and M. Raja rao, "Heat transfer augmentation for the flow of a viscous liquid in circular tubes using the twisted tape inserts", Int. J. Heat Mass Transfer, Vol. 39, No. 17, 1996, 3547-3557.

[12] R. M. Manglik and A. E. Bergles, "Heat transfer and pressure drop correlations for twisted –tape inserts in isothermal tubes: Part II- Transition and turbulent flows", Transaction of ASME, J. Heat Transfer, Vol. 115, 1993, 890-896.

[13] S. Al-Fahed and W. Chakroun, "Effect of tube- tape clearance on heat transfer for fully developed turbulent flow in a horizontal isothermal tube", Int. J. Heat and Fluid Flow, Vol. 17, No. 2, 1996, 173-178.

[14] L. D. Tijing, B. C. Pak, B. J. Baek and D.H. Lee, "A study on heat transfer enhancement using straight and twisted internal fin inserts", Int. Communications in Heat and Mass Transfer, Vol. 33, No. 6, 2006, 719-726.

[15] Y. A. Cengel, "Heat and Mass transfer", 5th edition, McGraw-Hill, 2008.

JJMIE

Volume 5, Number 6, Dec. 2011
ISSN 1995-6665
Pages 567 - 571

Jordan Journal of Mechanical and Industrial Engineering

Linearization of Nonlinear Dynamical Systems: A Comparative Study

M. Ababneh*[,a], M. Salah[a], K. Alwidyan[a]

[a]Mechatronics Engineering Department, Hashemite University, P.O. Box 330127, Zarqa 13133, Jordan

Abstract

Linearization of nonlinear dynamical systems is a main approach in the designing and analyzing of such systems. Optimal linear model is an online linearization technique for finding a local model that is linear in both the state and the control terms. In this paper, a comparison between the performance of both optimal linear model and Jacobian linearization technique is conducted. The performance of these two linearization methods are illustrated using two benchmark nonlinear systems, these are inverted pendulum system; and Duffing chaos system. These two systems where chosen because they are inherently nonlinear unstable systems.

Keywords: Nonlinear systems; linearization; inverted pendulum.

1. Introduction

Linearization of nonlinear dynamical systems makes use of available literature in the linear system to design and analyze nonlinear systems [1]. Optimal linear model is a promising linearization technique that continues to find wide acceptance in the areas of nonlinear and chaos systems [2, 3, 4]. This method was first introduced by Teixeira and Zak [5].

In fact, typical approach to handle nonlinear systems is to utilize linearization at their operating points, including Jacobian analysis for local dynamics of control systems. Optimal linear model is another method that generates optimal local models; it is an online linearization technique for finding a local model that is linear in both the state and the control terms. This technique provides a new tool to control nonlinear systems and it is briefly described in the next section.

Furthermore, the inverted pendulum problem has been used as benchmark to motivate the study of nonlinear control systems and techniques [6, 7]. This system is inherently nonlinear unstable non-minimum phase system and provides a challenging system to test different control techniques [8].

In addition, Duffing system is well-known chaos attractor and has used to address many practical applications in Engineering and Science [9, 10]. In this paper two Duffing systems are synchronized together. Where synchronization is when two systems come to behave in accordance with each other as time passes.

The rest of paper is organized as follows. In Section 2, the optimal linear model is discussed and generation of linearized models around operating points is shown In Section 3, the effectiveness of the optimal linear model is demonstrated and its performance is compared with the Jacobian method performance. Finally, conclusions are presented in section 4.

2. Optimal Linear Model of Non-linear Systems

Consider a nonlinear system model

$$\dot{x}(t) = F(x(t)) + G(x(t))u(t), \tag{1}$$

where $F:\Re^n \to \Re^n$ and $G:\Re^n \to \Re^{nxm}$ are nonlinear function, $x(t) \in \Re^n$ is the state vector, and $u(t) \in \Re^m$ is the control input. The optimal linear model objective is to find linearized models of a nonlinear dynamical system around operating points and it is described as follows.

Suppose that it is desired to have a local linear model (A_{op}, B_{op}) at the *i-th* operation point of interest (x_{op}, u_{op}), which is not necessarily an equilibrium point of the system. Let the linearized model be given as

$$\dot{x}(t) = A_{op}x(t) + B_{op}u(t) \tag{2}$$

where A_{op} and B_{op} are constant matrices of appropriate dimensions. For this purpose, Taylor expansion method is commonly used in this case, however, the truncation used in this method results in an affined rather than linear model. Suppose that the operating point (x_{op}, u_{op}) is an equilibrium point, where $x_{op}(t) \in \Re^n$ and $u_{op}(t) \in \Re^m$, that is,

$$F(x_{op}) + G(x_{op})\,u_{op} = 0. \tag{3}$$

The linear model then is expressed as:

$$\begin{aligned}\frac{d}{dt}(x - x_{op}) &= F(x_{op}) + G(x_{op})u_{op} + A_{op}(x - x_{op}) + B_{op}(u - u_{op}) \\ &= A_{op}(x - x_{op}) + B_{op}(u - u_{op}).\end{aligned} \tag{4}$$

---

[*] Corresponding author. e-mail: ababneh@hu.edu.jo

The model (4) can be represented in the following form:

$$\dot{x}(t) = A_{op}x(t) + B_{op}u(t) - (A_{op}x_{op} + B_{op}u_{op}). \tag{5}$$

The state equation (5) is an affined rather than a linear model due to the non-vanishing constant term in (5). One exception is the trivial case where the equilibrium point is zero, which, however, cannot be ensured throughout a nonlinear control process. The goal is to construct a local model, linear in state and also linear in control, that can well approximate the dynamical behavior of (1) around the operating point (x_{op}, u_{op}). In other words, two constant matrices, A_{op} and B_{op}, are to be found such that they are located in a neighborhood of x_{op},

$$F(x) + G(x)u \approx A_{op}x + B_{op}u \tag{6}$$

for any u,

and

$$F(x_{op}) + G(x_{op})u = A_{op}x_{op} + B_{op}u \tag{7}$$

for any u.

Since the control input u is to be designed, it is arbitrary, and therefore

$$B_{op} = G(x_{op}), \tag{8}$$

Furthermore,

$$F(x) \approx A_{op}x \tag{9}$$

And

$$F(x_{op}) = A_{op}x_{op} \tag{10}$$

Now let a_{op}^T denotes the *i*-th row of the matrix A_{op}. Then

$$F_i(x) \approx a_i^T x, \qquad i = 1,2,3,\cdots,n \tag{11}$$

and

$$F_i(x_{op}) = a_{op}^T x_{op}, \; i = 1,2,3,\cdots,n \tag{12}$$

where $F_i : \Re^n \to \Re$ is the *i*-th component of F. Then, expanding the left-hand side of (1) about x_{op}, and neglecting the second and higher order terms, the following equation can be obtained

$$F_i(x_{op}) + [\nabla F_i(x_{op})]^T (x - x_{op}) \approx a_i^T x, \tag{13}$$

where $\nabla F_i(x_{op}) : \Re^n \to \Re^n$ is the gradient column vector of F_i evaluated at x_{op}. Now, using (12), equation (13) can be written as

$$[\nabla F_i(x_{op})]^T (x - x_{op}) \approx a_i^T (x - x_{op}), \tag{14}$$

in which x is arbitrary but should be close to x_{op} so that the approximation is good. To determine a constant vector, a_i^T, such that it is as close as possible to $[\nabla F_i(x_{op})]^T$ and satisfies $a_i^T x_{op} = F_i(x_{op})$, consider the following constrained minimization problem:

$$\min \; E := \tfrac{1}{2}\left\|\nabla F_i(x_{op}) - a_i\right\|_2^2$$

subject to

$$a_i^T x_{op} = F_i(x_{op}) \tag{15}$$

Given that this is a constrained optimization problem; therefore, the first order necessary condition for a minimum of E is also sufficient, which is

$$\nabla_{a_i} E + \lambda \nabla_{a_i} (a_i^T x_{op} - F_i(x_{op})) = 0 \tag{16}$$

$$a_i^T x_{op} = F_i(x_{op}), \tag{17}$$

where λ is the Lagrange multiplier and the subscript a_i in ∇_{a_i} indicates that the gradient is taken with respect to a_i. Then

$$a_i - \nabla F_i(x_{op}) + \lambda x_{op} = 0. \tag{18}$$

Recalling the case where $x_{op} \neq 0$, so by solving (18), the following can be obtained

$$\lambda = \frac{x_{op}^T \nabla F_i(x_{op}) - F_i(x_{op})}{\left\|x_{op}\right\|_2^2}. \tag{19}$$

Substituting this λ into (18) gives

$$a_j = \nabla F_i(x_{op}) + \frac{F_i(x_{op}) - x_{op}^T \nabla F_i(x_{op})}{\left\|x_{op}\right\|_2^2} x_{op} \tag{20}$$

where $x_{op} \neq 0$ It is easily verified that when $x_{op} = 0$ equation (18) yields

$$a_i = \nabla F_i(x_{op}) \tag{21}$$

which is also a special case of (20).

3. Simulation Examples

Most often, control algorithms are tested on standard nonlinear models, and the objective is to first find the linearized model then to design suitable controller based on our skills with linear systems. These linearized models of the nonlinear model are valid only for small deviations of the state values from their nominal value. Such a nominal value is called the equilibrium point. Therefore, the linear models are acceptable around a small range of the operating point. In this section, the effectiveness of the above method described in previous section will be presented and its performance is compared with Jacobian method performance.

3.1. Inverted Pendulum:

The inverted pendulum, shown in Figure 1, is highly nonlinear system which can be considered as an important benchmark system for controller testing.

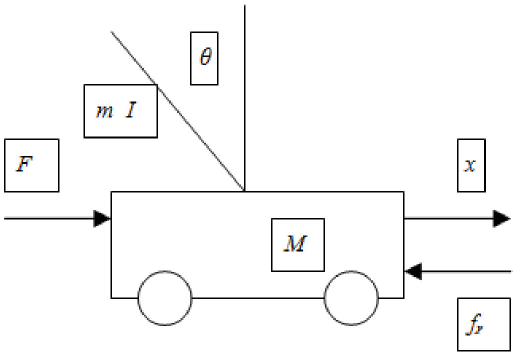

Figure 1: Inverted pendulum system.

The nonlinear dynamical equations of motion is given by [11].

$$\begin{aligned}&(m+M)\ddot{x}+f_r\dot{x}+ml\ddot{\theta}\cos\theta-ml\dot{\theta}^2\sin\theta=F\\&(I+ml^2)\ddot{\theta}-mgl\sin\theta+ml\ddot{x}\cos\theta=0\end{aligned} \tag{22}$$

where m is the pole mass, M is the cart mass, f_r is the cart friction coefficient, x is the horizontal displacement, l is the pole length, θ is the angle of the pole from upright position, F is the applied force on the cart, I is the pole moment of inertia, and g is the gravity. The state space model can be presented as follows:

$$\begin{bmatrix}x_1\\x_2\\x_3\\x_4\end{bmatrix}=\begin{bmatrix}0 & 1 & 0 & 0\\ 0 & \dfrac{-f_r(I+ml^2)}{(m+M)I+mMl^2} & \dfrac{m^2l^2g\cos x_3}{(m+M)I+mMl^2} & 0\\ 0 & 0 & 0 & 1\\ 0 & \dfrac{mlf_r\cos x_3}{mI+M(I+ml^2)} & \dfrac{-(m+M)mgl}{mI+M(I+ml^2)} & 0\end{bmatrix}\begin{bmatrix}x_1\\x_2\\x_3\\x_4\end{bmatrix}+\begin{bmatrix}0\\ \dfrac{(I+ml^2)}{(m+M)I+mMl^2}\\ 0\\ \dfrac{-ml\cos x_3}{mI+M(I+ml^2)}\end{bmatrix}u \tag{21}$$

Where

$[x_1\; x_2\; x_3\; x_4]^T=[\dot{x}\;\ddot{x}\;\dot{\theta}\;\ddot{\theta}]^T$.

Given equations (20) and (21) the optimal model

$$A_{op}=\begin{bmatrix}0 & 1 & 0 & 0\\ 0 & a & b(\cos x_3)-b(\sin x_3)x_3 & 0\\ 0 & 0 & 0 & 1\\ 0 & d(\cos x_3) & -d(\sin x_3)x_2+e & 0\end{bmatrix} \tag{24}$$

$$B_{op}=\begin{bmatrix}0\\c\\0\\h\cos x_3\end{bmatrix}\quad for\quad \|x\|_2^2=0\cos x_3$$

And

$$A_{op}=\begin{bmatrix}0 & 1 & 0 & 0\\ 0 & a+\dfrac{b(\sin x_3)x_3x_2}{\|x\|_2^2} & b(\cos x_3)-b(\sin x_3)x_3+\dfrac{b(\sin x_3)x_3^2}{\|x\|_2^2} & 0\\ 0 & 0 & 0 & 1\\ 0 & d(\cos x_3)+\dfrac{d(\sin x_3)x_2^2}{\|x\|_2^2} & -d(\sin x_3)x_2+e+\dfrac{d(\sin x_3)x_3x_2}{\|x\|_2^2} & 0\end{bmatrix} \tag{25}$$

$$B_{op}=\begin{bmatrix}0\\c\\0\\h\cos x_3\end{bmatrix}\quad for\quad \|x\|_2^2\neq 0$$

where

$$\|x\|_2^2=[x_1\;x_2\;x_3\;x_4][x_1\;x_2\;x_3\;x_4]^T,\; a=\frac{-f_r(I+ml^2)}{(m+M)I+mMl^2},\; b=\frac{m^2l^2g}{(m+M)I+mMl^2}$$

$$c=\frac{(I+ml^2)}{(m+M)I+mMl^2},\; d=\frac{mlf_r}{mI+M(I+ml^2)},\; e=\frac{-(m+M)mgl}{mI+M(I+ml^2)}$$

$$h=\frac{-ml}{mI+M(I+ml^2)}$$

The Jacobian model is gradient of the system is given by:

$$\frac{\partial F_i(x)}{\partial x}=\begin{bmatrix}0 & 1 & 0 & 0\\ 0 & a & b\cos x_3-b(\sin x_3)x_3 & 0\\ 0 & 0 & 0 & 1\\ 0 & d\cos x_3 & -d(\sin x_3)x_2+e & 0\end{bmatrix} \tag{26}$$

The inverted pendulum parameters are assigned the following values [11], m = 0.23 kg, M = 2.4 kg, l = 0.38 m. fr = 0.05 Ns/m, I = 0.099 kg.m2, and g = 9.81 m/s2. Furthermore, the simulation for the controllers, with pole placement at poles -1±j1 and -2±j1, was carried out in SimuLink of MatLab using a fifth-order Dormand-Prince algorithm with a fixed integration step of 0.005 and initial condition of [0, 0, 0, 1]T. The performances for both optimal linear model and Jacobian method are displayed in Figure 2. It is obvious that first method has less overshoot and better performance than the second method.

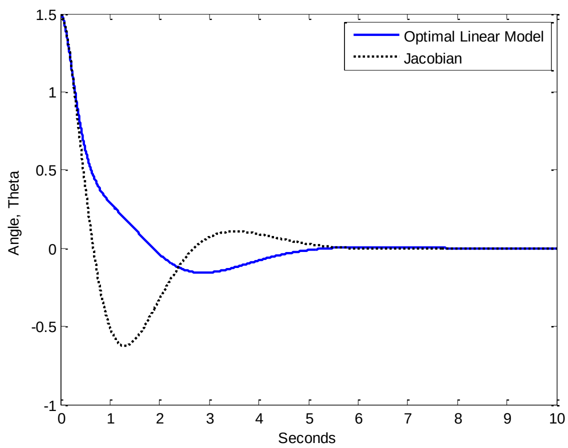

Figure 2: Comparison between Optimal linear model and Jacobian method.

  - Volume 5, Number 6 (ISSN 1995-6665)

3.2. Synchronization of Duffing System:

The chaotic Duffing system is a popular benchmark example in the study of nonlinear system. The Duffing system can be expressed as [4, 12]:

$$\begin{aligned} \dot{x}_1 &= x_2 \\ \dot{x}_2 &= -p_1 x_2 - p_2 x_1 - p_3 x_1^3 + q\cos(wt) \end{aligned} \tag{27}$$

with parameters p1 = -1.1, p2 = 0.4, p3 = 1, q = 1.8 and w =1.8, the system is chaotic and the attractor for uncontrolled system is shown Figure 3 below.

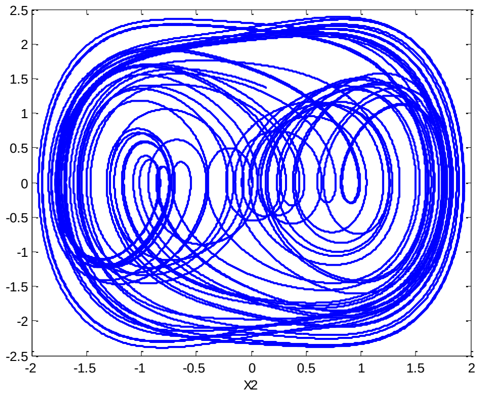

Figure 3: Duffing system chaotic attractor.

Applying equations (20) and (21), the optimal linear model is derived as:

$$A_{op} = \begin{bmatrix} 0 & 1 \\ -p_2 - 3p_3 x_{k1}^2 & -p_1 \end{bmatrix} \qquad for \quad \|x\|_2^2 = 0$$

$$A_{op} = \begin{bmatrix} 0 & 1 \\ -p_2 - 3p_3 x_1^2 + \dfrac{2p_3 x_1^4}{\|x\|_2^2} & -p_1 + \dfrac{2p_3 x_1^3 x_2}{\|x\|_2^2} \end{bmatrix} \quad for \quad \|x\|_2^2 \neq 0 \tag{28}$$

$$B_k = [0 \quad 1]^T$$

and

$$C_k = [1 \quad 0]$$

where and $\|x\|_2^2 = [x_1, x_2]^T [x_1, x_2]$ is the square magnitude of the operating point.

In general, synchronization is when two systems come to behave in accordance with each other as time passes; an example is the transmitter / receiver unit in communication system. The goal here is to consider the synchronization problem from the point of view of control theory [3]. Mathematically speaking, consider two dynamical systems,

$$\begin{aligned} \dot{x}(t) &= f(x(t)), \quad x(0) = x_0 \\ y(t) &= h(x(t)) \end{aligned} \tag{29}$$

and

$$\begin{aligned} \dot{\hat{x}}(t) &= \hat{f}(\hat{x}(t), y(t)), \quad \hat{x}(0) = \hat{x}_0 \\ \hat{y}(t) &= h(\hat{x}(t)) \end{aligned} \tag{30}$$

the two systems are said to be synchronized if

$$\lim_{t \to \infty} \|x(t) - \hat{x}(t)\| = 0 \tag{31}$$

For the optimal linearized model

$$\begin{aligned} \dot{x}(t) &= A_{op} x(t) + B_{op} u(t), \; x(0) = x_0 \\ y(t) &= Cx(t) \end{aligned} \tag{32}$$

with A_{op} and B_{op} are the matrices from optimal linear model, then an observer can be designed as

$$\begin{aligned} \dot{\hat{x}}(t) &= A\hat{x}(t) + Bu(t) + K_o(y(t) - \hat{y}(t)), \; \hat{x}(0) = \hat{x}_0 \\ \hat{y}(t) &= C\hat{x}(t) \end{aligned} \tag{33}$$

where K_o is the observer gain matrix.

The simulation for this synchronization was carried out in SimuLink of MatLab using a fifth-order Dormand-Prince algorithm with a fixed integration step of 0.005 and initial condition of [0, 5]T. Note that state x2 is the state that not measurable. The performance of synchronization for Duffing system is shown in Figure 4 for the optimal linear model and in Figure 5 for the Jacobian method. It is obvious that first method is superior to the second method, and it was able to synchronize completely with non-measurable state x2 but the Jacobian method fail to do so and the error was huge for most of the time.

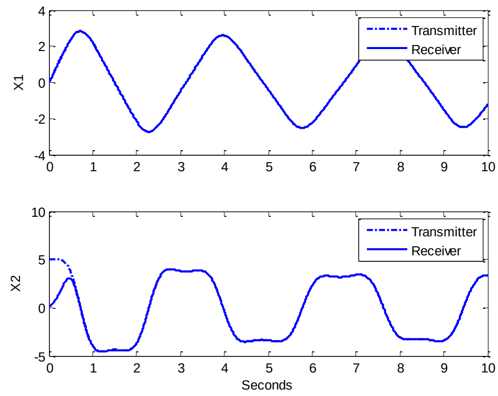

Figure 4: Synchronization of Duffing system using optimal linear model.

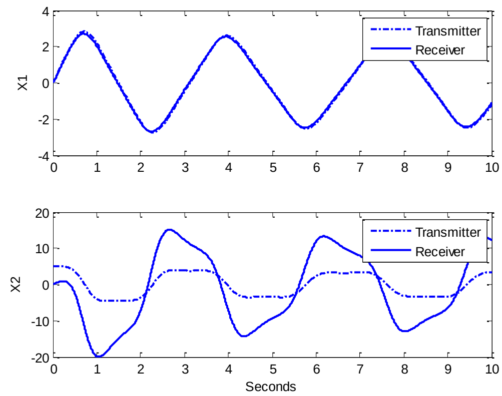

Figure 5: Synchronization of Duffing system using Jacobian method.

4. Conclusions

A linearization technique of optimal linear model was briefly presented in this paper, and its performance was compared with a popular Jacobian method. Two typical nonlinear benchmark examples were used to compare the two linearization methods; these are inverted pendulum and chaotic Duffing system. In the inverted pendulum example, the controllers were designed with pole placement for both cases, and as shown in Figure 2 the performance of first method was superior to the second method with much less overshoot. Furthermore, the synchronization of Duffing system was performed, as shown by the convincing simulation results in Figure 4 and 5, the optimal linear model was able to perfectly reproduce the non-measurable state x2, but the Jacobian failed to do so with large error. It is obvious from these results that optimal linear model has better performance than the Jacobian method, especially when the system is highly nonlinear. Future work might be in conducting performance comparison between optimal linear model and feedback linearization method.

References

[1] Fujimura, K., and Kiureghian, D. K., "Tail-equivalent linearization method for nonlinear random vibration" Probabilistic Engineering Mechanics, Volume 22, issue 1, 63-76, 2007.

[2] Tsai, J.S.H., Lu, F.-C., Provence, R.S., Shieh, L.S., and Han, Z., "A new approach for adaptive blind equalization of chaotic communication: The optimal linearization technique" Computers and Mathematics with Applications, 58, 1687-1698, 2009.

[3] Ababneh, M. K., "Digital Redesign of Uncertain Nonlinear Control Systems", Ph. D. Dissertation, University of Houston, Houston, 2004.

[4] Barajas-Ramirez, J, -G, Guangrong, R., C., Shieh, L. G, "Hybrid chaos synchronization", Computers and Mathematics with Applications, Vol. 13, No, 1197-1216, 2003.

[5] Teixeira, M. C. M. & Zak, S. H., "Stabilizing Controller Design for Uncertain Nonlinear Systems Using Fuzzy Models", IEEE Trans. on Fuzzy Systems, Vol. 7, No. 2, 133-142, 1999.

[6] Marzi, H., "Fuzzy control of an inverted pendulum using AC induction motor actuator", IEEE international conference in computational intelligent for measurement systems and applications, 2006.

[7] Xie, J. M., Xu, X., Xie., K Zak, S. H., "Modelling and simulation of the inverted pendulum based on granular hybrid system", Control and decision conference, 2008.

[8] Lozano, R., Fantoni, I., Block, D. J., "Stabilization of the inverted pendulum around its homoclinic orbit", Systems & control letters, Vol. 40, issue 3, 197-204, 2000.

[9] Panayotounakos, D. E., Theotokoglou, E.T., Markakis, M. P., "Exact analytic solutions for the damped Duffing nonlinear oscillator", C. R. Mecanique, 334, 311-31, 2006.

[10] Feng, Z., Chen, G., Hsu, S., "A qualitative study of the damped Duffing equation and applications", Discrete control systems, Ser. B5 (6), 1097-1112, 2006.

[11] Feedback Ltd, "Digital pendulum control experiments", 33-949S Experiments manual, Feedback instrument Ltd, 1999.

[12] Chen, G, Dong, X., “From chaos to order: Methodologies, perspectives and applications, World Scientific, Singapore, 1998.

المملكة الأردنية الهاشمية

الجامعة الهاشمية

المجلة الأردنية
للهندسة الميكانيكية والصناعية

JJMIE

مجلة علمية عالمية محكمة

http://jjmie.hu.edu.jo/

ISSN 1995-6665

المجلة الأردنية للهندسة الميكانيكية والصناعية

مجلة علمية عالمية محكمة

المجلة الأردنية للهندسة الميكانيكية والصناعية: مجلة علمية عالمية محكمة تصدر عن عمادة البحث العلمي و الدراسات العليا في الجامعة الهاشمية بالتعاون مع صندوق دعم البحث العلمي في الأردن.

ترسل البحوث إلى العنوان التالي:

رئيس تحرير المجلة الأردنية للهندسة الميكانيكية والصناعية

عمادة البحث العلمي والدراسات العليا

الجامعة الهاشمية

الزرقاء - الأردن

هاتف : 3903333 5 00962 فرعي 4147

Email: jjmie@hu.edu.jo

Website: www.jjmie.hu.edu.jo